Yang-Mills Thermodynamics of Photons and Its Application in Cosmology and Astroparticle Physics

BERGISCHE
UNIVERSITÄT
WUPPERTAL

This dissertation was carried out by

Janning Meinert at the

Bergische Universität Wuppertal, Fakultät 4,

Mathematik und Naturwissenschaften, Fachgruppe Physik

under the supervision of

Prof. Dr. Karl-Heinz Kampert

and

PD Dr. Ralf Hofmann

Institut für Theoretische Physik

Fakultät für Physik und Astronomie

Ruprecht-Karls-Universität Heidelberg

Wuppertal, the 17$^{\text{th}}$ of February 2025

this page is intentionally left blank

Zusammenfassung:

Diese Dissertation untersucht eine Reihe von Forschungsfragen in der Astroteilchenphysik und Kosmologie. Sie analysiert UHECR-Anisotropien in der Ankunftsrichtung, die durch das Magnetfeld der Milchstraße beeinflusst werden, sowie die Ausbreitung kosmischer Strahlen im lokalen Universum durch die kosmische Mikrowellenhintergrundstrahlung (CMB) unter Berücksichtigung einer modifizierten Temperatur-Rotverschiebungs-Beziehung ($T(z)$ oder T-z). Zusätzlich untersuchen wir grundlegende physikalische Konzepte, die eine modifizierte T-z-Relation im Rahmen eines dekonfinierenden SU(2)-Yang-Mills-Plasmas nahelegen könnten. Darüber hinaus befasst sich diese Arbeit mit einem Leptonmodell, das auf einer gemischten SU(2)-Yang-Mills-Thermodynamik basiert und eine Verbindung zwischen dem Leptonmassespektrum und dem Massenspektrum ultraleichter Axionen herstellt, welche als Kandidaten für die Dunkle Materie des Universums vorgeschlagen werden.

Eine Motivation aus der Kosmologie zur Betrachtung einer modifizierten CMB T-z Relation sind die aktuellen Spannungen (wie H_0, σ_8, S_8) im kosmologischen Standardmodell ΛCDM. Eine vorgeschlagene Erweiterung, $\mathrm{SU}(2)_{\mathrm{CMB}}$, beschreibt kosmische Mikrowellenhintergrund-Photonen im Rahmen einer SU(2)-Eichtheorie anstelle einer U(1)-Eichgruppe. Dies impliziert eine abgeflachte Temperatur-Rotverschiebungs-Relation. Dadurch werden einige dieser Spannungen reduziert, die Epoche der Rekombination zu höheren Rotverschiebungen verschoben und die CMB-Photonendichte bei gleicher Rotverschiebung effektiv verringert.

Darüber hinaus diskutiert diese Dissertation die Auswirkungen der modifizierten kosmischen Mikrowellenhintergrund-Evolution auf Multimessenger-Studien. Insbesondere untersuchen wir die Effekte der oben genannten ΛCDM-Erweiterung auf den Propagationshorizont ultrahochenergetischer kosmischer Strahlen (UHECR), erhöhte kosmogene Neutrinoflüsse und die veränderten Eigenschaften der Quellen, die aus dem UHECR-Spektrum abgeleitet werden. In verwandten Studien analysieren wir den Einfluss galaktischer Magnetfelder auf die Ausbreitung und Isotropie von UHECRs. Interessanterweise können bereits geringe zeitliche Variationen ($\sim$30%) im kosmischen Strahlungsfluss in den letzten mehrere Hunderttausend Jahre einen Dipol in der Ankunftsrichtung von UHECRs erzeugen, wie ihn die Auger-Kollaboration beobachtet.

Mehrere Ansätze zur experimentellen Überprüfung der oben genannten erwähnten, geänderten $T(z)$-Relation werden diskutiert. Während der Sunyaev–Zel'dovich-Effekt es nicht erlaubt, diese $T(z)$-Relation direkt aus den Daten zu extrahieren, ist die Ausbreitung ultrahochenergetischer kosmischer Strahlen dafür empfindlich. Es scheint, dass $\mathrm{SU}(2)_{\mathrm{CMB}}$ UHECR-Quellen wie Sternburst-Galaxien mit einer relativ stabilen Produktionsrate gegenüber aktiven galaktischen Kernen als primäre Quelle von UHECRs bevorzugt. Wir schließen daraus, dass die Frage nach der Natur der primären UHECR-Quellen direkt von der angenommenen Temperatur-Rotverschiebungs-Relation der CMB beeinflusst wird.

Darüber hinaus befasst sich diese Arbeit mit dem ARCADE 2-Radioüberschuss im CMB-Spektrum bei kleinen Frequenzen, welchen wir nicht als Vordergrundstrahlung, sondern als eine intrinsische Eigenschaft von Schwarzkörperstahlung interpretieren. Basierend auf $\mathrm{SU}(2)_{\mathrm{CMB}}$ untersuchen wir zudem theoretisch und experimentell spektrale Schwarzkörper-Anomalien bei höheren Temperaturen als der aktuellen CMB-Temperatur von $T_{\mathrm{CMB}} = 2.725$ K. Die Konsequenzen einer Erweiterung des kosmologischen Modells ΛCDM im Sinne von $\mathrm{SU}(2)_{\mathrm{CMB}}$ für Dunkle Materie und Dunkle Energie, den sogenannten dunklen Sektor, werden kurz diskutiert.

Summary:

This thesis explores a range of research questions in astroparticle physics and cosmology. It examines UHECR anisotropies in arrival direction, which are influenced by the Milky Way's magnetic field and the propagation of cosmic rays in the local Universe through the cosmic microwave background (CMB) with a modified temperature-redshift ($T(z)$ or T-z) relation. Additionally, we explore fundamental physics that may suggest a modified T-z relation within the framework of a deconfining SU(2) Yang-Mills plasma. Furthermore, this thesis also examines a lepton model based on mixed SU(2) Yang-Mills thermodynamics, linking the lepton mass spectrum to the mass spectrum of ultralight axions, which are proposed as candidates for the Universe's dark matter.

A motivation from cosmology to consider a modified CMB T-z relation is the current parameter tensions (such as H_0, σ_8, S_8) in the cosmological standard model ΛCDM. A proposed extension called $\mathrm{SU(2)_{CMB}}$ describes thermal cosmic microwave background photons in the framework of an SU(2) gauge theory instead of using the conventional U(1) gauge theory, which implies a flattened temperature-redshift relation. This reduces some of these tensions, pushes the recombination epoch to higher redshifts, and effectively reduces the CMB photon density at one and the same redshift.

Moreover, this thesis discusses the impact of the modified Cosmic Microwave Background evolution on multimessenger studies. In particular, we investigate the effects of the above-mentioned ΛCDM extension on the ultra-high-energy cosmic ray (UHECR) propagation horizon, increased cosmogenic neutrino fluxes, and the changes in source properties inferred from the UHECR spectrum. In related studies, we investigate the impact of galactic magnetic fields on the propagation and isotropy of UHECRs. Interestingly, only small temporal variations ($\sim$30%) in the cosmic ray flux within the last couple of several hundred-thousand years are able to reproduce a dipole in arrival direction of UHECRs as seen by the Auger collaboration.

Several venues to test the proposed changed $T(z)$ relation are discussed. Due to the redshift independence of the thermal Sunyaev–Zel'dovich effect, this T-z relation cannot be extracted from data. On the other hand, ultra-high-energy cosmic ray propagation is sensitive to this relation. It seems that $\mathrm{SU(2)_{CMB}}$ favours UHECR sources, such as starburst galaxies with a relatively steady production rate, over active galactic nuclei as the primary source class of UHECRs. We conclude that the question about the nature of primary sources of UHECRs is directly affected by the assumed T-z relation of the CMB.

Finally, we try to link the ARCADE 2 radio excess to an intrinsic feature of $\mathrm{SU(2)_{CMB}}$, a blackbody anomaly instead of a radio foreground. Based on an $\mathrm{SU(2)_{CMB}}$ model, we also investigate theoretically and experimentally spectral blackbody anomalies at higher temperatures than the current CMB temperature of $T_{\mathrm{CMB}} = 2.725$ K. The consequences of an extension of the ΛCDM cosmological model in the sense of $\mathrm{SU(2)_{CMB}}$ for dark matter and dark energy, the so-called dark sector, are briefly discussed.

Eidesstattliche Erklärung:

Hiermit versichere ich, dass ich die Arbeit selbstständig verfasst, keine anderen als die angegebenen Quellen und Hilfsmittel benutzt sowie Zitate kenntlich gemacht habe. Bei dieser Arbeit handelt es sich um eine kumulative Dissertation, die aus sechs Artikeln besteht [1, 2, 3, 4, 5, 6]. Jeder Artikel wurde im Wortlaut in ein jeweils eigenständiges Kapitel übernommen (Kapitel 2–7). Leichte Änderungen, bspw. bei der Anordnung von Grafiken sowie Formulierung von Gleichungen, wurden vorgenommen, um den Lesefluss zu erhöhen. Am Ende jeden Kapitels steht der Beitrag des Autors dieser Arbeit (JM) zu dem jeweiligen Artikel. Zwei der Artikel erscheinen in dieser Arbeit das erste Mal als Preprint (Kapitel 2, 5). Darüber hinaus gibt es Überschneidungen von Kapitel 3 mit dem Konferenzbeitrag [7], Kapitel 6 mit dem Konferenzbeitrag [8], sowie von Kapitel 7 mit dem Konferenzbeitrag [9].

Wuppertal, den 17.02.2025 ______________________________

this page is intentionally left blank

Contents

1 Introduction **1**
1.1 Project a): UHECR Anisotropy and Composition . . . 3
1.2 Project b): UHECRs as Probe of the CMB Photon Density . . . 4
1.3 Project c): Frequency-Redshift Evolution . . . 5
1.4 Project d): Blackbody Anomaly at Low Temperatures . . . 6
1.5 Project e): Electroweak Parameters . . . 7
1.6 Project f): The Dark Sector in Yang-Mills Thermodynamics . . . 8

2 Anisotropy and UHECR Flux Composition **9**
2.1 Introduction . . . 10
2.2 Latency of UHECRs in PlanckJF12b . . . 11
2.3 Flux Modulation induced Anisotropy . . . 12
2.4 Summary and Outlook . . . 15
2.5 Appendix . . . 16
2.6 Simulation Setup . . . 17
2.6.1 Emission and Initial Conditions . . . 17
2.6.2 Magnetic Field Model and Propagation . . . 17
2.6.3 Observer Setup and Data Collection . . . 17
2.6.4 Simulation Parameters and Execution . . . 18
2.6.5 Summary of Key Parameters . . . 18

3 *T*-*z* Relation and UHECR Propagation **19**
3.1 Introduction . . . 20
3.2 T(z) Relation of $SU(2)_{CMB}$ . . . 21
3.3 Changes in Propagation Length . . . 22
3.4 Observational Consequences for UHECR Energy Spectra . . . 24
3.5 Cosmogenic Neutrinos . . . 27
3.6 Summary . . . 28

4 Frequency–Redshift Relation of the CMB **33**
4.1 Introduction . . . 34
4.2 Observational T-z Relation Extractions from a v-z Relation . . . 35
4.2.1 Absorber Clouds in the Line of Sight of a Quasar or a Bright Galaxy . . . 36
4.2.2 The Thermal Sunyaev-Zel'dovich Effect . . . 37
4.3 T-z Relation and ν-z Relation in $SU(2)_{CMB}$: Theoretical Basis . . . 38
4.3.1 T-z Relation in $SU(2)_{CMB}$ . . . 38
4.3.2 Anisotropic Photon Emission by Electrons . . . 41
4.3.3 Thermalisation-Dependent Mixing of Two SU(2) Gauge Theories . . . 42
4.4 Summary . . . 43

5 Search for a Blackbody Anomaly **45**
5.1 Introduction . . . 46
5.2 Experimental Setup and Noise-Power Amplification . . . 47
5.2.1 Design and components of experiment . . . 47
5.2.2 Error estimates . . . 49
5.3 Experimental Results . . . 49
5.4 Interpretation of Noise-Power Excess at Low Temperatures . . . 51
5.5 Discussion and Summary . . . 53

6 Electroweak Parameters from YMTD **57**
6.1 Introduction . . . 58
6.2 Three Phases of SU(2) Yang-Mills Thermodynamics . . . 62
6.2.1 Deconfining phase (I) . . . 62
6.2.2 Preconfining phase (II) . . . 64
6.2.3 Confining phase (III) . . . 64
6.2.4 Summary of phase structure of SU(2) Yang-Mills thermodynamics . . . 65

6.3 Selfintersecting Center-Vortex Loop and Magnetic Moment . . . 65
6.4 Value of Electromagnetic Fine-Structure Constant . . . 67
6.4.1 Trapping a single monopole or antimonopole inside the droplet's bulk . . . 67
6.4.2 Thin-shell approximation . . . 67
6.4.3 Averaging the droplet's effective charge over monopole locations . . . 68
6.5 SU(2) Gauge Group Mixing in the Droplet . . . 70
6.5.1 Thermal SU(2) gauge-theory mixing and comparison with electroweak theory . . . 70
6.5.2 Mixing angle θ_{W} . . . 72
6.5.3 Value of α . . . 74
6.5.4 Impact of mixing on mass formula and length-scale hierarchy in powers of α . . . 74
6.6 Discussion and Summary . . . 76

7 The Dark Sector in YMTD **81**
7.1 Introduction . . . 82
7.2 Axion Mass Squared via The Veneziano-Witten Formula at Finite Temperature . . . 84
7.3 The Veneziano-Witten Integral for Deconfining SU(2) YMTD . . . 84
7.3.1 The topological susceptibility χ on a Harrington-Shepard (anti)caloron . . . 84
7.3.2 Do thermal quasiparticle fluctuations contribute to χ? . . . 87
7.4 Cosmological Implications: Bose Condensation of Axions . . . 87
7.5 Summary and Outlook . . . 89

8 Summary and Acknowledgments **95**
8.1 Summary . . . 96
8.2 Acknowledgments . . . 98

List of Figures **99**

Bibliography **101**

1 Introduction

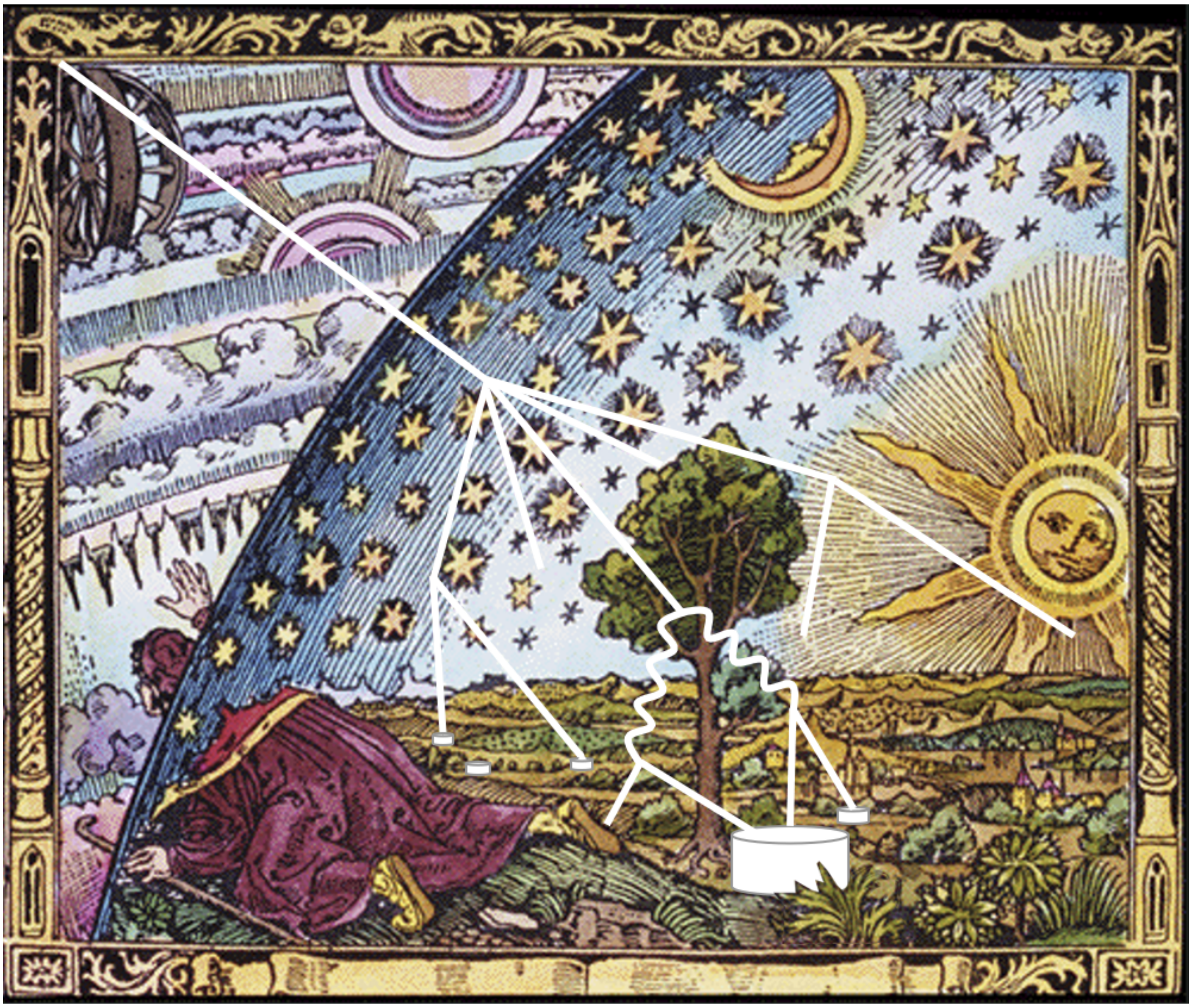

Figure 1.1: A traveler gazes through a gap in the heavens. Illustration from Camille Flammarion's L'atmosphère: météorologie populaire (Paris: Hachette, 1888), p. 163, colorized and modified.

Contents

1.1 Project a): UHECR Anisotropy and Composition **3**
1.2 Project b): UHECRs as Probe of the CMB Photon Density **4**
1.3 Project c): Frequency-Redshift Evolution **5**
1.4 Project d): Blackbody Anomaly at Low Temperatures **6**
1.5 Project e): Electroweak Parameters **7**
1.6 Project f): The Dark Sector in Yang-Mills Thermodynamics **8**

Introduction

The study of cosmic rays has a rich history that intertwines with the development of particle physics. In a series of daring balloon experiments, Austrian physicist Victor Hess found that this ionizing radiation originates from space rather than the Earth's crust [10]. Initially, it was believed that cosmic rays were primarily gamma rays due to their penetrating power. However, subsequent research by Jacob Clay revealed that these particles are predominantly charged, such as protons and atomic nuclei [11]. In 1938 Pierre Auger and his students discovered extensive air showers at the Jungfraujoch in Switzerland and the Pic du Midi in France [12], caused by cosmic rays striking the atmosphere and generating high-energy secondary particles. This insight enabled the first correlated detector arrays for air shower detection, as performed by the groups led by Bruno Rossi in the USA and Georgi Zatsepin in Russia in the 1940s and 1950s. In the last forty years, cosmic ray observational experiments continuously improved their sensitivity to the highest energetic particles. The experiment Fly's Eye pioneered the use of atmospheric fluorescence and detected ultra-high-energy cosmic rays (UHECRs) such as the famous "Oh-My-God particle" with an energy of 3×10^{20} eV [13]. KASCADE focused on medium to high-energy cosmic rays ($10^{14} - 10^{17}$ eV)[1] by measuring extensive air showers using scintillator muon detectors for cosmic-ray composition analysis, and hadron calorimeters. The Auger Observatory employs a hybrid method of surface detectors and fluorescence telescopes and was designed to study UHECRs and their phenomena, such as the Greisen–Zatsepin–Kuzmin (GZK) cutoff, as well as to determine the origin of UHECRs. The Greisen–Zatsepin–Kuzmin cutoff is a theoretical limit on the energy of cosmic rays travelling through space, proposed in 1966 [14, 15]. This cutoff occurs because ultra-high-energy cosmic rays interact inelastically with photons from the cosmic microwave background (CMB), producing pions and losing energy in the process. This interaction limits the propagation length of cosmic rays, e.g. protons can travel up to roughly 10 — 100 Mpc at the highest energies ($E > 5 \times 10^{19}$ eV), meaning that cosmic rays above this energy are unlikely to reach Earth from further distant sources. Moreover, the Pierre Auger Observatory is sensitive to ultra-high-energy neutrinos (UHE neutrinos), which are neutrinos with energies typically greater than 10^{15} eV. Those neutrinos can interact with the Earth's crust or the atmosphere, producing electromagnetic and hadronic cascades. The neutrino detection is particularly focused on tau neutrinos (ν_τ) in upcoming showers, and constraints can be made for beyond the standard model (BSM) physics on this basis [16, 17]. For example, the mass of hypothetical heavy dark matter particles can be constrained, which is typically assumed to be in the range of $m_{\rm DM} \sim 10$ GeV — PeV. These experiments are based on the idea that tauons produced in the Earth's crust can escape into the atmosphere, where they decay into Standard Model particles that initiate extensive air showers detectable by Auger's water Cherenkov tanks. This provides complementary insights: neutrinos trace sources deep within dense astrophysical regions, helping to uncover the origins of cosmic rays. Although UHE neutrinos have not yet been detected in this experiment, the Pierre Auger Observatory's capability to observe them highlights its role as a valuable multimessenger experiment, providing valuable insights into the highest energy cosmic phenomena over the past two decades.

Yet, despite studying cosmic rays for well over a century, the origin of the highest-energetic cosmic rays as well as their acceleration mechanisms are still elusive [18, 19]. This is partially due to our own galactic magnetic field (GMF) changing the trajectory of charged particles and thereby obscuring the direction of their origin. Therefore, this will be the starting point for the first out of six projects, which are presented in this work. Two of these projects are still in preparation for publication (see project a) and d) in Fig. 1.2), while four projects are already published (see project b), c), e) and f) in Fig. 1.2). Each project is given a chapter of this thesis, and all projects have been conducted in cooperation with researchers from the University of Wuppertal, Bochum, and Heidelberg. At the end of each chapter, there is a list of contributions of the author of this thesis (JM) to the respective article. In addition to researchers from Wuppertal and Heidelberg, the blackbody cavity experiment in project d) has been conducted by researchers from the Istituto Nazionale di Ricerca Metrologica (INRiM), Torino, the Politecnico di Torino, and the Physikalisch-Technische Bundesanstalt (PTB), Berlin. The central theme of this thesis is to utilize cosmic rays as probes across progressively larger physical scales: starting with galactic magnetic fields, the study extends to cosmic ray interactions with CMB photons, tests of ΛCDM extensions. In addition, we explore fundamental lepton and photon properties theoretically in thermal Yang-Mills theory and experimentally via a terrestrial blackbody anomaly. Ultimately, we are investigating condensates of ultra-light axions, which are linked to the lepton mass spectrum [20], see project f), at the largest cosmological scales. In the following, a brief introduction is given to all individual projects of this thesis.

[1] Although the data as shown in Fig. 1.3 is only in the energy range $10^{15} - 8 \times 10^{16}$ eV.

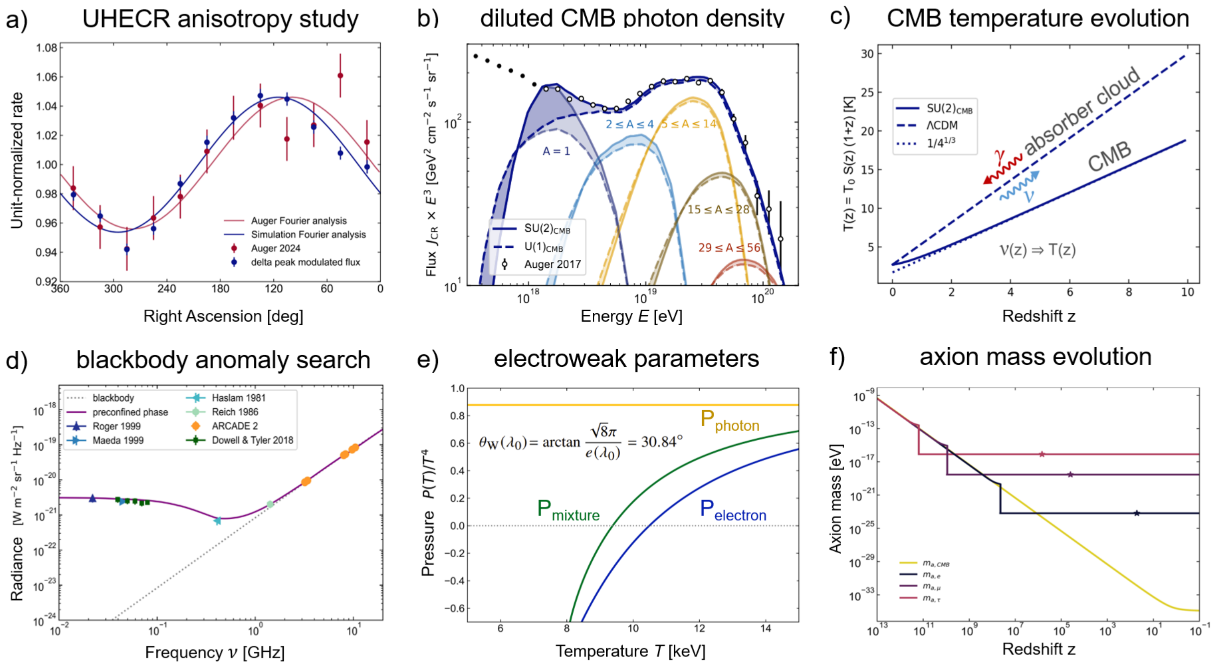

Figure 1.2: Overview of the projects of this thesis: a) the study of anisotropy of UHECR arrival directions caused by a modified cosmic ray flux; b) the interaction of UHECRs with the CMB as a crude measure of the CMB temperature probing our Universe locally; c) the difficulties of extracting the redshift dependence of the cosmic microwave background temperature; d) search for a spectral blackbody anomaly which could independently justify such a deviating CMB temperature evolution in redshift; e) the determination of the fine structure constant and electroweak mixing angle within the framework of mixed SU(2) Yang-Mills thermodynamics; f) and the determination of the T-dependent axion masses in the same framework of SU(2) Yang-Mills thermodynamics based on the Veneziano-Witten formula.

1.1 Project a): UHECR Anisotropy and Composition

In research project a), we aim to gain a deeper understanding of the impact of our own galactic magnetic field on the propagation of UHECRs and their directional anisotropy as seen by the Auger Collaboration, compare Fig. 1.2 a). Thereby, we put an emphasis on the UHECR mass composition and study the energy dependent dipole amplitude evolution for different UHECR nuclei. At energies at which the Pierre Auger Observatory can measure the arrival direction of cosmic rays, that is above 4×10^{18} eV, they propagate mainly ballistically. With decreasing energy starting at around ankle energies $(5 \times 10^{18}\,\mathrm{eV})^2$, cosmic rays start propagating quasi-diffusely. This means that the magnetic field can deflect the UHECRs without trapping them in our Galaxy for extended periods of time (~ 300 kilo years, which is implies propagation lengths $\gtrsim 100$ kpc). In comparison, the Milky Way has a diameter of approximately 30 kpc. This propagation length has been selected to enable multiple revolutions of cosmic rays within the galaxy. This inability to trap cosmic rays arises from the negligible impact of the turbulent magnetic field component at energies between the second knee (10^{17} eV) and the ankle, which is essential for their confinement. The setup of the simulation involves 3D propagation of protons and nuclei with a mass composition consisting of four elements (H, He, Ni and Fe) that are homogeneously injected at 20 kpc away from the center of our Galaxy into a galactic magnetic field model and to an observer sphere with a radius of 1 kpc. Thereby, we investigate different magnetic field models, mainly JF12 (Jansson & Farrar, 2012) adjacent magnetic fields but also the UF24 (Unger & Farrar, 2024) model. The JF12 model and UF24 model are both large-scale models of the Galactic magnetic field. The JF12 model combines a coherent (regular) component, a turbulent component, and a stratified component to describe the GMF structure based on observational constraints such as Faraday rotation measures and synchrotron emission. The UF24 model

[2] Please refer to Fig. 1.3 for an overview of the cosmic ray flux spectrum as measured on Earth, including the spectral features called 'ankle' and 'knee'.

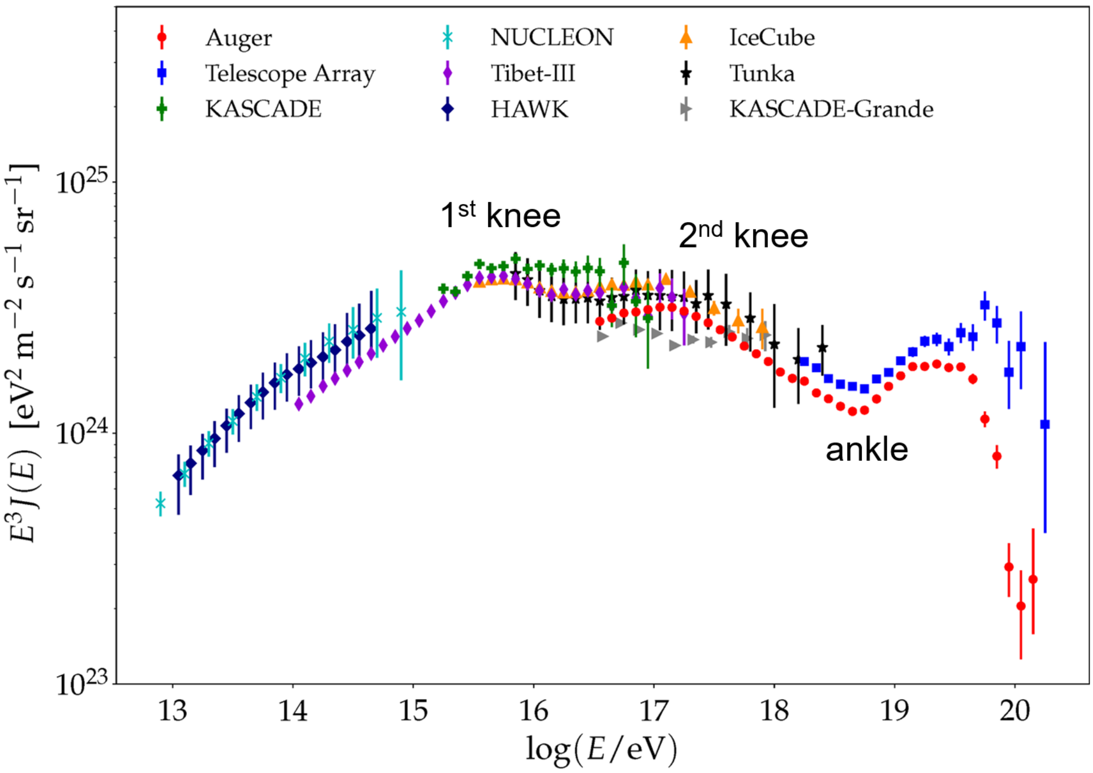

Figure 1.3: The cosmic ray flux as observed on Earth by multiple experiments as a function of energy multiplied by E^3. The data are taken from the Auger collaboration (red circle) [21], the Telescope Array (blue square) [22], KASCADE (green cross) [23], the NUCLEON experiment (turquoise x) [24], Tibet-III (purple small diamond) [25], HAWC (ultramarine diamond) [26], IceCube (yellow upward triangle) [27], Tunka (black star) [28], and KASCADE-Grande (gray right pointing triangle)[29]. The original graphic with more experiments can be found online [30].

refines and expands upon JF12, incorporating updated data and improved parameterizations to provide a more accurate representation of the GMF's impact on cosmic ray propagation and deflection. However, it does not have a turbulent component yet. The first insight of project a) is that a mild fluctuation in cosmic ray flux production ($\sim 30\%$) can induce anisotropy of the arrival direction of UHECRs as observed on Earth, even when the cosmic rays are injected homogeneously. This temporal modulation is not completely disjoint from directional information: selecting a certain propagation length (and thus time period in the past) to boost cosmic ray production always has a directional component associated with the injection sphere within our simulation setup. This is because not all particles are travelling multiple rounds within the Galaxy before hitting the capture sphere in our simulation setup. Especially at the highest energies, most particles travel to the observer sphere in a rather straight way. The second insight is that heavy elements show the tendency of an increased dipole amplitude at higher energies, and that no dipole amplitude evolution occurs for a pure proton composition [1]. This may lead to another way of constraining the UHECR mass composition, independent of the conventional study of $X_{\max}$, in the future. In this context, $X_{\max}$ refers to the depth in the atmosphere (measured in g/cm^2) at which the extensive air shower, triggered by the cosmic ray's initial interaction with e.g. nitrogen in the atmosphere, reaches its maximum particle density. It is the standard approach for inferring the mass of a primary cosmic ray particle using $X_{\max}$. This is feasible as showers caused by heavier primary particles like iron reach their maximum particle density in higher layers of the atmosphere, and earlier from the point of first interaction than lighter particles such as protons.

1.2 Project b): UHECRs as Probe of the CMB Photon Density

Project b) aims to explore the potential of ultra-high-energy cosmic rays as probes for cosmological models by examining the cumulative effects of cosmic microwave background photon density over their propagation distances. By utilizing the interaction of cosmic rays with CMB photons, we investigate potential connections between cosmic ray propagation and cosmology, for a small class of cosmological models which change the CMB photon density. This test is only possible if we have plenty of UHECR sources, evenly distributed up to redshift $z = 1$–2, which all have a similar acceleration mechanism and mass spectrum. If ultra-high-energy cosmic rays (UHECRs) observed on Earth were predominantly originating from a single nearby source, this would significantly complicate efforts to test these particular extensions of the ΛCDM model. In such a scenario, the observed UHECR signal would be heavily influenced by local source properties, rather than reflecting the statistical properties of the large-scale Universe. Consequently, it would be necessary to develop robust methods to disentangle this dominant foreground contribution from the more isotropic background produced by distant, cosmologically distributed sources. The reason that we wish to test the CMB photon density is one particular extension of the standard model of cosmology, ΛCDM (Lambda Cold Dark Matter), known as $\mathrm{SU(2)_{CMB}}$. ΛCDM is the standard cosmological model, describing the evolution of the Universe dependent on dark energy (Λ), cold dark matter, ordinary matter, and radiation at high redshifts within the framework of general relativity. As the name $\mathrm{SU(2)_{CMB}}$ suggests, the CMB and blackbody radiation more generally is described with an SU(2) rather than a U(1) theory [31] within this cosmological extension. The advantage of a pure Yang-Mills theory describing the photon in the deconfining phase is the mitigation of the Hubble tension and the $\mathrm{S_8}$ tension [32, 33, 34]. The Hubble tension refers to the discrepancy between the locally measured and cosmologically inferred values of the Hubble parameter (H_0) [35], while the S_8 tension arises from a mismatch between the observed and predicted amplitude of matter clustering in the Universe. The biggest disadvantage of this particular ΛCDM extension is the increased amount of fitting parameters to the CMB multipoles (9 instead of 6), and a fundamental change in leptogenesis, which are expected to change aspects of Big Bang nucleosynthesis and may lead to tension therein. In particular, the baryon density extracted from CMB fits in the framework of $\mathrm{SU(2)_{CMB}}$ is currently lower than in ΛCDM, while the latter is in a good agreement with current CMB simulations [36, 37]. Nonetheless, the $\mathrm{SU(2)_{CMB}}$ baryon density extracted from CMB fits roughly matches results of local censuses [38, 39]. One of the key characteristics of this ΛCDM extension is the changed temperature-redshift relation: the cosmic microwave radiation cools down more slowly than in ΛCDM. In this model, recombination occurs earlier at $z_* \sim 1700$ [33], while the CMB temperature at decoupling and today remains unchanged, as Thomson scattering and other decoupling processes are unaffected by the modified T-z relation.

1.3 Project c): Frequency-Redshift Evolution

The dominant opinion in the literature currently is that the standard temperature-redshift relation of the CMB is $T(z)_{\Lambda\mathrm{CDM}} = T_0\,(1+z)$ and can be inferred from the Lyman-alpha forrest and the thermal Sunyaev-Zel'dovich effect. With $T_0 = 2.725\,\mathrm{K}$ being the current temperature of the CMB. The Lyman-alpha (Ly-α) line is a spectral feature of hydrogen, created when an electron transitions between the first excited state (n=2) and the ground state (n=1), emitting or absorbing ultraviolet light at a wavelength of 121.57 nm. The conventional assumption is that the temperature of hydrogen clouds can be determined from the Lyman-alpha forest by analysing the thermal broadening of absorption lines in quasar spectra, which is directly sensitive to the gas temperature. In project c), we demonstrate that any assumed frequency-blueshift relation necessarily implies a corresponding temperature-redshift relation under the assumption that the radiation is in thermal equilibrium [3]. Therefore, these two methods are not sensitive to the actual temperature of the CMB in the past, and merely test the blackbody nature of the CMB at those times; at most those techniques are sensitive to the temperature of the hydrogen in the observed systems. The only non-local method to measure the temperature of the CMB seems to be via the interaction of CMB photons with cosmic rays. This is the main motivation for project b). In essence, project b) can be summarized with the finding that the modified temperature redshift relation, in the framework of SU(2) cosmology, cannot generally be excluded. Diluting the CMB photon density extends the propagation distance, effectively increasing the total number of propagated ultra-high-energy cosmic rays below $10^{18.5}$ eV [2, 7]. In particular, mild tendencies can be seen for the dominant source class of UHECRs: weakly evolving UHECR sources, such as starburst galaxies with a relatively steady production rate, are preferred over strongly evolving sources like active galactic nuclei (AGNs). Therefore, the viability of SU(2) cosmology would be heavily constrained if the primary sources of UHECRs would independently turn out to be AGNs. And vice versa, if by other means the validity of $\mathrm{SU(2)_{CMB}}$ could be demonstrated, weakly evolving UHECR sources would be favoured over AGNs.

1.4 Project d): Blackbody Anomaly at Low Temperatures

The framework of SU(2) cosmology was developed in the last two decades [31, 40, 41]. The description of photons in thermal equilibrium is built around the formal argument that in an SU(2) theory the photon is quantized automatically due to the non-abelian nature of the SU(2) gauge group, while for a U(1) gauge group quantization needs to put in by hand. In an SU(2) theory for photons, the gauge bosons (analogous to photons) are non-abelian, meaning they can interact with each other due to the structure of the SU(2) Lie algebra. In a thermodynamical context, this self-interaction allows non-perturbative physical phenomena, such as confinement, screening, or effective, dynamical gauge symmetry breaking [31]. The phase diagram due to non-trivial ground state of SU(2) Yang-Mills thermodynamics (YMTD) photon theory is shown in Fig. 1.4.

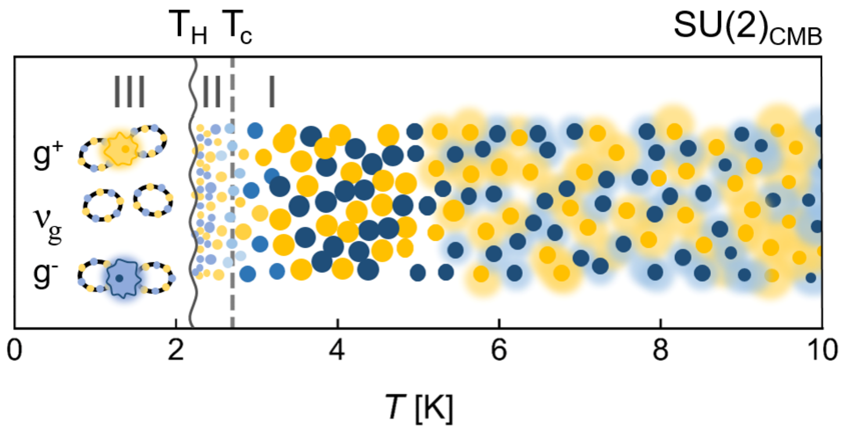

Figure 1.4: Phase diagram of $\mathrm{SU(2)_{CMB}}$ with $T_c = 2.725\,\mathrm{K}$ in the infinite-volume limit. There are three distinct phases: (I) deconfining phase, (II) preconfining, and (III) confining phase. In phase III an additional fourth, very light lepton family emerges whose charged members can be called gammaron and antigammaron with a mass of $m_e\,\Lambda_{\mathrm{CMB}}/\Lambda_{\mathrm{e}} = 1.5 \times 10^{-2}\,\mathrm{eV}$. The preconfining ground state of $\mathrm{SU(2)_{CMB}}$ decays, among others, into such charged leptons at the Hagedorn temperature $T_H \sim 2.3\,\mathrm{K}$.

The three thermodynamic phases are summarized in project e), Chapter 6.2, an in-depth introduction can be found in [31]. The experimental search for screening effects due to monopoles in the deconfining phase is the subject of project d). In this context, the search for screening effects means that we search in a cryogenic cavity experiment for a deviation from the expected blackbody noise power at low frequencies (5–11.5 GHz) and temperatures which are comparable to the current temperatures of the CMB ($T_{0,\mathrm{CMB}} = 2.725\,\mathrm{K}$). Those deviations from Planck's radiation law are expected close to a so called Hagedorn phase transition. A Hagedorn phase transition marks the shift from a confined phase with fermionic particles (e.g., leptons in phase III in Fig. 1.4) to a deconfined phase with freely moving quasi-particles (e.g., monopoles in phase I in Fig. 1.4). In a pure $\mathrm{SU(2)_e}$ gauge theory, this shift is expected to occur at a temperature of roughly $\mathrm{T_{H,e}} = 6.63\,\mathrm{keV}$ [5]. However, for $\mathrm{SU(2)_{CMB}}$ the temperature of the Hagedorn phase transition is $T_{\mathrm{H}} \sim 2.3\,\mathrm{K}$ and the critical temperature $T_{\mathrm{c}} \equiv T_{0,\mathrm{CMB}} = 2.725\,\mathrm{K}$. For $\mathrm{SU(2)_e}$ this transition can be calculated with the lepton mass and stability constraints on the electron, as done in project e). For $\mathrm{SU(2)_{CMB}}$, we do not know a prior a lepton mass of a potential fourth lepton species, as it has never been observed yet. Therefore, the phase transition and critical temperature in the latter theory cannot be determined purely theoretically. They need to be determined empirically. The balloon borne experiment ARCADE 2 measured in its 2005 and 2006 flights a significant excess in CMB radiation, which hints towards a non-trivial configuration of the photon ground state, compare Fig. 1.5[3]. This CMB line-temperature anomaly is used to anchor the critical temperature T_{c} to the current CMB temperature. The more conservative scenario is that other astrophysical sources outshine the CMB at low frequencies, though it remains unclear which specific sources are responsible [42]. In order to test whether the excess CMB radiation as observed by ARCADE 2 and other ground based experiments is of astrophysical origin or a feature of blackbody radiation itself, we need sophisticated Earth based cavity experiments. If similar radiation excess as shown in Fig. 1.5 can be measured in a terrestrial laboratory, astrophysical

[3]Please refer to [42, Fig. 4] for a clearer representation of the excess in form of a line-temperature excess.

foregrounds could be severely constrained or even ruled out as source for this deviation. In the framework of SU(2) Yang-Mills theory, this CMB radiation excess would be caused by Meissner massive photons in the preconfined phase where U(1) is effectively broken by a monopole condensate. This serves as the primary motivation for Project d). In a pilot study, initial measurements were conducted by INRiM. In this study, we search for deviations predicted to occur for $T > T_c \sim T_{0,\mathrm{CMB}}$ which are due to an effective, radiative photon screening at intact U(1) gauge symmetry.

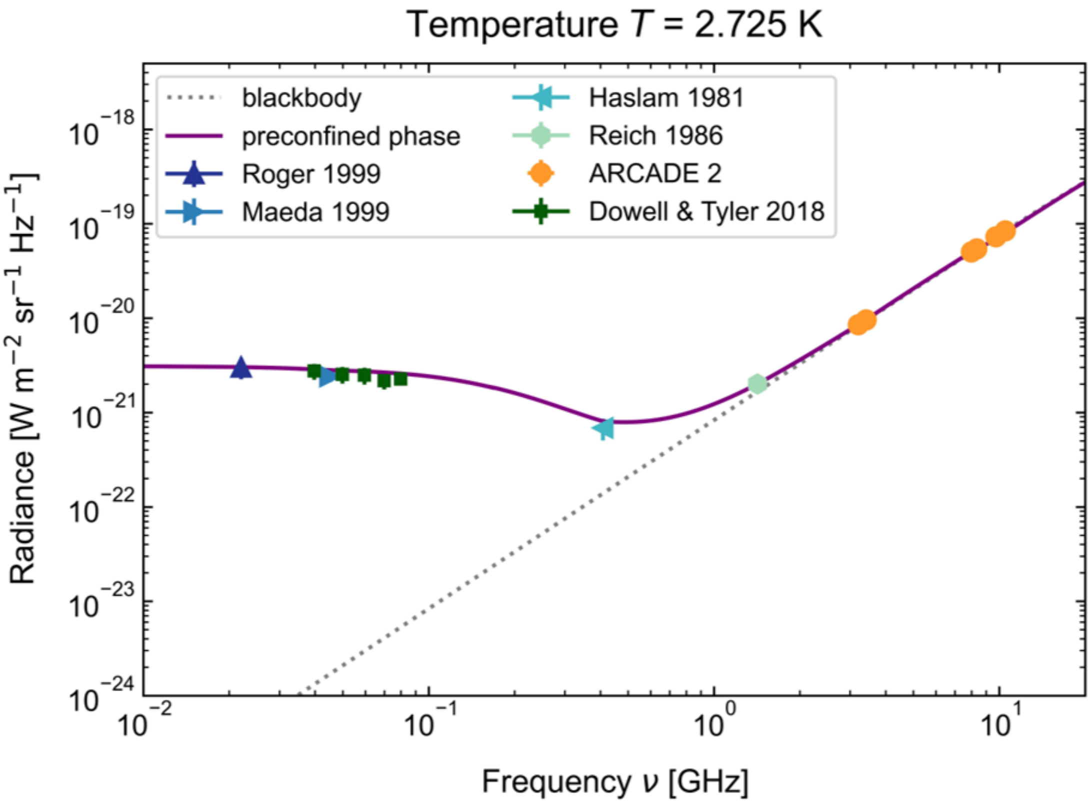

Figure 1.5: The radio excess as observed by CMB observations could be explained by Meissner massive photons in the preconfined phase of $SU(2)_{\mathrm{CMB}}$. In purple, a fit to the data is shown, the gray dotted line indicates the expected Rayleigh-Jeans behaviour.

1.5 Project e): Electroweak Parameters

In the context of Yang-Mills thermodynamics, we also investigated the effect of mixing the deconfined phase of the SU(2) theories, which are associated with the thermal the photon and electron [43, 44] in project e). Only with the condition of stabilizing the electron (bulk pressure of the deconfined phase being zero), an electroweak mixing angle can be obtained, which can be interpreted as the Weinberg angle [5]. This defining feature of an isolated electron not being point-like due to localized SU(2) thermodynamics is different to the SM, in which it is point-like at all temperatures [ibid.]. Note that, even in YMTD, the electron appears point-like when boosted to relativistic velocities, as in collider physics [ibid.]. However, quantities derived in thermodynamic equilibrium, such as the fine-structure constant, are inherited from the rest frame to the otherwise featureless situation of a relativistic electron [ibid.].

Therefore, one key aspect of $SU(2)_{\mathrm{CMB}}$ as an extension of ΛCDM is that it is also motivating an extension of the standard model of particle physics. Note that far from thermodynamic equilibrium, the standard model is not only a great approximation, but superior in its descriptive power, in particular with respect to scattering processes at collider experiments.

1.6 Project f): The Dark Sector in Yang-Mills Thermodynamics

There are many other implications of the Yang-Mills thermodynamic framework in cosmology. The dark sector is particularly affected if one describes the thermal ground state not only of photons with an SU(2) gauge group, but each lepton family in local thermodynamic equilibrium (electron, muon, tauon). Dark matter is a hypothetical particle species, which could for example couple only gravitationally or additionally very weakly with particles of the standard model. Two of the many possible dark matter candidate classes are ultra-light, Planck-scale axions and weakly interacting massive particles. Experimental evidence for dark matter comes from observations of the bullet cluster [45], galaxy rotation curves and the CMB [46, 47]. In YMTD, dark energy is represented by the energy density of a super horizon size axion condensate. The particles of this condensate obey a Peccei-Quinn scale close to the Planck mass $f_{\mathrm{a,YMTD}} = M_{\mathrm{P}} \sim 10^{28}\,\mathrm{eV}$ [20, 48, 41]. The Peccei-Quinn (PQ) scale f_{a} is the energy scale at which the hypothetical global chiral $\mathrm{U}(1)_{\mathrm{PQ}}$ symmetry, originally introduced to solve the strong CP problem, spontaneously breaks. On top of this spontaneous breaking, there is an anomalous, explicit breaking induced by topological charge carriers. This gives rise to a mass of the would-be Goldstone boson, the axion, of $m_a \sim \Lambda^2/f_a$ where Λ is the Yang-Mills scale of the gauge theory providing the field configurations of non-trivial topological charge. The QCD scale Λ_{QCD} is around 200 MeV, below which quarks and gluons become confined into hadrons. For the QCD axion, the Peccei-Quinn scale is typically expected to be around $f_{\mathrm{a,QCD}} \sim 10^{18}$ — $10^{21}\,\mathrm{eV}$. The QCD axion is therefore $m_{\mathrm{a,QCD}} \propto \Lambda^2_{\mathrm{QCD}}/f_{\mathrm{a,QCD}} = (200\,\mathrm{MeV})^2/f_{\mathrm{a,QCD}} \simeq 10^{-2}$ — $10^{-5}\,\mathrm{eV}$. In Yang Mills thermodynamics, with a significantly heavier PQ scale, axion are ultra-light ($\leq 10^{-18}\,\mathrm{eV}$) and their coupling to the electromagnetic field is suppressed with the Planck mass, so that no Primakov conversion is expected during the lifetime of the Universe. Within this framework, the lightest axion species $m_{a,\gamma} \sim 10^{-35}\,\mathrm{eV}$ is associated with the Yang-Mills scale of the photon $\Lambda_{\mathrm{CMB}} \sim 10^{-4}\,\mathrm{eV}$ and can be interpreted as dark energy, and three axion species interpreted as fuzzy and cold dark matter $m_{a,\ell} \sim 10^{-24} - 10^{-18}$ eV are associated with the Yang-Mills scales of the leptons ($\Lambda_{\mathrm{e}} = 3.6\,\mathrm{keV}$, $\Lambda_\mu \simeq 744\,\mathrm{keV}$, $\Lambda_\tau \simeq 12.5\,\mathrm{MeV}$)[4]. In project f) the temperature dependent axion mass was calculated for the deconfining phase of each axion species, which is independent of the explicit symmetry breaking scale Λ and f_a in the deconfining phase of the associated SU(2) Yang-Mills theory. These masses are proportional to $m_a \propto T^2/M_P$ if the Peccei-Quinn scale can be assumed to be the Planck mass M_P. Interestingly, all of those axion species in YMTD almost always occur as a Bose-Einstein condensate facilitated by gravity [49], right after getting massive at the Planck scale.

The projects of this work cover a broad range of topics within astroparticle physics and cosmology. Key insights include additional indications for a heavy composition of the UHECR flux composition, derived from our anisotropy study in project a), as well as the ability to probe the CMB photon density along the propagation of UHECRs in project b). In addition, the secondary theme is to connect those areas of research by testing the hypothesis of Yang-Mills thermodynamics phenomenologically. Thereby, this work presents a range of considerations that hint at a potentially complex thermodynamical constitution of photons and leptons, along with the possibility of a dark sector comprising four Planck-scale axion species. Further research will be required to evaluate the validity of this hypothesis.

[4] Those Yang-Mills scales are fixed by first calculating $\Lambda_{\mathrm{e}} = 3.6\,\mathrm{keV}$ [5] and then using the lepton mass ratios to deduce $\Lambda_\mu = \Lambda_{\mathrm{e}} \times m_\mu/m_e$ and likewise $\Lambda_\tau = \Lambda_{\mathrm{e}} \times m_\tau/m_e$.

2 Anisotropy and UHECR Flux Composition

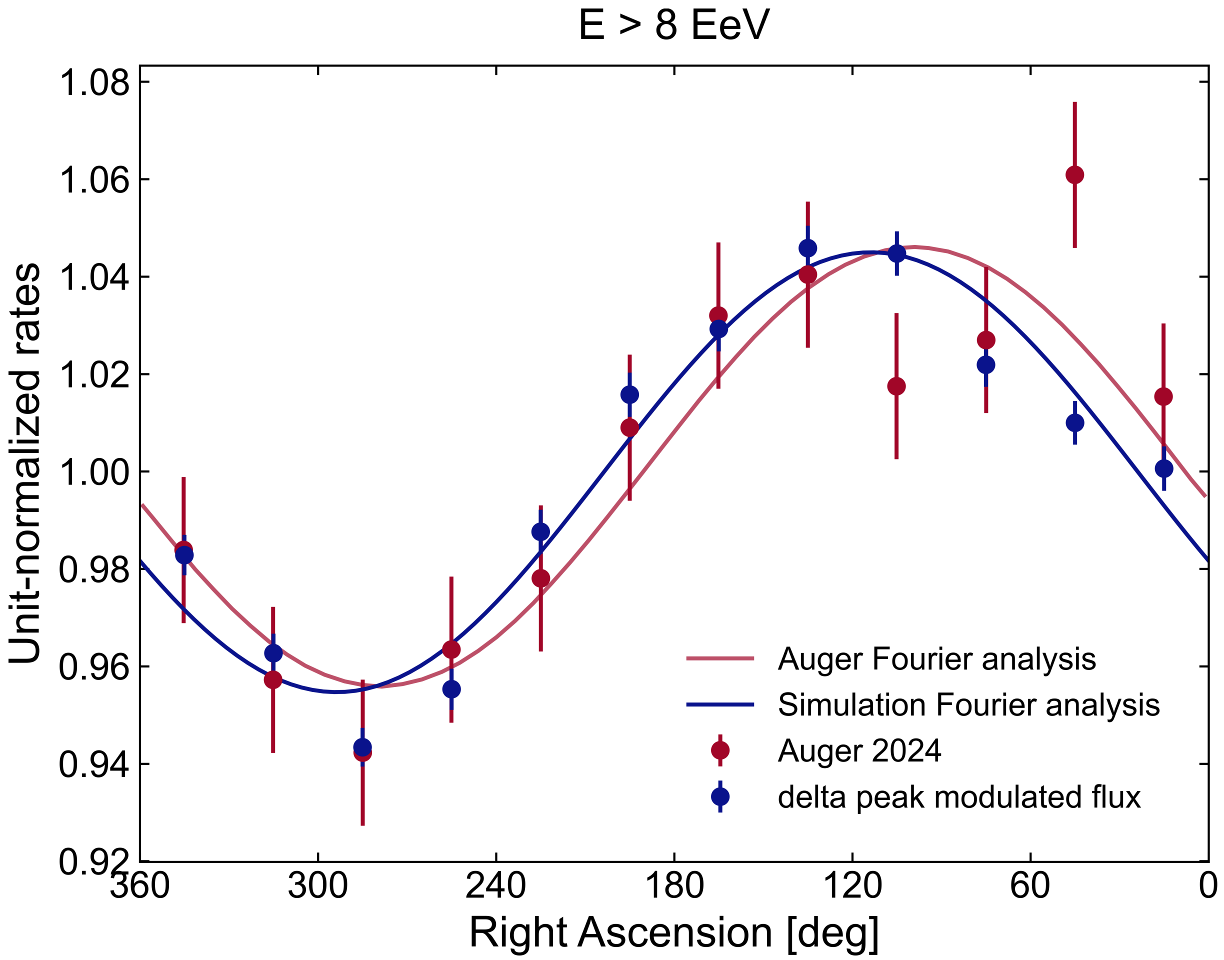

Figure 2.1: Comparison of flux modulation induced dipole with a mass composition based on an EPOS-LHC fit (simulation) with Auger data 2024, compare [50]. For Auger data, all energies E > 8 EeV have been taken into account, for the modulated flux simulation the energy range 8 EeV < E < 64 EeV has been assumed. The modulated flux is shown in Fig. 2.5.

This chapter presents original research, published here for the first time, and serves as a preprint [1]. It is a collaborative effort within SFB 1491, with the associated project designated as A3.

Contents

2.1 Introduction . . . 10
2.2 Latency of UHECRs in PlanckJF12b . . . 11
2.3 Flux Modulation induced Anisotropy . . . 12
2.4 Summary and Outlook . . . 15
2.5 Appendix . . . 16
2.6 Simulation Setup . . . 17
2.6.1 Emission and Initial Conditions . . . 17
2.6.2 Magnetic Field Model and Propagation . . . 17
2.6.3 Observer Setup and Data Collection . . . 17
2.6.4 Simulation Parameters and Execution . . . 18
2.6.5 Summary of Key Parameters . . . 18

Janning Meinert[1,2], Leonel Morejón[1], Veronika Vašíčková[1], Lukas Merten[3], Sophie Aerdker[3], Julia Tjus[3], Karl-Heinz Kampert[1]

[1]Bergische Universität Wuppertal, Department of Physics, Gaußstraße 20, D-42103 Wuppertal

[2]Institut für Theoretische Physik, Universität Heidelberg Philosophenweg 12, D-69120 Heidelberg

[3]Ruhr-Universität Bochum, Theoretische Physik IV, Universitätsstraße 150, D-44801 Bochum

Abstract

The origin of the large-scale anisotropy in ultra-high-energy cosmic rays (UHECRs) remains unclear. We explore the influence of a time-dependent cosmic-ray flux variation, which could imprint an anisotropic signature. We explore this idea by investigating the energy- and composition-dependent residence time of extragalactic cosmic rays entering our Galaxy. Using CRPropa 3.2 and current Galactic magnetic field models, particularly PlanckJF12b, we introduce a time modulation in the cosmic ray flux to induce anisotropy in an otherwise homogeneously injected UHECR distribution. Similarly to simulations which only introduce spacial anisotropy in UHECR source distribution, we find a good agreement with the observed right ascension only by altering the cosmic-ray flux in time, with a homogenous source distribution. This study is a proof of concept, and a potential advantage of our approach could be matching the energy dependent dipole evolution to more complex past variations in cosmic-ray flux in future studies (Gaussian modulation, multiple bursts, instead of a single delta function like temporal modulation as done in this study). We find the best agreement with the Auger dipole for an increased cosmic ray flux of about 34% in the past 46–55 kilo years (14–17 kpc) when the UHECR flux composition of EPOS-LHC is employed. Furthermore, we find the energy evolution of the dipole amplitude to depend on rigidity, which we control in the simulation setup by changing the mass composition of ultra-high-energy cosmic rays: for a pure proton composition, the dipole amplitude remains constant from $4 - 64\,\mathrm{EeV}$, while heavier elements like nitrogen and iron show a tendency for an increasing dipole amplitude with energy. The time-varying UHECR flux approach in this research aims to provide a new avenue for testing UHECR mass composition at the highest energies.

2.1 Introduction

The origin of ultra-high-energy cosmic rays (UHECRs) remains an open question [18, 19]. A key challenge in determining their origin is the influence of our own Galactic magnetic field (GMF), which alters the trajectories of charged particles, thereby obscuring the direction of their origin. A feature of the UHECR flux spectrum which has the potential to shed light on the origin of UHECRs is the mild but statistically significant anisotropy in arrival direction of ultra-high-energy cosmic rays [50]. The Pierre Auger Collaboration analysed nineteen years of UHECR data, and observed the dipole anisotropy with a $\sim 6\%$ amplitude above $8\,\mathrm{EeV}$ with $> 5\sigma$ significance [ibid.]. No significant higher-order multipoles were found, and the dipole amplitude remained stable within the observation period. The observed mild anisotropy in arrival direction of ultra-high-energy cosmic rays is often interpreted as the anisotropy in source distribution [51]. This approach aims to find a prime candidate for the dominant UHECR source class with directional studies [52]. In this work, we analyse the influence of a time-varying UHECR flux on the anisotropy observed today with the Auger Observatory, while maintaining an otherwise homogeneous source distribution. The question is if a time-varying UHECR flux alone is enough to match the observed anisotropy data.

Such a flux modulation may have been triggered by a single UHECR bursting event in a nearby galaxy, such as Centaurus A, as suggested by [53]. Although a local bursting would also induce a spacial anisotropy, the spacial anisotropy may be isotropiesed by UHECRs being reflected in larger magnetic structures, i.e. the council of giants [ibid.]. Such echoes of a bursting event can be approximated as a brief global increase in UHECR flux, an assumption we adopt throughout this study. This simplification positions our work as a proof-of-principle analysis. In addition to a time-varying UHECR flux, we use this simulation setup to study the composition and energy-dependent evolution of the dipole amplitude. To investigate the impact of the GMF on UHECR propagation and residence time in our Galaxy, we examine different magnetic field models. The PlanckJF12b model [54] and the UF24 model [55] are large-scale representations of the Galactic magnetic field commonly used in UHECR studies. The PlanckJF12b model is an updated version of the JF12 model [56], incorporating improved constraints on the Galactic magnetic field derived from Planck satellite data. Both the JF12 model and the PlanckJF12b combine a coherent (regular) component, a turbulent component, and a stratified component to describe the GMF structure, based on observational constraints such as Faraday rotation measures and synchrotron emission. The UF24 model offers a similar approach with an updated magnetic field configuration, however, currently without a turbulent component. This is the main reason to rely on the PlanckJF12b model and use the UF24 model for internal validation[1]. More sophisticated models, such as those that include the matter distribution in our local cosmic neighbourhood [51], have been proposed to improve the understanding of how the GMF influences cosmic ray propagation over large distances. Simpler injection geometries have also been considered, highlighting the significance of galactic magnetic fields when studying the UHECR dipole [57].

Our findings include a reasonable good agreement with the time-varied UHECR flux for all injected nuclei species individually (H, He, N, Fe) for a mildly increased flux of $\sim 30\%$ in the past 46–55 kilo years (14–17 kpc). We also base the injected composition on an EPOS-LHC fit to 2017 Auger data, in order to have a realistic mass composition. In this scenario, a flux modulation of 34% is necessary in order to be in agreement with Auger dipole data for the same modulated time period. In addition, we observe in our simulation setup, that the dipole amplitude for heavier elements, such as nitrogen, increases with energy, from $\sim 3\%$ in the smallest energy bin (8–16 EeV) to $\sim 6\%$ in the highest energy bin (32–64 EeV). This is in contrast to a pure proton composition, in which the dipole amplitude remains energy-independent. We identify this feature as a rigidity effect, as particles with a smaller rigidity spend more time propagating within our Galaxy and have thus more time to be 'isotropiesed'. More sophisticated simulation setups need to follow, in order to constrain the UHECR compositional data with the energy dependent dipole amplitude evolution.

2.2 Latency of UHECRs in PlanckJF12b

We use the magnetic field model PlanckJF12bField [56], within the cosmic ray simulation framework CRPropa 3.2 [58, 59] in order to study UHECR propagation in our GMF. We inject protons homogeneously with a Lambertian distribution at 20 kpc from the Galactic center in the energy range $10^{16} - 10^{21}$ eV, following a spectral index of E^{-1}, as shown in Fig. 2.2 a). Using a ballistic propagation model—appropriate for high-energy cosmic rays with minimal deflections, we track particles reaching the 1 kpc capture sphere, which is 8.5 kpc away from the center of the Milky Way. A smaller energy range of $10^{18.6} - 10^{20.2}$ eV was used for all following studies with a spectral index of $E^{-2.7}$. In Fig. 2.2 a) the energy dependent propagation distance is shown for 1,970,000 particles which are reaching the capture sphere. Around ten times more particles are simulated, which do not reach Earth in the designated simulation time or which leave the Galaxy. Particles are not propagated further when the propagation length reaches 100 kpc, or when particles are leaving our Galaxy. The latter scenario is detected by a second capture sphere with a radius of 22 kpc.

Latency effects, such as the decrease in propagation length at ankle energies ($10^{18.5}$ eV) as seen in Fig. 2.2 a), are robust even when varying the capture sphere size, changing the position of the capture sphere in the Milky Way, and also when using the newer GMF model UF24. The latter model was not used for the simulation of this work due to the lack of a turbulent module implementation in CRPropa. An additional turbulent component could be introduced; however, this would not be supported by the available data. Overall, the propagational effects as seen in Fig. 1 a) were similar in both magnetic fields. This leads us to conclude that likely the large scale magnetic field structure causes the suppression of propagated distances at ankle energies.

For PlanckJF12b, we see in Fig. 2.2 a) that the Galactic magnetic field shields Earth from the arrival of UHECRs for energies below 10^{18} eV, leading to an almost complete suppression of UHECRs below 10^{17} eV. TF17 has a less severe shielding at low energies. Interestingly, all JF12 adjacent Galactic magnetic field models exhibit a suppression of propagated distances around that ankle energy ($10^{18.5}$ eV). We find this to be a combination of two effects: shielding of ballistically propagating ultra-high-energy

[1] A detailed comparison of the two models will appear in the Appendix in a later version of this paper.

cosmic rays at higher energies, which is counterbalanced at lower energies by the onset of quasi-ballistic propagation between $10^{17} - 10^{18.5}$ eV. We identify unchanged propagation distances in Fig. 2.2 a) above a rigidity of $10^{19.5}$ V to be a characteristic of ballistic propagation. In Fig. 2.2 b) the injection of cosmic rays has been adjusted to $E^{-2.7}$. In order to incorporate information on the energy-dependent composition, we use an EPOS-LHC fit to Auger 2017 data for our composition, compare [60, Fig. 3].

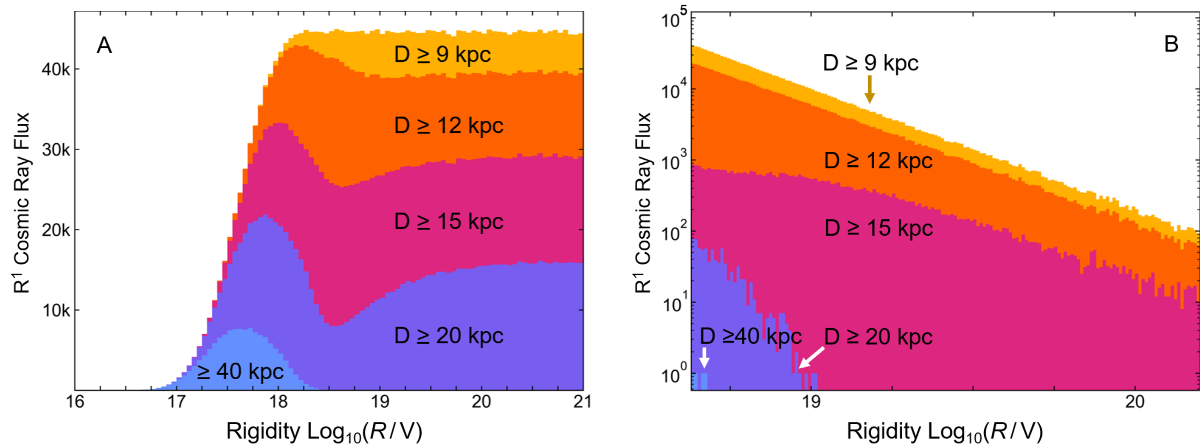

Figure 2.2: The energy dependent absolute number of protons which reach the capture sphere is shown for propagated distance in PlanckJF12b. The protons were injected with a spectral index of E^{-1} in **A** and with a spectral index of $E^{-2.7}$ in **B**. Distances in both figures which are larger than $\geq$ 9 kpc are indicated in yellow, $\geq$ 12 kpc (orange), $\geq$ 15 kpc (magenta), $\geq$ 20 kpc (indigo), $\geq$ 40 kpc (azure).

In order to have a realistic mass composition of UHECR, we employ an EPOS-LHC fit to 2017 Auger data, as shown in Fig. 2.3 a). These flux ratios, which are used from individually $10^{18.6} - 10^{20.2}$ eV, are multiplied with E^3, and normalized by the highest mass composition, which is nitrogen at $10^{19.5}$ eV. After normalization, we use up to one-hundredth batches of 40 million propagated particles each and repeat the simulation as shown in Fig. 2.2 b) for four nuclei species (H, He, N, Fe) with an injection index of $E^{-2.7}$ for the whole energy range of $10^{18.6} - 10^{20.2}$ eV. Please refer to the Appendix, section 2.6, for a detailed description of the simulation setup which was used for each batch of propagated particles. The compositional information of the EPOS-LHC fit is binned for 16 energy bins, and accordingly batches of each nuclei species are combined in order to represent the composition within a given energy bin. The nuclei specific number of batches are also shown in the Appendix in Table 1. Fig. 2.3 b) shows the propagated distances for particles which reaches the capture sphere with an EPOS-LHC composition, also multiplied with E^3.

2.3 Flux Modulation induced Anisotropy

The time a cosmic ray takes to propagate in our Galaxy before reaching Earth as seen in Fig. 2.2 a) cannot be determined for individually particles experimentally[2][3]. Thus, we measure all particles which reach Earth, without knowing their precise path through the galactic magnetic field. If the particles are injected homogeneously, according to Liouville's theorem, the isotropy should be conserved for any stationary observer. This is why there is no anisotropy evident if one does not distinguish for the propagation time of cosmic rays within our Galaxy, as seen in Fig. 2.4 (dark red line). In our simulation setup, where propagated distances can be distinguished, a deviation from isotropy becomes apparent when selecting subsets of propagated distances. A dipole is apparent for young particles, for example, particles which travelled from the injection sphere directly to Earth (9–15 kpc, orange), as well as for relatively old particles (distances $\geq$ 40 kpc, azure) in Fig. 2.4. Note that the dipole for older particles

[2]If the source of UHECRs was known, with photo-disintegration and hadronic interactions, statistical statements could be made, since the mass composition is known at the highest energies of UHECRs [60].

[3]Note, that we use the term "time" and "distance" a cosmic ray travelled within our Galaxy interchangeable throughout this work.

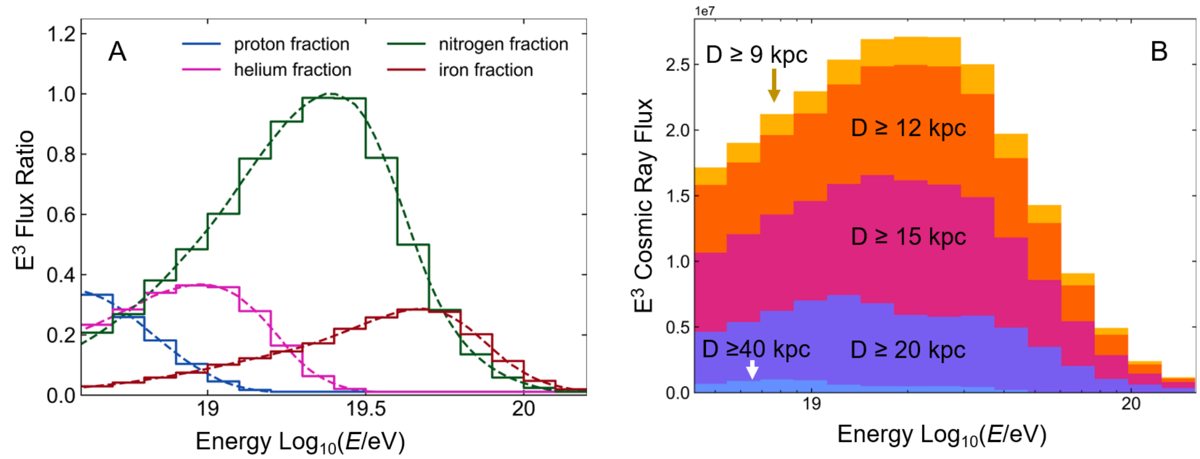

Figure 2.3: **A** The ratios of H, He, N, and Fe that best fit the Auger $X_{\max}$ distributions, using templates produced by the EPOS-LHC high-energy interaction model, based on Auger 2019 data. The data of this figure are taken from [61], Fig. 1. Shown in solid lines are the implemented nuclei fractions in Fig. 2.3 b) for the energy bins 4-8 EeV, 8-16 EeV, 16-32 EeV and 32-64 EeV. The composition of the last energy bin was taken to be equal to the third energy bin. The energy binning scheme uses logarithmic intervals from $10^{18.6}$–$10^{18.7}$ eV to $10^{20.0}$–$10^{20.2}$ eV. Each bin width follows a constant step size of 0.1 in the exponent, ensuring a uniform logarithmic spacing. **B** The energy dependent absolute number of an UHECR composition based on an EPOS-LHC fit (on Auger 2017 data, [60]) which reach the capture sphere is shown for propagated distance in PlanckJF12b. The nuclei were injected with a spectral index of $E^{-2.7}$. Distances $\geq$ 9 kpc are indicated in yellow, $\geq$ 12 kpc (orange), $\geq$ 15 kpc (magenta), $\geq$ 20 kpc (indigo), $\geq$ 40 kpc (azure).

exhibits a phase shift in right ascension, resulting in a direction opposite to that of younger particles. In order to reproduce the dipole as seen by the Auger collaboration, we modulate the cosmic ray flux in the past by modulating the total cosmic ray flux with a delta-like function as shown in Fig. 2.5 a).

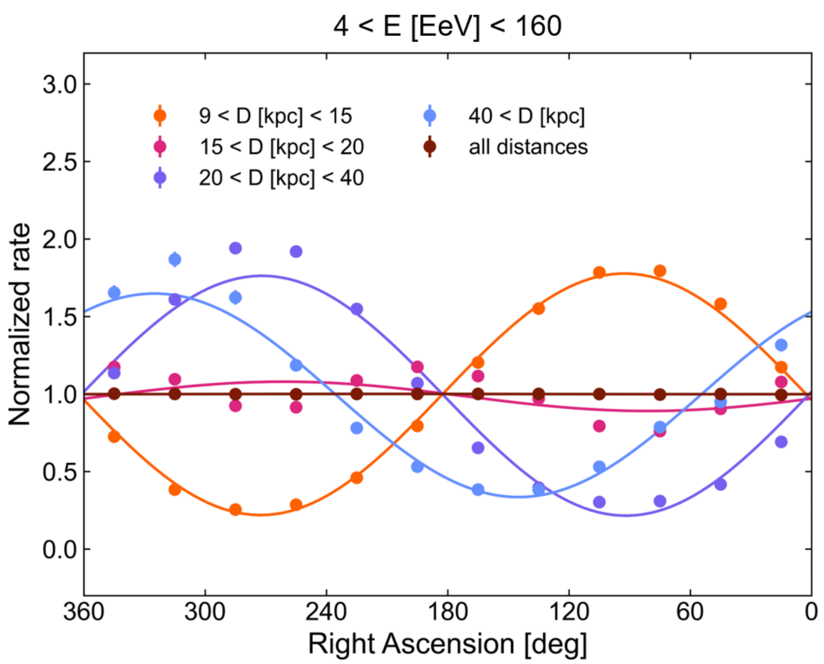

Figure 2.4: The propagation length dependent (an)isotropy is shown for cosmic rays which travelled between 9-15 kpc (orange); between 15-20 kpc (magenta); between 20-40 kpc (indigo); all particles which propagated longer than 40 kpc are shown in azure. The anisotropy for all distances is shown in red. This figure is based on the simulation, as shown in Fig. 2.2 a).

However, due to the simulation setup and the ballistic propagation of cosmic rays at the highest energies, temporal information cannot be fully disentangled from spatial information. Boosting cosmic rays with a propagation length below 30 kpc effectively selects rings of origin within the injection sphere. These rings are significantly more isotropic than the assumptions in standard point source searches, as they encompass a broader and more evenly distributed emission region. Nonetheless, the temporal modulation of the UHECR flux is sufficient to induce the anisotropy as observed by the Auger collaboration.

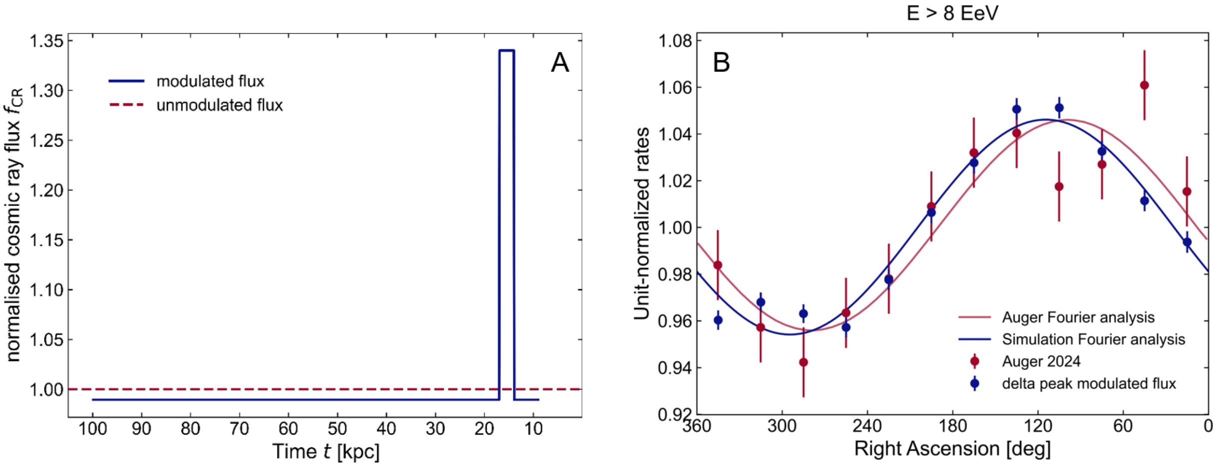

Figure 2.5: **A** Modulation of the UHECR flux with a delta-peak-like modulation from $14-17$ kpc. The total flux is conserved, while for ten thousand years the flux is increased by 34%. There are no cosmic rays from 0-9 kpc since from injection outside the Galaxy, the particles need to travel at least 9 kpc in order to reach the observer sphere. **B** Comparison of flux modulation induced dipole (simulation) with Auger data 2024, compare [50]. For Auger data, all energies $E > 8$ EeV have been taken into account, for the modulated flux simulation the energy range $8\,\text{EeV} < E < 64\,\text{EeV}$ has been assumed.

While the total flux is preserved, increasing the flux within a period of roughly ten thousand years (from 46 to 55 kilo years) by 34% leads to a right ascension which is in a reasonably good agreement with observations by the Auger collaboration [50], as seen in Fig. 2.5 b). The amplitude and timing of the delta-peak-like cosmic ray flux modulation was adjusted to be in good agreement with the combined Auger data for energies between 8–64 EeV. The amplitude of the delta-like increased cosmic ray flux determines the height of the dipole amplitude in Fig. 2.5 b). Shorter durations of increased flux can be compensated by a higher flux modulation and vice versa. In addition, we find the right ascension is linked with the rigidity of the injected particles: While a pure proton composition peaks around a right ascension of 60°, nitrogen dominated composition peak around 120°, compare Fig. 2.8 in the Appendix.

To compare our simulation with anisotropy data from the Auger collaboration, we use the same energy bins in this work which have been selected in previous studies: 4–8 EeV, 8–16 EeV, 16–32 EeV and 32–64 EeV. The delta-peak modulation induced anisotropy together with the EPOS-LHC mass composition can be seen in ultramarine in Fig. 2.6. While the tendency of an increasing dipole amplitude for higher energies is apparent for nitrogen, the overall match with the dipole evolution is quite poor for all individually propagated nuclei and also the EPOS-LHC mass composition. We find that at low energies, heavier elements experience greater deflection in the magnetic field, causing them to propagate longer in the GMF than a light UHECR mass composition. We identify the very high dipole amplitude for nitrogen in the smallest energy bin (4–8 EeV) to be an artifact of our simulation setup: The particles are not propagated long enough, causing the younger particles to induce a dipole. This is detected by our null-hypothesis cross-check in Fig. 2.7 for the EPOS-LHC composition, which is dominated by nitrogen. Accounting for all propagated distances together should result in no anisotropy, which is not the case for Fig. 2.7 a), b) and to some extent also Fig. 2.7 c). The anisotropy dipole amplitudes in the lowest energy bin are therefore erroneous for the EPOS-LHC fit composition and nitrogen, and are marked with an additional cross to indicate this in Fig. 2.6. The key insight provided by Fig. 2.6 is that heavy elements induce an increased dipole amplitude at higher energies, and that no dipole amplitude evolution is apparent for a pure proton composition. This approach of a time-varied UHECR flux may become another way of excluding a pure proton composition at the highest energies in the future for more sophisticated temporal modulations, independent of the conventional study of $X_{\max}$.

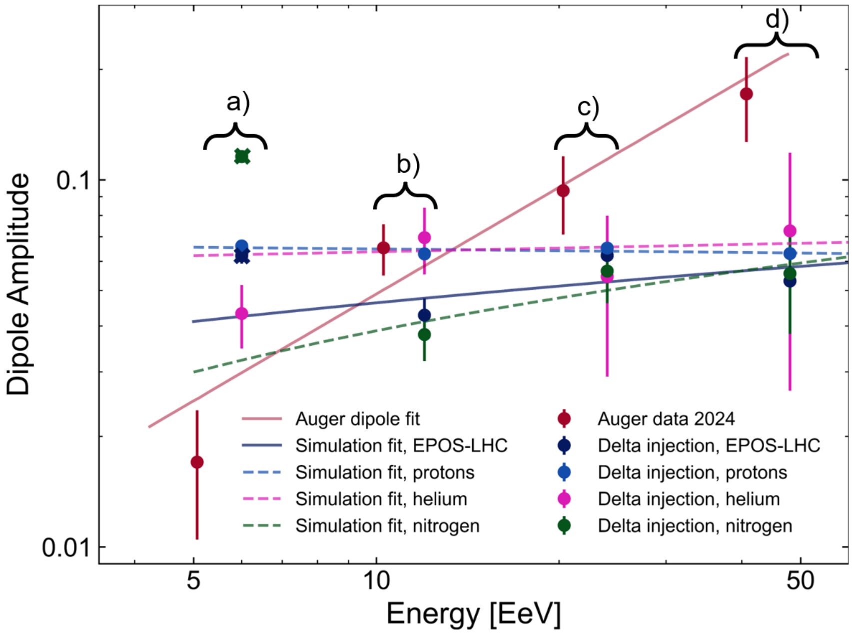

Figure 2.6: Comparison of the evolution of the dipole amplitude with energy, for the delta-like flux modulation as in Fig. 2.5 a) with Auger 2024 data (red), compare [50]. Four energy bins are shown in EeV: a) 4-8, b) 8-16, c) 16-32, d) $\leq$ 32 for Auger data and d) 32-64 for simulation. The Auger data are compared with four simulation setups: A cosmic ray mass composition based on an EPOS-LHC fit to 2017 Auger data (ultramarine, solid line fit), compare Fig.2.3 b). A cosmic ray composition of pure protons (light blue, dashed fit), compare Fig. 2.2 b). As well as a pure helium composition (pink, dashed fit) and a pure nitrogen composition (green, dashed fit), analogous to Fig. 2.2 b). The lowest energy bins have been ignored for the fits for the EPOS-LHC composition and the nitrogen simulations. The fits are intended only as a visual aid.

2.4 Summary and Outlook

In this work, we study the impact of the Galactic magnetic field of the Milky Way on arrival time and on the observed dipole in arrival direction of UHECRs. Thereby, we use CRPropa 3.2 simulations and current models of the galactic magnetic field, in particular PlanckJF12bField. Our findings indicate that cosmic rays exhibit quasi-ballistic propagation below the ‘ankle’ energy (5×10^{18} eV) and experience significant suppression below 10^{17} eV. We use a mild increase of $\sim 30\%$ in the flux of ultra-high-energy cosmic rays within the past 46–55 thousand years, to induce anisotropies in the arrival direction of UHECRs as observed by the Auger collaboration (Fig. 2.5 b)). Furthermore, we investigate the energy and composition dependent dipole amplitude evolution (Fig. 2.6). Heavy elements seem to play a key role in reproducing the energy-dependent dipole amplitude evolution, but this tendency needs to be validated with higher propagation times, higher statistics and more sophisticated temporal modulations. Future studies on anisotropies, employing more advanced methodologies, may offer valuable insights into the mass composition of ultra-high-energy cosmic rays, potentially enabling a deeper understanding of their origins and behavior. Overall, this work emphasizes the need to have good galactic magnetic field models and highlights the importance of residence time effects to cosmic rays propagation in our Galaxy.

Data availability
The Python scripts and notebooks which have been used for the simulations in this paper are available after publication on GitLab[4].

Acknowledgements
This work is supported by SFB 1491 (Project A3). LM's work is supported by the DFG under grant number 445990517 (KA 710).

Contributions of the author JM
Contributions include writing the manuscript, including drafting the first version, simulation and analysis, figure preparation, conceptualization, methodology, and review & editing.

2.5 Appendix

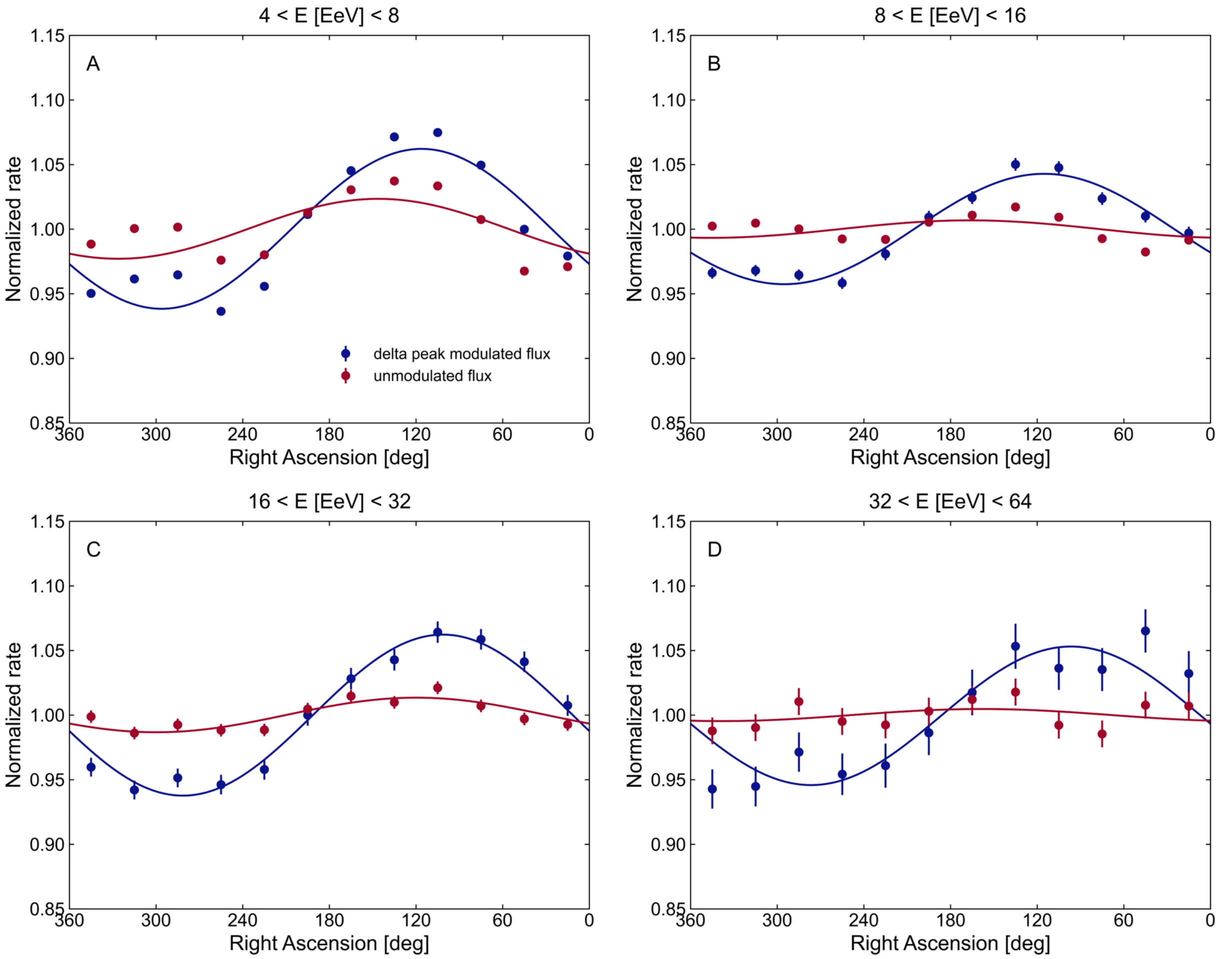

Figure 2.7: The UHECR flux modulation as shown in Fig. 2.5 a) is applied in six different energy bins in order to study the energy dependent evolution of the dipole amplitude in Fig. 2.6. The mass composition, as shown in Fig.2.3 b) is used both for the unmodulated (red) and the modulated flux (ultramarine) in all subfigures. This composition is based on a EPOS-LHC fit to the X_{max} of 2019 Auger data. The four energy bins are (A: 4-8, B: 8-16, C: 16-32, D: 32-64) EeV.

[4] https://git.uni-wuppertal.de/meinert/uhecr-flux-modulation-induced-anisotropy

2.6 Simulation Setup

To study the propagation of ultra-high-energy cosmic rays through the galactic magnetic field of the Milky Way, we employ the CRPropa 3.2 framework [58]. For easier data management, and in particular for the EPOS-LHC composition, we chose to simulate in batches of 40 million particles each. In the following, our simulation setup is detailed, which has been employed for four different nuclei species. The EPOS-LHC composition utilizes sixteen energy bins in total, from $10^{18.6}$–$10^{20.2}$ eV in logarithmic intervals. The number of batches for each nuclei species can be seen in Fig.2.3 a), as well as in Table 2.1 below. All Python scripts are available online after publication.

Nucl.	bin 1	bin 2	bin 3	bin 4	bin 5	bin 6	bin 7	bin 8	bin 9	bin 10	bin 11	bin 12	bin 13	bin 14	bin 15	bin 16
H	33	26	18	10	5	2	1	1	1	1	1	1	1	1	1	1
He	23	28	34	36	36	28	16	6	2	1	1	1	1	1	1	1
N	21	27	38	48	60	79	91	99	98	79	50	28	14	6	2	1
Fe	3	4	6	7	10	12	15	17	22	26	28	28	20	11	5	2

Table 2.1: Summary of simulation batches for four nuclei species (H, He, N, Fe) across 16 energy bins, normalized to nitrogen at $10^{19.4}$ eV. Each batch consists of 40 million particles, with up to 100 batches per species, following the EPOS-LHC fit. The energy binning scheme uses logarithmic intervals from $10^{18.6}$–$10^{18.7}$ eV to $10^{20.0}$–$10^{20.2}$ eV. Each bin width follows a constant step size of 0.1 in the exponent, ensuring a uniform logarithmic spacing.

2.6.1 Emission and Initial Conditions

We inject nuclei isotropically from a spherical shell of radius $R_{\mathrm{em}} = 20\,\mathrm{kpc}$ around the Galactic center, ensuring a uniform distribution using the `SourceLambertDistributionOnSphere` method, which employs a Lambertian distribution. The injected nuclei are assigned an energy spectrum following a power-law distribution,

$$\frac{\mathrm{d}N}{\mathrm{d}E} \propto E^{\gamma}, \tag{2.1}$$

with a spectral index of $\gamma = -2.7$, spanning the energy range $10^{18.5} - 10^{20.5}$ eV, using the function `SourcePowerLawSpectrum`. Only for the simulation shown in Fig.2.2 a), a spectral index of $\gamma = -1$, in the energy range $10^{16} - 10^{21}$ eV has been employed. The particle type is set using `SourceParticleType`, allowing for the simulation of different nuclei species. In this study, we focus on hydrogen, helium, nitrogen and iron. For example, helium is implemented using the nuclei ID: (`nucleusId(4,2)`), where the first entry represents the mass number and the second denotes the number of protons.

2.6.2 Magnetic Field Model and Propagation

The simulation includes a large-scale galactic magnetic field, implemented with the `PlanckJF12bField` model, which is an updated version of the JF12 field [56]. Charged particle propagation is handled using the `PropagationCK` module, which numerically integrates particle trajectories while considering magnetic deflections. The propagation step size is set to 0.1 pc. Each particle is propagated up to a maximum trajectory length of 100 kpc before being terminated via the `MaximumTrajectoryLength` module. The propagation is also terminated, if the capture sphere is reached or if the particles leave the Galaxy. The latter condition is checked with a second capture sphere at a radius of $R_{\mathrm{cancel}} = 22\,\mathrm{kpc}$ from the Galactic center.

2.6.3 Observer Setup and Data Collection

To detect particles reaching the vicinity of the Earth, we define observer surfaces at a distance of $R_{\oplus} = -8.5\,\mathrm{kpc}$ from the Galactic center on the x-Axis in Cartesian coordinates, which is corresponding to the Solar System's location. The observer is implemented using the `ObserverSurface` module, with a spherical capture region of radius 1 kpc. The observer deactivates particles upon detection (`setDeactivateOnDetection(True)`), preventing further propagation and potential double counting. All detected particle data, including arrival directions, energies, and species, are stored in an output file using the `TextOutput` module. The output format includes all available particle information (`Output.Everything`), with spatial coordinates expressed in kiloparsecs.

2.6.4 Simulation Parameters and Execution

The simulation is executed for $N_{\mathrm{cand}} = 40,000,000$ injected particles, ensuring statistical robustness when multiple batches are combined. The entire simulation pipeline is run with progress tracking enabled (`setShowProgress(True)`).

2.6.5 Summary of Key Parameters

Parameter	**Value**
Emission radius (R_{em})	20 kpc
Observer radius ($R_{\oplus}$)	−8.5 kpc on the x-Axis
Observer capture sphere radius (R_{obs})	1 kpc
Outer capture sphere radius (R_{cancel})	22 kpc
Energy range	$10^{18.5} - 10^{20.5}$ eV
Spectral index (γ)	−2.7
Magnetic field model	PlanckJF12bField
Propagation step size	0.1 pc
Maximum trajectory length	100 kpc
Number of simulated particles (N_{cand})	40, 000, 000

Table 2.2: Summary of simulation parameters used in CRPropa per batch.

This setup enables the study of UHECR propagation in the Galactic environment, providing insights into the influence of the GMF on cosmic ray anisotropy.

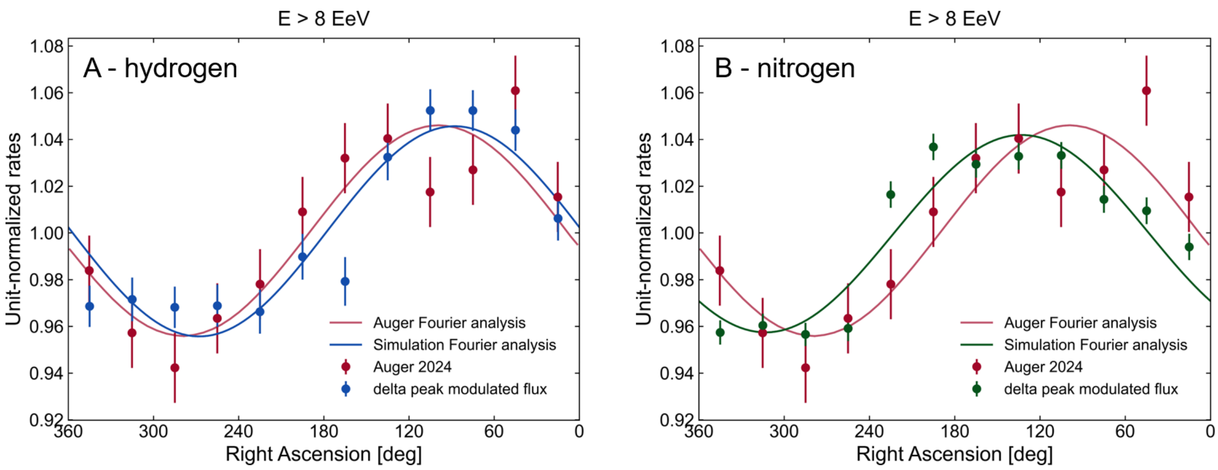

Figure 2.8: **A** Comparison of simulated hydrogen with a 23% increased UHECR flux for propagation distances between 14–17 kpc (compare the delta function like flux modulation in Fig. 2.5 a)) with 2024 Auger data, compare [50]. **B** Comparison of simulated nitrogen with a 37% increased UHECR flux for propagation distances between 14–17 kpc with 2024 Auger data, compare [50]. For Auger data, all energies E > 8 EeV have been taken into account, for the modulated flux simulation the energy range 8 EeV < E < 64 EeV has been assumed.

3 *T-z* Relation and UHECR Propagation

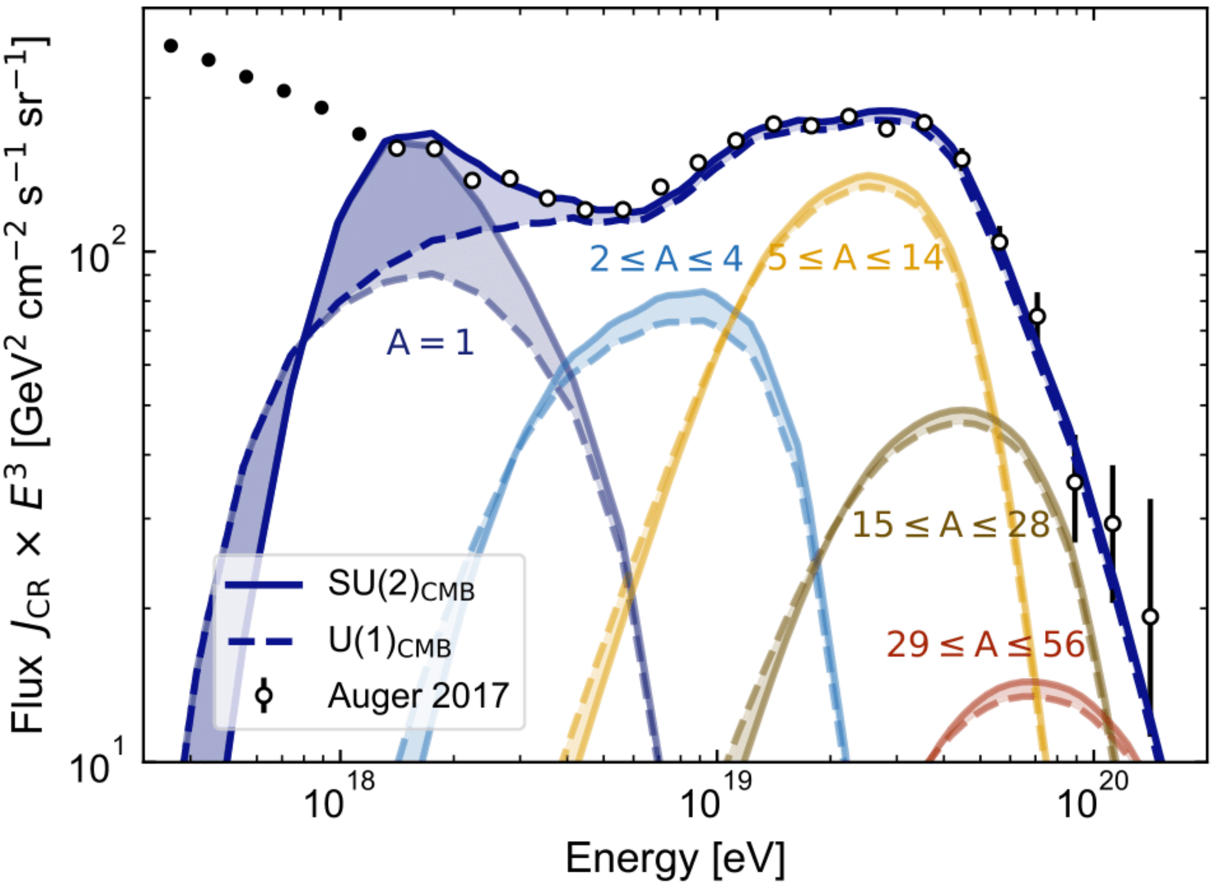

Figure 3.1: Spectral fit using a gradient descent algorithm to the 2017 Auger spectral flux data, $X_{\max}$ and $\sigma(X_{\max})$ data [60]. The fluxes of the normal U(1) and modified SU(2) temperature redshift relations are shown as dashed and full lines, respectively. The χ^2 was computed, including all the white dots.

This chapter is based the publication "Modified Temperature-Redshift Relation and Ultra-high-energy Cosmic Ray Propagation" [2] as well as the conference proceeding [7].

Contents

3.1 Introduction **20**
3.2 T(z) Relation of SU(2)$_{CMB}$ **21**
3.3 Changes in Propagation Length **22**
3.4 Observational Consequences for UHECR Energy Spectra **24**
3.5 Cosmogenic Neutrinos **27**
3.6 Summary **28**

Janning Meinert[1,2], Leonel Morejón[1], Alexander Sandrock[1], Björn Eichmann[3], Jonas Kreidelmeyer[4], Karl-Heinz Kampert[1]

[1]Bergische Universität Wuppertal, Department of Physics, Gaußstraße 20, D-42103 Wuppertal

[2]Institut für Theoretische Physik, Universität Heidelberg Philosophenweg 12, D-69120 Heidelberg

[3]Ruhr-Universität Bochum, Theoretische Physik IV, Universitätsstraße 150, D-44801 Bochum

[4]Institut für Experimentalphysik, Universität Hamburg, DESY, Luruper Chaussee 149, D-22761 Hamburg

Abstract

We re-examine the interactions of ultra-high energy cosmic rays (UHECRs) with photons from the cosmic microwave background (CMB) under a changed, locally non-linear temperature redshift relation $T(z)$. This changed temperature redshift relation has recently been suggested by the postulate of subjecting thermalised and isotropic photon gases such as the CMB to an SU(2) rather than a U(1) gauge group. This modification of ΛCDM is called $\mathrm{SU(2)_{CMB}}$, and some cosmological parameters obtained by $\mathrm{SU(2)_{CMB}}$ seem to be in better agreement with local measurements of the same quantities, in particular H_0 and S_8. In this work, we apply the reduced CMB photon density under $\mathrm{SU(2)_{CMB}}$ to the propagation of UHECRs. This leads to a higher UHECR flux just below the ankle in the cosmic ray spectrum and slightly more cosmogenic neutrinos under otherwise equal conditions for emission and propagation. Most prominently, the proton flux is significantly increased below the ankle (5×10^{18} eV) for hard injection spectra and without considering the effects of magnetic fields. The reduction in CMB photon density also favours a decreased cosmic ray source evolution than the best fit using ΛCDM. In consequence, it seems that $\mathrm{SU(2)_{CMB}}$ favours sources that evolve as the star formation rate (SFR), like starburst galaxies (SBG) and gamma-ray bursts (GRB), over active galactic nuclei (AGNs) as origins of UHECRs. We conclude that the question about the nature of primary sources of UHECRs is directly affected by the assumed temperature redshift relation of the CMB.

3.1 Introduction

The cosmic microwave background (CMB) is the cornerstone of modern Cosmology. Modelling its properties correctly is, however, not only relevant for Cosmology but also vital for the correct description of ultra-high energy cosmic ray (UHECRs) propagation. While there are well known features such as the cold spot and anisotropies [62], a lesser-known anomaly is the excess of CMB line temperature at low frequencies, starting at around 1 GHz [63, 42, 64]. One suggested explanation for this extra radiation involves radio sources in the galactic foreground, but fails to account for the isotropic nature of the excess radiation [42, 65]. Another potential foreground source could be the decay of axions with a mass of around $30\,\mu$eV (8 GHz); compare [66] for a general discussion of axion decays at radio frequencies. Instead of a radio source in the foreground, the CMB line temperature excess can also be interpreted as an intrinsic feature of the CMB itself [67].

Associating CMB photons with a thermal SU(2) gauge theory, the so-called $\mathrm{SU(2)_{CMB}}$, instead of the commonly considered thermal U(1) theory, introduces two interesting phase boundaries [31]. The CMB occurs in the deconfining phase, where the SU(2) gauge symmetry is broken down to U(1) due to densely packed topological field configurations, the Harrington-Shepard anti-calorons and calorons [68]. In the thin preconfining phase, U(1) is reduced to the magnetic center group Z_2 which is broken, in turn, in the confining phase. The transition from the deconfining to the preconfining phase occurs at a critical temperature T_c, which can be identified to be close to the current temperature of the CMB [67]. Spontaneously breaking the U(1) gauge group in the preconfined phase then leads to a Meissner mass of the photon of around 10 peV (100 MHz), compare [67]. This alternative explanation of the radiation excess as an intrinsic feature of the cosmic microwave background (CMB) implies changes of the current cosmological model ΛCDM.

Most noticeably, the temperature redshift relation $T(z)$ of the CMB photons is changed. Within flat ΛCDM and in adiabatically evolving cosmological models, the $T(z)$-relation is $T(z)/T_0 = (1 + z)$, where $T_0 = 2.725\,\mathrm{K}$ is the present CMB temperature [69]. Implementing an SU(2) gauge group into ΛCDM leads to $T(z)/T_0 = 1/4^{1/3}\,(1+z)$ for large redshifts $z \gg 1$ see also [40]. This means that the CMB photons are cooling down slower with the expansion of the Universe in SU(2)$_{\rm CMB}$ than in ΛCDM. The changed $T(z)$ thus requires recombination to occur at a higher redshift. Fitting the CMB multipoles with the changed $T(z)$, recombination occurs at $z_{*,\rm SU(2)} = 1715 \pm 0.19$ [33] and is thereby at a significantly higher redshift than in normal ΛCDM with $z_{*,\rm U(1)} = 1089.92 \pm 0.25$ [36].

When implementing the modified $T(z)$ under SU(2) in CMB fits, some cosmological parameters are in better agreement with locally obtained values than with ΛCDM [33]. In particular, the Hubble parameter of SU(2)$_{\rm CMB}$, $H_0 = 74.24 \pm 1.46\,\mathrm{km\,s^{-1}\,Mpc^{-1}}$, is in agreement with local values obtained by distance ladders [32]. Similarly, the mild tension in σ_8 and $\Omega_{\rm m,0}$ [70] is alleviated with $\sigma_8 = 0.709 \pm 0.020$ and $\Omega_{\rm m,0} = 0.384 \pm 0.006$ [33] especially when trying to break degeneracy independently of any cosmological model [71]. The relatively high recombination redshift has mainly two consequences: the fit to CMB multipoles does not work, unless more matter is introduced to the cosmological model at some point after recombination [33]. This is resolved by splitting the dark matter content into two parts, one which is introduced before recombination and one afterwards. This sets some constraints to the nature of dark matter, preferring ultra light dark matter classes such as fuzzy dark matter [41]. The second consequence of this high recombination redshift is stretching the CMB photon density over longer periods of time, which thus effectively reduces the CMB spatial density and produces an increase in the interaction lengths of ultra-high energy cosmic rays.

While there are many attempts to measure the $T(z)$-relation of the CMB indirectly, for example with absorber clouds [72], it is not obvious that those indirect methods are sensitive to the actual CMB temperatures at finite redshifts [3]. They might only probe the temperature of the absorber clouds and the blackbody nature of the CMB. There is a need of determining the temperature redshift relation of the CMB directly. In this work, we dilute the CMB photon density in comparison to the standard cosmological model ΛCDM, by assuming the so-called SU(2)$_{\rm CMB}$ model [67, 33, 31, 34, 3]. The purpose of this paper is to discuss how these potential changes to the CMB photon density influence the propagation of UHECRs. Previous discussions of the consequences of an SU(2)$_{\rm CMB}$ description on UHECR interactions were limited to considering the handedness of the photons, SU(2)$_{\rm L}$ [73]. A fully consistent understanding of the SU(2)$_{\rm CMB}$ model requires applying Yang-Mills thermodynamics and obtaining the modified $T(z)$. Furthermore, the effect of this modified temperature redshift relation on the CMB density produces non-trivial redshift dependences on the UHECR interactions that need to be considered in depth. Firstly, the modified $T(z)$ relation is outlined in section 3.2. The consequences of this relation for all the interactions of UHECRs are discussed in section 3.3. Section 3.4 compares fits of UHECRs spectral energy and composition measured by the Pierre Auger Observatory with both U(1) and SU(2) $T(z)$ relations. The corresponding cosmogenic neutrino fluxes are presented in section 3.5.

3.2 T(z) Relation of SU(2)$_{\rm CMB}$

In the following, we briefly review the $T(z)$ relation of deconfining SU(2)$_{\rm CMB}$ thermodynamics. For a longer version of the argument, the reader is referred to [74, 3]. The core idea is that the additional degrees of freedom in an SU(2) gauge group lead to the topological constant $1/4^{1/3}$, so that the $T(z)$ relation is for $z \gg 1$ given by

$$T(z)/T_0 = \left(\frac{1}{4}\right)^{1/3} (1+z)\,, \qquad (T(z) \gg T(z=0)). \tag{3.1}$$

To derive this constant, a flat Friedmann-Lemaître-Robertson-Walker (FLRW) universe is assumed:

$$\frac{\mathrm{d}\rho}{\mathrm{d}a} = -\frac{3}{a}\,(\rho + P)\ , \tag{3.2}$$

where ρ denotes the energy density, and P the pressure of the deconfined phase in SU(2) thermodynamics. The scale factor a is dimensionless, $a(T(z=0)) = 1$, and related to the redshift z according to $1/a = z+1$.

Eq. (3.2) has the solution

$$\begin{aligned} a &= \exp\left(-\frac{1}{3}\int_{\rho(T(z=0))}^{\rho(T)} \frac{\mathrm{d}\rho}{\rho + P(\rho)}\right) \\ &= \exp\left(-\frac{1}{3}\int_{T(z=0)}^{T} \underbrace{\frac{1}{T'}\frac{\mathrm{d}\rho}{\mathrm{d}T'}}_{\kappa}\frac{\mathrm{d}T'}{s(T')}\right), \end{aligned} \tag{3.3}$$

where the entropy density s is defined as $s = (\rho + P)/T$. By using the Legendre transformation

$$\rho = T\frac{\mathrm{d}P}{\mathrm{d}T} - P\,, \tag{3.4}$$

the term κ can be expressed as

$$\kappa = \frac{1}{T}\frac{\mathrm{d}\rho}{\mathrm{d}T} = \frac{\mathrm{d}^2 P}{\mathrm{d}T^2} = \frac{\mathrm{d}s}{\mathrm{d}T}\,. \tag{3.5}$$

Substituting Eq. (3.5) into Eq. (3.3) finally yields

$$a = \exp\left(-\frac{1}{3}\log\frac{s(T)}{s(T(z=0))}\right)\,. \tag{3.6}$$

The formal solution (3.6) is valid for any thermal and conserved fluid subject to expansion in an FLRW universe. If the function $s(T)$ is known, then $T(z)$ can be derived. The ground-state of the deconfining phase is independent of the $T(z)$ relation, since the equation of state for ground-state pressure P^{gs} and energy density ρ^{gs} is $P^{\mathrm{gs}} = -\rho^{\mathrm{gs}}$ [see also 31]. Asymptotic freedom occurs nonperturbatively for $T(z) \gg T(z=0)$ [75, 76, 31], and therefore $s(T)$ is proportional to T^3. Due to a decoupling of massive vector modes at $T(z=0)$, excitations represent a free photon gas. Therefore, $s(T(z=0))$ is also proportional to $T^3(z=0)$. Correspondingly, the ratio $s(T)/s(T(z=0))$ in Eq. (3.6) reads

$$\frac{s(T)}{s(T(z=0))} = \frac{g(T)}{g(T(z=0))}\left(\frac{T}{T(z=0)}\right)^3\,,\ (T \gg T(z=0))\,, \tag{3.7}$$

where g refers to the number of relativistic degrees of freedom at the respective temperatures. SU(2) has one massless gauge mode with two polarisations and two massive gauge modes with three polarisations each, so $g(T) = 2\times 1 + 3\times 2 = 8$, for U(1) there is only one massless mode, $g(T(z=0)) = 2\times 1$. Substituting this into Eq. (3.7), inserting the result into Eq. (3.6), and solving for T, one arrives at the high-temperature $T(z)$ relation

$$T(z) = \left(\frac{1}{4}\right)^{1/3}(z+1)\,T(z=0)\,,\quad (T \gg T(z=0))\,. \tag{3.8}$$

Due to two massive vector modes contributing to $s(T)$ at low temperatures, the $T(z)$ relation is modified to

$$T(z) = \mathcal{S}(z)(z+1)\,T(z=0)\,,\quad (T \geq T(z=0))\,, \tag{3.9}$$

where the nonlinear function $\mathcal{S}(z)$ is depicted in Fig. 3.2 and derived in [33]. The function $\mathcal{S}(z)$ can be approximated reasonably well with the analytical function

$$\mathcal{S}(z)_{\mathrm{SU(2)}} \approx \exp(-1 - 1.7\,z) + \left(\frac{1}{4}\right)^{1/3}\,. \tag{3.10}$$

This approximation will be used in section 3.3. However, the numerical solution was applied for all following sections.

3.3 Changes in Propagation Length

In this section, we discuss the changes to the propagation of ultra-high energy cosmic rays produced by employing the modified temperature relation $T(z)$ from $\mathrm{SU(2)_{CMB}}$ as derived in the previous section, Eqs. 3.8 and 3.9.

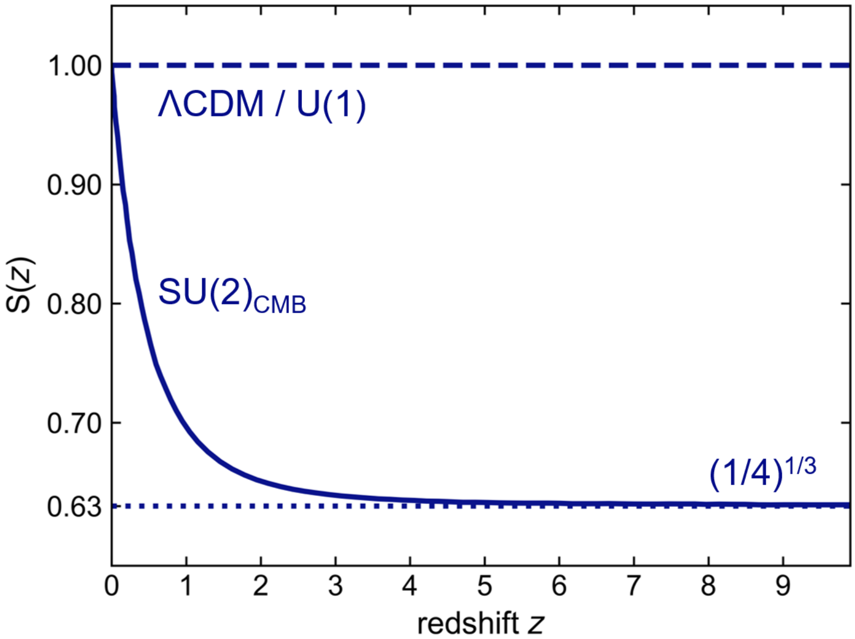

Figure 3.2: Plot of function $\mathcal{S}(z)$ in Eq. (3.9) for $\mathrm{SU(2)_{CMB}}$ in solid. The conventional $T(z)$ relation of the CMB, as used in the cosmological standard model ΛCDM, associates with the dashed line $\mathcal{S}(z) \equiv 1$. The high-temperature value $1/4^{1/3}$ is approximated by the dotted line $\mathcal{S}(z) = 0.63$.

The redshift dependence of the CMB temperature results in scaling and shifting of the differential CMB photon number density $n_{\mathrm{CMB}}(\epsilon, z)$

$$n_{\mathrm{CMB}}(\epsilon, z) = \left(\frac{T(z)}{T_0}\right)^2 n_{\mathrm{CMB}}\left(\epsilon\left(\frac{T(z)}{T_0}\right)^{-1}, 0\right), \tag{3.11}$$

where ϵ is the energy of the photons, and n_{CMB} as derived from the Planck distribution is

$$n_{\mathrm{CMB}}(\epsilon, z) = \frac{1}{\pi^2 c^3 \hbar^3} \frac{\epsilon^2}{\exp(\epsilon/k_B T(z)) - 1} \tag{3.12}$$

where k_B is the Boltzmann constant. The redshift dependence of UHECR interactions with the CMB is reflected in the expression for the energy loss length [77]

$$-\frac{1}{E}\frac{\mathrm{d}E}{\mathrm{d}x} = \int_{\epsilon_0}^{\infty} \mathrm{d}\epsilon' \, \frac{k_B T\, \sigma(\epsilon') f(\epsilon')\epsilon'}{2\pi^2 \Gamma^2 c^3 \hbar^3} \left\{ -\ln\left[1 - \exp\left(-\frac{\epsilon'}{2\Gamma k_B T}\right)\right]\right\}$$

where E is the energy and Γ is the Lorentz boost of the UHECRs, and $\sigma(\epsilon')$ is the cross-section of the corresponding interaction (photodisintegration, photomeson, pair-production) and $f(\epsilon')$ is the average inelasticity of the interaction. The scaling of the CMB density produces a corresponding scaling of the interaction rates $\lambda(\Gamma, z)$:

$$\lambda(\Gamma, z) = \left(\frac{T(z)}{T_0}\right)^3 \lambda\left(\frac{T(z)}{T_0}\Gamma, z = 0\right). \tag{3.13}$$

The comparison of the energy loss lengths for U(1) and SU(2) is shown in Fig. 3.3 (protons) and in Fig. 3.4 (iron) for $z = 1$. The interaction processes with the CMB are represented separately (photopion, photodisintegration, pair production) while they are grouped into one curve for extragalactic background light (EBL, dotted dark red)[1]. For protons at redshift $z = 1$ the energy loss length at the GZK-limit (E$\sim$ 50 EeV) is shifted by a factor of $\sim$2 to higher energies for SU(2) and the propagation lengths for both pair production and photopion production are increased by nearly a factor 3. For iron nuclei at the same redshift, the corresponding photodisintegration limit is also shifted to higher energies by a factor $\sim$2 for the SU(2). However, because the energy loss lengths are also increased due to the reduced CMB density, the interactions with the EBL are the dominant ones for cosmic ray energies below 10^{20} eV and therefore

[1] In this work we do not include the CMB nor the radio background into the description of the EBL. The EBL remains unchanged under the assumption of an SU(2) gauge group for thermal photons, as the EBL is not thermalized.

the total energy loss length is not increased as much as in the case of protons. This is representative of the case for all intermediate nuclear species with masses between the proton and iron. The increase in energy loss lengths implies the expansion of the horizon for UHECRs: for protons at all energies, for nuclei at the highest energies starting from about $\sim 10^{19}$ eV. With such an increase, protons from sources at redshift 1 and energies $1 - 40$ EeV would propagate for several hundreds of megaparsecs more than in the case of the U(1), whereas protons at higher energies (where the photopion interactions prevail) would propagate for more than ten megaparsecs.

These increases of propagation horizons are only important when the contribution from distant sources is the dominant one. As the redshift evolves to the present, the U(1) and $SU(2)_{CMB}$ densities converge and by distances of 20 Mpc from Earth the loss lengths differ by only 1.5 %. Thus, although protons can propagate further away from sources beyond ∼200 Mpc in the SU(2) case, they completely lose their energy before reaching our galaxy and only the secondary neutrinos reach us, much like in the U(1) case.

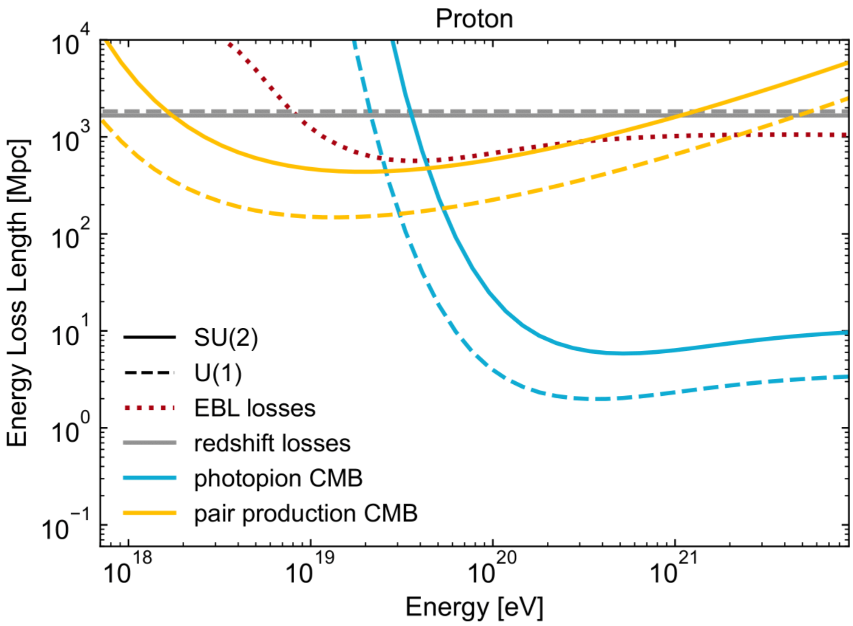

Figure 3.3: Propagation length of protons at redshift $z = 1$ as a function of the initial particle energy. The normal U(1) and the SU(2) induced $T'(z)$ propagation lengths are shown as dashed and full lines, respectively.

Nonetheless, protons coming from sources marginally closer are able to reach our galaxy: at a distance of 200 Mpc Eq. 3.13 yields a reduction in the interaction rates of ∼9 % for the SU(2) scenario, see Fig. 3.3. For nuclei the increased propagation is, however, much less relevant since their propagation lengths are limited to a few dozens of Mpc. For such distances, the reduction in interaction rates with the CMB is of $2 - 4$ % for SU(2). However, those interactions are overshadowed by the dominant interactions with the EBL.

3.4 Observational Consequences for UHECR Energy Spectra

We evaluate the impact on the propagation of UHECRs by employing the fit obtained by [78] to data from the Pierre Auger Observatory [60] under a conventional temperature redshift relation (ΛCDM). The changes in spectral energy and composition produced with the same fit values under $SU(2)_{CMB}$ are obtained by employing the modified $T(z)$-relation. The propagation of UHECRs was performed using PriNCe [78], which is an efficient code to integrate the transport equations for the evolution of cosmic rays at cosmological scales. It includes all the relevant interactions and allows for custom modifications, however, it does not account for the effect of magnetic fields. The propagation scenario considers a population of sources with a continuous distribution in redshift proportional to $(1 + z)^m$ with source evolution parameter m obtained from the fit. The sources are assumed to be isotropically distributed

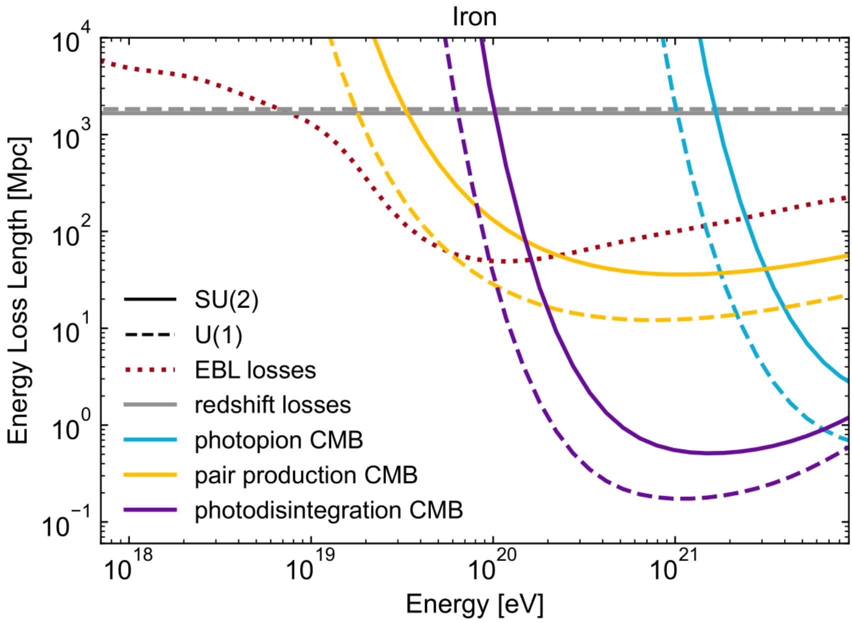

Figure 3.4: As Fig. 3.3 for the propagation length of iron nuclei.

and to eject a rigidity-dependent spectral energy flux according to

$$J_A(E) = \mathcal{J}_A\, f_{\rm cut}(E, Z_A, R_{\rm max})\,(1+z)^m \left(\frac{E}{E_0}\right)^{-\gamma}, \tag{3.14}$$

with five nuclear mass groups indicated by the index $_A$ (denoting the nuclear species ^{1}H, ^{4}He, ^{14}N, ^{28}Si, and ^{56}Fe). They share the same spectral index γ and the maximal rigidity $R_{\rm max} = E_{\rm max}/Z_A$. The cutoff of the injection spectra $f_{\rm cut}$ is defined as

$$f_{\rm cut}(E) = \begin{cases} 1, & E < Z_A R_{\rm max} \\ \exp\left(1 - E/(Z_A R_{\rm max})\right), & E > Z_A R_{\rm max}. \end{cases} \tag{3.15}$$

$\mathcal{J}_A$ represents the flux of particles of species A emitted per unit of time, comoving volume, and energy. The elemental injection fractions f_A are defined as $f_A = \mathcal{J}_A/(\Sigma_{A'}\,\mathcal{J}_{A'})$ at the reference energy $E_0 = 10^{18}$ eV. Integrating over the injected fluxes J_A leads to the integral fractions of the energy density I_A, which are independent of the choice of E_0:

$$I_A = \frac{\int_{E_{\rm min}}^{\infty} J_A E\,{\rm d}E}{\Sigma_{A'}\int_{E_{\rm min}}^{\infty} J_{A'} E\,{\rm d}E} = \frac{\int_{E_{\rm min}}^{\infty} f_A\, f_{\rm cut}(E, Z_A)\, E^{1-\gamma}{\rm d}E}{\Sigma_{A'}\int_{E_{\rm min}}^{\infty} f_{A'}\, f_{\rm cut}(E, Z_{A'})\, E^{1-\gamma}{\rm d}E}, \tag{3.16}$$

where $E_{\rm min} = 10^{18}$ eV. For the sake of completeness, we provide both f_A and I_A in the following sections. For SU(2)$_{\rm CMB}$ the following cosmological parameters were used for the propagation: the Hubble parameter H_0= 74.24 km s^{-1}Mpc^{-1}, a dark energy fraction of $\Omega_\Lambda = 0.616$, and the local matter density $\Omega_{\rm m,0} = 0.384$, compare with [33]. For U(1)$_{\rm CMB}$ (ΛCDM) the values from the Planck Collaboration were used [36, p. 15, Table 2], where $H_0 = 67.36$ km s^{-1}Mpc^{-1}, $\Omega_\Lambda = 0.6847$ and $\Omega_{\rm m,0} = 0.3153$ (TT,TE,EE+lowE+lensing).

The best fit parameters obtained by [78] for the conventional ΛCDM relation are reported in Table 3.1 and plotted in Figure 3.5 for reference (dashed lines). Fixing these source parameters and propagating the injected UHECR through the SU(2)$_{\rm CMB}$ with its modified $T(z)$ relation yields the solid lines in the same figure. As can be seen, the resulting total flux for SU(2) is virtually unchanged for energies above 6×10^{18} eV, while the fluxes for individual nuclear groups show slightly more pronounced peaks. This effect is a consequence of the modest increase in the horizons. At the same time, the reduction in the pair production losses produces sharper peaks because the effect of energy redistribution corresponding to the U(1) cases is less prominent for SU(2). For protons at the lowest energies, the differences are much more pronounced due to the change in pair production rates as the energies approach 10^{18} eV from above.

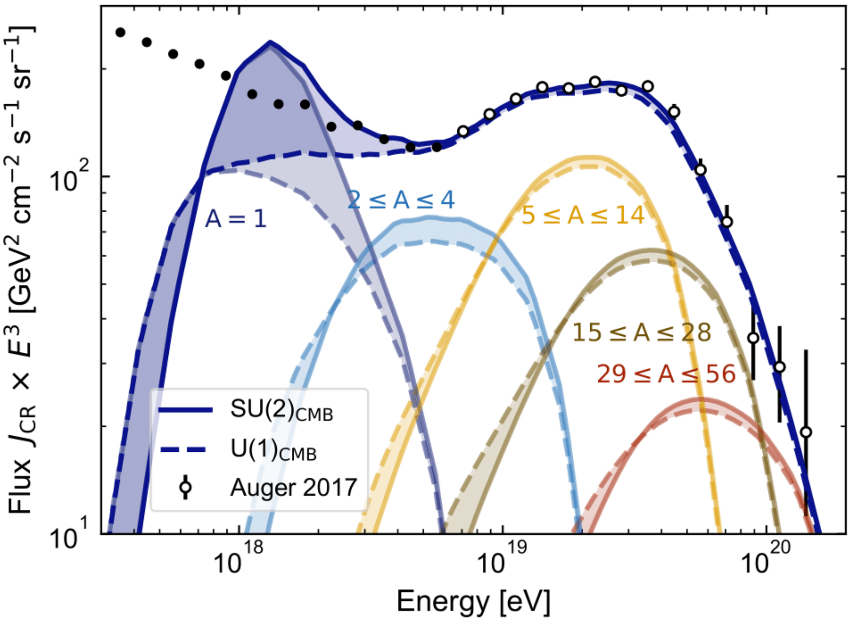

Figure 3.5: Spectral fit to the 2017 Auger spectral flux data [60] from the best fit parameters in [78], see Tab. 3.1. The fluxes of the normal U(1) and modified SU(2) temperature redshift relations are shown as dashed and full lines, respectively. The χ^2 only considers data points above the ankle region (white dots), as was done in [78].

EBL	Gilmore et al.	Element	f_A %	I_A %
models	TALYS & Sibyll 2.3c	H	0.0	0.0
redshifts	1 − 0	He	82.0	9.91
γ	-0.8	Ni	17.3	69.99
$R_{\max}$	1.6×10^{18} V	Si	0.6	16.91
m	4.2	Fe	0.02	3.19

Table 3.1: Best fit parameters from [78], Table 3.

Repeating now the combined E, $X_{\max}$, and $\sigma(X_{\max})$ fit to the same data set of [60] employing a gradient descent algorithm [79, p. 33 ff.] for all data points above 1×10^{18} eV in the SU(2)$_{\text{CMB}}$ model, we find the best fit parameters shown in Table 3.2 and plotted in Fig. 3.6 as full lines. For this fit, the proton excess of SU(2)$_{\text{CMB}}$ below the ankle is reduced and the main contributing factor is the shallower source evolution ($m = 2.7$) in contrast to the stronger evolution $m = 4.2$ for U(1) in Heinze's best fit. The injected chemical composition and the spectral index are only mildly changed, which suggests that the shallower source evolution is enough to compensate for the increased proton horizon and the pileup below the ankle. Note that the proton fraction below the ankle is still too high, in disagreement with the chemical composition inferred from the $X_{\max}$ data. Below the ankle, an additional galactic component is expected with a heavier composition. To better illustrate the SU(2) impact on UHECR propagation, Fig. 3.7 contrasts the cosmic ray fluxes resulting with a conventional U(1) propagation employing the best fit parameters from Table 3.2 and scaling the CMB photon density by different factors as shown in the curve labels. The red dotted line in Fig. 3.7 corresponds to SU(2)$_{\text{L}}$, where CMB photons interact only with half of the UHECRs due to their handedness.

EBL	Gilmore et al.	Element	f_A %	I_A %
models	TALYS & Sibyll 2.3c	H	0.001	0.0
redshifts	1 − 0	He	82.3	9.74
γ	-0.89	Ni	17.4	76.9
$R_{\max}$	1.74×10^{18} V	Si	0.35	11.6
m	2.7	Fe	0.01	1.72

Table 3.2: Best fit gradient descent parameters for the SU(2)$_{\text{CMB}}$ model.

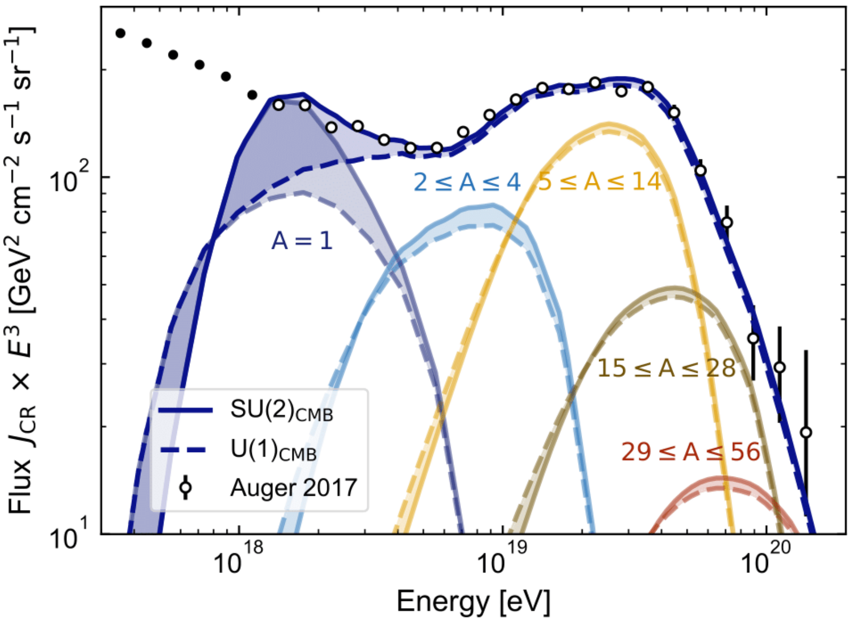

Figure 3.6: Spectral fit using a gradient descent algorithm to the 2017 Auger spectral flux data, $X_{\max}$ and $\sigma(X_{\max})$ data [60]. The fluxes of the normal U(1) and modified SU(2) temperature redshift relations are shown as dashed and full lines, respectively. The χ^2 was computed including all the white dots.

The excess in proton flux below the ankle is correlated with the CMB photon density, because these protons come from the disintegration of nuclei. However, this relation is dependent on the injection spectral index, and it is hard to distinguish an increased proton flux from an additional UHECR source and source evolution. Detailed directional studies which also consider the effects of magnetic fields as well as a better understanding of the chemical composition below the ankle are necessary in order to favour or disfavour the correlation between the slope of the UHECR flux below the ankle and $T(z)$. Note also that only hard spectra, i.e. $\gamma \leq 0$ can increase significantly the UHECR flux below the ankle, because of the larger contribution of the highest energies in secondary protons. Soft injection spectra, e.g. $\gamma \approx 2$ as expected by shock acceleration, do not significantly increase the UHECR flux under SU(2)$_{\text{CMB}}$.

3.5 Cosmogenic Neutrinos

The expected cosmogenic neutrino fluxes are shown in Fig. 3.8 for the modified temperature redshift relation under SU(2)$_{\text{CMB}}$ and the normal $T(z)$ for the best fit values from the gradient descent method, Table 3.2. The neutrino fluxes for SU(2)$_{\text{CMB}}$ peak at slightly higher energies and are slightly increased. The former feature is a consequence of the changed redshift dependence, which increases the energy of the GZK limit in SU(2)$_{\text{CMB}}$ compared to U(1). The latter effect results from the increase in the propagation horizon of the source protons. Figure 3.8 shows that changes in the $T(z)$ relation of the CMB only affect the cosmogenic neutrino flux for energies around 10^{17} eV. The peak at around 10^{15} eV, stemming mostly from the decay of neutrons from photodisintegration (see e.g. [80]) is mostly unaffected except for being slightly narrower due to reduced pair production losses.

In addition to the cosmogenic neutrinos, the photopion production with the CMB also generates γ-rays and the resulting flux at Earth in the case of a SU(2)$_{\text{CMB}}$ would be slightly enhanced compared to the U(1)$_{\text{CMB}}$ due to the increased horizon in the absence of $\gamma\gamma$-pair production. However, $\gamma\gamma$-pair production and inverse Compton scattering with the EBL are the dominant interactions, in particular for γ-ray energies $\lesssim 100$ TeV, therefore, after the cascading of photon we expect no significant difference in the cosmogenic γ-ray flux between the SU(2)$_{\text{CMB}}$ and the U(1)$_{\text{CMB}}$.

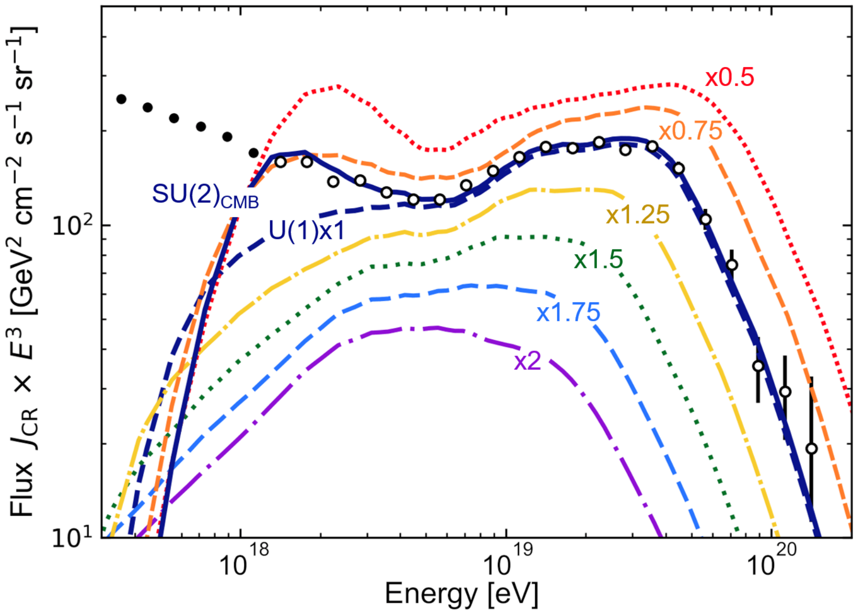

Figure 3.7: The effect of seven modified CMB photon densities on the total cosmic ray flux is shown in comparison to the normal U(1) temperature redshift relation, as obtained in [78] (navy blue, dashed) on top of Auger data from 2017. The best fit parameters of the gradient descent method are used, compare Table 3.2. The total CR flux for an SU(2) $T(z)$ relation is shown in navy blue. 0.5 $\times$ U(1) is shown in red dotted lines, 0.75 $\times$ U(1) orange dashed , 1.25 $\times$ U(1) yellow dot-dashed , 1.5 $\times$ U(1) green dotted , 1.75 $\times$ U(1) light blue dashed , 2 $\times$ U(1) purple dot-dashed.

3.6 Summary

In this paper, we examined the impact of locally non-linear modification of the CMB temperature redshift relation $T(z)$ on the fit to ultra-high energy cosmic rays and the corresponding cosmogenic neutrinos. The reduction of the CMB densities is found to affect significantly the interaction lengths of UHECRs with CMB photons in the redshift range of relevance for UHECR propagation, resulting in extended horizons for protons and UHECR nuclei. However, the increase in interaction lengths has only a modest effect on the observed UHECR flux due to interactions with the EBL, which then become dominant for the energies of relevance. Hence, a comparison to an existing fit of UHECRs yields similar flux of UHECRs nuclei but differs considerably for protons where a pronounced bump appears below the ankle for the SU(2)$_{\mathrm{CMB}}$ for hard injection spectra.

In order not to exceed the total UHECR flux and to agree with Auger data in the case of a hard injection spectrum, a shallower source evolution of cosmic ray sources of $m \approx 2.7$ is needed, which is more in line with SBGs and GRBs than with AGNs. This is in agreement with recent studies that consider arrival directions and extragalactic magnetic fields for energies beyond the ankle ($\geq 5 \times 10^{18}$ eV) [85]. While the confirmation of the SU(2)$_{\mathrm{CMB}}$ description requires further studies, the present work provides constraints for its validity. The independent determination of the redshift evolution of UHECR sources has the potential to reject the SU(2)$_{\mathrm{CMB}}$ temperature redshift relation for *hard* injection spectra: for a steeper cosmic ray source evolution, the predicted proton contribution below the ankle would be in tension with observations.

Since there is currently no firm preference for a specific UHECR source class [86], we would like to add modified $T(z)$ and in particular in the case of SU(2)$_{\mathrm{CMB}}$ to the discussion. This adds another tool to discriminate potential source classes and vice versa, constraining the sources by other means while simultaneously improving the knowledge of the UHECR composition may lead to a direct probe of $T(z)$ of the CMB in the future.

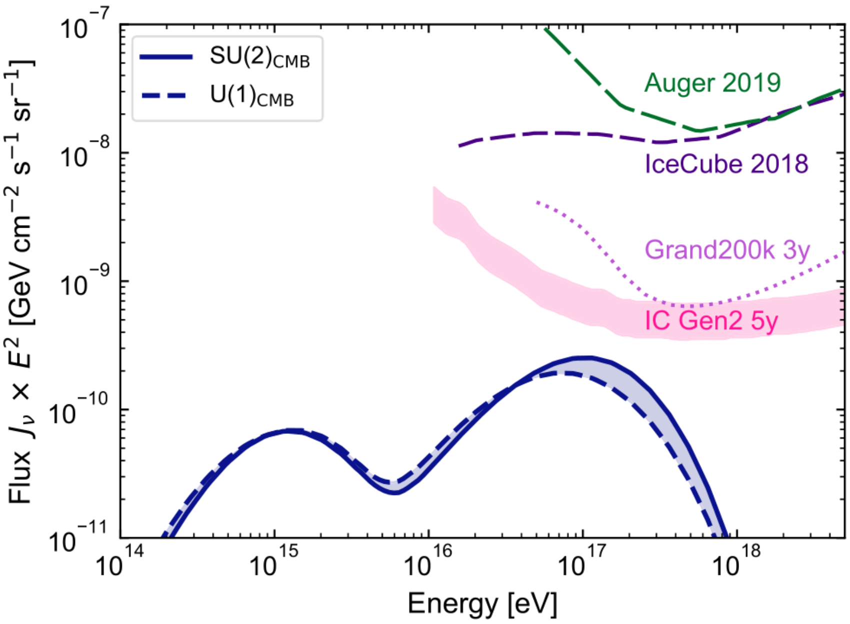

Figure 3.8: The cosmogenic neutrino flux obtained from the gradient descent fit, Table 3.2. $SU(2)_{CMB}$ is shown in navy blue, normal ΛCDM with the corresponding cosmological parameters and U(1) photon propagation is shown in a navy blue dashed line. The pink shaded area represents the projected sensitivity for the IceCube Gen2 radio upgrade after 5 years of observation, compare Fig. 5 in [81]. The lavender dotted line indicates the expected sensitivity for Grand200k after 3 years [82]. The dark purple and green dashed lines show 90% CL limits from the IceCube and Pierre Auger Collaboration, respectively [83, 84].

Data availability

This work modifies the existing cosmic ray propagation program PriNCe [78], the additional Python notebooks and scripts used in this study are available on GitLab[2].

Acknowledgements

JM acknowledges insightful discussions with Ralf Hofmann and Wolfgang Rhode. This work is supported by SFB 1491 (Project A3) and partially by the Vector Foundation under grant No. P2021-0102. LM's work is supported by the DFG under grant No. 445990517 (KA 710).

Contributions of the author JM

Contributions include writing the manuscript, including drafting the first version, simulation and analysis, figure preparation, conceptualization, methodology, validation, and review & editing.

[2]https://git.uni-wuppertal.de/meinert/modified-temperature-redshift-relation-and-uhecr-propagation

Appendix A: Best fit Heinze SU(2)$_{\mathrm{CMB}}$

The best fit from [78] is reproduced in Fig. 3.9 a) alongside the cosmogenic neutrino flux, Fig. 3.9 b), the $X_{\max}$ data Fig. 3.9 c) and $\sigma(X_{\max})$ data, Fig. 3.9 d) overlaid by three hadronic interaction models. All χ^2 for the $X_{\max}$ of the best fit in Fig. 3.9 c) and the χ^2 for $\sigma(X_{\max})$ of the best fit in Fig. 3.9 d) are shown in table 3 of the original publication [2].

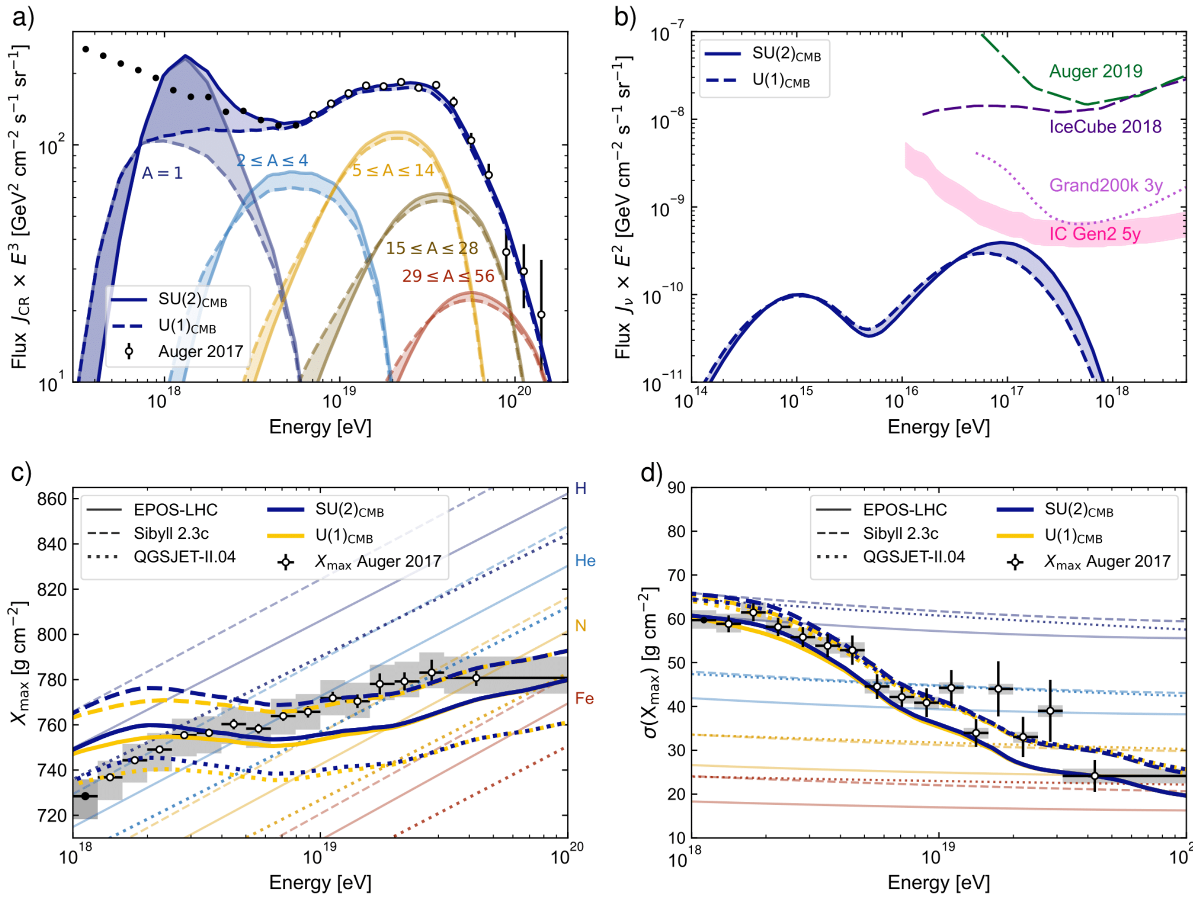

Figure 3.9: **a)** Spectral fit to the 2017 Auger spectral flux data from the best fit parameters in [78], see Tab. 3.1. [78] assume a normal U(1) temperature redshift relation (dashed lines, total flux dashed navy blue). The total cosmic ray flux with an SU(2) temperature redshift relation is shown with a blue solid line. The χ^2 only consider data points including the ankle region (white dots), according to Heinze's choice. **b)** The cosmogenic neutrino flux obtained from the fit in (a) in SU(2)$_{\mathrm{CMB}}$ is shown in navy blue solid, [78] in navy blue dashed lines. The pink shaded area represents the projected sensitivity for the IceCube Gen2 radio upgrade after 5 years of observation, compare Fig. 5 in [81]. The lavender doted line indicates the expected sensitivity for Grand200k after 3 years [82]. The dark purple dashed line shows 90% CL limits from the IceCube Collaboration (2018) [83]. And the green dashes line represents the 90% CL limit from the Pierre Auger Collaboration (2019) [84]. **c)** The Auger 2017 $\langle \mathrm{X}_{\max}\rangle$ and **d)** $\sigma(\mathrm{X}_{\max})$ data [87], on top of three different air-shower model expectations: Epos-LHC [88] (solid lines), Sibyll 2.3c [89] (dashed bold lines) and QGSJET-II.04 [90] (dotted lines). For calculating the relative χ^2 the same energy ranges as in Fig. 3.10 c) and d) have been chosen for better compatibility.

Appendix B: Best fit SU(2)$_{\text{CMB}}$

In order to mitigate the proton excess below the ankle in the reproduced model from [78], a descending algorithm is used. It minimizes the χ^2 for the white spectral data points in Fig. 3.10 a), X_{max} in Fig. 3.10 c) and $\sigma(X_{\text{max}})$ in Fig. 3.10 d). The best fit parameter to the Pierre Auger Collaboration data from 2017 are shown in Table 3.2. All χ^2 for the X_{max} of the best fit in Fig. 3.10 c) and the χ^2 for $\sigma(X_{\text{max}})$ of the fit in Fig. 3.10 d) are given in table 4 of the original publication [2].

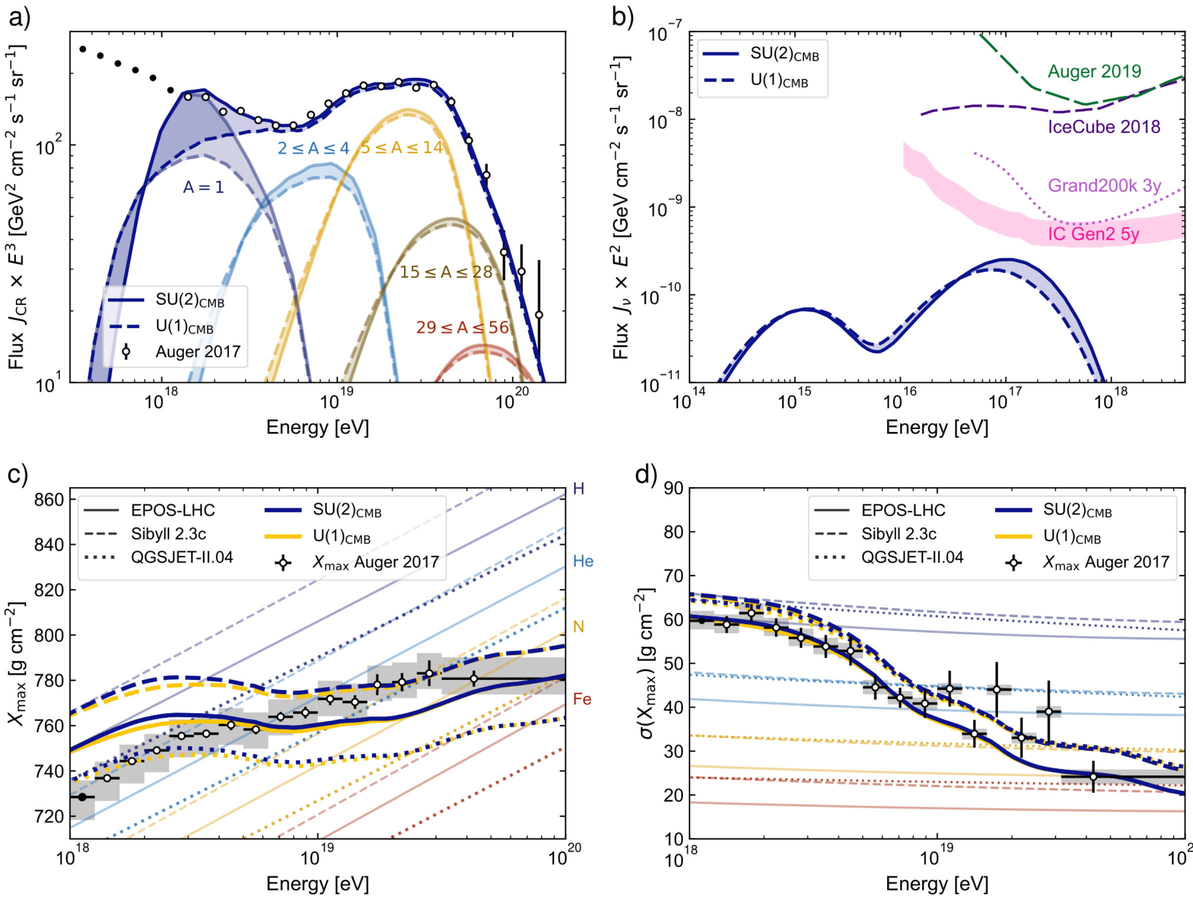

Figure 3.10: **a)** Spectral fit to the 2017 Auger spectral flux data from the best fit parameters in [78], see Tab. 3.1. [78] assume a normal U(1) temperature redshift relation (dashed lines, total flux dashed navy blue). The total cosmic ray flux with an SU(2) temperature redshift relation is shown with a blue solid line. The χ^2 only consider data points including the ankle region (white dots), according to Heinze's choice. **b)** The cosmogenic neutrino flux obtained from the fit in (a) in SU(2)$_{\text{CMB}}$ is shown in navy blue solid, [78] in navy blue dashed lines. The pink shaded area represents the projected sensitivity for the IceCube Gen2 radio upgrade after 5 years of observation, compare Fig. 5 in [81]. The lavender doted line indicates the expected sensitivity for Grand200k after 3 years [82]. The dark purple dashed line shows 90% CL limits from the IceCube Collaboration (2018) [83], and the green dashes line represents the 90% CL limit from the Pierre Auger Collaboration (2019) [84]. **c)** The Auger 2017 $\langle X_{\text{max}} \rangle$ and **d)** $\sigma(X_{\text{max}})$ data [87], on top of three different air-shower model expectations: Epos-LHC [88] (solid lines), Sibyll 2.3c [89] (dashed bold lines) and QGSJET-II.04 [90] (dotted lines).

this page is intentionally left blank

4 Frequency–Redshift Relation of the CMB

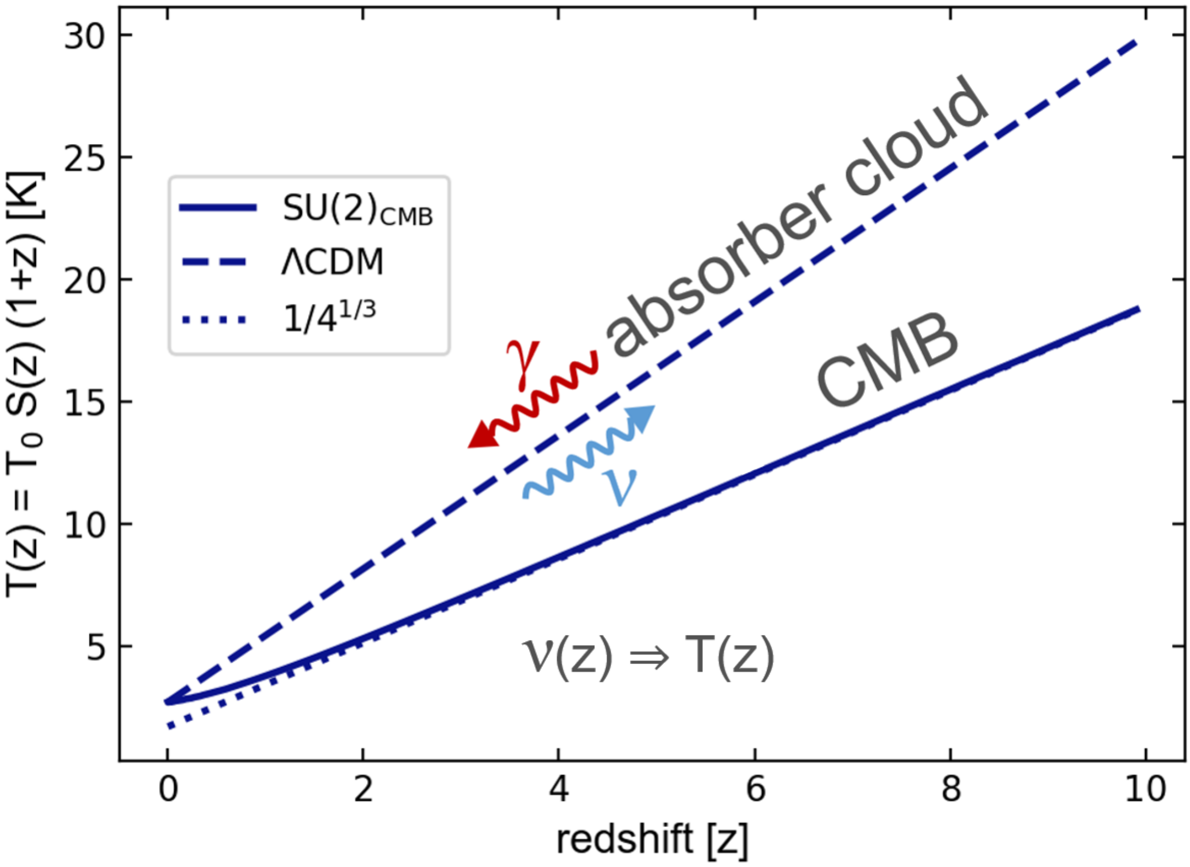

Figure 4.1: The temperature redshift relation of the CMB under $SU(2)_{CMB}$ (ultramarine solid) and under ΛCDM (ultramarine dashed). Any presumed frequency-redshift relation induced a temperature-redshift relation for blackbody radiation. Thus, probes like the thermal Sunyaev–Zel'dovich effect may not be sensetive to the actual CMB T-z relation, but only the blackbody nature of the CMB.

This chapter is based on the publication "The Frequency–Redshift Relation of the Cosmic Microwave Background" [3].

Contents

4.1 Introduction . . . 34
4.2 Observational T-z Relation Extractions from a v-z Relation . . . 35
4.2.1 Absorber Clouds in the Line of Sight of a Quasar or a Bright Galaxy . . . 36
4.2.2 The Thermal Sunyaev-Zel'dovich Effect . . . 37
4.3 T-z Relation and ν-z Relation in $SU(2)_{CMB}$: Theoretical Basis . . . 38
4.3.1 T-z Relation in $SU(2)_{CMB}$ . . . 38
4.3.2 Anisotropic Photon Emission by Electrons . . . 41
4.3.3 Thermalisation-Dependent Mixing of Two SU(2) Gauge Theories . . . 42
4.4 Summary . . . 43

Ralf Hofmann[1] and **Janning Meinert**[2,1]

[1]Institut für Theoretische Physik, Universität Heidelberg Philosophenweg 12, D-69120 Heidelberg
[2]Bergische Universität Wuppertal, Department of Physics, Gaußstraße 20, D-42103 Wuppertal

Abstract

We point out that a modified temperature–redshift relation (T-z relation) of the cosmic microwave background (CMB) cannot be deduced by any observational method that appeals to an a priori thermalisation to the CMB temperature T of the excited states in a probe environment of independently determined redshift z. For example, this applies to quasar-light absorption by a damped Lyman-alpha system due to atomic as well as ionic fine-splitting transitions or molecular rotational bands. Similarly, the thermal Sunyaev-Zel'dovich (thSZ) effect cannot be used to extract the CMB's T-z relation. This is because the relative line strengths between ground and excited states in the former and the CMB spectral distortion in the latter case both depend, apart from environment-specific normalisations, solely on the dimensionless spectral variable $x = \frac{h\nu}{k_B T}$. Since the literature on extractions of the CMB's T-z relation always assumes (i) $\nu(z) = (1+z)\,\nu(z=0)$, where $\nu(z=0)$ is the observed frequency in the heliocentric rest frame, the finding (ii) $T(z) = (1+z)\,T(z=0)$ just confirms the expected blackbody nature of the interacting CMB at $z > 0$. In contrast to the emission of isolated, directed radiation, whose frequency–redshift relation (ν-z relation) is subject to (i), a non-conventional ν-z relation $\nu(z) = f(z)\,\nu(z=0)$ of pure, isotropic blackbody radiation, subject to adiabatically slow cosmic expansion, necessarily has to follow that of the T-z relation $T(z) = f(z)\,T(z=0)$ and vice versa. In general, the function $f(z)$ is determined by the energy conservation of the CMB fluid in a Friedmann–Lemaître–Robertson–Walker universe. If the pure CMB is subject to an SU(2) rather than a U(1) gauge principle, then $f(z) = (1/4)^{1/3}\,(1+z)$ for $z \gg 1$, and $f(z)$ is non-linear for $z \sim 1$.

4.1 Introduction

Angular correlations between directionally dependent temperature and polarisation fluctuations of the cosmic microwave background (CMB) radiation [91] are important probes for the extraction of cosmological parameters [92]. Since the observed angular correlations are mainly influenced by curvature-induced dark-matter potentials, which in turn cause acoustic oscillations of the baryon–electron–photon plasma prior to recombination, these parameters depend on high-z physics when extracted from CMB data. Therefore, they are very sensitive to the temperature–redshift relation (T-z relation) that is assumed in expressing the CMB's energy density $\rho(T)$ in terms of z. If the CMB is subject to a quantum U(1) gauge theory, then, according to the Stefan–Boltzmann law and energy conservation in a Friedmann–Lemaître–Robertson–Walker (FLRW) universe, the T-z relation is $T(z)/T(z=0) = z+1$, where $T(z=0)$ is today's CMB temperature $T(z=0) = 2.726$ K [91]. Such a U(1) T-z relation is identical to the frequency–redshift relation (ν-z relation) $\nu(z)/\nu(z=0) = z+1$ describing electromagnetic waves emitted by compact astrophysical objects and traveling through an expanding FLRW universe towards the observer [93].

The thermodynamics underlying the CMB and the thermodynamics of a dense gas of absorber–emitter particles may be richer than they appear, such that the two situations need to be distinguished. While the CMB can be represented by a photon gas within its bulk, absorber–emitter particles thermalise via electromagnetic waves whose emissions and absorptions are enabled by electronic transitions. Therefore, the conventional T-z relation may not hold universally but, depending on how the above two extreme situations are mixed, is modified as $T(z)/T(z=0) = f(z)$, where the function $f(z)$ is specific to the generalizing theory. Thermodynamics then immediately implies that the ν-z relation is also of the form $\nu(z)/\nu(z=0) = f(z)$. Such is the case, for example, if the thermal photons (and low-frequency waves) of the CMB are identified with the Cartan modes of a single thermal SU(2) Yang–Mills theory, $\mathrm{SU(2)_{CMB}}$, in the deconfining phase [94, 74]. These modes interact only feebly within a small range of low temperatures and frequencies with the two off-Cartan quasiparticle vector modes. The fact that all gauge modes, massless and massive, are excitations of one and the same thermal ground state adds additional T-dependent energy density to that of thermal fluctuations: the ground-state energy density rises linearly in T in contrast to the rapidly attained Stefan–Boltzmann law $\propto T^4$ associated with thermal fluctuations [94].

If the CMB as a bulk thermal photon gas is indeed subject to $SU(2)_{CMB}$ thermodynamics (single Yang–Mills theory in its deconfining phase) from $T = 7.99$ keV (or $T = 1.09 \times 10^8$ K) to $T = 2.3 \times 10^{-4}$ eV (or $T = 2.726$ K), then a number of implications arise (see [34, 33, 95, 96] for the CMB large-angle anomalies, [40, 33] for the modified high-z cosmological model implied by a modified temperature–redshift relation [74], [41] for dark-sector physics, and [97] for neutrinos. The purpose of the present paper is to point out that past observational extractions of the CMB's T-z relation from background-light absorbing systems, which are assumed to thermalize with the CMB in a conventional way, are bound to extract the standard U(1) T-z relation if participating frequencies (observed absorption lines) are blueshifted accordingly. This is also true of the observation of spectral CMB distortions inflicted by its photons scattering off hot electrons belonging to X-ray clusters along the line of sight, i.e., the thermal Sunyaev-Zel'dovich effect (thSZ). In Section 4.2, we discuss these two observational approaches in more detail. First, we analyse the extraction of $T(z)$ from absorption lines within the continuous spectrum of a background source caused by a cloud in its line of sight, which is assumed to be thermalised with the CMB. Second, we discuss the distortions of the CMB spectrum according to the thSZ effect. In the former case, the frequency of the absorption line $\nu(z) = (z + 1)\nu(z = 0)$, which is assumed to coincide with the exciting CMB frequency, is used to extract a temperature $T(z)$. Note that in this case $T(z)$ coincides with the present CMB's temperature $T(z = 0)$ only if it is redshifted as $T(z)/(z + 1) = T(z = 0)$.

In other words, ignoring the value of a known transition frequency $\nu^*(z)$ of the system in using a different ν-z relation for $\nu(z)$, $\nu(z) = f(z)\nu(z = 0)$, the extracted CMB temperature would only have redshifted to its present value under the use of $T(z)/f(z) = T(z = 0)$. Therefore, it appears that in a given absorber system, interaction with the CMB occurs by a local shift of the CMB frequency $\nu(z)$ and temperature $T(z)$ to the line frequency $\nu^*(z) = (z + 1)\nu(z = 0)$ and cloud temperature $T^*(z) = (z + 1)T(z = 0)$ of the absorbing molecules. For deconfining SU(2) Yang–Mills thermodynamics, $\nu(z) \to \nu^*(z)$ is an upward shift (see Section 4.3). The thermalisation within a photon gas far away from any charges is different from the thermalisation within absorber clouds. This is because the degrees of freedom invoked are not the same. As a result, $T^*(z) = (z + 1)T(z = 0)$ is interpreted as the CMB's T-z relation, while it is actually $T(z) = f(z)T(z = 0)$. In exploiting the thSZ effect for the CMB's T-z relation extractions, we observe a similar situation. In Section 4.3, we review [94, 74] how a modified T-z relation (and then the ν-z relation) arises if the CMB is subject to deconfining SU(2) rather than U(1) quantum thermodynamics and how the Yang-Mills scale of such an SU(2) model, in the following referred to as $SU(2)_{CMB}$, is fixed by observation. To achieve this, the CMB radio excess in line temperature, see, e.g., [63, 64], is interpreted as an effect due to the transition between deconfining and preconfining SU(2) Yang–Mills thermodynamics. We also discuss a number of alternative explanations of this effect.

Moreover, we discuss how another SU(2) model, $SU(2)_e$ [43, 44, 31], whose two stable solitonic excitations in the confining phase represent the first-family lepton doublet, mixes with $SU(2)_{CMB}$. Such a mixing depends, up to temperatures of ~ 7.99 keV, on the degree of thermalisation prevailing in a local environment of electromagnetically interacting electronic charges within a certain range of frequencies and charge densities. The aforementioned upward shift in the CMB frequency $\nu(z)$ to absorption line frequency $\nu^*(z)$, accompanied by a shift in the CMB temperature $T(z)$ to cloud temperature $T^*(z)$, would then be a consequence of an incoherent mixture of the Cartan modes of $SU(2)_{CMB}$ (thermal photonic fluctuation) with those of $SU(2)_e$ (thermalised electromagnetic waves) when moving from empty space to the interior of the cloud. Finally, in Section 4.4, we summarise the results of this paper; mention an observational signature that is sensitive to the CMB's T-z relation, the spectrum of ultra-high energy cosmic rays (UHECRs); and briefly discuss implications for Big Bang nucleosynthesis. From now on, we work in natural units $c = k_B = \hbar = 1$, where c denotes the speed of light in vacuum, k_B is Boltzmann's constant, and $\hbar$ refers to the reduced quantum of action.

4.2 Observational T-z Relation Extractions from a v-z Relation

In this section, we discuss two principle probes used in the literature to extract the redshift dependence of the CMB temperature $T(z)$ up to $z \sim 6.34$; see [72] for a useful compilation, and how these extractions are prejudiced by an assumed ν-z relation of CMB frequencies. The first class of probes comprises absorbing clouds of known redshifts, e.g., parts of damped Lyman-α systems, in the line of sight of a distant quasar or a bright galaxy. Here, the assumed thermalisation with the CMB populates the fine-structure levels of the ground states of certain atoms or ions [98, 99, 100, 101, 72] or excites rotational levels of certain

molecules [100, 102, 103], whose population ratios can be obtained from the respective absorption-line profiles within the broad background spectra. Modelling environmentally dependent contributions to level populations, such as particle collisions or pumping by UV radiation, the relative level populations yield upper-limit estimates of $T(z)$ at the redshift of the cloud. The limitations of this method are discussed in [104]. Note that in [105], a solution of the rotational excitations of various molecular species could be provided directly from their spectra.
The second class of probes refers to the observation of the CMB spectrum within certain frequency bands along the lines of sight of X-ray clusters of known redshifts. A characteristic spectral distortion, known as the thermal Sunyaev-Zel'dovich effect (thSZ) [106, 107] and caused by the inverse Compton scattering of CMB photons off free, thermal electrons of these clusters is exploited to estimate $T(z)$.

4.2.1 Absorber Clouds in the Line of Sight of a Quasar or a Bright Galaxy

Estimates of $T(z)$ using the relative populations due to the excitation of atomic (ionic) fine-structure transitions and molecular rotation levels by the CMB have a long history; see [108] for the theoretical basis and [102, 103, 98, 100, 105, 72] for applications. Since sources of level excitations other than the CMB (e.g., collisions, UV pumping) have to be modelled for a given absorber, the extracted $T(z)$ is usually seen as an upper bound on the true CMB temperature. If the CMB is assumed to be the sole source of level population, then the extraction of $T(z)$ is facilitated in terms of the column density of the absorber species, depending on the measured line strength in the continuous spectrum of the background source, the transition frequencies, the temperature at which the levels are thermalised, and the integrated opacity of the line. Apparently, this method was validated by the measurement in [109] of the CMB temperature $T(z=0) = (2.726^{+0.023}_{-0.031})$ K in our Galaxy, analysing CN rotational transitions in five diffuse interstellar clouds. The value extracted in this way, $T(z=0)$, agreed well with the spectral CMB fit by COBE [91] of $T(z=0) = (2.726 \pm 0.010)$ K. So what about $z > 0$? In [105], a molecular rich cloud within a spiral galaxy at $z = 0.89$ was observed towards the radio-loud, gravitationally lensed blazar PKS 1830-211 at redshift $z = 2.5$. Within the cloud, the rotational temperature $T_{\rm rot}$ is defined via

$$\frac{n_u}{n_l} = \frac{g_u}{g_l}\exp\left(-\frac{2\pi\nu^*(z)}{T_{\rm rot}}\right)\,, \tag{4.1}$$

where n_u (g_u) and n_l (g_l) are the populations (degeneracies) of the upper and lower level, respectively, and $\nu^*(z)$ denotes the transition frequency in the cloud's rest frame. For the rotational excitations of ten molecules, $T_{\rm rot}$ was interpreted to universally represent $T(z=0.89)$ because the molecular gas was estimated to be sub-thermally excited (rotational levels solely radiatively coupled to the CMB, negligible impact of collisions and the local radiation field). Observations were performed within three wavelength bands at around $\lambda = 2, 3, 7$ mm using two different instruments. In one (simplified) approach, the extraction of $T_{\rm rot}$ from the two transitions in each molecular species was performed by pinning down the intersection of the two column densities $N_{\rm LTE}$ depending on $T_{\rm rot}$. For a given transition, $N_{\rm LTE}$ is defined as

$$N_{\rm LTE} = \frac{3}{4\pi^2\mu^2 S_{ul}}Q(T_{\rm rot})\frac{\exp\left(\frac{E_l}{T_{\rm rot}}\right)}{1-\exp\left(-\frac{2\pi\nu^*(z)}{T_{\rm rot}}\right)}\int \tau {\rm d}v\,, \tag{4.2}$$

where E_l is the energy of the lower level, $Q(T_{\rm rot})$ the partition function including all rotational excitations, μ the dipole moment, S_{ul} the observed line strength, and $\int \tau dv$ the integrated (observed) opacity of the line. Across the absorption lines of all molecular species considered, this approach produces values of $T_{\rm rot}$, which are quite consistent with the expectation $T(z=0.89) = (1+0.89)T(z=0) = 5.14$ K. Setting $T_{\rm rot} = T^*(z)$ in Equation (4.2) and using $\nu^*(z) = (1+z)\nu(z=0)$ is only consistent with the participating CMB photons being distributed according to a blackbody spectrum if $T^*(z)$ also redshifts as $T^*(z) = (1+z)T(z=0)$. Here $\nu(z=0)$ denotes the observed frequency of the transition in the heliocentric restframe. Therefore, this is an in-built feature of the model even though the CMB may, in reality, exhibit a different T-z relation (and then also ν-z relation)[1].

The situation is similar for the observation of atomic/ionic fine-structure transitions in absorbers at $z > 0$. Also, here, the very assumption of these excitations thermalising with the CMB ties the extracted T-z

[1] One may think of the true CMB temperature (which would be lower in $SU(2)_{\rm CMB}$) and participating CMB frequency being elevated by the same factor to $T^*(z)$ and $\nu^*(z)$ of a rotational excitation, respectively, by the incoherent mixing of a Cartan mode in $SU(2)_{\rm CMB}$ and a Cartan mode of $SU(2)_{\rm e}$ as the observer moves from empty space outside the cloud towards its interior.

relation to the ν-z relation used in converting observed (heliocentric) frequencies to transition frequencies in an absorber's restframe: the proper use of $f(z) = 1 + z$ for absorption lines produces a higher cloud temperature $T^*(z)$ than CMB temperature $T(z)$ if the latter is assumed to be described by an unmixed SU(2) model; see Section 4.3. In Section 4.3.2, we will discuss in more detail a degree-of-thermalisation-dependent mixing of Cartan excitations in two SU(2) gauge groups explaining why directed radiation, as issued by the background source and observed in a spectrally resolved way after having passed the absorber, obeys a conventional ν-z relation while the ν-z relation of CMB photons necessarily follows that of the T-z relation, which may well be unconventional [74].

4.2.2 The Thermal Sunyaev-Zel'dovich Effect

The thermal Sunyaev-Zel'dovich effect (thSZ) is a distortion of the blackbody shape of the CMB spectrum that is induced by the inverse Compton scattering of CMB photons off thermalised electrons in the X-ray plasmas of a given cluster of galaxies [106, 107]. Neglecting contributions from the weakly relativistic high-end part of the electrons' velocity distribution, the thSZ effect can be expressed in terms of a frequency-dependent (line-temperature) shift ΔT with respect to CMB baseline temperature T at the cluster's redshift z as [110]

$$\frac{\Delta T}{T}(x, \vec{n}) = \left[\frac{\sigma_T}{m_e}\int \mathrm{d}s\, n_e(s,\vec{n})\, T_e(s,\vec{n})\right] \times \left[x \coth\left(\frac{x}{2}\right) - 4\right] . \tag{4.3}$$

Here, m_e and σ_T refer to the mass of the electron and the Thomson cross-section, respectively. Both the electron temperature T_e and the electron number density n_e depend on the proper distance parameter s along the direction $\vec{n}$ of the line of sight under which CMB photons interacting with a given X-ray cluster are observed. The dimensionless variable x is defined as $x \equiv \frac{2\pi\nu}{T}$. As Equation (4.3) indicates, the thSZ effect factorises into an environmental part, determined by the thermodynamics of the X-ray cluster at redshift z and dubbed the thSZ flux, and into a part that solely depends on x. We note that the zero x_0 of the second factor is

$$x_0 \sim 3.83 = \frac{\nu_0}{T(z=0)} , \tag{4.4}$$

where $T(z = 0) = 2.726$ K [91] denotes the CMB temperature today. As a consequence, the thSZ effect predicts $\nu_0 \sim 217$ GHz. The z dependence of T can already be extracted by focusing on the frequency ν_0 at which $\frac{\Delta T}{T}(x, \vec{n})$ vanishes. By virtue of Equation (4.4), a blueshift of ν_0 according to the ν-z relation

$$\nu_0^*(z) = f(z)\nu_0 \tag{4.5}$$

then yields the T-z relation

$$T(z) = \frac{f(z)\nu_0}{x_0} = f(z)T(z=0) . \tag{4.6}$$

Therefore, whatever the assumption on $f(z)$ in the ν-z relation of Equation (4.5), this assumption necessarily transfers to the T-z relation of Equation (4.6) if the intensity of the unperturbed CMB at any redshift $z > 0$ is to possess a blackbody frequency distribution [2]. To suppress the statistical error in extractions of $T(z)$, a set of frequency bands, centered at $\{\nu_i\}$, is usually invoked in fitting the modelled thSZ emission law to the observations with respect to X-ray clusters within a given redshift bin δ. For example, in [110], the Planck frequency bands at 100, 143, 217, 353, and 545 GHz were used in multiple redshift bins, the stacking of patches in a given redshift bin δ and frequency band centered at ν_i was performed, and the thSZ emission law was modelled by integrating Equation (4.3) over bandpasses and by normalising it with the bandpass-averaged calibrator emission law. Relevant fit parameters turned out to be the (stacked) thSZ flux Y^δ, T^δ, and the radio-source flux contamination F^δ_{rad}, which were subsequently estimated by a profile likelihood analysis.

[2] According to a very good approximation, the spectral intensity $I(\nu)$ of today's CMB is given as $I_{z=0}(\nu)\mathrm{d}\nu = 16\pi^2 \frac{\nu^3}{\exp\left(\frac{2\pi\nu}{T(z=0)}\right)-1}\mathrm{d}\nu$ [91]. If we assume a T-z relation of $T(z=0) = \frac{1}{f(z)}T(z)$ and a ν-z relation of $\nu(z=0) \equiv \frac{1}{g(z)}\nu'$ with $f(z) \neq g(z)$, then the Stefan–Boltzmann law would still have redshifted according to the T-z relation: $\int \mathrm{d}\nu I_{z=0}(\nu) = \frac{\pi^2}{15}T^4(z=0) = \frac{\pi^2}{15}\left(\frac{T(z)}{f(z)}\right)^4 = \left(\frac{1}{g(z)}\right)^4 \int \mathrm{d}\nu' I_z(\nu')$. However, the maximum $\nu_{\max} = \frac{2.821}{2\pi}T(z=0)$ of the distribution $I_{z=0}(\nu)\mathrm{d}\nu$ converts to a maximum $\nu'_{\max} = \frac{2.821}{2\pi}\frac{g(z)}{f(z)}T(z)$ of the distribution $I_z(\nu')\mathrm{d}\nu' = 16\pi^2 \frac{(\nu')^3}{\exp\left(\frac{f(z)}{g(z)}\frac{2\pi\nu'}{T(z)}\right)-1}\mathrm{d}\nu'$. Thus, $I_z(\nu')$ would no longer be a blackbody spectrum.

The crucial point here is that, in the modelling of the thSZ emission law within redshift bin δ, a blueshift of observation frequency ν_i to $\nu_i^* = f(z)\nu_i$ needs to be applied, implying again the T-z relation

$$T(z) = \frac{f(z)\nu_i}{x_i} = f(z)T(z=0)\,, \tag{4.7}$$

where x_i is now the solution to

$$\frac{F_i^\delta}{Y^\delta} = \coth\left(\frac{x_i}{2}\right) - 4\,, \tag{4.8}$$

and F_i^δ denotes the stacked, observed thSZ flux within redshift bin δ. In [110], the use of $\nu_i^* = (1+z)\nu_i$ thus necessarily leads to the conventional T-z relation $T(z) = (1+z)T(z=0)$. To the best of the authors' knowledge, the use of $f(z) = 1+z$ in the ν-z relation is, however, common to all extractions of $T(z)$ that appeal to the thSZ effect. When the CMB gauge field represents the Cartan subalgebra of an SU(2) Yang–Mills theory, $\mathrm{SU(2)_{CMB}}$, it can be shown [74] that $f(z)$ is different from $f(z) = 1+z$ in the T-z relation (see Section 4.3.1) and therefore also in the ν-z relation. This is because, in addition to thermal photons, the thermal ground state in the deconfining phase of an SU(2) Yang–Mills theory is excited towards two vector modes subject to a temperature-dependent mass. A feeble coupling of these two kinds of excitations leads to spectral distortions of CMB radiance deeply within the Rayleigh–Jeans regime [34], which is not targeted by Planck frequency bands. In Section 4.3 we review how this T-z relation arises and discuss why a corresponding non-conventional ν-z relation is to be expected from a thermalisation process that is dependent on the mixing angle between the Cartan modes of two SU(2) gauge models subject to disparate Yang–Mills scales.

4.3 T-z Relation and ν-z Relation in $\mathrm{SU(2)_{CMB}}$: Theoretical Basis

In this section, we discuss in detail why a thermal gas of electromagnetic disturbances (far away from any emitting surface on the scale of a typical inverse frequency ν^{-1}) and with an isotropic and spatially homogeneous flux density of practically incoherent photons obeys a T-z relation and an associated ν-z relation that are different from the ν-z relation of directed, (partially) coherent radiation.

4.3.1 T-z Relation in $\mathrm{SU(2)_{CMB}}$

A pronounced distortion of the blackbody spectrum of radiance deep within the Rayleigh–Jeans part was observed in [63, 64] and the references therein. To explain this highly isotropic CMB radio excess at frequencies below 1 GHz, we argued in [67] that the critical temperature $T(z=0)$ for the deconfining–preconfining phase transition of SU(2) Yang–Mills thermodynamics is very close to the present temperature of the CMB of $T(z=0) = 2.726$ K [91]. This may seem to be a somewhat fine-tuned situation. However, the difference with the ordinary tuning of parameters by hand is that the dual gauge coupling thermodynamically rises rapidly as the temperature drops into the preconfining phase. Since the Cartan mode's extracted thermal quasiparticle mass is 100 MHz, which is around three orders of magnitude smaller than the critical temperature T_c, it follows that $T(z=0)$ needs to be very close to T_c. However, due to a presently incomplete understanding of the supercooling of the deconfining into the preconfining phase and the associated tunnelling, there is a tolerance of $\sim 10\,\%$ in this dynamic tuning of the two temperatures, which corresponds to about 1 Gy of cosmic evolution [111]. The exact assignment $T(z=0) = T_c$, addressed further below, implies a Yang–Mills scale $\Lambda_{\mathrm{CMB}} = 1.064 \times 10^{-4}$ eV, and thus it is justified to refer to the SU(2) Yang–Mills model, whose deconfining thermodynamics are assumed to describe the CMB, as $\mathrm{SU(2)_{CMB}}$. We quote below a number of alternative approaches to explaining the CMB radio excess. Let us now review [74] how the T-z relation of deconfining $\mathrm{SU(2)_{CMB}}$ thermodynamics is derived from energy conservation in an Friedmann–Lemaître–Robertson–Walker (FLRW) universe of cosmological scale factor a, normalised such that today $a(T(z=0)) = 1$. One has

$$\frac{\mathrm{d}\rho}{\mathrm{d}a} = -\frac{3}{a}\left(\rho + P\right)\,, \tag{4.9}$$

where ρ and P denote the energy density and pressure of deconfining $\mathrm{SU(2)_{CMB}}$ thermodynamics, respectively. As usual, redshift z and scale factor a are related as follows: $a^{-1} = z+1$. Equation (4.9) has the formal solution

$$a = \exp\left(-\frac{1}{3}\int_{\rho(T(z=0))}^{\rho(T)} \frac{\mathrm{d}\rho}{\rho + P(\rho)}\right) = \exp\left(-\frac{1}{3}\int_{T(z=0)}^{T} \mathrm{d}T' \,\frac{\frac{1}{T'}\frac{\mathrm{d}\rho}{\mathrm{d}T'}}{s(T')}\right), \tag{4.10}$$

where the entropy density s is defined as

$$s = \frac{\rho + P}{T}\,. \tag{4.11}$$

By virtue of the Legendre transformation

$$\rho = T\frac{\mathrm{d}P}{\mathrm{d}T} - P\,, \tag{4.12}$$

one has

$$\frac{1}{T}\frac{\mathrm{d}\rho}{\mathrm{d}T} = \frac{\mathrm{d}^2 P}{\mathrm{d}T^2} = \frac{\mathrm{d}s}{\mathrm{d}T}\,. \tag{4.13}$$

Substituting Equation (4.13) into Equation (4.10) finally yields

$$a = \frac{1}{z+1} = \exp\left(-\frac{1}{3}\int_{T(z=0)}^{T} \mathrm{d}T' \,\frac{\mathrm{d}}{\mathrm{d}T'}\left[\log\frac{s(T')}{M^3}\right]\right) = \exp\left(-\frac{1}{3}\log\frac{s(T)}{s(T(z=0))}\right). \tag{4.14}$$

Here, M denotes an arbitrary mass scale. The formal solution (4.14) is valid for any thermal and conserved fluid subject to expansion in an FLRW universe. If the function $s(T)$ is known, then (4.14) can be solved for the T-z relation $T(z)$. Equations (4.11) and (4.14) exclude a ground-state dependence of the T-z relation, since the equation of state for ground-state pressure $P^{\rm gs}$ and energy density $\rho^{\rm gs}$ is $P^{\rm gs} = -\rho^{\rm gs}$ [31]. In deconfining SU(2)$_{\rm CMB}$ thermodynamics, asymptotic freedom [75, 76] occurs non-perturbatively for $T \gg T(z=0)$ [31]. The Stefan–Boltzmann limit is then well saturated, and therefore $s(T)$ is proportional to T^3. Moreover, at $T(z=0)$, due to a decoupling of massive vector modes, excitations represent a free photon gas. Therefore, $s(T(z=0))$ is proportional to $T^3(z=0)$. As a consequence, the ratio $s(T)/s(T(z=0))$ in Equation (4.14) reads

$$\frac{s(T)}{s(T(z=0))} = \frac{g(T)}{g(T(z=0))}\left(\frac{T}{T(z=0)}\right)^3 = \left(\left(\frac{g(T)}{g(T(z=0))}\right)^{\frac{1}{3}}\frac{T}{T(z=0)}\right)^3, \quad (T \gg T(z=0))\,, \tag{4.15}$$

where g refers to the number of relativistic degrees of freedom at the respective temperatures. We have $g(T) = 2\times1+3\times2 = 8$ (two photon polarizations plus three polarisations for each of the two vector modes) and $g(T(z=0)) = 2\times1$ (two photon polarisations). Substituting this into Equation (4.15), inserting the result into Equation (4.14), and solving for T, we arrive at the high-temperature T-z relation

$$T = \left(\frac{1}{4}\right)^{\frac{1}{3}}(z+1)\,T(z=0) \approx 0.629\;(z+1)\,T(z=0)\,, \quad (T \gg T(z=0))\,. \tag{4.16}$$

Due to two vector modes of a finite, T-dependent mass contributing to $s(T)$ at low temperatures, the T-z relation is modified to give

$$T = \mathcal{S}(z)(z+1)\,T(z=0)\,, \quad (T \geq T(z=0))\,, \tag{4.17}$$

where the function $\mathcal{S}(z)$ is depicted in Figure 4.2.

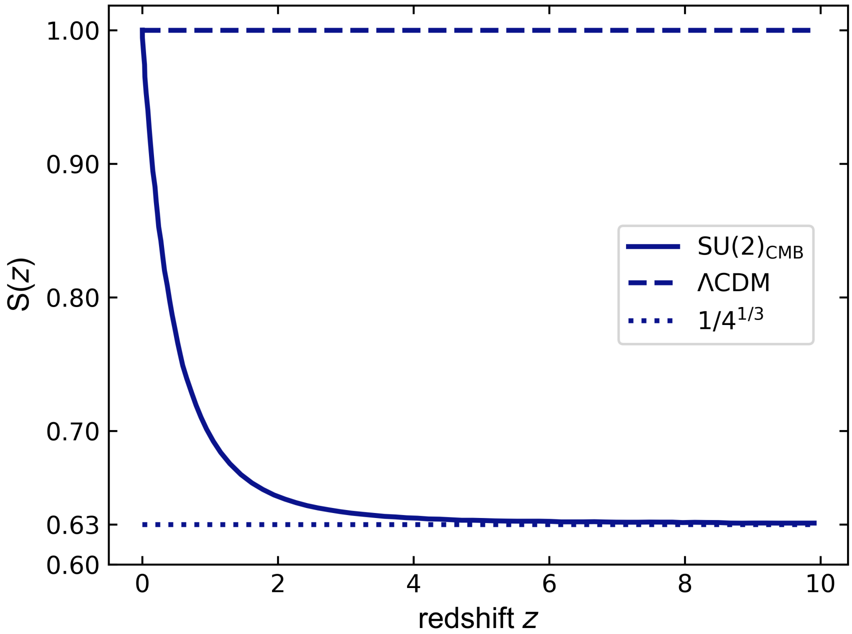

Figure 4.2: Plot of function $\mathcal{S}(z)$ in Equation (4.17). The curvature in $\mathcal{S}(z)$ at a low z indicates the breaking of conformal invariance in the deconfining SU(2) Yang–Mills plasma for $T \gtrsim T(z=0)$ with a rapid approach towards $(1/4)^{1/3}$ as z increases. The conventional T-z relation of the CMB, as used in the cosmological standard model ΛCDM, is associated with the dashed line $\mathcal{S}(z) \equiv 1$. Figure adapted from [33].

In Section 4.3.1, we reviewed why $T(z=0) \lesssim T_c$. We now argue why $T(z=0)$ is excluded to be larger than T_c: there is another contribution to the excess in line temperatures at low frequencies from the fact that the frequency of waves (populating the deep Rayleigh–Jeans spectrum up to const$/T^2$) and the frequency of photons (starting to represent the spectrum for frequencies larger than const$/T^2$) redshift differently. On the other hand, the baseline temperature $T(z)$ redshifts like the frequency of photons. That is, wavelike modes redshift as $\nu(z) = (1+z)\nu(z=0)$ while temperature (photon frequency) redshifts more weakly as $T(z) = S(z)(z+1)T(z=0)$ with a numerically known function $S(z) < 1$ of negative slope $\frac{\mathrm{d}S(z)}{\mathrm{d}z} \sim -1$ for $z \ll 1$; see Figure 4.2. This also contributes to an increase in the line temperature at low frequencies compared to the Rayleigh–Jeans law, since low frequencies are redshifted as usual but the baseline temperature redshifts slower when lowering z in the vicinity of $z = 0$; see Figure 4.3 and Equation (4.18). Observationally [63], the onset of this effect could be visible at $\nu \sim 1$ GHz, which implies that the wavelengths of low-frequency waves are larger than 30 cm, in turn implying a critical temperature lower than 11.6 K [31]. For the differential evolution of the baseline temperature, we have

$$\mathrm{d}T = T(z=0)\left(\frac{\mathrm{d}S(z)}{\mathrm{d}z}(1+z) + S(z)\right)\mathrm{d}z\,. \tag{4.18}$$

Since the present CMB's line temperature rises steeply with a spectral index of −2.6 when lowering the frequency [63, 64], the effect of Equation (4.18), which (modulo a mild stacking of low frequencies) is frequency-independent for $\nu <$ const$/T^2$, does not explain these large and variable line temperatures. Thus, we are again led to set $T(z=0) \sim T_c$ to explain the observed steep rise in terms of wave evanescence (thermal Meissner mass). Therefore, the tuning $T(z=0) \sim T_c$ is entirely explained by observation and does not require any ad hoc parameter coincidence.

Note that large and variable line temperatures cannot be explained in terms of the diffuse free–free emission facilitated by cosmological reionisation [112, 113]. Interestingly, synchrotron radiation induced by weakly interacting massive particles (WIMPs) annihilations or decays in extra-galactic halos could match the low-frequency excess in CMB line temperature if a thermal annihilation cross-section for light WIMPs is invoked [114]. Galactic radio emission is excluded as an explanation by the isotropy of the signal [42]. In [115], stochastic frequency diffusion is used to explain the low-frequency excess in the present CMB (also dubbed 'space roar') in terms of a primordial epoch of non-equilibrium conditions in the plasma. These conditions are modelled by a mild violation of the Einstein relation in the Kompaneets equation to allow for low-frequency localisation in the evolving photon distribution. The formation of the

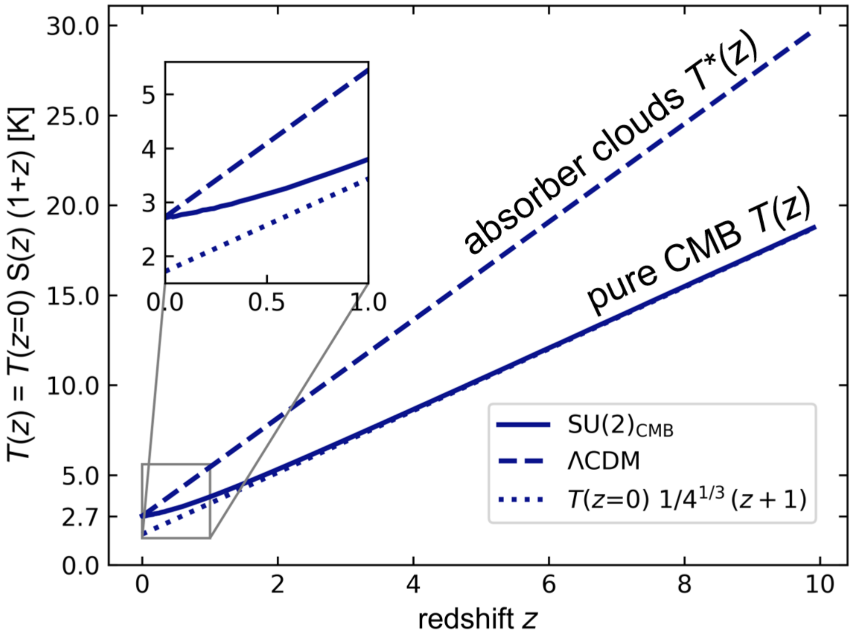

Figure 4.3: Plot of the T-z relation $\mathcal{S}(z)(1+z)$ in deconfining SU(2) Yang–Mills thermodynamics with $T(z=0) \equiv T_{\rm c}$. The conventional quantum U(1) T-z relation of the CMB, employed in the cosmological standard model ΛCDM, is depicted by the dashed line. Here T^* denotes the higher value of the temperature within the cloud, deduced from a conventional ν-z relation of the line whose profile is analysed.

first generation of supermassive, cosmological black holes is speculated to explain the space roar in terms of synchrotron emission from the remnants [116]. If the line-temperature excess can, indeed, be shown to persist to higher redshifts, including the onset of reionisation (cosmic dawn), then a potential explanation of the anomalously strong absorption of the redshifted 21 cm line by neutral hydrogen measured by an experiment to detect the global epoch of the reionisation signature (EDGES) [117] is enabled. This would falsify our proposal that the present space roar is solely a very-low-redshift phenomenon due to an admixture of Gaussian distributed evanescent waves to the conventional low-frequency Rayleigh–Jeans CMB spectrum[3]. However, the strong absorption of the redshifted 21 cm line can also be explained by the dark-matter-induced cooling of the absorbing cosmic gas without having to invoke the excess intensity of the CMB at low frequencies throughout cosmic dawn [118].

4.3.2 Anisotropic Photon Emission by Electrons

In the framework of the SU(2) Yang–Mills theory, why is it that spectral lines redshift according to the conventional ν-z relation $\nu(z) = (1+z)\,\nu(z=0)$ while the bulk of frequencies within the CMB follow a ν-z relation associated with the T-z relation of Section 4.3.1? The electron and its neutrino are modelled by a onefold self-intersecting, figure-eight-like center-vortex loop and a single center-vortex loop, respectively; see [43, 44] and [31]. These excitations are immersed into the confining ground state of the SU(2) Yang–Mills theory. A mass formula can be derived for the electron that equates the frequency of a breathing monopole [119, 120] (or the quantum selfenergy [121, 122]), contained within an extended ball-like blob associated with the region of vortex intersection, with the sum of the static monopole's rest mass and the energy content of the deconfining SU(2) Yang–Mills thermodynamics of the blob (considering the mixing of two thermal gauge theories SU(2)$_{\rm CMB}$ and SU(2)$_{\rm e}$ at a temperature $T_0 = 1.18\,T_{c,{\rm e}}$ where the pressure vanishes [5]). By invoking the value of the electron mass $m_{\rm e} = 511$ keV, this formula yields a value of the SU(2) Yang–Mills scale $\Lambda_{\rm e} = 3.62$ keV or a critical temperature $T_{c,{\rm e}} = 7.99$ keV for the deconfining–preconfining phase transition in SU(2)$_{\rm e}$ [5]. In addition, one obtains a blob radius $r_0 \sim a_0$, where a_0 denotes the Bohr radius $a_0 = 0.592$ Å. Also, the reduced Compton radius r_c, which roughly coincides with the core radius of the monopole r_c [119, 120], turns out to be $r_c \sim \alpha\, r_0$ where $\alpha \sim 1/137$ is the electromaganetic fine-structure constant. Modulo the electron's magnetic moment, carried by two

[3] This admixture would arise due to phase tunnelling occurring when supercooling the deconfining phase into the preconfining phase in SU(2)$_{\rm CMB}$.

closed vortex lines connecting to the blob, this matches with de Broglie's original interpretation of the electron [121, 122] and with the interpretation of the square of the wave function in wave mechanics [123] as a probability density for locating a point particle [124]. Namely, in its restframe, the electron represents an extended (spatially homogeneous) vibration induced by a charged monopole whose core size is negligible on the scale of the blob size and whose rate of jump-like location changes within the blob volume matches the vibration frequency ν_0 ($m_0 = h\nu_0$, where m_0 is electron mass).

If the global temperature of a photon gas is smaller than $T_{c,\mathrm{e}}$, then these photons must be thermalised with respect to $\mathrm{SU(2)_{CMB}}$ for $T_{c,\mathrm{CMB}} \sim 10^{-4}\,\mathrm{eV} \ll 7.99\,\mathrm{keV} \sim T_{c,\mathrm{e}}$. On the other hand, a directedly propagating electromagnetic field (a wave) represents a non-thermalised mode and thus cannot be subject to the gauge group $\mathrm{SU(2)_{CMB}}$ but rather is described by SU(2) Yang–Mills theories of much larger Yang–Mills scales [31]. The process of converting these isolated waves, emitted by the charge carriers that do not penetrate into the volume bounded by a closed, emitting spatial surface, into a thermal photon gas contained within this volume hence proceeds by chopping their coherent intensity distribution into grainy and short-lived energy-momentum packets by the increasing homogenisation and isotropisation of energy transport as more and more differently directed waves of varying oscillation frequencies superposition away from the emitting surface. This process of thermalisation, producing a photon gas with the temperature of the emitting surface, can effectively be understood as a rotation of SU(2) modes of theories with large Yang–Mills scales into those of $\mathrm{SU(2)_{CMB}}$.

4.3.3 Thermalisation-Dependent Mixing of Two SU(2) Gauge Theories

For simplicity and due to its practical relevance[4], we consider the interplay of gauge groups $\mathrm{SU(2)_{CMB}}$ and $\mathrm{SU(2)_e}$. The discussion in Section 4.3.2 can then be summarised as

$$\begin{aligned} \bar{a}_\mu^{\mathrm{CMB}} &= a_\mu^{\mathrm{CMB}} \cos\theta_W + a_\mu^{\mathrm{e}} \sin\theta_W \,, \\ \bar{a}_\mu^{\mathrm{e}} &= -a_\mu^{\mathrm{CMB}} \sin\theta_W + a_\mu^{\mathrm{e}} \cos\theta_W \,, \end{aligned} \tag{4.19}$$

where ($\bar{a}_\mu^{\mathrm{CMB}}$,$\bar{a}_\mu^{\mathrm{e}}$) refers to the rotated state reached from the initial state (a^{CMB}, a^{e}) for the effective gauge fields in the deconfining phases of $\mathrm{SU(2)_{CMB}}$ and $\mathrm{SU(2)_e}$. The thermodynamically determined mixing angle θ_W turns out to be close to the electroweak mixing angle ($\theta_W = 30.84^\circ$) if mixing within the interior of the blob—representing the center of the region of self-intersection of the center-vortex loop—is considered. Within this central domain, the mixed deconfining-phase pressure must vanish [5]. Note that in the case of infinite-volume thermodynamics at high temperatures (high-z cosmology), such a stability constraint on a finite-volume region is irrelevant, and one has $\theta_W = 45^\circ$.

In general, a change in the state of thermalisation induces a change in the rotation angle $\theta = \theta(\eta, T^*, T)$. In particular, for the interaction of the CMB with absorber clouds, θ depends on the degree of thermalisation η invoked by the initial states of electromagnetically interacting electrons of temperature T^* within the cloud and the temperature T of the CMB. Note that the thermalisation of these electronic states is influenced by these very lines dissipating directed background light. Via the degree of thermalisation η, the mixing angle θ also depends on the range of frequencies $\nu_l \le \nu \le \nu_u$ of wavelike modes in $\mathrm{SU(2)_{CMB}}$ and $\mathrm{SU(2)_e}$, which mediate the interactions between the electrons. Due to the present CMB exhibiting the largest low-frequency interval of excitations associated with waves throughout its cosmological history (see Section 4.3.1), and since the main frequency used for the extraction of $T(z=0)$ from background source–absorber cloud systems in the Milky Way [109] is 113.6 GHz, which is to the left of the peak frequency $\nu = 160.4$ GHz of the present CMB's blackbody spectrum, it is qualitatively understandable that the same temperature as in the CMB blackbody spectral fit in [91] is observed for these systems. Due to the strong compression of the CMB wave spectrum with a factor $\propto T^{-2}$, it is also plausible that temperatures extracted from a background source–absorber cloud system at earlier epochs differ from the associated CMB temperatures because the mixing between $\mathrm{SU(2)_{CMB}}$ and $\mathrm{SU(2)_e}$ within the cloud then is tilted towards $\mathrm{SU(2)_e}$. The quantitative computation of θ in a situation where a system of interacting (bound) electrons of a given number density, invoking a range of frequencies $\nu_l \le \nu \le \nu_u$ for these interactions, is immersed into the CMB is a complex task which we hope to gain more insight about in the future.

[4] Charge carriers subject to SU(2) theories of larger Yang–Mills scales, represented by the charged leptons of the standard model $\mu^\pm$ and $\tau^\pm$, are unstable due to weak decay and therefore do not qualify as material within the emitting surfaces of a blackbody cavity.

4.4 Summary

In this paper, we discussed two main approaches to extract the CMB temperature at finite redshifts: the analysis of absorption line profiles originating from gases of atoms, ions, or molecules within the line of sight of a broad-spectrum and bright background source, and the thermal Sunyaev-Zel'dovich effect (thSZ). In the literature, the assumption of a conventional frequency–redshift relation (ν-z relation) for CMB photons, considered to thermalise with relevant transitions in the cloud systems in the former case or to represent CMB spectral distortions in the latter situation, yields a conventional temperature–redshift relation (T-z relation) for the CMB. We argued, based on the blackbody spectrum at all redshifts, that this is a consequence of thermodynamics. Whatever the assumed ν-z relation, observations necessarily produce the associated T-z relation and vice versa. If the CMB is subject to an SU(2) rather than a U(1) quantum gauge principle, we reviewed how the corresponding T-z relation changes. Consequently, the CMB's ν-z relation is changed. Finally, on a qualitative level, we provided reasons for which the temperature of a cloud of known redshift may differ from the temperature of a pure photon gas representing the CMB far away from the cloud. This is because thermalisation in the cloud, in addition to the interaction of bound electrons with wavelike CMB disturbances, also proceeds via emissions and absorptions of wavelike modes by bound electrons. These modes, however, are subject to another (confining-phase) SU(2) Yang–Mills theory of a much higher critical temperature: $\mathrm{SU(2)_e}$. The existence of $\mathrm{SU(2)_e}$ impacts Big Bang nucleosynthesis. Specifically, if the electron is subject to an SU(2) gauge-theory model, involving the two factors $\mathrm{SU(2)_{CMB}}$ and $\mathrm{SU(2)_e}$ [43, 44, 5] (see also [41]), then the Hagedorn temperature $T_H = 6.66$ keV of $\mathrm{SU(2)_e}$ implies that the primordial Helium mass fraction of $Y = \frac{1}{4}$ ($Y = \frac{2f_i}{1+f_i}$, where f_i denotes the neutron-to-proton ratio at the onset of nucleosynthesis) is not induced by the nucleosynthesis of the light elements setting in at $T = 65$ keV, subject to $f_i = \frac{1}{7}$ (the freeze-out value $f = \frac{1}{5}$ at $T \sim 800$ keV being reduced to $f_i = \frac{1}{7}$ at $T = 65$ keV due to neutron decay). Rather, nucleosynthesis would start at $T = 65$ keV with $f_i = 1$, implying a Helium mass fraction of $Y = 1$ prior to the Hagedorn transition. The value of Y would subsequently be reduced to $Y \sim \frac{1}{4}$ through collective Helium photo-disintegration by gamma quanta that are released across the Hagedorn transition.

Our conclusion regarding the extractions of the CMB temperature using the thSZ effect pursued in the literature is that they confirm the CMB blackbody spectrum at a finite redshift. However, under the assumed conventional ν-z relation, the result of the T-z relation extraction is necessarily conventional as well. The extraction of the CMB's T-z relation from an assumed thermalisation within absorber clouds, which also uses a conventional ν-z relation for the relevant absorption lines, is questionable since the two systems, (i) a cloud immersed into the CMB and (ii) a pure CMB, exhibit different thermal degrees of freedom at a sufficiently high redshift: waves for (i) and photons for (ii). One possibility for determining the effect of the T-z relation subject to $\mathrm{SU(2)_{CMB}}$ is to study the flux of ultra-high-energy cosmic rays (UHECRs). In particular, there is a sensitive region below the ankle, that is, for $1 \times 10^{18}\,\mathrm{eV} \leq E \leq 6 \times 10^{18}\,\mathrm{eV}$. Due to the reduced CMB photon density at the same finite redshift, there is a higher flux of UHECRs under otherwise equal conditions for emission and propagation. Most prominently, the flux of protons is significantly increased in comparison to the use of the conventional T-z relation when fitted to UHECR data [2].

Data availability

This work did not require additional scripts. However, the Python notebooks for creating the figures are available upon request.

Acknowledgements

This work was inspired by an intense and fruitful exchange about a recent publication (Hofmann et al. 2023) between the two referees and the current authors. JM acknowledges insightful discussions with Karl-Heinz Kampert and Alexander Sandrock. This work is support by the Vector Foundation under grant number P2021-0102.

Contributions of the author JM

Contributions include writing the manuscript, figure preparation, methodology, validation, funding acquisition, and review & editing.

this page is intentionally left blank

5 Search for a Blackbody Anomaly

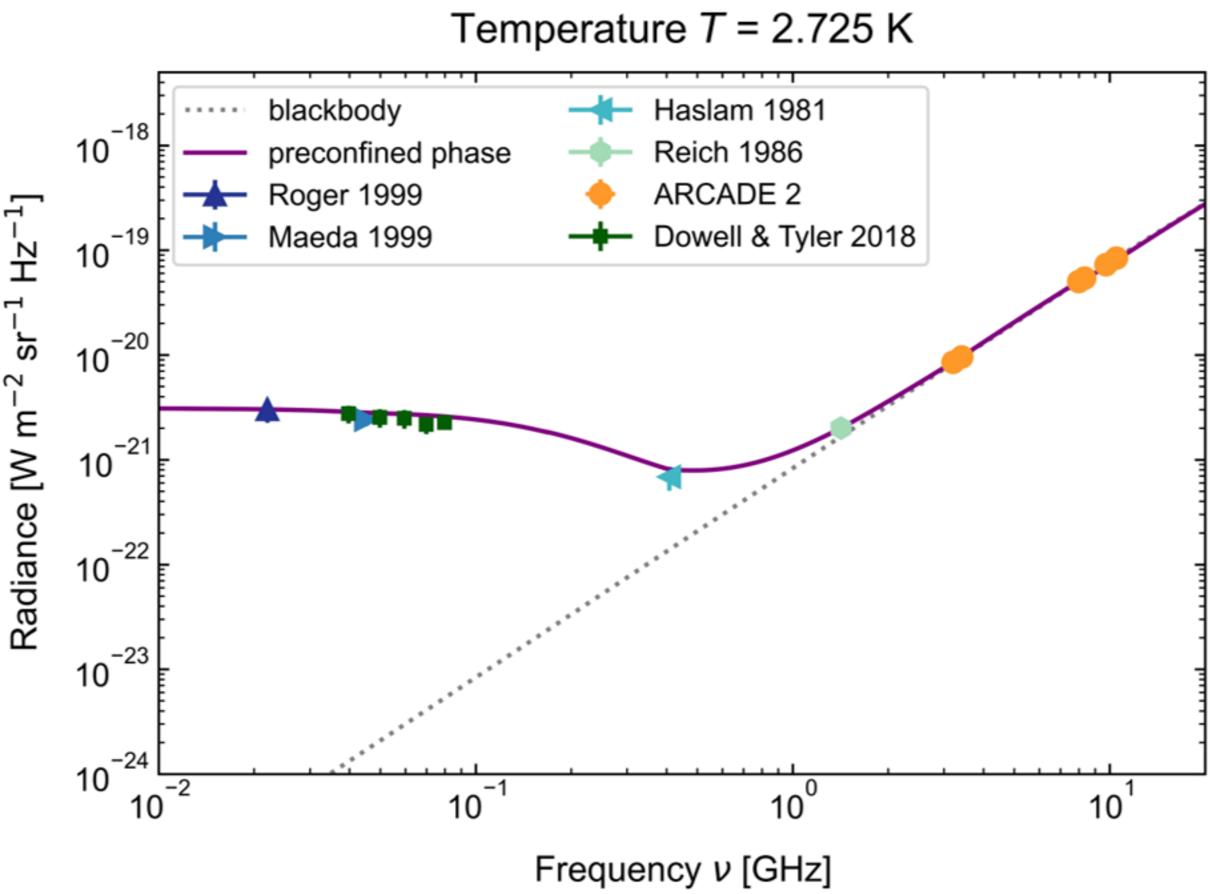

Figure 5.1: The radio excess as observed by multiple terrestrial CMB observations and ARCADE 2 can be interpreted as Meissner massive photons in the preconfined phase of $SU(2)_{CMB}$ [67]. In purple, a fit to the data is shown; the gray dotted line indicates expected Rayleigh-Jeans behaviour.

This chapter presents original research, published here for the first time, and serves as a preprint [4]. It is building upon previous work by Carlos Falquez and Ralf Hofmann [125]. The data were taken by Roberto Gavioso, Giorgio Brida, Dario Imbraguglio at the Istituto Nazionale di Ricerca Metrologica (INRiM).

Contents

5.1 Introduction **46**
5.2 Experimental Setup and Noise-Power Amplification **47**
5.2.1 Design and components of experiment 47
5.2.2 Error estimates 49
5.3 Experimental Results **49**
5.4 Interpretation of Noise-Power Excess at Low Temperatures **51**
5.5 Discussion and Summary **53**

Janning Meinert[1,2], Roberto Gavioso[3], Giorgio Brida[3], Dario Imbraguglio[3], Simone Corbellini[4], Christof Gaiser[5], Ralf Hofmann[2]

[1]Bergische Universität Wuppertal, Department of Physics, Gaußstraße 20, D-42103 Wuppertal

[2]Institut für Theoretische Physik, Universität Heidelberg Philosophenweg 12, D-69120 Heidelberg

[3]Istituto Nazionale di Ricerca Metrologica (INRiM), Strada delle Cacce 91, I-10135 Torino

[4]Electronics and Telecommunications Department, Politecnico di Torin, I-10129 Torino

[5]Physikalisch-Technische Bundesanstalt (PTB), Abbestrasse 2-12, D-10587 Berlin

Abstract

We report measurements of radiometric power in the frequency range 5.0 to 11.5 GHz and temperature range 10 to 53 K, using a monopole antenna immersed in a cylindrical blackbody cavity ($d = 179$ mm, $h = 190$ mm). Up to 0.15 dBm of excess power (corresponding to a ∼3.5% increase relative to the expected Nyquist noise power of a 50 Ω resistor) was observed. Simultaneous thermometry revealed a temperature gradient within the cavity, with the top consistently hotter than the bottom by up to 0.15 K. The measured power differences between antennas are consistent with this gradient, with the hotter top emitting more thermal radiation than the colder bottom. The frequency dependence of the effect, particularly in the antenna viewing the colder region, can be attributed to spatially varying coupling efficiency and the characteristics of thermal emission in the Rayleigh-Jeans regime. No indication of additional physical mechanisms beyond standard blackbody thermodynamics is required to explain the observed excess. Future experiments with improved thermal homogenization, larger cavity dimensions, and higher radiometric precision may help further constrain or isolate potential non-standard effects.

5.1 Introduction

Max Planck's discovery of the law of spectral energy density $I(\omega;T)\mathrm{d}\omega$ of the radiation that prevails inside an ideal blackbody [1],

$$I_{\mathrm{U}(1)}(\omega;T)\mathrm{d}\omega = \frac{1}{\pi^2}\frac{\omega^3}{\mathrm{e}^{\omega/T}-1}\mathrm{d}\omega\,, \tag{5.1}$$

marks the beginning of quantum mechanics. A blackbody is an idealized physical object that absorbs all incident electromagnetic radiation, regardless of frequency or angle of incidence. It is also a perfect emitter of radiation, with its emission spectrum dependent solely on its temperature, as described by Planck's radiation law in Eq. (5.1). The emissivity is assumed to be $\epsilon = 1$ and at a temperature T. Here, $\omega = 2\pi\nu$ denote circular and ν ordinary (wave-photon) frequency while $d\omega$ is some frequency bandwidth of observation. Note that spectral radiance $R_{\mathrm{U}(1)}$ and $I_{\mathrm{U}(1)}$ are the same in natural units.

The association of the quantum of action $\hbar$ with Eq. (5.1) reflects the postulate of propagating packets of energy ω: photons. Photons are not subject to classical equipartition of electromagnetic wave energy, which would imply the Rayleigh-Jeans limit $I_{\mathrm{U}(1)}(\omega \ll T;T)\,\mathrm{d}\omega = \omega^2 T\,\mathrm{d}\omega/(\pi^2)$. Treating thermal electromagnetic disturbances classically, throughout the *entire* spectrum, implies a catastrophic and unphysical ultraviolet divergence of the total energy density $\rho = \int_0^\infty \mathrm{d}\omega\, I_{\mathrm{U}(1)}(\omega;T)$. The quantum behaviour of thermal radiation at higher frequencies, expressed by Eq. (5.1) instead ensures a finite (Stefan-Boltzmann) value $\rho = \pi^2 T^4/15$. Planck's thermal photon gas rests on Maxwell's electrodynamics, which is a U(1) gauge theory. In addition, quantized electromagnetic field energy and Bose-Einstein statistics must be invoked ad hoc [126, 127]. From the theoretical side, a propagating solution to the classical SU(2) Yang-Mills equations in 4D Minkowski spacetime, which embodies the photon without ad hoc quantisation, was constructed recently in [128].

Planck's radiation law is ubiquitous. Its fundamental nature is best expressed by the fact that the universe's most extended thermal photon gas, the Cosmic Microwave Background (CMB), obeys Eq. (5.1) at one-percent precision for frequencies $\nu > 3$ GHz and at $T_{\mathrm{CMB},0} = 2.726$ K [63, 129, 130]. However, deviations from this radiation law are reported to be highly significant for $\nu < 3$ GHz, see [63] and references

[1]In this work, if not explicitly stated otherwise, we work in natural units $\hbar = k_B = c = 1$ where $\hbar$ denotes Planck's reduced quantum of action, k_B is Boltzmann's constant, and c refers to the speed of light in vacuum.

therein. Many possible explanations were put forward to explain this low-frequency anomaly, see, e.g. [114, 115, 116]. A galactic origin of the excess is excluded by the extreme isotropy of the signal [42], and it cannot be explained in terms of the diffuse free–free emission facilitated by cosmological reionisation [112, 113]. In [67] the low-frequency CMB excess of [63] was interpreted as evanescence of low-frequency modes. Evanescence, in turn, is explained by the onset of the Meissner effect: electric-magnetically dual monopoles in a deconfining SU(2) Yang-Mills plasma, whose tree-level massless modes (TLMM) is the thermalized photon, start to condense at the critical temperature T_c of the deconfining-preconfining phase transition [31]. The ensuing assignment $T_{\mathrm{CMB},0} = T_c$, suggesting the name SU(2)$_{\mathrm{CMB}}$, has significant consequences for the cosmological model at high redshifts [3, 33, 40]. Therefore, it is important to perform terrestrial laboratory experiments to either support or rule out the theoretical SU(2)$_{\mathrm{CMB}}$ association with thermal photon gases. In particular, one should focus on SU(2)$_{\mathrm{CMB}}$'s prediction of anomalous noise powers in the deconfining phase [131, 132] not far above T_c and for low frequencies. Note that in contrast to [67] where, by virtue of $T_{\mathrm{CMB},0} = T_c$, noise-power excess is linked to the Meissner effect, the prediction we aim to test in the present work rests on a spectral gap which is generated radiatively for $T > T_{\mathrm{CMB},0}$.

5.2 Experimental Setup and Noise-Power Amplification

5.2.1 Design and components of experiment

Blackbody cavity and temperature control

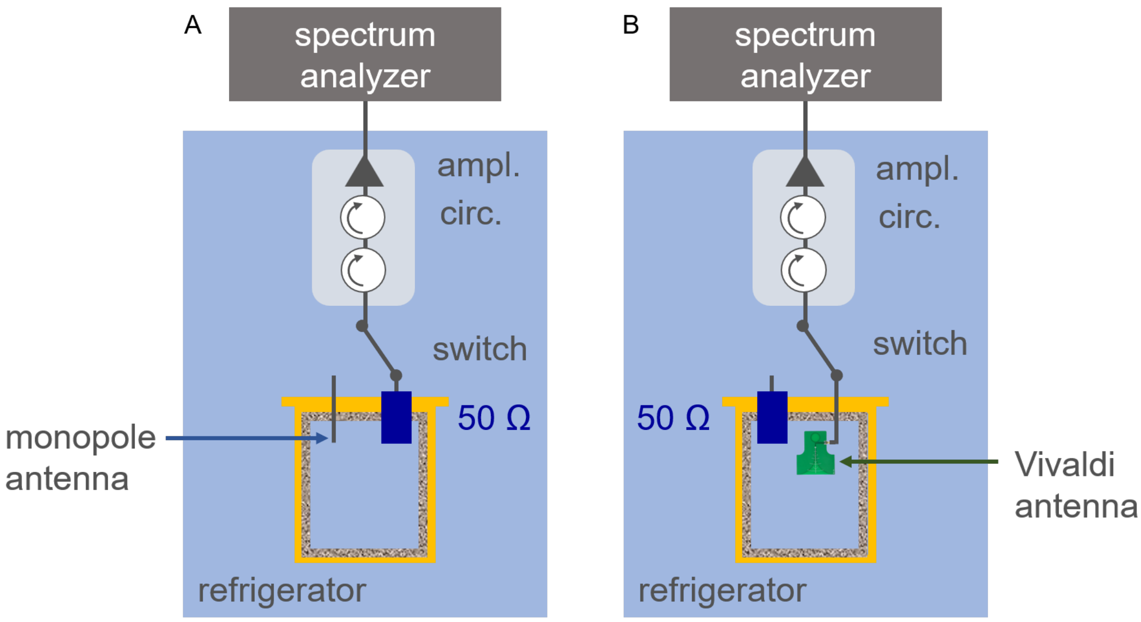

Figure 5.2: Illustration of the experimental setup of cavity with cryogenic amplification chain and experimental setup at INRiM. The amplification chain consists out of an amplifier (ampl.) and two circulators (circ.), in order to avoid back reflections into the cavity, as well as one cryogenic Dicke switch shortly before the cavity. A schematic drawing of the monopole antenna is shown in **A**, a picture of the Vivaldi antenna is included in **B**. The position of the antenna and resistor in the cavity has been exchanged for the Vivaldi antenna. For all following graphics, excluding the Appendix: **A** refers to analysis using monopole antenna data, and **B** refers to data taken with the Vivaldi antenna.

The description of the cryostat design in this subsection 5.2.1 is adapted from [133]. The apparatus is shown in Fig. 5.9, closed but without the first cooling stage in a), with the monopole antenna in b), with a switched position of antenna and resistor, as well as a Vivaldi antenna in c). The design of the cryostat itself is inspired by recent developments in single-pressure Refractive Index Gas Thermometry (RIGT) apparatuses [134]. To control the temperature of the microwave cavity within a range of 9 K to ambient temperature, a cryostat comprising three main vacuum-tight stages was designed and assembled, as shown in Fig. 5.9 in the Appendix. It utilizes a pulse-tube cryocooler (PTC), Sumitomo model SRP-082B2S-F70H, which provides a cooling power of 0.9 W at 4.2 K. The innermost stage of the cryostat consists of a cylindrical copper vessel with an internal diameter of 200 mm, which serves as the microwave cavity. The cavity lining is made of Laird Eccosorb HR 25 polyurethane foam, 25 mm thick and impregnated with carbon black dispersions. The frequency-dependent reflectivity of the material can be found in the manufacturer's data sheet[2] (page 2). Across the main flange of the cavity, multiple coaxial and single-pin feedthroughs are welded onto three stainless steel flanges. These enable the transmission of microwave signals and provide electrical connections to the thermometer terminals.

In addition, a custom flanged copper block, internally bored with a 4 mm hole, facilitates evacuation and helium filling of the experimental vessel. The measurements are performed in an evacuated cavity at a pressure of approximately 10^{-4} bar. Surrounding the microwave cavity is a larger vacuum-tight cylindrical copper vessel (250 mm in diameter), which acts as a thermal switch stage. This stage is equipped with the same number and types of hydraulic and electrical feedthroughs as the inner cavity. Its function is to regulate heat transmission between the PTC and the cavity, either enhancing or minimizing heat transfer as needed. Thermal contact between the PTC's second stage and the outer flange of the thermal switch is ensured by cylindrical copper posts and rectangular plates. These components provide vertical and radial clearance for feedthroughs, connectors, and thermal anchoring of cables and tubing.

The next outermost stage is a cylindrical copper enclosure (320 mm in diameter) serving as a radiation shield. This minimizes heat losses between the first stage of the PTC, the thermal switch, and the ambient temperature tank. Thermal linkage between the radiation shield and the PTC is achieved using copper posts and plates similar to those in the thermal switch. The entire system is enclosed in a stainless steel, vacuum-tight cylindrical tank with an internal diameter of 500 mm and a depth of 500 mm. This tank is equipped with multiple welded ConFlat® flanges for signal feedthroughs, gas inlet and outlet flows, electrical heater connections, and auxiliary temperature sensors. To further reduce radiation heat losses, Mylar foil is incorporated between the cryostat's different stages. In addition, the primary and secondary flanges of both the experimental and thermal switch vessels are sealed using indium wire to ensure vacuum and pressure-tightness. The assembled cryostat was tested for vacuum integrity using a helium leak detector. However, additional heat losses introduced by cables and gas tubes limited the minimum achievable operating temperature of the system to approximately 9 K. Four calibrated Cernox® thin film resistance temperature sensors are deployed within the cavity and behind the foam lining, in order to determine the temperature gradient of the cavity. Due to the precise temperature control, the maximal uncertainty in temperature, can be assumed to be smaller than 100 mK. The amplification chain consists of an amplifier (ampl. in Fig. 5.2) and two circulators to prevent back reflections into the cavity, with a cryogenic Dicke switch (Radiall Ramses SP6T) placed just before the cavity.

Noise powers of monopole antenna and Nyquist resistor

The derivation of noise power $N_{\mathrm{U}(1)}(\nu;T)$ in SI units from radiance for the U(1) case, where the antenna faces a solid angle of $\Omega = 4\pi$ and is subject to the effective apertures $\bar{A}_{\mathrm{eff}}$, under the condition $h\nu \ll k_B T$, is given as follows:

$$\begin{aligned} N_{\mathrm{U}(1)}(\nu;T)\,\mathrm{d}\nu &= I_{\mathrm{U}(1)}(\nu;T) \times \bar{A}_{\mathrm{eff}} \times \Omega\,\mathrm{d}\nu \\ &= \frac{4\nu^2}{c^2} k_B T \times \frac{c^2}{4\pi\nu^2} \times 4\pi\,\mathrm{d}\nu \\ &= 4\,k_B T\,\mathrm{d}\nu\,, \end{aligned} \tag{5.2}$$

where $\Omega = 4\pi$ denotes the full solid angle. antenna reflectance, resistor reflectance.

Dicke switch, amplification stages, measurement strategy

The goal is to measure the noise power of the antenna relative to the noise power of the Nyquist resistor. While the latter one being a solid state body, it can always be assumed to follow Planck's radiation law, while the antenna probes the blackbody nature of the cavity. The core idea is to use one amplification chain for both probes and a cryogenic Dicke switch shortly before the cavity to switch between the antenna and the resistor, compare the illustration in Fig. 5.2 a). Each channel was used for a duration of two minutes before switching, during which the measured powers were integrated over time. In order to mitigate the risk of impedance mismatches in the last two connections from the Dicke switch to the antenna / resistor, as well as at the antenna connection, the position of the antenna and the resistor was

[2] https://media.distrelec.com/Web/Downloads/_t/ds/Laird_Eccosorb_HR_eng_tds.pdf

changed, as depicted in Fig. 5.2 b). Furthermore, the antenna type was altered to a Vivaldi antenna, which has a complementary antenna profile (forward cone) to the monopole antenna (torus like), as well as a lower reflection coefficient Γ_{source}, as shown in Fig. 5.8 in the Appendix. The measured power differences for the monopole and Vivaldi antenna with the Nyquist resistor each are shown in Fig. 5.4 a) and b) respectively.

5.2.2 Error estimates

Statistical error

To average the noise power deviation, data was collected with a bin width of 100 MHz in frequency and 1 K in temperature. Each bin contains hundreds of data points, making the error of the mean at least an order of magnitude smaller than the systematic errors. For a detailed discussion of statistical errors in a similar experimental setup, see [63] on ARCADE 2 integration times and bandwidths, including temperature averaging.

Systematic errors

There are two main error classes, of which any combination could influence the observed deviation from Rayleigh-Jeans behaviour at low frequencies and temperatures. First, errors in the cryogenic amplification chain, such as impedance mismatches caused by feedthroughs, uncertainties due to amplification, and the two short cables ($\sim$7 cm) from the cryogenic Dicke switch to the monopole antenna and the resistor. The second error class consists of unaccounted-for noise-power sources, such as thermometers or their cabling within the blackbody cavity itself. This particular example is unlikely to cause pollution, as two thermometers use DC current and the other thermometers operate at very low current, which wouldn't generate noise power in the GHz range. To estimate the real part of the amplification gain of the antenna and resistor, $G_{21,A}$ and $G_{21,R}$, respectively, we measure the scattering parameter S_{21} as well as the mismatches at the source and load Γ_{output} and Γ_{source}. Refer to Fig. 5.8 in the Appendix for measured spectra of S_{21}, Γ_{output}, and Γ_{source}. The mismatch at the input, Γ_{input}, is calibrated to be 1. The gain G_{21} is given by

$$G_{21} = |S_{21}|^2 \frac{1 - |\Gamma_{\text{source}}|^2}{1 - |\Gamma_{\text{output}}|^2} \times \frac{1}{|1 - \Gamma_{\text{input}}\Gamma_{\text{source}}|^2}. \tag{5.3}$$

Thereby, Γ_{output} is the output reflection coefficient and Γ_{source} is the source reflection coefficient. Since the source and output reflection coefficients of the network are of the order of -10 dB for the antenna and the resistor, the main contribution to G_{21} is S_{21}. The total gain estimated for the antenna and the resistor, $G_{21,A}$ and $G_{21,R}$ are shown in Fig. 5.3. S_{21} was measured at room temperature, and only ΔS_{21} was used for the error propagation, since $\Delta\Gamma_{\text{source}}$ and $\Delta\Gamma_{\text{output}}$ are negligible, as can be inferred from Fig. 5.8 in the Appendix. The total errors in dB for the power difference, are thus given by

$$\Delta P_{\text{A-R}} = \sqrt{\Delta G_{21,\text{A}}^2 + \Delta G_{21,\text{R}}^2}\,, \tag{5.4}$$

and shown in Fig. 5.4 and Table 5.1.

ν [GHz]	5.3 ± 0.05	8.8 ± 0.05
$\overline{\Delta P}_{\text{A-R}}$ [dB]	0.025	0.039

Table 5.1: The average $\overline{\Delta P}_{\text{A-R}}$ over 100 MHz bins of the estimate in Eq. (5.4) for two central frequencies where the gain errors are particularly small. Since both antenna types have nearly identical gain amplification, they share the same error budget.

5.3 Experimental Results

Inspecting Fig. 5.3, we identify two sweet spots at $\nu = 5.3$ GHz and $\nu = 8.8$ GHz with very low average gain error $\overline{\Delta P}_{\text{A-R}}$, see Tab. 5.1. With this error estimate, $P_{\text{A-R}}$ is shown in Fig. 5.4.

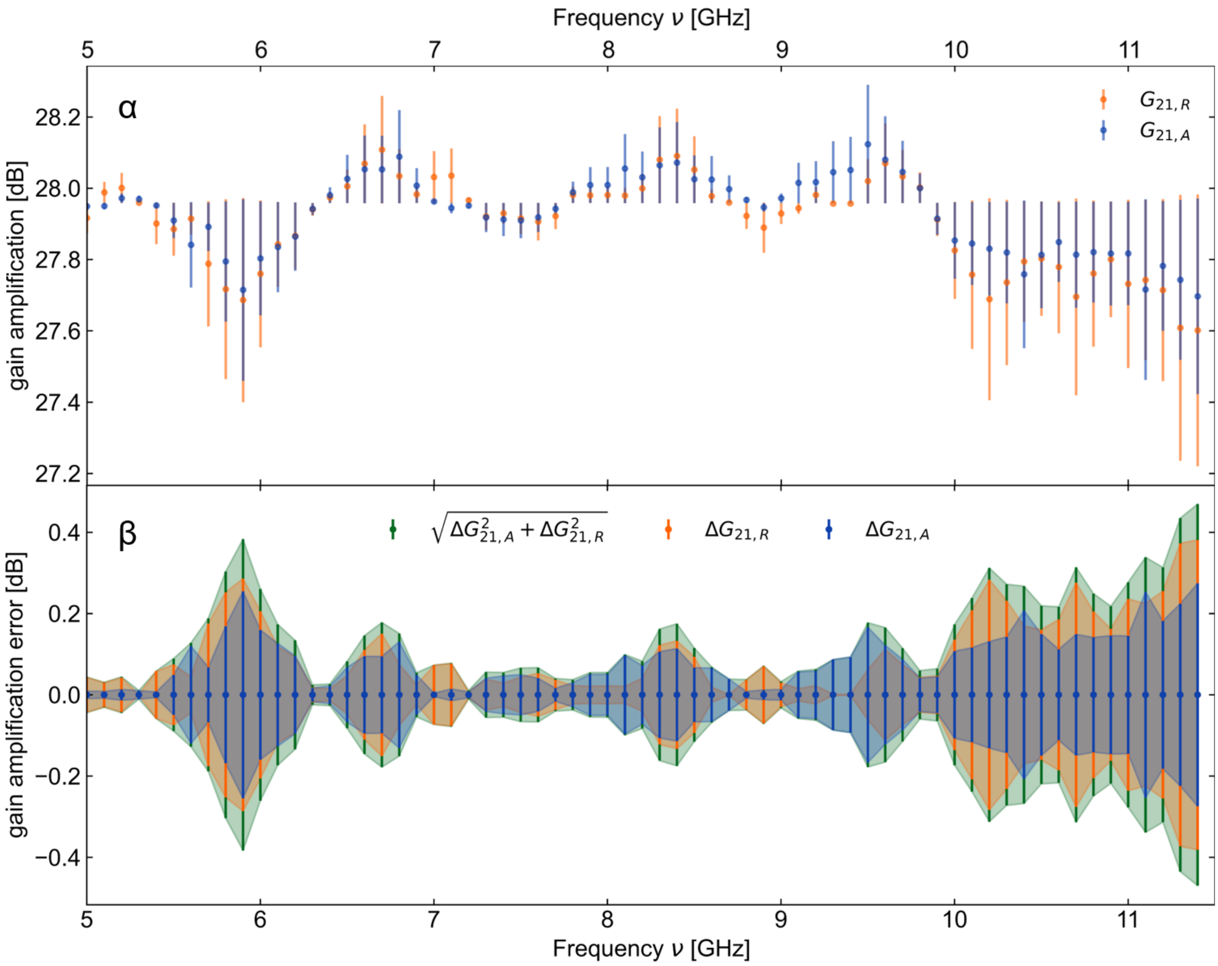

Figure 5.3: The gain for the antenna $G_{21,\mathrm{A}}$ (blue) and the resistor $G_{21,\mathrm{R}}$ (orange) are shown in dB from 5–11.5 GHz in dB, is shown in the upper part of the figure α). Their respective errors as well as the total error in dB for the power difference $\Delta P_{\text{A-R}} = \sqrt{\Delta G_{21,\mathrm{A}}^2 + \Delta G_{21,\mathrm{R}}^2}$ in green are shown in the bottom part of the figure β).

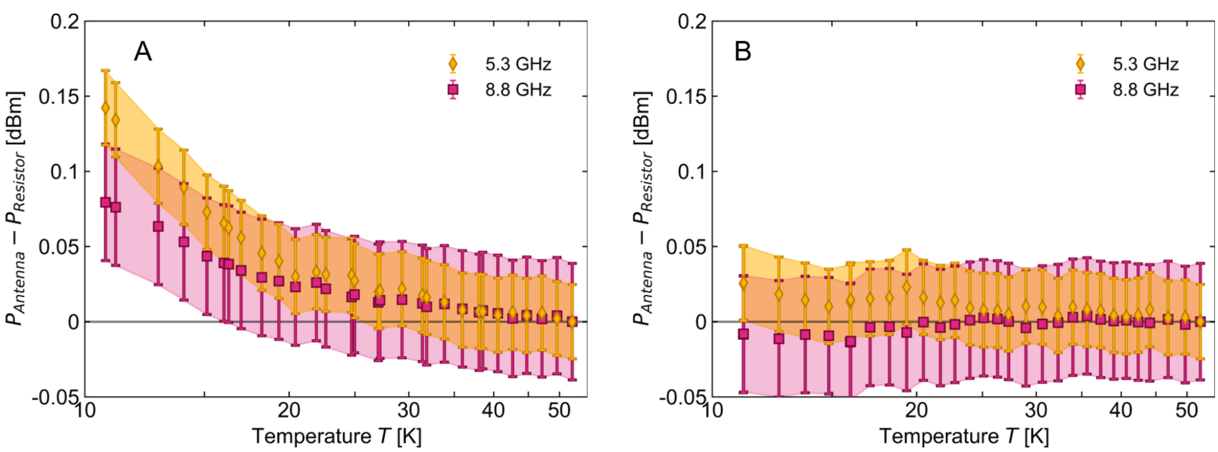

Figure 5.4: The power difference (in dBm) between the monopole antenna and resistor in **A**, and the Vivaldi antenna and resistor in **B**, along with systematic error estimates for two frequencies, is shown: 5.3 GHz in yellow and 8.8 GHz in purple. All noise powers are normalized at $T = 53\,\mathrm{K}$ to correct for different mode couplings to antenna and resistor. For any given central frequency and temperature, the data was averaged over bins of 100 MHz bin and 1 K, respectively.

5.4 Interpretation of Noise-Power Excess at Low Temperatures

Here, we analyse to what extent the results of Sec. 5.3 can be understood in a model of thermal photon gases which invoke mixed degrees of freedom stemming from distinct phases of two SU(2) Yang-Mills theories of vastly disparate Yang-Mills scales [4]. In the following, we work again in natural units $c = \hbar = k_B = 1$. In [131] the Feynman rules of the effective theory of deconfining SU(2) Yang-Mills thermodynamics [31] were applied to compute the transverse screening function G of the tree-level massless mode of four-momentum p (in unitary-Coulomb gauge) and emergent dispersion law $p^2 = G$ from the gap equation

$$\frac{G}{T^2} = \int \mathrm{d}\xi \int \mathrm{d}\rho\, e^2\lambda^{-3}\left(-4+\frac{\rho^2}{4e^2}\right)\rho \times \frac{n_B\left(2\pi\lambda^{-3/2}\sqrt{\rho^2+\xi^2+4e^2}\right)}{\sqrt{\rho^2+\xi^2+4e^2}}\,, \tag{5.5}$$

subject to the following condition

$$|(p+k)^2| = \left|G + 2\,k\cdot p + 4e^2|\phi|^2\right| \leq |\phi|^2\,, \tag{5.6}$$

where k represents the four momentum of the two tree-level heavy modes running in the loop of the associated tadpole diagram (the other one-loop diagram vanishes due to 4-momentum conservation in the two three-vertices [31]). In Eqs. (5.5) and (5.6) we define: $|\phi| = \sqrt{\Lambda^3/(2\pi T)}$ and $k^2 = 4e\,|\phi|^2$, $\vec{y} = \vec{k}/|\phi|$,

$$y_1 = \rho\,\cos\varphi\,, \quad y_2 = \rho\,\sin\varphi\,, \quad y_3 = \xi\,. \tag{5.7}$$

Λ, $\lambda \equiv 2\pi T/\Lambda$, and $e(\lambda)$ denote the Yang-Mills scale, the dimensionless temperature, and the effective gauge coupling, respectively [31]. Since the lowest temperature is 10 K, which is considerable higher than $T_c = 2.725\,\mathrm{K}$, we can set $e = \sqrt{8}\pi$. This is the value of $e(\lambda)$ deep within the deconfining phase [ibid.]. As a consequence of $p^2 = G$, a T dependent gap frequency $\omega_*(T) = 2\pi\nu_*(T)$ (propagation for $p_0 = \omega > \omega^*(T)$, evanescence for $p_0 = \omega \leq \omega^*(T)$) is predicted [131]. Setting $T_{\mathrm{CMB},0} = T_c$, one obtains for $8\,\mathrm{K} \leq T \leq 50\,\mathrm{K}$ an excellent fit as [132]

$$\frac{\nu_*(T)}{\mathrm{GHz}} = 42.70\left(\frac{T}{\mathrm{K}}\right)^{-0.53} + 0.21\,. \tag{5.8}$$

Spectral noise power is obtained from spectral radiance by multiplication with an effective aperture $A = l^2/(4\pi)$, where l denotes the propagating wavelength, and spectral radiance, in turn, is obtained from spectral energy density by multiplication with the group velocity $\mathrm{d}\omega/\mathrm{d}\mid\vec{p}\mid$. In the Rayleigh-Jeans limit $\omega/T = 2\pi\nu/T \ll 1$ of Eq. (5.1) this yields a U(1) spectral noise power $N_{\mathrm{U(1)}}\,\mathrm{d}\nu = 2\,T\,\mathrm{d}\nu$. Like in [67], where at $T = T_{\mathrm{CMB},0}$ the gap for transverse polarisations of the tree-level massless mode is produced by the onset of the Meissner effect at $T \sim T_{\mathrm{CMB},0}$ and not by radiatively induced screening at $T > T_{\mathrm{CMB},0}$ considered in the present work, we model the $\mathrm{SU(2)_{CMB}}$ spectral noise power for $\nu \leq \nu_*$ by a Gaussian of zero mean and standard deviation $\nu_*(T)$

$$N_{\mathrm{SU(2)_{CMB}}}\,\mathrm{d}\nu = F(T)\,\exp[-\nu^2/(2\nu_*^2(T))]\,\mathrm{d}\nu\,. \tag{5.9}$$

Here, $F(T)$ is obtained by demanding continuity at $\nu = \nu_*$ when transitioning to $N_{\mathrm{U(1)}}$: $F(T) = 4\,\mathrm{e}^{1/2}T$. Since the cavity is small and the emission of electromagnetic waves into its hohlraum occurs via the transition between thermalised quantum states of electrons immersed, according to [5], into the confining phase of an SU(2) Yang-Mills theory of scale $\sim 3.6\,\mathrm{keV}$, we must consider a cavity specific mixing between thermal effective U(1) waves, radiated into the hohlraum by the cavity walls, and the tree-level massless modes of $\mathrm{SU(2)_{CMB}}$, which are emitted by this theory's thermal ground state. This mixing of two SU(2) Yang-Mills theories is parametrized by the angle θ. Therefore, the difference of D of the dBm of mixed spectral noise power vs. standard U(1) Rayleigh-Jeans spectral noise power $N_{\mathrm{U(1)}}$ reads

$$D = 10\,\log_{10}\left(\cos^2\theta + \exp\left[-\nu^2/(2\nu_*^2(T)) + \frac{1}{2}\right]\sin^2\theta\right)\,, \tag{5.10}$$

for $\nu \leq \nu_*(T)$. For $\nu > \nu_*(T)$ we have $D \equiv 0$. In Fig. 5.5 the prediction for the T dependence of D according to Eq. (5.10) is shown for $\nu = 5.3$ and 8.8 GHz when matching the means of the experimental data at $T = 10\,\mathrm{K}$. Notice that at the blue dashed lines (at 11.7 K) in Fig. 5.5 a) and b), an entire caloron coarse-graining volume fits within the blackbody cavity. Here, *coarse-graining* refers to a process in which microscopic or quantum-level details are averaged over a characteristic spatial scale to produce

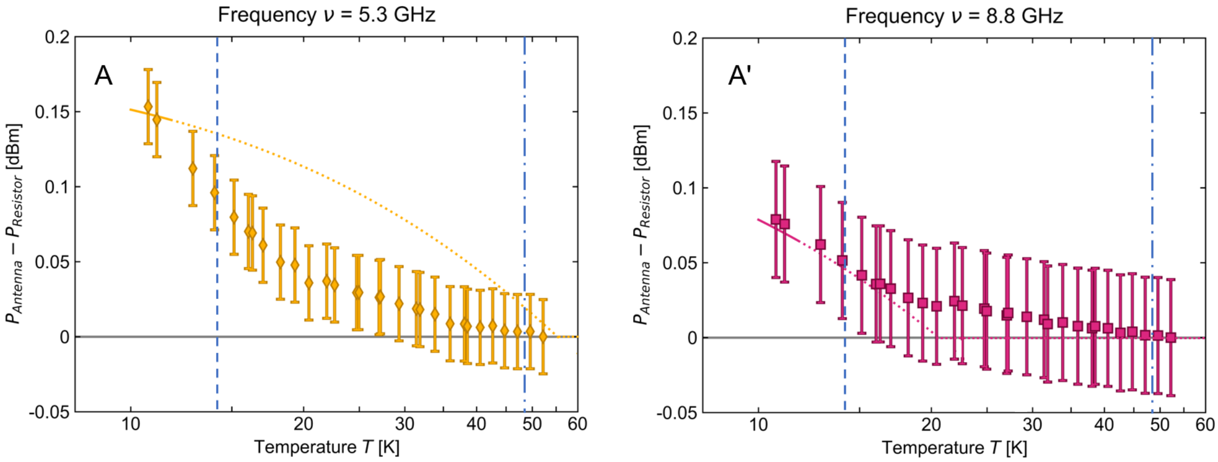

Figure 5.5: The noise power difference between the monopole antenna P_{Antenna} and the $50\,\Omega$ resistor P_{Resistor} is shown in dBm for $\nu = 5.3\,\text{GHz}$ in **A** and for $\nu = 8.8\,\text{GHz}$ in a'), the same data which was also shown in Fig. 5.4 a). The power-law model D of Eq. (5.10) is shown to describe the excess radiation at the lowest available temperatures. The model has been calibrated to match the experimental average values at a temperature of $T = 10\,\text{K}$. The range where the model aligns with the experimental data is highlighted by a solid yellow line in panel **A** and a solid purple line in panel **A'**. The zero touching point of the radiation excess model D (dotted lines) is determined by the gap frequency $\nu_*(T)$. At the blue dashed lines (11.7 K), a full caloron coarse-graining volume fits into the blackbody cavity, while at the blue dot-dashed lines (46.7 K), only half fits.

an effective, macroscopic description. In the case of calorons, this characteristic scale is the size of the caloron itself, which defines a spherical region in space. At this temperature, the physical size of the blackbody cavity is large enough to fully contain one such caloron sphere. Assuming $T_c = T_{\text{CMB},0}$, the diameter d of this region's volume (setting $T_{\text{CMB},0} = T_c$) is given as [31]

$$d(\lambda/\lambda_c) = \frac{0.01056}{2\pi}\,\lambda_c^{3/2}\left(\frac{\lambda}{\lambda_c}\right)^{1/2}\,\text{m}\,, \tag{5.11}$$

where $\lambda_c = 13.87$ the dimensionless critical temperature. To the right of the blue dot-dashed lines in Fig. 5.5, the $\text{SU}(2)_{\text{CMB}}$ infinite-volume theory, which motivates the model in Eq. (5.10), is not applicable. Those lines indicate the temperature at which the radius of the cavity's cylinder equals $\frac{1}{2}\,d$. In Fig. 5.6 an extraction of the mixing angle θ from the (spline extrapolated) data at $T = 10\,\text{K}$ is shown as a function of frequency ν.

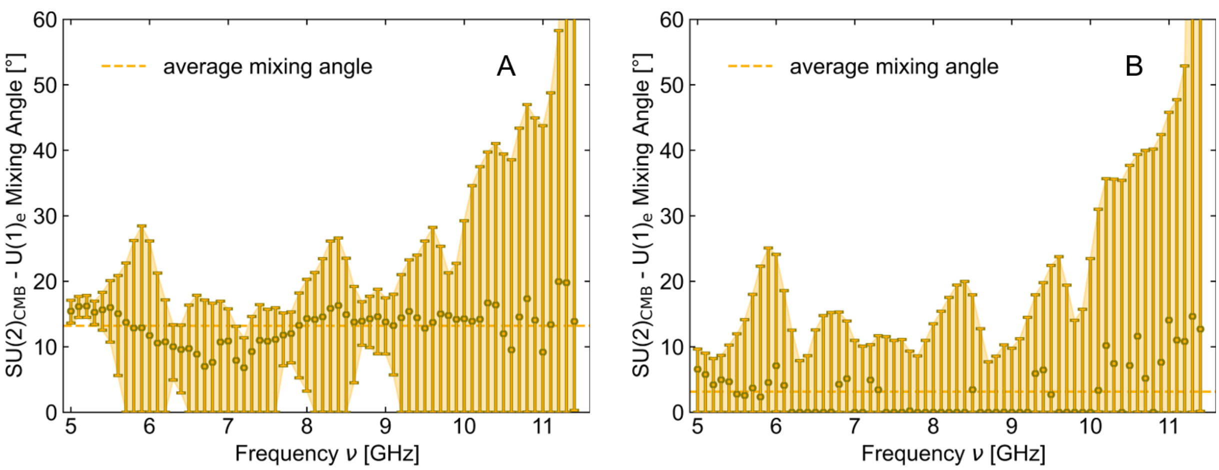

Figure 5.6: The frequency dependence of the mixing angle θ according to Eq. 5.10 is shown for frequencies from 5.0 - 11.5 GHz. The mixing angle and its gain errors is averaged over 100 MHz bands, determined at $T = 10\,\text{K}$. The average mixing angle is $13.21°$ (yellow dashed line) for the monopole antenna in **A**, and $3.12°$ (also yellow dashed line) for the Vivaldi antenna in **B**.

5.5 Discussion and Summary

In this article we have reviewed on how a radiatively induced modification of the thermal photon's dispersion law emerges due to transverse screening / antiscreening, mediated by a resummation of the one-loop polarisation tensor to all orders in the photon's propagator and taking place within the deconfining phase of an SU(2) Yang-Mills theory. The effect is predicted to occur sizeably within the Rayleigh-Jeans regime if temperature is not far above $T_c \sim 10^{-4}\,$eV and radiation is thermalised in a spatially isotropic and homogeneous way. In a next step, we have considered both the spectral manifestation of the radiance anomaly at a fixed temperature and the modified Rayleigh-Jeans law of radiance at a fixed frequency as a function of temperature. For a terrestrial experiment testing these predictions, temperature variation is usually more practical than frequency variation. The associated gap frequency $\nu_*(\mathrm{T})$ was calculated, determining the temperature below which deviations from the Rayleigh-Jeans law are expected for a given frequency.

We discuss the process of directed emission of radiation from the thermalized cavity walls and its subsequent thermalization into isotropic and homogeneous radiation towards the center of a sufficiently extended cavity. We consider an admixture of SU(2) (photons/waves stemming from $\mathrm{SU(2)_{CMB}}$ of Yang-Mills scale $\sim 10^{-4}\,$eV) with U(1) radiance (waves stemming from $\mathrm{SU(2)_e}$ of Yang-Mills scale $\sim 3.6\,$keV). This U(1) admixture arises due to the proximity of the antenna to the cavity walls and the relatively small volume of the cavity (small in comparison by the wave length of the measured frequencies). We initially found the U(1) contribution to be dominating the noise power at 10 K, with an average mixing angle of 13.2° in the frequency range of 5–11.5 GHz for the monopole antenna, compare Fig. 5.6 a). In comparison, the excess radiation could be interpreted as a substantially smaller mixing angle for the Vivaldi antenna, compare Fig. 5.6 b). For the monopole antenna, this is equivalent to $\sin^2(13.2°) \sim 5\%$ of SU(2) radiation within the cavity. The deviation from Rayleigh-Jeans noise power is statistically significant at 5.3 GHz and the lowest experimentally accessible temperatures.

Despite the above summarized efforts to interpret the power offset with a mixing of two photon dispersion laws, the observed power differences between the two antennas are consistent with a thermal gradient within the cavity, where the top is hotter than the bottom. This temperature gradient is confirmed by direct thermometry (purple trace), and it provides a natural explanation for the asymmetric blackbody emission: the monopole antenna viewing the hotter top detects excess thermal radiation, while the Vivaldi antenna viewing the colder bottom detects a deficit.

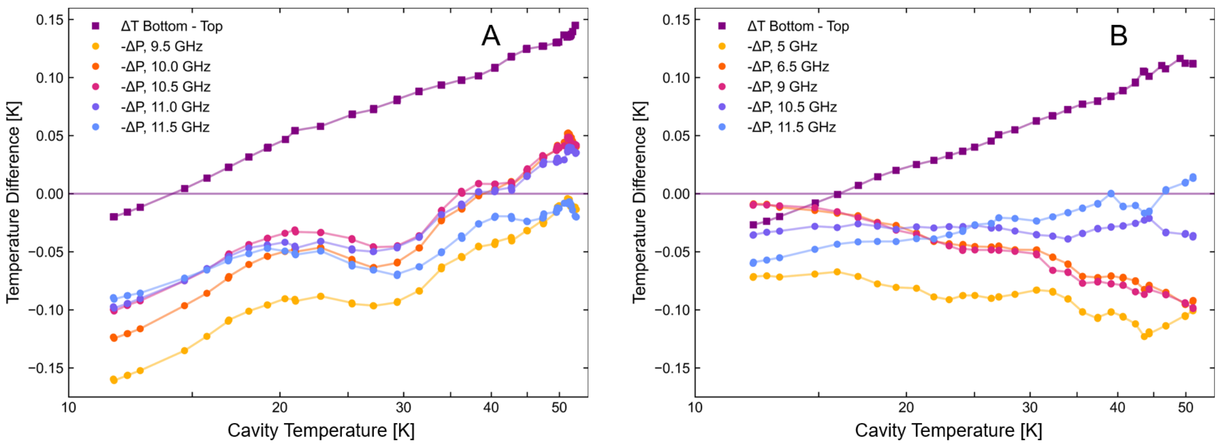

Figure 5.7: Measured power differences $-\Delta P$ (resitor-antenna) as a function of cavity temperature for two antenna configurations: **A** a monopole antenna viewing mostly the top of the cavity, and **B** a Vivaldi antenna viewing mostly the bottom. The power was averaged over a bin size of 0.25 GHz and 3 K. The purple squares show the measured temperature difference $\Delta T = T_{\mathrm{bottom}} - T_{\mathrm{top}}$, indicating that the top of the cavity is consistently hotter than the bottom. Negative $-\Delta P$ values indicate higher received power relative to the reference, while positive values indicate lower power. Each trace corresponds to a different measurement frequency. This strongly suggests, that the measured signal originates from the temperature gradient within the cavity.

The frequency dependence observed in Fig. 5.7B is likely due to a combination of physical and instrumental factors. At lower frequencies, the antenna pattern may sample a larger effective volume of the cavity, averaging over a greater vertical extent and thus integrating more of the temperature gradient. Additionally, the thermal emission at lower frequencies remains firmly in the Rayleigh-Jeans regime, where the power per unit bandwidth remains linear in temperature, making any temperature differences appear more directly in the measured power. At higher frequencies, reduced antenna sensitivity and the exponential suppression of power in the Wien regime may lead to a weaker apparent signal difference.

While the observed signal can be attributed to a temperature gradient within the cavity rather than a clear spectral signature of SU(2) thermodynamics, this outcome does not invalidate the theoretical motivation nor the experimental strategy. On the contrary, our findings underscore the importance of pursuing further investigations under improved conditions. In particular, extending measurements to lower temperatures and frequencies, where the predicted deviations from the Rayleigh-Jeans law are expected to be most pronounced, remains a promising path. Moreover, the use of larger cavities would mitigate wall-proximity effects and reduce contamination from U(1)-like modes, enabling a cleaner isolation of the SU(2) contribution. With refined cavity design, optimized antenna configurations, and stringent thermal stabilization, future experiments may yet uncover the subtle signatures of modified photon dispersion, a fundamental prediction of non-Abelian thermal field theory.

Data availability

The experimental data as well as the Python notebook which has been used for their evaluation are available after publication on GitLab[3].

Acknowledgements

This work is supported by the Vector Foundation under grant number P2021-0102. The authors would like to thank Karl-Heinz Kampert, Gray Rybka, Leslie Rosenberg and Dale J. Fixsen for their support and insightful discussions. JM would like to thank Fabian Becker, Nick Schmeißer, Julian Rautenberg and Christian Pauly for discussing the gain error estimation, as well as Sven Fabian for corrections to the early draft.

Contributions of the author JM

Contributions include writing the manuscript, including drafting the first version (except for the introduction, interpretation, and summary, which were written by Ralf Hofmann). Additional contributions include data analysis, figure preparation, funding acquisition, conceptualization, methodology, validation, and review & editing.

[3] `https://git.uni-wuppertal.de/meinert/inrim-data-analysis`

Appendix

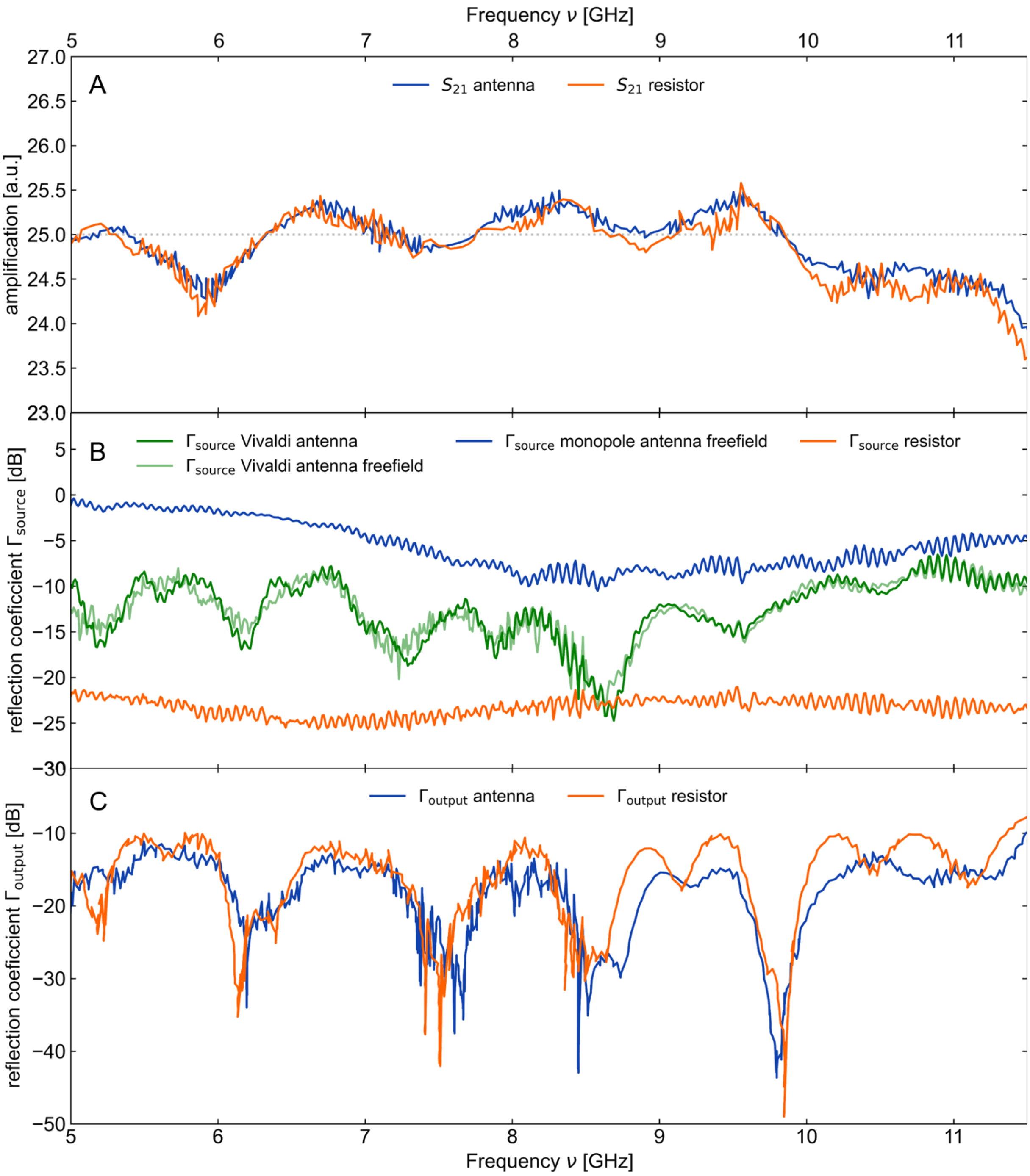

Figure 5.8: The scattering parameters used for calculating the gain amplification in Eq. 5.3 as well as the gain amplification error in Eq. 5.4. All measurements were performed using a network analyser (VNA) under room temperature conditions. The following scattering parameters were taken **A**: the real amplification from the cryogenic amplification chain, including amplifier, circulators, and switch for the pathway to the antenna (blue) and resistor (orange). **B**: the reflection coeficcient Γ_{source} for the free field monopole antenna (blue), the Vivaldi antenna in the cavity (green), the free field Vivaldi antenna (light green), as well as the Nyquist resistor (orange). **C**: the reflection coeficcient Γ_{output}, from the source to the network analyser, for the free field antenna mount (blue), as from the resistor mount (orange).

Figure 5.9: The apparatus is shown closed without the first cooling stage in **A**, (C1–C4) are Cernox® temperature sensors. For our measurement, there are additional temperature sensors within the cavity, behind the lining. The apparatus with an open cavity and monopole antenna in **B**, and open with a switched antenna-resistor position and a Vivaldi antenna in **C**. Fig. 5.9 a) has been adapted from [133, Fig. 4].

6 Electroweak Parameters from YMTD

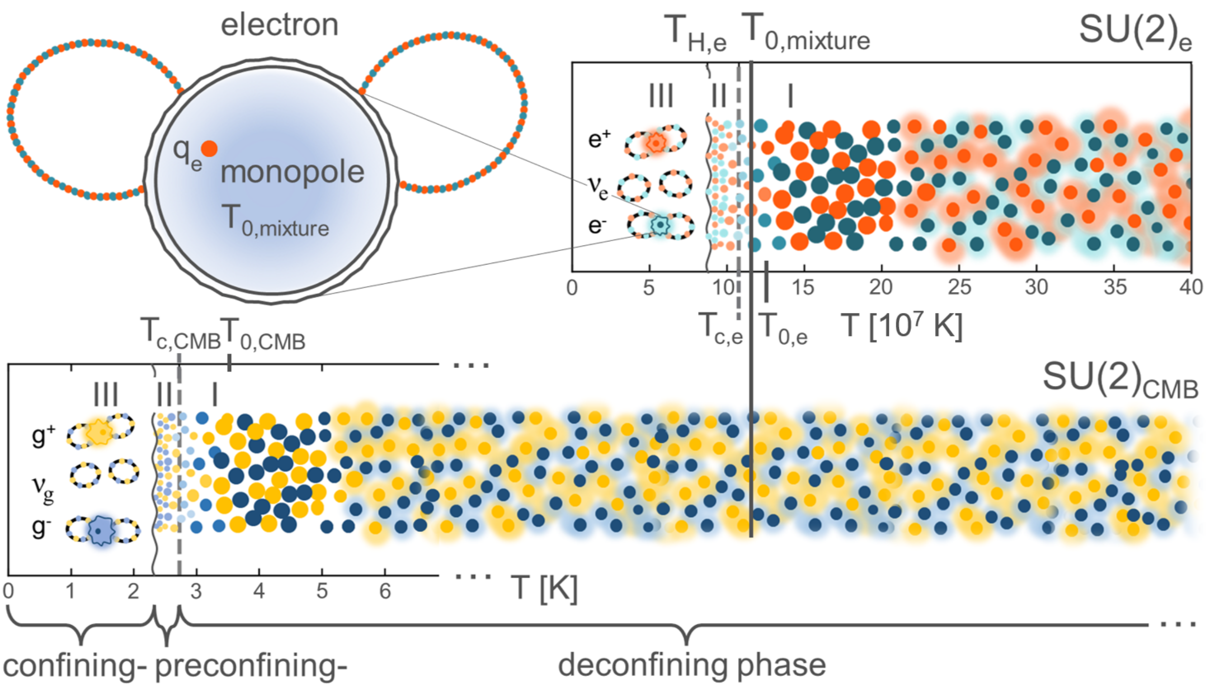

Figure 6.1: The electroweak mixing angle is defined by the point of zero pressure $T_{0,\mathrm{mixture}}$ of the mixture of deconfining ground states of the electron and photon theories.

This chapter is based on "Electroweak parameters from mixed SU(2) Yang-Mills Thermodynamics" [5] and the conference proceedings [8].

Contents

6.1 Introduction . . . 58
6.2 Three Phases of SU(2) Yang-Mills Thermodynamics . . . 62
6.2.1 Deconfining phase (I) . . . 62
6.2.2 Preconfining phase (II) . . . 64
6.2.3 Confining phase (III) . . . 64
6.2.4 Summary of phase structure of SU(2) Yang-Mills thermodynamics . . . 65
6.3 Selfintersecting Center-Vortex Loop and Magnetic Moment . . . 65
6.4 Value of Electromagnetic Fine-Structure Constant . . . 67
6.4.1 Trapping a single monopole or antimonopole inside the droplet's bulk . . . 67
6.4.2 Thin-shell approximation . . . 67
6.4.3 Averaging the droplet's effective charge over monopole locations . . . 68
6.5 SU(2) Gauge Group Mixing in the Droplet . . . 70
6.5.1 Thermal SU(2) gauge-theory mixing and comparison with electroweak theory . 70
6.5.2 Mixing angle θ_W . . . 72
6.5.3 Value of α . . . 74
6.5.4 Impact of mixing on mass formula and length-scale hierarchy in powers of α . 74
6.6 Discussion and Summary . . . 76

Janning Meinert[1,2] **and Ralf Hofmann**[2]

[1]Bergische Universität Wuppertal, Department of Physics, Gaußstraße 20, D-42103 Wuppertal

[2]Institut für Theoretische Physik, Universität Heidelberg Philosophenweg 12, D-69120 Heidelberg

Abstract

Based on the thermal phase structure of pure SU(2) quantum Yang-Mills theory, we describe the electron at rest as an extended particle, a droplet of radius $r_0 \sim a_0$, where a_0 is the Bohr radius. This droplet is of vanishing pressure and traps a monopole within its bulk at a temperature of $T_c = 7.95\,\mathrm{keV}$. The monopole is the Bogomolny-Prasad-Sommerfield (BPS) limit. It is interpreted in an electric-magnetically dual way. Utilizing a spherical mirror-charge construction, we approximate the droplet's charge at a value of the electromagnetic fine-structure constant α of $\alpha^{-1} \sim 134$ for soft external probes. It is shown that the droplet does not exhibit an electric dipole or quadrupole moment due to averages of its far-field electric potential over monopole positions. We also calculate the mixing angle $\theta_\mathrm{W} \sim 30^\circ$ which belongs to deconfining phases of two SU(2) gauge theories of very distinct Yang-Mills scales ($\Lambda_\mathrm{e} = 3.6\,\mathrm{keV}$ and $\Lambda_\mathrm{CMB} \sim 10^{-4}\,\mathrm{eV}$). Here, the condition that the droplet's bulk thermodynamics is stable determines the value of θ_W. The core radius of the monopole, whose inverse equals the droplet's mass in natural units, is about 1% of r_0.

6.1 Introduction

The electroweak interactions between leptons in the Standard Model of Particle Physics (SM) are mediated by quantised gauge fields, associated with the group $\mathrm{U(1)}_Y \times \mathrm{SU(2)}_\mathrm{W}$. In the SM, asymptotic lepton states are associated with point particles whose localisation characteristics relate to quantum states of relativistic matter waves, described by solutions to the Dirac equation, and which depend on the presence or absence of external potentials. Electroweak interactions are assumed to be governed by small gauge couplings: $g' < 1$ for $\mathrm{U(1)}_Y$ and $g < 1$ for $\mathrm{SU(2)}_\mathrm{W}$. The SM is extremely successful and efficient in delivering a quantitative description of scattering cross-sections, decay rates, branching ratios, production and oscillation rates, as well as bound-state properties. Renormalisability of the electroweak sector of the SM [135, 136, 137] assures that corrections to an asymptotic state are calculable to any desired order in the couplings g' and g without having to introduce parameters in addition to those of the defining Lagrangian. By resummation of renormalised Feynman diagrams, these parameters evolve with the resolution scale externally applied to a physical process. Generally speaking, a parameter value obtained at a given four-momentum transfer P can be converted to that at a different four-momentum transfer P' by a rescaling that depends on logarithms of the ratio P/P'.

While the electroweak sector of the SM reliably predicts the running of its parameters and the amplitudes of associated processes, it is unable to compute *absolute* parameter values at any given resolution. Most prominently, the electromagnetic fine-structure constant α [138], which at low four-momentum transfer assumes the experimental value [139],

$$\alpha_\mathrm{exp} = \frac{q^2}{4\pi\epsilon_0\hbar c} = \frac{1}{137.035999206}\,, \tag{6.1}$$

is not subject to calculation within the SM. That is, given ϵ_0 (permittivity of the vacuum), $\hbar$ (reduced quantum of action), and c (speed of light in vacuum), the electric charge of the electron q is a free parameter whose value needs to be measured. In what follows, we assume that the constants of nature ϵ_0, c, and $\hbar$ are independently measured and thus are not considered free parameters of the SM[1]. These constants and Boltzmann's constant k_B are all set equal to unity in the present report (natural units).
In the electroweak sector of the SM [140, 141, 142] the electromagnetic coupling q, due to mixing between the Cartan-algebras of $\mathrm{SU(2)}_\mathrm{W}$ and $\mathrm{U(1)}_Y$, is obtained from the (perturbative) coupling g of $\mathrm{SU(2)}_\mathrm{W}$ or from the (perturbative) coupling g' of $\mathrm{U(1)}_Y$ as

$$q = g\sin\theta_\mathrm{W} \qquad \text{or} \qquad q = g'\cos\theta_\mathrm{W}\,. \tag{6.2}$$

[1]They can be argued to emerge from pure SU(2) Yang-Mills theory, see [31].

Here, $28.7^\circ \leq \theta_{\rm W} \leq 29.3^\circ$ [143, 144] denotes the weak mixing (or Weinberg) angle, measured at variable four-momentum transfer. In addition to condition (6.2), one imposes for the electric charge operator Q and the hypercharge matrix Y of each left-handed lepton family that $Y = Q - \frac{1}{2}\sigma_3$ where $\sigma_3 = {\rm diag}(1, -1)$ denotes the third Pauli matrix, see [145] for a comprehensive review. Like q, $\theta_{\rm W}$ is a free parameter of the SM whose value has to be inferred experimentally at a given resolution. One can pick resolution to be vanishing, and we argue in the present work that, under clearly stated assumptions, in this limit the values of the dimensionless electroweak parameters α and $\theta_{\rm W}$ can be approximated thermodynamically. Such an approach is based on ideas by Louis de Broglie providing the foundations for wave mechanics [122, 146]. Namely, the electron as a propagating matter wave emerges by applying a Lorentz boost to a spatially extended and internally oscillating system (a standing wave). De Broglie also noticed that the transformations of wave frequency and the frequency of internal oscillation are distinct in the same way as the transformations of particle energy and internal heat are. This, however, reveals the existence of a close link between relativistic thermodynamics and the physical insights that are at the heart of wave mechanics.

The present work takes up these profound ideas by de Broglie, supplemented by concrete notions of what the source of oscillation, the oscillating medium, and the boundary of this medium are in the framework of pure SU(2) Yang-Mills thermodynamics in four spacetime dimensions. As we shall argue, this enables derivations of the values of the electroweak parameters α and θ_W. To put this into perspective, we would also like to mention other approaches. The experimental value of α in Eq. (6.1) is either represented by numerology or linked to physics beyond that of the SM. Pure numerology without a defined physical basis can generate an impressive proximity to the value in Eq. (6.1), mostly invoking combinations of primes, and prominent transcendental numbers in elementary functions or continued fractions. These results are reviewed in [147]. Other approaches, including Dirac's large number hypothesis as well as Weyl's hypothesis, both invoking the classical radius of the electron, Casimir's mousetrap model, Kaluza-Klein theories, open-string scattering, invariants under certain ad hoc symmetries and others are reviewed in [148]. Regarding the electroweak mixing angle θ_W, the assumption that quarks have integer electric charges as in the Han-Nambu scheme solves the orthogonality condition between the Z-boson field and the photon-field γ by a value $\sin^2\theta_W = 1/4$ or $\theta_W = 30^\circ$ which is close to experiment [149]. For discussions on how the Weinberg angle relates to consistency conditions in breaking the symmetry groups of grand unified theories (GUT) in four or higher dimensions, see [150] and references therein.

The strength of the SM is that parameters such as α and θ_W can be evolved accurately to describe particle transitions that are characterised by large four-momentum transfers. To such processes, thermodynamics is not applicable. This is already suggested by the fact that in the center-of-mass (COM) frame of two colliding electrons the square of COM energy is given as $s = 4\,m_e^2(1-v^2)^{-1}$ and that the temperature T_0 in each particle's restframe is, by invariance of local entropy under Lorentz boosts [146], decreased as $T = \sqrt{1-v^2}T_0$. Here, $\pm v$ are the respective particle speeds. Letting $v \nearrow 1$, we notice that, as $s \to \infty$, the temperature of each droplet vanishes, $T \searrow 0$. This associates a strongly boosted electron with the confining phase of SU(2) Yang-Mills thermodynamics by depriving it of its 3D structure. Alternatively, an observer in the center-of-mass frame instead of seeing colliding, spherical droplets sees 2D 'pancakes' due to a strong Lorentz contraction along the boosted coordinate. Therefore, the deconfining phase, whose restframe thermodynamics mainly constitutes the droplet and defines its Lorentz invariant properties mass m_e and electric charge Q, is invisible in the center-of-mass frame at large s, see Secs. 4 and 5.

The process of pair creation of an electron and a positron, both separated well at late times, by a pair of initially well separated photons is another example of large four-momentum transfer during the transition. Here, a highly nonthermal, intermediate state of even locally inhomogeneous energy density is generated. This intermediate state emerges from local energy deposition into the ground state of the confining phase of an SU(2) Yang-Mills theory. The round-point center vortex loops composing this ground state are stretched and twisted by such an energy composition [31]. Subsequently, this intermediate state equilibrates into a final state, the electron. In the restframe of the ensuing electron, a thermal droplet at rest is well separated spatially from the boosted thermal droplet – the positron. In Quantum Electrodynamics (QED) and to lowest order in α the nonthermal, intermediate of a pair creation process, where both particles are not fully developed and close by, is described by the electron propagator connecting the two vertices of the associated Feynman diagram. This propagator mediates off-shell propagation of positive and negative energy states forward and backward through limited time intervals, and it is well known how effective and precise the associated QED cross sections describe the experimental data on pair creation [151]. Therefore, QED (and more generally the SM) is a powerful tool to quantitatively assess collisional transitions of asymptotic particle states whose intrinsic thermodynamics is of no use to describe such processes. Yet, as we will argue in the present work, defining particle properties can be obtained from a thermodynamical approach operating in their restframes. A situation that QED and the SM is unlikely to describe well, however, is the physics of a dense and thermal[2] state of electrons and positrons in terms of particle and energy transport, charge and spin fluctuations as well as correlation functions of particle number densities and particle speeds. An important signature to search for in this regard is the creation of electron-positron pairs by macroscopic droplet evaporation, in terms of their gamma-ray annihilation lines originating outside the droplet. The formation of such extended droplets is facilitated by localised deposition of ultra-high energy density through compact, ultra-high contrast, femtosecond lasers focused to relativistic intensities onto targets composed of aligned nanowire arrays [152]. This experiment achieves a local energy density of 8×10^{16} J/m^3 across a spot size of $\sim 5\,\mu$m which would guarantee the creation of macroscopic droplet dimensions.

In this paper, we consider the simultaneous presence of all phases (deconfining / preconfining / confining) of 4D SU(2) Yang-Mills thermodynamics within a ball-like spatial region of radius r_0, a droplet. In particular, we demonstrate how the mixing within the deconfining phase of two SU(2) Yang-Mills theories of vastly disparate scales, $\mathrm{SU(2)_{CMB}}$ and $\mathrm{SU(2)_e}$, appears to yield a realistic value for the electroweak mixing angle due to vanishing bulk pressure and at vanishing external energy-momentum transfer. The Yang-Mills scales (or critical temperatures) of $\mathrm{SU(2)_{CMB}}$ and $\mathrm{SU(2)_e}$ are derived from experiment. Namely, the Yang-Mills scale of $\mathrm{SU(2)_{CMB}}$ is suggested to be $\Lambda_{\mathrm{CMB}} \sim 10^{-4}\,$eV from the excess of CMB line temperatures for frequencies $\nu < 3\,$GHz [63] or from a potential detection of screening effects in a laboratory blackbody experiment at low temperatures. Here, screening effects generate a gap for propagating blackbody radiation at low frequencies ($< 17\,$GHz) shortly above the deconfining/preconfining phase transition of $\mathrm{SU(2)_{CMB}}$ [34, 4] [3]. The Yang-Mills scale of $\mathrm{SU(2)_e}$ is deduced in the present work from the mass of the electron as $\Lambda_{\mathrm{e}} \sim 3.60\,$keV, see also [43, 44] for mildly deviating earlier estimates that neglected gauge-theory mixing. The mixing between the deconfining, preconfining, and confining phases of $\mathrm{SU(2)_e}$ and the deconfining phase of $\mathrm{SU(2)_{CMB}}$ creates a thick boundary shell to the droplet whereas the bulk region is described by the deconfining phases of $\mathrm{SU(2)_e}$ and $\mathrm{SU(2)_{CMB}}$ trapping an $\mathrm{SU(2)_e}$ monopole[4]. The thick boundary shell thus is a region of high electric conductivity due to condensed monopoles in the preconfining phase of $\mathrm{SU(2)_e}$. It is an essential assumption of the present paper that in the limit of a static equlibirium the thick boundary shell is sharply delineated from the bulk at $\bar{r} < r_0$. That is, for each volume element within the thick boundary shell contracting forces, stemming from the mixing of deconfining and preconfining phases of $\mathrm{SU(2)_e}$, are cancelled by the expanding force due to the plasma of the deconfining phase of $\mathrm{SU(2)_{CMB}}$[5]. In any case, the pressure vanishes on the confining-phase side of the Hagedorn transition in $\mathrm{SU(2)_e}$, that is, outside the droplet for $r > r_0$ [31]. We also assume:

(i) effective hydrostatic equilibrium of the thick boundary shell. After spatio-temporally averaging, the bulk pressure P_{bs} vanishes, $P_{\mathrm{bs}} \equiv 0$,

(ii) that phase segregation and therefore a maximum radius for radial averages over monopole positions is given by the mean radius $\bar{r}$ of the initial, non-phase segregated thin-boundary shell droplet, and

(iii) that the energy density within the thick boundary shell is comparable to the bulk energy density. Notice that in the absence of an external force bulk homogeneity $T(r) = T_0 = \mathrm{const}$ and therefore vanishing bulk pressure, $P_{\mathrm{bulk}} \equiv 0$, are due to hydrostatic and thermodynamic equilibrium and the continuity condition of vanishing pressure at bulk-boundary-shell separation $r = \bar{r}$, $P_{\mathrm{bulk}}(\mathrm{r}{=}\bar{r}){=}P_{\mathrm{bs}}(r = \bar{r}) = 0$. Namely, $\mathrm{d}P_{\mathrm{bulk}}/\mathrm{d}r = \mathrm{d}P_{\mathrm{bulk}}/\mathrm{d}T\,\mathrm{d}T/\mathrm{d}r \equiv 0 \Rightarrow \mathrm{d}T/\mathrm{d}r \equiv 0 \Rightarrow T(r) = T_0 = \mathrm{const}$ which, together with $P_{\mathrm{bulk}}(r = \bar{r}) = P_{\mathrm{bs}}(r = \bar{r}) = 0$, yields $P_{\mathrm{bulk}} \equiv 0$.

[2] Here, *dense* refers to densities of the order of 1/(droplet volume), namely $\sim 1.8 \times 10^{28}\,\mathrm{m}^{-3}$, and *thermal* corresponds to temperatures comparable to the stabilisation temperature of the associated Yang-Mills theories, namely $T_0 \sim 9.4\,$keV, or an energy density $\sim 5 \times 10^{14}$ J m^{-3}.

[3] This gap is filled by evanescent modes with a spectrum differing distinctly from Rayleigh-Jeans: Rather than decaying $\propto \nu^2$ with decreasing frequency ν the evanescent mode spectrum grows because modes with decreasing ν possess a decreasing spatial decay length, therefore less energy, and thus are easier excitable.

[4] This requires an electric-magnetic dual interpretation of U(1) charges in SU(2) Yang-Mills theory, see [153, 31].

[5] To avoid making this assumption a treatment of the thick boundary shell in terms of imperfect-fluid hydrodynamics would require a derivation of an effective, selfconsistent, and r dependent equation of state by a spatio-temporal coarse-graining of the phase and gauge-theory mixture. On this basis, the solution to the hydrostatic fluid equations of the thick boundary shell could be obtained. This is technically hard and beyond the scope of the present paper, however.

On one hand, the quantum mass of the droplet is $m_0 = \omega_0$, monopole breathing associating with the (circular) frequency ω_0 [122, 43, 44]. On the other hand, the spatial extent of the electron refers to a dynamical equilibrium which is very close to the static equilibrium assumed in (i). This can be pictured as follows: The thick boundary shell could effectively produce negative pressure by an imbalance of the partial pressures stemming from phase mixing in $\mathrm{SU(2)_e}$ (negative) and gauge theory mixing with $\mathrm{SU(2)_{CMB}}$ (positive). The bulk surface would then have to impose a positive counter pressure (homogeneous in the bulk due to the quantum correlation length $|\,\phi\,|^{-1}$ being much larger than the droplet's extent), that is $T > T_0$. Alternatively, the thick boundary shell could exhibit an imbalance of partial pressures to effectively produce positive pressure to which the bulk surface would react by pull (negative pressure). This describes the droplet's breathing around a stable equilibrium where bulk and boundary-shell pressures independently vanish. In the absence of external forces, breathing amplitudes for the deviations of droplet radii and pressures away from this equilibrium are small[6]. Therefore, assuming an overall vanishing of pressures is justified for an initial estimate of monopole charge distribution, bulk gauge-theory mixing, and droplet mass. Regarding assumption (ii), we argue in Sec. 6.4.3 that shortly after pair creation in each droplet Yang-Mills phases are not segregated and that therefore, the only radial scale $\bar{r}$ to determine segregation is the radial mean subject to a homogeneous probability density over the droplet volume. Assumption (iii) allows for a quick estimate of droplet mass, see Eq. (6.50), since for the boundary shell it is a priori not clear what the effective mixing angle between $\mathrm{SU(2)_{CMB}}$ and $\mathrm{SU(2)_e}$ and what the effective phase mixing within $\mathrm{SU(2)_e}$ are. Note that the fraction of boundary-shell volume to droplet volume is $\sim 27/64 \sim 0.42$ and that therefore deviations of the true energy density within the boundary shell from the assumed bulk energy density should not influence the droplet mass estimate on the right-hand side of Eq. (6.50) strongly.

It is the equivalent descriptions of the system in terms of effective (and only implicit quantum) bulk thermodynamics on one hand and explicit quantum physics on the other hand that allow to address essentials of the droplet physics, see Eq. (6.50). The purpose of the present paper is to demonstrate in such a context what assumptions (i), (ii), and (iii) actually imply for the values of the dimensionless parameters in electroweak theory. This paper is organised as follows. For the benefit of readability and better access to our derivations we review in Sec. 2 the thermal phase structure of a (3+1)-dimensional Minkowskian and effectively quantum SU(2) Yang-Mills theory as it emerges from a 4-dimensional, fundamental, and classical SU(2) Yang-Mills theory defined on the Euclidean cylinder $\mathbf{R}^3 \times S_1$. In particular, we discuss the nature of the transitions from deconfining via preconfining to the confining phase and how the respective (thermal) ground states emerge by dense packings of fundamental topological defects whose central regions are not resolved in the respective effective theories. Sec. 3 is devoted to a brief review of previous work on finite-volume SU(2) Yang-Mills thermodynamics inside the droplet that represents the spatial region of selfintersection of a center-vortex loop, immersed into the confining phase. Such a droplet traps a perturbed Bogmolnyi-Prasad-Sommerfield (BPS) monopole causing monopole and plasma vibrations. A stepwise approach towards a droplet model capable of approximating the experimental value of the electromagnetic fine-structure constant α is developed in Sec. 4. This model, which is short of mixing two SU(2) gauge theories within the droplet's bulk, invokes all three phases of SU(2) Yang-Mills thermodynamics. It also uses a spherical mirror-charge construction to yield the effective droplet charge as seen by an external electromagnetic probe of long wavelength. Moreover, the model introduces the mean of the radial position of the monopole over the entire droplet volume to segregate a thick boundary shell from deconfining-phase bulk thermodynamics. Finally, the droplet charge is expressed as a bulk-volume average. In Sec. 5 the mixing of two SU(2) Yang-Mills theories is considered to describe the thermodynamically stable bulk of a droplet. Here, the conditions of monopole-charge universality and zero bulk pressure determine both the bulk temperature in units of one theory's critical temperature for the deconfining-preconfining phase transition as well as the mixing angle. The latter turns out to be close to experimental values of the weak mixing angle θ_{W}, the Weinberg angle. When accounting for gauge-theory mixing, the model developed in Sec. 4 yields a value of α not far from the experimental low-energy value. Sec. 5 computes the ratio between reduced Compton radius r_c, which is roughly equal to the core radius of the monopole, and droplet radius r_0 from a quantum-thermodynamical electron-mass formula. As it turns out, r_0 is smaller but comparable to the Bohr radius a_0. In Sec. 6 we present a brief summary and an outlook on how the present framework can be applied to understand the emergence and weak decay of the other two charged lepton species of the SM.

[6] It is the monopole with a mass fraction of less than 10 % [43] that drives breathing and, due the defined phase structure of $\mathrm{SU(2)_e}$, the boundary shell cannot compress/expand itself indefinitely.

6.2 Three Phases of SU(2) Yang-Mills Thermodynamics

SU(2) Yang-Mills thermodynamics occurs in three distinct phases as shown in Fig. 6.2. Here, we briefly review associated concepts and results, closely following [31]. The infinite-volume limit is assumed throughout.

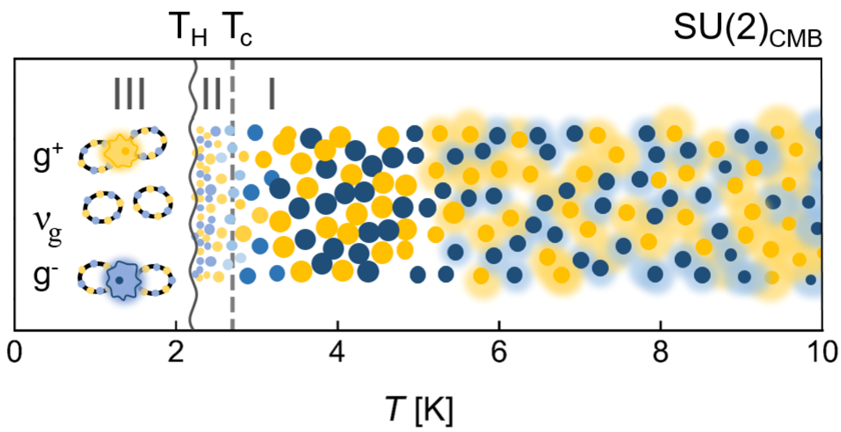

Figure 6.2: Phase diagram of $\mathrm{SU(2)_{CMB}}$ with $T_c = 2.725\,\mathrm{K}$ in the infinite-volume limit. There are three distinct phases: (I) deconfining phase, (II) preconfining, and (III) confining phase. In phase III a very light lepton family emerges whose charged members can be called gammaron and antigammaron and which posses a mass of $1.5 \times 10^{-2}\,\mathrm{eV}$. The ground state of $\mathrm{SU(2)_{CMB}}$ partly transitions into such charged leptons at the Hagedorn temperature $T_{c'} \sim 2.27\,\mathrm{K}$.

6.2.1 Deconfining phase (I)

The deconfining phase takes place for $T \geq T_c$. Its thermal ground state can be derived from a spatially coarse-grained two-point field-strength correlator, evaluated on a trivial-holonomy caloron or anticaloron [68] whose respective contributions are superimposed. The reason for the use of a trivial-holonomy rather than a nontrivial-holonomy caloron or anticaloron is its stability under one-loop quantum fluctuations [154]. (Anti)calorons are (anti)selfdual solutions to the fundamental Yang-Mills equations on the Euclidean cylinder $\mathbf{R}_3 \times S_1$, parametrised by $0 \leq r < \infty, 0 \leq \varphi \leq 2\pi, 0 \leq \theta \leq \pi, 0 \leq \tau \leq \beta \equiv \frac{1}{T}$ (T denoting temperature). Therefore, these gauge-field configurations are void of pressure and energy-density, that is, they do not propagate. The spatial coarse-graining is performed over the central spatial dependence of the field-strength correlation. This amounts to an integral over the 3D spatial ball, referred to as 'center' in the following, at any given value of τ. In the singular gauge that the (anti)caloron is constructed in, this ball centrally locates the topological charge. Specifically, this means that integrating the Chern-Simons current over a 3-sphere of radius $\rho \gg \epsilon > 0$, centered at the position of the maximum of the action density at $r = 0, \tau_0$, yields a result which does not depend on ϵ. Here ρ denotes the (anti)caloron radius[7]. The average over (anti)caloron radii ρ yields a normalisation which cubically rises with the upper cutoff. This integral produces a rapidly saturating, harmonic τ-dependence.
Dense spatial packing of centers (spatial homogeneity at the resolution set by a (anti)caloron center's radius) gives rise to an inert, temporally winding, and adjoint scalar field ϕ of modulus $|\phi| = \sqrt{\Lambda^3/2\pi T}$ which breaks the fundamental gauge symmetry SU(2) down to U(1). Here Λ denotes the Yang-Mills scale of the deconfining phase. Dense packing implies the overlap of (anti)caloron peripheries (the complements of their centers) with centers and with one another. After spatial coarse-graining, the collective presence of all other (anti)caloron peripheries at the position of a given (anti)caloron center accurately is captured by a pure-gauge solution a_μ^{gs} to the effective Yang-Mills equation. Out of vanishing pressure and energy density in a situation, where only the dense packing of centers is considered, the inclusion of peripheral overlap produces finite ground-state energy density ρ^{gs} and pressure P^{gs}. One has

$$\rho^{\mathrm{gs}} = -P^{\mathrm{gs}} = 4\pi\Lambda^3 T\,. \tag{6.3}$$

[7]Throughout the paper the symbol ρ is used to denote various quantities in different contexts: caloron radius, plasma energy density, and probability density for the location of a monopole within the droplet's bulk. What is meant when will be clear from the context.

This vacuum equation of state is an important aspect of the 'thermal ground state'. Microscopically, (anti)caloron overlap transiently changes the (anti)caloron's holonomy from trivial to mildly nontrivial which introduces the negative ground-state pressure described by Eq. (6.3)[154].

By virtue of the adjoint Higgs mechanism invoked by field ϕ, two out of three components (dimension of SU(2) algebra $\mathfrak{su}(2)$ equals three) of the effectively propagating gauge field a_μ are massive where mass m depends on T (quasiparticle mass). This can be seen after de-winding the field ϕ and nullifying the effective ground-state gauge field $a_\mu^{\rm gs}$ by a singular but admissible gauge transformation. Under such a gauge transformation, the Polyakov loop, evaluated on $a_\mu^{\rm gs}$, changes its value from the center element $-\mathbf{1}_2$ to the center element $\mathbf{1}_2$. This confirms that the theory is in a deconfining phase, that is, the electric center symmetry $\mathbf{Z}_2$ is broken dynamically.

Effective, propagating excitations can be grouped into purely quantum thermal for all frequencies (massive modes) and classical, off-shell or quantum thermal, depending on frequency (massless mode). The one-loop approximation to thermodynamical bulk quantities like pressure P or energy density ρ, subjecting noninteracting excitations to the presence of the thermal ground state, is 99 % accurate. Small corrections to this estimate can be computed in terms of higher loops. They collectively describe the effects of rare dissociations by large holonomy shifts in (anti)calorons. The dissociation products are screened monopole-antimonopole pairs.

Demanding that one-loop fluctuations and the thermal ground-state estimate are thermodynamically consistent (implicit T-dependences cancel in Legendre transformations: $\frac{\mathrm{d}P}{\mathrm{d}m}=0$, P the one-loop pressure, m the quasiparticle mass) one derives the following first-order ordinary differential equation [31]

$$\partial_a\lambda = -\frac{24\lambda^4 a}{(2\pi)^6}\frac{D(2a)}{1+\frac{24\lambda^3a^2}{(2\pi)^6}D(2a)}\,, \tag{6.4}$$

where

$$a \equiv \frac{m}{2T} = 2\pi e\lambda^{-3/2} \tag{6.5}$$

and

$$D(y) \equiv \int_0^\infty \mathrm{d}x\,\frac{x^2}{\sqrt{x^2+y^2}}\frac{1}{\exp\left(\sqrt{x^2+y^2}\right)-1}\,. \tag{6.6}$$

Here, e denotes the effective gauge coupling in the deconfining phase, and dimensionless temperature is defined as $\lambda \equiv \frac{2\pi T}{\Lambda}$. The evolution described by Eq. (6.4) possesses two fixed points: $a=0$ and $a=\infty$. The latter associates with a critical temperature λ_c of value $\lambda_c = 13.87$, the former describes the behaviour at asymptotically high temperatures. For $a \ll 1$ the downward-in-temperature evolution described by Eq. (6.4) is solved by

$$a(\lambda) = 4\sqrt{2}\pi^2\lambda^{-3/2}\left(1-\frac{\lambda}{\lambda_i}\left[1-\frac{a_i\lambda_i^3}{32\pi^4}\right]\right)^{1/2}\,, \tag{6.7}$$

subject to the initial condition $a(\lambda_i)=a_i \ll 1$ and $\lambda_i \gg 1$. The attractor $a(\lambda)=4\sqrt{2}\pi^2\lambda^{-3/2}$ implies, by virtue of Eq. (6.5), that the effective gauge coupling e is a constant almost everywhere:

$$e \equiv \sqrt{8}\pi\,. \tag{6.8}$$

Eq.(6.7) indicates that the condition $a \ll 1$, under which it was derived, is violated at small temperatures. Since the exact solution continues to grow with decreasing λ (negative definiteness of right-hand side of Eq. (6.4)) the right-hand side of Eq. (6.4) will be suppressed exponentially. This implies a behaviour $a(\lambda) \propto -\log(\lambda-\lambda_c)$ for $\lambda \searrow \lambda_c$ and therefore a logarithmic singularity at λ_c also for $e(\lambda)$, see Fig. 6.3. Physically, such a singularity implies masslessness for isolated screened monopoles, liberated by the dissociation of large-holonomy (anti)calorons and collectively associable to effective radiative corrections [155]. Therefore, as $\lambda \searrow \lambda_c$, the holonomy of a typical (anti)caloron moves from small to large [156].

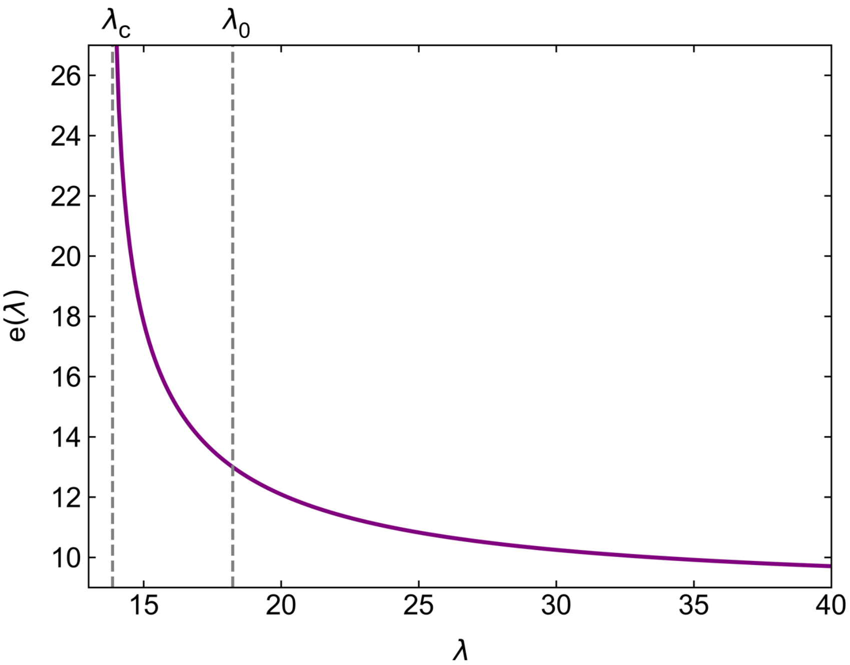

Figure 6.3: The effective gauge coupling of the deconfining phase in SU(2) Yang-Mills thermodynamics as a function of dimensionless temperature $\lambda = \frac{2\pi T}{\Lambda} \geq 13.87 = \lambda_c$ where Λ denotes the Yang-Mills scale, and T_c is the critical temperature for the deconfining-preconfining phase transition. Temperature $\lambda_0 = 18.31$ refers to the point of vanishing pressure.

6.2.2 Preconfining phase (II)

The preconfining phase extends from $\lambda_c = 13.87$ (onset of monopole condensation, second-order phase transition, pressures on both side of the phase boundary match, thermal energy density of monopole-antimonopole-condensed system with one massive photonic vector excitation is higher on the preconfining than on the deconfining side of the phase boundary with one massless photonic vector excitation, coexistence of deconfining and preconfining phases, phase tunneling) via $\lambda = \lambda_* = 12.15$ (preconfining-phase energy density matches supercooled thermal energy density of deconfining ground state with one massless photonic excitation, phase tunneling suppressed) to $\lambda_{c'} = 11.57$ (massive photon decouples, entropy vanishes, onset of Hagedorn transition, discontinuous phase changes of order parameter [157] associate with tunneling towards (magnetic) $\mathbf{Z}_2$ degenerate ground state, associated center-flux creation). Microscopically, the thermal ground state of the preconfining phase is constituted from massless magnetic monopoles and antimonopoles. In physics models, these are dually interpreted and therefore represent electric monopoles and antimonopoles [153].

Dense packing of monopole and antimonopole cores is described by an effective, inert, complex scalar field φ which breaks the remaining gauge symmetry U(1) dynamically. The overlap of all peripheries at the position of a given monopole or antimonopole core is described by an effective pure-gauge configuration $a_\mu^{D,\mathrm{gs}}$. In the preconfining phase, the Polyakov loop, evaluated on the effective ground-state gauge field $a_\mu^{D,\mathrm{gs}}$, is unity in both winding and unitary gauge. This is indicative of the fact that the preconfining phase already confines infinitely heavy, fundamental test charges, although massive, propagating gauge modes can still be excited. The pressure throughout the deconfining phase is *negative*. If it were not for phase mixing, the ground state of the preconfining phase would be a superconductor. But even in the presence of phase mixing, electric conductance is expected to be very high for $\lambda_{c'} \leq \lambda \leq \lambda_c$ compared to the deconfining and confining phases. At λ_c the effective U(1) gauge coupling g vanishes with mean-field exponent $\frac{1}{2}$, at $\lambda_{c'}$ g diverges logarithmically [31].

6.2.3 Confining phase (III)

At $\lambda_{c'}$ massive Abrikosov-Nielsen-Oleson vortex loops without selfintersections, which are instable defects for $\lambda_c' < \lambda \leq \lambda_c$ due to their finite, resolvable core-sizes, become massless and metastable. These massless solitons, so-called thin center-vortex loops, break the magnetic center symmetry $\mathbf{Z}_2$ dynamically [157] upon their condensation. Condensation is enabled by shrinkage to round, massless points [158]. The ensuing new $\mathbf{Z}_2$ degenerate ground state, which confines fundamental test charges and does not support thermal gauge-mode excitation anymore, can be shown to possess no energy density and to exert no pressure [31]. The liberation of thin center-vortex loops at $\lambda_{c'}$ from the ground state of the preconfining phase initiates the Hagedorn transition. Effectively, this process is described in terms of phase changes by $\pm\pi$ of a complex scalar field Φ.Such phase changes accompany tunneling events through tangentially convex regions of a potential uniquely determined by $\mathbf{Z}_2$ symmetry. Collisions of center-vortex loops lead to twistings and the formations of stable regions of selfintersections which, in their restframes, are characterised by the droplets of radius r_0 that we have alluded to in Sec. 1, see also Sec. 3. The density of states $\Omega(E)$ of solitons, which are subject to an arbitrary number of selfintersections, rises more than exponentially in energy E. Therefore, no partition function exists for $\lambda \sim \lambda_{c'}$ (confining phase), and thermodynamics is not a valid description anymore. (This can already be inferred from the fact that for $\lambda \searrow \lambda_{c'}$ the entropy density vanishes which violates Nernst's theorem.)

6.2.4 Summary of phase structure of SU(2) Yang-Mills thermodynamics

To summarise, SU(2) Yang-Mills thermodynamics comes in three phases, see Fig. 6.2. The deconfining phase (phase I) breaks SU(2) to U(1) in terms of a thermal ground state estimate which is composed of trivial-holonomy anticalorons and calorons of topological charge $k = \mp 1$. For $\lambda \gg \lambda_c$ rare dissociations of (anti)calorons, induced by large holonomy shifts, create isolated monopoles and antimonopoles which, however, are spatially not resolved in the effective theory. For $\lambda \sim 2\ldots 3\,\lambda_c$ the distance between monopoles and antimonopoles is comparable to the spatial resolution set by $|\phi|^{-1}$, and therefore they become explicit and isolated degrees of freedom. In the effective theory, the collective imprint of these monopoles and antimonopoles onto thermodynamical quantities (a $\sim 1\%$ effect compared to the free quasiparticle approximation [31]) or dispersion laws for propagating gauge modes can be studied in terms of (resummed) radiative corrections. There is a temperature, $\lambda_0 \sim 1.32\,\lambda_c$, where a finite-size system can be stabilised due to vanishing pressure. At λ_c monopoles and antimonopoles become massless, pointlike defects that are densely packed: they represent a would-be superconductive condensate. However, phase mixing reduces conductivity to finite values. Pressure is negative throughout the preconfining phase. At $\lambda_{c'} = 0.83\,\lambda_c$ the monopole-antimonopole condensate of the preconfining phase undergoes a violent decay into center-vortex loops of any selfintersection number $n \geq 0$. This initiates the (nonthermal) Hagdorn transition. The new ground state is composed of massless, shrunk-to-points center-vortex loops, possesses no energy density and exerts no pressure. Each selfintersection point of a center-vortex loop represents the droplet of radius r_0 (scaled by the ratio of the respective Yang-Mills scales) that is addressed in the next section. At a finite resolution, provided by nonthermal, external electromagnetic fields, only center-vortex loops with $n = 0, 1$ can be regarded stable solitons.

6.3 Selfintersecting Center-Vortex Loop and Magnetic Moment

A thin center vortex can be understood as a chain of unresolved monopoles and antimonopoles whose flux is confined to a thin tube [159]. The stable, massive soliton, represented by a center-vortex loop with $n = 1$, then originates from a localised investment of energy (pair creation) into round-point center-vortex loops with $n = 0$. These round points constitute the ground state of the confining phase. Such an investment of energy implies stretching / twisting / pinching and the eventual release of a monopole or an antimonopole from the tube. As a consequence, points of vortex selfintersection are defined. Since a monopole or antimonopole cannot exist as isolated defects in the confining vacuum, each point of selfintersection needs to evolve into an extended ball-like spatial region (a droplet). The deconfining, pressureless bulk of such a droplet facilitates a finite-mass and finite-extent monopole or antimonmopole at the temperature $T = T_0 = 1.32\,T_c$. The droplet comprises a boundary shell, which exhibits a temperature gradient, where positive pressure generated by turbulences (Hagedorn transition) is superimposed by the negative pressures contributed by preconfining and deconfining phases. On temporal and spatial average, zero pressure of the boundary shell is assumed in the remainder of this paper to continue the vanishing pressure of the confining phase outside the droplet. The center flux external to the droplet forms a flux configuration which is of figure-eight topology.

Let us now discuss why such a topology relates to the spin-$\frac{1}{2}$ nature of the electron and how an according magnetic moment $\vec{\mu}$ emerges. Dually interpreted, a quantum of magnetic center flux represents a quantum of electric center flux, in turn, inducing a quantum of magnetic moment. Fig. 6.4 depicts the center-vortex loop with $n = 1$. Since the electric center flux is two-fold degenerate (it can flow along or counter a fixed tangential vector to the vortex loop) the projection of $\vec{\mu}$ onto a quantisation axis is also twofold degenerate, and one has in the isolated case

$$\vec{\mu} = -g\,\mu_{\rm B}\,\vec{S}\,, \tag{6.9}$$

where $g = 2$, $\mu_{\rm B} \equiv -\frac{q}{2m_{\rm e}}$ is the Bohr magneton, $m_{\rm e}$ and q are the electron's mass and charge, respectively, and $\vec{S}$ is the spin vector. The two possible projections of $\vec{S}$ are $\pm\frac{1}{2}$. Notice that the quantisation axis is parallel to the normal $\hat{n}$ of the plane that the figure-eight configuration is considered to be immersed in, for certain characteristics of curve-shrinking planar figure-eight configurations, see [160]. Picturing the droplet charge, modulo quantum jitter [161, 162], to move along a circle of radius comparable to a_0 (Bohr radius), see Sec. 6.5.4, the Bohr magneton describes its effective revolution in time Δt as triggered by the revolution within the same span of time of one of the unresolved monopoles or antimonopoles along the thin vortex loop. Namely, in associating with $\vec{L} = -g\vec{S}$ the orbital angular momentum of the droplet subject to $|\vec{L}| = a_0 \cdot m_{\rm e} \cdot 2\pi a_0/(\Delta t)$, the magnetic moment $\vec{\mu}$ of Eq. (6.9) can simply be interpreted as $\vec{\mu} = \pm I\,\pi a_0^2\,\hat{n}$ which is the magnetic moment induced by a circular current loop of radius a_0 carrying the current $I = \frac{q}{\Delta t}$. Since a center-vortex loop in reality is not isolated (it is immersed into the CMB, and it connects to a fluctuating thick boundary shell) one expects a slight deviation from the value $g = 2$ which to a high precision is computable in Quantum Electrodynamics [163]. A derivation of $\mu_{\rm B}$ from jittery revolutions of the droplet is beyond the scope of the present paper, however. Ignoring for the moment the complications of electroweak decays, mixing effects, and the tendency of vortex loops to shrink under a lowering of external resolution [160], we propose the three lepton families to match with doublets of center-vortex loops ($n = 0, 1$). Each doublet would then emerge within one of three SU(2) Yang-Mills theories, whose scales relate to charged lepton masses, see Sec. 5.4 for a derivation of droplet size and T_c from the mass of any given charged lepton. For the first lepton family, where the soliton with $n = 1$ (electron) is stable, the implications of such an assignment are pursued in the remainder of this paper.

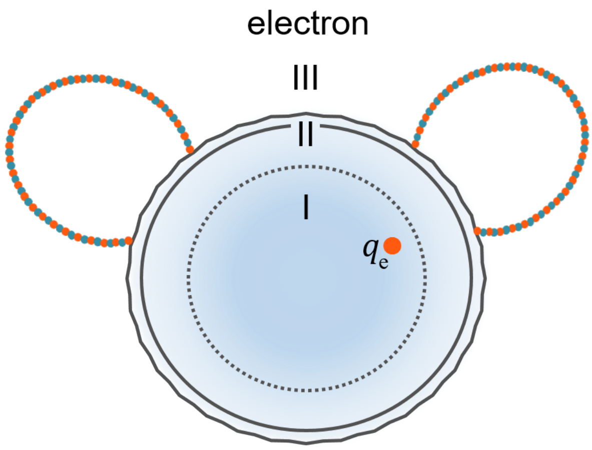

Figure 6.4: The electron as a soliton in SU(2) Yang-Mills theory. For simplicity, mixing effects with another SU(2) Yang-Mills theory are ignored in this figure. The bulk of the droplet, containing an isolated BPS monopole, is in the deconfining phase (I) at vanishing pressure (temperature T_0), the thick boundary shell (II) radially interpolates between a thermal 2nd-order like (inner part of shell, onset of superconductivity / preconfining phase) and a nonthermal Hagedorn phase transition (outer part of shell, full superconductivity). On average, this boundary shell should be of vanishing pressure due to the mixing of all three phases and possesses a high electric conductance. The confining phase (III) prevails outside of the droplet. Isolated gauge modes may propagate as waves in this phase if their frequency is lower than a limit set by the Yang-Mills scale. The monopole within the bulk of the droplet breathes at a frequency $m_{\rm e}$ (rest mass of electron [43]) and generates a time dependent vibration of spatially constant amplitude throughout the droplet. Connected to the thick boundary shell are center-vortex lines, which induce the magnetic moment of the soliton. Topologically, these form a figure eight with the vortex-line selfintersection - producing an isolated monopole or antimonopole - being responsible for the origination of the droplet, see text.

6.4 Value of Electromagnetic Fine-Structure Constant

6.4.1 Trapping a single monopole or antimonopole inside the droplet's bulk

Let us first discuss the simplified situation in which the physics of a droplet is governed by a single gauge theory: $SU(2)_e$. We aim to derive the dual charge[8] of such a system. A monopole or an antimonopole is immersed into the droplet's bulk of deconfining phase at temperature T_0. From now on we consider the situation of a trapped monopole only, since that of a trapped antimonopole simply is described by sign inversions of all charges considered. As discussed previously, $T_0 = 1.32\,T_{c,e}$ is the temperature where the pressure of the droplet vanishes [44]. Due to the high conductance of the boundary shell ($\bar{r} \le r \le r_0$) and for $\bar{r} \sim r_0$ a spherical mirror-charge construction [164] can be used to approximate the droplet charge for probes of long wavelengths. This construction is depicted in Fig. 6.5. Here s or s' denote the respective distances between observer and monopole or observer and mirror charge. Monopole and mirror charge are both positioned on a radial ray pointing away from the droplet center. As seen from the droplet center, angle θ subtends the direction of the observer and the direction of this ray. The distance between observer and droplet center is denoted by o. In thin-shell approximation, we set $\bar{r} = r_0$.

Since a mirror charge construction for boundary conditions on a spherical surface operates with Coulomb potentials for the inducing and the mirror charge [164], it is essential to secure that a Yukawa factor $\exp(-s/l_s)$ for the potential associated with the monopole's charge inside the ball can be treated as unity. Here l_s denotes the charge screening length that arises from other screened and stable dipoles in the infinite-volume plasma [31]. Let us thus check the selfconsistency of only one explicit monopole or antimonopole inhabitating the droplet of radius r_0. This requires an estimate of $l_s/r_0 \gg 1$. In [44] it was found for a pure $SU(2)_e$ theory describing the droplet that

$$r_0 = \frac{4.043}{\pi T_0} = 0.44\,\Lambda_e^{-1}\,. \tag{6.10}$$

In Sec. 6.5.4 we derive a deviating estimate of r_0 which includes the mixing of $SU(2)_{\rm CMB}$ and $SU(2)_e$. The screening length $l_s = 71.43\,/\,T$ was extracted from a two-loop radiative correction to the pressure at large temperatures, $T \gg T_0$, see [165]. For an estimate, we may continue this asymptotic result to T_0 to obtain

$$\frac{l_s}{r_0} \sim 55.5 \gg 1\,. \tag{6.11}$$

Therefore, for $0 \le s \le 2\,r_0$ a Yukawa factor $\exp(-s/l_s)$ to the Coulomb potential, which could arise from other explicit monopoles and antimonopoles within the droplet, can be set equal to unity. Thus, the assumption of a single monopole being trapped in the bulk of the droplet indeed is selfconsistent.

6.4.2 Thin-shell approximation

In deriving the effective charge of the droplet at bulk temperature $T = T_0$ and in the long-wavelength limit, we first analyse the limits of vanishing shell thickness $r_0 = \bar{r}$ and superconductivity of the boundary shell, see Fig. 6.4. Moreover, we neglect the effects of monopole breathing [119, 120] and implied position changes in this section. Under these simplifying assumptions, the static potential outside the droplet reads [164]

$$\begin{aligned} V(o,r,\theta) &= \frac{1}{4\pi}\left(\frac{q_e}{s} + \frac{q_e'}{s'}\right) \\ &= \frac{q_e}{4\pi}\left(\frac{r-r_0}{r}\frac{1}{o} + \frac{(r^2 - b r_0)\cos\theta}{r}\frac{1}{o^2}\right. \\ &\quad + \frac{(r^3 - b^2 r_0)(1 - 3\cos^2\theta)}{2r}\frac{1}{o^3} \\ &\quad \left. + \,\mathcal{O}\left(\frac{1}{o^4}\right)\right)\,, \quad (o > r_0)\,, \end{aligned} \tag{6.12}$$

where $s \equiv \sqrt{o^2 + r^2 - 2or\cos\theta}$, $s' \equiv \sqrt{o^2 + b^2 - 2ob\cos\theta}$, $b \equiv \frac{r_0^2}{r}$, and $q_e' \equiv -q_e \frac{r_0}{r}$. From Eq. (6.12) and for $o \gg r_0$ we read off the effective charge g_e of the droplet from the coefficient of $\frac{1}{o}$ as

$$g_e = \frac{r - r_0}{r}\,q_e\,. \tag{6.13}$$

[8]The magnetic charge of the monopole is physically interpreted as an electric charge, see [153, 31].

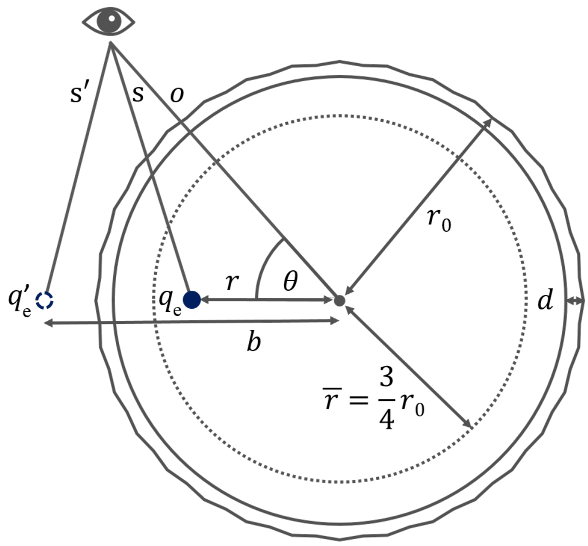

Figure 6.5: Construction of the effective droplet charge by superposition of the Coulomb potentials of the monopole charge q_e with a mirror charge q'_e outside the droplet due to superconductivity of a thin boundary shell. In reality, a finite radial range $r_0 - d \leq r \leq r_0$ associates with the Hagedorn transition. The reason why $\bar{r} = \frac{3}{4}\,r_0$ (dotted line) delineates region II from region I, compare with Fig. 6.4, is discussed in Sec. 6.4.3.

6.4.3 Averaging the droplet's effective charge over monopole locations

Droplet creation and thermalisation

When a droplet of radius r_0, containing a trapped monopole, forms in an $\mathrm{SU(2)_e}$ gauge theory it is a priori not thermalised, and the monopole's location within the droplet, which is a mixed state of all three phases, is equally likely everywhere in the ball apart from a thin boundary shell. A uniform a priori distribution of monopole location in Cartesian coordinates is then cast into a nonflat probability density $\rho(r,\theta)$ in spherical coordinates for $0 \leq r < r_0$ and for a polar angle $0 \leq \theta < \pi$, see Sec. 6.4.3. The thin boundary shell of the droplet (the radial location $r \sim r_0$ where the Hagedorn transition to the confining phase takes place) is characterised by decoupled dual Abelian gauge modes and off-Cartan modes which, due to their large masses, cannot be redistributed into the interior of the droplet. Only after bulk thermalisation is attained for a central radial region does an extended boundary region materialise – a thick boundary shell ($\bar{r} = \xi r_0 < r < r_0$ with $0 < \xi < 1$) exhibiting a temperature gradient and defining the transition from the deconfining via the preconfining to the confining phase via phase mixing. As the trapped monopole enters this region, it rapidly changes its identity[9].

Let us discuss this situation and its consequences in more detail. If, after bulk thermalisation, the monopole is kicked towards the thick boundary shell then it undergoes mass and charge reduction until it becomes a part of the (spatially inhomogeneous) monopole-antimonopole condensate contributing to the phase mixture there [31]. Yet, to explicitly conserve charge (or 3D winding number) and droplet mass, another monopole, formerly part of the condensate, needs to act in place of the original monopole in the bulk of the droplet (deconfining phase). Ignoring correlations between monopoles and antimonopoles inside and close to the condensate within the boundary shell, one may approximate a given monopole's probability density of location by the a priori distribution $\rho(r,\theta)$. However, the monopole's charge q_e (and its mass) is a function of r which is flat and finite in the droplet's bulk (deconfining phase) but rapidly approaches zero as the radial location approaches $\bar{r} = \xi r_0$. Since no length scale other than r_0 characterises the a priori distribution $\rho(r,\theta)$ in the limit of vanishing probe four-momentum transfer, we are led to associate ξ with the mean radial position of the monopole (fluctuations of this mean can be

[9]The monopole is exposed to the caloron's 4D winding number, which is localised spatially deeply within its center [31]. This 4D Euclidean winding is associated with the quantum of action $\hbar$ [31] and therefore exerts undeterministic kicks and position changes onto the monopole at the breathing frequency of the monopole.

neglected at vanishing four-momentum transfer, see Sec. 6.4.3) according to ρ,

$$\frac{\langle r\rangle_\rho}{r_0} \equiv \xi = \frac{3}{4}\,. \tag{6.14}$$

Physically, the droplet's bulk is subject to a mixing of two thermal gauge theories, $SU(2)_e$ and $SU(2)_{CMB}$, see Sec. 6.5.2. This, however, does not invalidate the above argument, since the (nonthermal) probe field always resides in $SU(2)_e$ [31] and therefore is sensitive only to the physics acted out by (thermal) $SU(2)_e$ gauge fields inside the droplet.

Naive thin-shell approximation and value of fine-structure constant α

The droplet's effective charge, when probed with an energy-momentum transfer small compared to the Yang-Mills scale Λ_e, due to the frequent changes of monopole location inside the droplet's bulk (kicks issued by a combination of Planck's quantum of action $\hbar$ and the lowest breathing frequency of the monopole [119, 120, 44, 43]) compared to the frequency of an external probe field, will represent itself as an angular and radial average subject to the following a priori probability density ρ prior to thermalisation (uniform distribution in Cartesian coordinates over ball volume)

$$\rho(r,\theta) = \frac{3r^2}{4\pi r_0^3}\sin\theta\,, \quad (0\le r<r_0,\, 0\le\theta<\pi)\,. \tag{6.15}$$

Performing the θ-average of $V(o,r,\theta)$ in Eq. (6.12) w.r.t. the distribution $\rho(r,\theta)$ in Eq. (6.15), we conclude that there is no dipole (and no quadrupole) contribution to the electric charge distribution of the droplet – in agreement with experimental bounds on a potential, feeble CP violation by an electric dipole moment [166].
In particular, the droplet's charge is obtained by an average of the static system's charge in Eq. (6.13) w.r.t. the probability density $\rho(r,\theta)$ in Eq. (6.15). It is given as

$$\langle g_e\rangle_\rho = 3\int_0^{r_0} dr\,\frac{r(r-r_0)}{r_0^3}\,q_e = -\frac{1}{2}\,q_e\,. \tag{6.16}$$

Let us discuss why this result is statistically stable. The monopole changes its position within the droplet at a rate comparable to its breathing frequency $\omega_0 = m_e$ [122] where m_e denotes the electron mass [119, 120, 44, 43]. If the droplet is probed by an external electromagnetic wave of frequency $\omega_p \ll \omega_0$ then the distribution $\rho(r,\theta)$ of Eq. (6.15) is sampled independently $N = \frac{\omega_0}{\omega_p} \gg 1$ many times during each probe oscillation. Therefore, the value of g_e, averaged over one probe oscillation, has mean

$$\bar g_e \equiv \frac{1}{N}\sum_{i=1}^{N}\langle g_{e,i}\rangle_\rho = \langle g_e\rangle_\rho = -\frac{1}{2}\,q_e\,, \tag{6.17}$$

and standard deviation $\sigma_{g_e}/\sqrt{N}$ where $\sigma_{g_e} = \frac{\sqrt{3}}{2}\,q_e$ is the standard deviation of g_e with respect to $\rho(r,\theta)$. In the limit of vanishing four-momentum transfer ($N\to\infty$), the droplet's effective charge hence does not fluctuate and is given by Eq. (6.16). Such an argument in favour of the non-fluctuativity of the effective chargecan be extended to assure the nonfluctuativity of any observable function $f(r)$ of the random variable r. For example, one may consider the mean radial position, $f(r) = r$, see also Eq. (6.14), for which one has

$$\bar r \equiv \frac{1}{N}\sum_{i=1}^{N}\langle r_i\rangle_\rho = \langle r\rangle_\rho = \frac{3}{4}\,r_0 \tag{6.18}$$

with a standard deviation $\sigma_r/\sqrt{N}$ where $\sigma_r = \sqrt{3/80}\,r_0$.
Since the external gauge field probing the droplet's charge resides in the Cartan algebra of $SU(2)_e$ [31] and ignoring the effects due to a finite boundary-shell thickness, this would yield a value of the inverse electromagnetic fine-structure constant α^{-1} of

$$\alpha^{-1} = \frac{4\pi}{\bar g_e^2} = 4\frac{e^2(\lambda_0)}{4\pi} = 53.464\,, \tag{6.19}$$

where $e(\lambda_0) = 12.96$, see [43, 44]. Obviously, this is too low compared to the value $\alpha^{-1}\sim 137$ associated with Eq. (6.1). Therefore, in Sec. 6.4.3 we consider a model implementing the effects of a thick boundary shell.

Modelling a thick boundary shell after thermalisation

According to the discussion of Secs. 6.4.3 and 6.4.3 about droplet generation the only length scale available to radially separate bulk thermodynamics (deconfining phase) from the thick boundary shell, where the transitions from deconfining via preconfining to confining phase take place and where an isolated monopole cannot exist, is $\bar{r} = \xi r_0$ with $\xi = \frac{3}{4}$, see Eqs. (6.14) and (6.18). This corrects the thin-shell approximation for the droplet charge $q_{\rm e}$ to

$$\bar{g}_{\rm e} = \langle g_{\rm e}\rangle_\rho = 3\int_0^{\frac{3}{4}r_0} {\rm d}r\,\frac{r(r-r_0)}{r_0^3}\,q_{\rm e} = -\frac{27}{64}\,q_{\rm e}\,. \tag{6.20}$$

The inverse electromagnetic fine-structure constant α^{-1} would then compute as

$$\alpha^{-1} = \frac{4\pi}{\bar{g}_{\rm e}^2} = \left(\frac{64}{27}\right)^2\frac{e^2(\lambda_0)}{4\pi} = 75.099\,. \tag{6.21}$$

Although this value is higher than the one of Eq. (6.19), it is still quite far off the experimental value associated with Eq. (6.1). One may think that this discrepancy arises because thin-shell perfect-conductor boundary conditions were used to model a thick boundary shell of finite conductance. Certainly, there is a (not easy to compute) correction to Eq. (6.21) to compensate for this simplification. However, a far more important conceptual ingredient is missing in Eq. (6.19): mixing effects due to the two gauge theories $SU(2)_{\rm e}$ and $SU(2)_{\rm CMB}$ providing a stable mix of deconfining-phase plasmas in the bulk of the droplet to yield an environment that allows the existence of an isolated monopole for each theory. It is the $SU(2)_{\rm e}$ component of this mixture whose monopole together with its mirror charge determine the charge distribution of an electron as seen by a directed, external $SU(2)_{\rm e}$ probe field. To analyse this, is the subject of the next section.

6.5 SU(2) Gauge Group Mixing in the Droplet

6.5.1 Thermal SU(2) gauge-theory mixing and comparison with electroweak theory

Outside the droplet (confining phase of $SU(2)_{\rm e}$, deconfining phase of $SU(2)_{\rm CMB}$ due to the presence of the Cosmic Microwave Background), the directedly propagating (nonthermal) gauge field is the effective Cartan gauge field $a^3_{\mu,{\rm e}}$ [167, 31]. The Standard Model of Particle Physics (SM) describes this nonthermal electromagnetic mode by a global mixture of the gauge mode B_μ of $U(1)_Y$ and the Cartan gauge mode W^0_μ of $SU(2)_{\rm W}$. However, due to the finite extent of the deconfining $SU(2)_e$ plasma in the present approach mixing of $SU(2)_{\rm CMB}$ and $SU(2)_{\rm e}$ occurs only inside the droplet due to outside temperatures being much smaller than the critical temperature $T_{c,e}$ of the deconfining-preconfining phase transition of $SU(2)_e$. De-mixing of the two theories outside the droplet takes place because each is in a different phase. Here, we consider a mixing between the full gauge groups $SU(2)_{\rm e}$ and $SU(2)_{\rm CMB}$ inside the droplet. That is, inside the droplet, due to thermalisation in one and the same deconfining phase the fields $f_{\rm CMB}$ and $f_{\rm e}$ are actively rotated as

$$\begin{pmatrix} f_{\rm CMB} \\ f_{\rm e}\end{pmatrix} \longrightarrow \begin{pmatrix} \cos\theta_{\rm W} & -\sin\theta_{\rm W} \\ \sin\theta_{\rm W} & \cos\theta_{\rm W}\end{pmatrix}\begin{pmatrix} f_{\rm CMB} \\ f_{\rm e}\end{pmatrix}\,, \tag{6.22}$$

where $\theta_{\rm W}$ denotes the mixing (or Weinberg) angle, and field f stands for either the fundamental field strength tensor $F_{\mu\nu}$ or the effective gauge field a_μ in unitary-Coulomb gauge [31]. An effective, propagating external field $a^3_{\mu,{\rm e}}$ thus couples to the droplet charge as

$$\begin{aligned} q = \bar{g}_{\rm e}(\lambda_0)\cos\theta_{\rm W}(\lambda_0) &= -\frac{27}{64}q_{\rm e}(\lambda_0)\cos\theta_{\rm W}(\lambda_0) \\ &= -\frac{27}{64}\frac{4\pi}{e(\lambda_0)}\cos\theta_{\rm W}(\lambda_0)\,, \end{aligned} \tag{6.23}$$

compare with Eqs. (6.20) and (6.22). Note that we continue to define the dimensionless temperature λ as $\lambda \equiv \frac{2\pi T}{\Lambda_{\rm e}}$ where $\Lambda_{\rm e}$ denotes the Yang-Mills scale of $SU(2)_{\rm e}$, amounting to a few keV [44]. The precise value under gauge-theory mixing is computed in Sec. 6.5.4. Also, we now denote by λ_0 the temperature where the pressure of the *mixing plasmas* of SU(2)$_{\rm CMB}$ and SU(2)$_{\rm e}$ vanishes. Likewise, an effective, external field $a^3_{\mu,\rm CMB}$ would couple to a reduced monopole charge

$$q_{\rm CMB}(\lambda_0)\sin\theta_{\rm W}(\lambda_0) = \frac{4\pi}{e(\kappa^{-1}\lambda_0)}\sin\theta_{\rm W}(\lambda_0)\,. \tag{6.24}$$

Since SU(2)$_{\rm CMB}$ is in the deconfining phase inside and outside the droplet, there is no mirror-charge factor. Also, due to the small value of the Yang-Mills scale $\Lambda_{\rm CMB}$ the directed propagation of $a^3_{\mu,\rm CMB}$ is constrained to long wavelengths [167, 31]. Here, we introduce

$$\kappa \equiv \Lambda_{\rm CMB}/\Lambda_{\rm e} \ll 1\,, \tag{6.25}$$

based on $\Lambda_{\rm CMB} \sim 10^{-4}$ eV. Note that $e(\kappa^{-1}\lambda_0) = \sqrt{8}\pi$ to a very good approximation. In the droplet's bulk, however, (thermal) gauge fields $a^3_{\mu,\rm e}$ and $a^3_{\mu,\rm CMB}$ couple with reduced strength as

$$q_{\rm e}(\lambda_0)\cos\theta_{\rm W}(\lambda_0) = \frac{4\pi}{e(\lambda_0)}\cos\theta_{\rm W}(\lambda_0) \tag{6.26}$$

and as in Eq. (6.24) to their respective monopoles. As in the SM [168, 140, 141], the universality of the two reduced couplings in Eqs. (6.26) and (6.24) (mixed gauge field couples to each charge with the same strength) thus requires

$$q_{\rm CMB}(\lambda_0)\sin\theta_{\rm W}(\lambda_0) = q_{\rm e}(\lambda_0)\cos\theta_{\rm W}(\lambda_0)\,. \tag{6.27}$$

Eq. (6.27) is the definition exploited in Sec. 6.5.2 to thermodynamically determine the value of $\theta_{\rm W}$. Eq. (6.27) also implies the following correspondences between the Cartan algebra in SU(2)$_{\rm CMB}\times$SU(2)$_{\rm e}$ and the Cartan algebra (unitary gauge) in the gauge group of the Standard Model SU(2)$_{\rm W}\times$U(1)$_Y$ at λ_0:

$$\begin{aligned}&\text{Cartan}(\mathfrak{su}(2)_{\rm e}) = \text{u}(1)_Y\,,\\&\text{Cartan}(\mathfrak{su}(2)_{\rm CMB}) = \text{Cartan}(\mathfrak{su}(2)_{\rm W})\,.\end{aligned} \tag{6.28}$$

Considering that SU(2)$_{\rm CMB}$ is deeply in its deconfining phase close to the droplet surface at $\lambda_{c'}$, keeping the quasiparticle masses of its off-Cartan fluctuations at values well below 10^{-4} eV, see also the discussion in Sec. 6, we are led to make the following assignment between off-Cartan members of the algebras of SU(2)$_{\rm CMB}\times$SU(2)$_{\rm e}$ and SU(2)$_{\rm W}\times$U(1)$_Y$ at $\lambda_{c'}$, however:

$$\text{off-Cartan}(\mathfrak{su}(2)_{\rm e}) = \text{off-Cartan}(\mathfrak{su}(2)_{\rm W})\,. \tag{6.29}$$

That is, in the SU(2)$_{\rm CMB}\times$SU(2)$_{\rm e}$ model $\theta_{\rm W}$ may change as a process relegates its focus from the deconfining bulk (definition of droplet's charge in interaction with long-wavelength external probes) to the boundary shell (electroweak conversions from heavier to lighter charged leptons).
In the SM's (extremely successful) nonthermal, weak-coupling approach and complete (rather than stepwise) SU(2) gauge-symmetry breaking, invoked by a fundamentally charged Higgs-field of (unitary-gauge) neutral vacuum expectation $v_{\rm H} = 246$ GeV, the Weinberg angle $\theta_{\rm W}$ can also be defined via

$$\cos\theta_{\rm W} = \frac{m_{W^\pm}}{m_{Z_0}}\,, \tag{6.30}$$

where $m_{W^\pm}$ and m_{Z_0} denote the masses of the vector bosons mediating the weak force.
In the SU(2)$_{\rm CMB}\times$SU(2)$_{\rm e}$ model proposed here, the large hierarchy of measured vector-boson mass of 80.4 GeV ($W^\pm$) and 90.2 GeV (Z^0) characterises the decoupling of effective gauge fields in SU(2)$_{\rm e}$ at the deconfining-preconfining ($W^\pm$) and preconfining-confining (Z^0) phase boundaries as a consequence of divergent effective coupling constants. Collectively, this physics takes place within the thick boundary shell. The effective Higgs mechanisms at play are an adjoint one in the former and an Abelian one in the latter situation. Therefore, although the effective *nonthermal* Cartan mode of SU(2)$_{\rm e}$, $a^3_{\mu,\rm e}$, is modelled by the gauge group U(1)$_Y$ in the Standard Model, the effective off-Cartan modes of SU(2)$_{\rm e}$, $a^{1,2}_{\mu,\rm e}$, close to the Hagedorn transition play the role of the massive vector bosons $W^\pm_\mu$ of SU(2)$_{\rm W}$ in the Standard Model. Also, the effective dual, massive U(1) mode of the preconfining phase in SU(2)$_{\rm e}$ plays the role of the massive vector boson Z_0 in the Standard Model. Due to phase mixture in SU(2)$_{\rm e}$, setting in slightly below $T_{c,\rm e}$, the masses $m_{W^\pm}$ and m_{Z_0} cannot be defined thermodynamically in the SU(2)$_{\rm CMB}\times$SU(2)$_{\rm e}$ model. Because of this and since, thermodynamically, all massive gauge bosons are solely generated in SU(2)$_{\rm e}$ a definition of $\theta_{\rm W}$ via Eq. (6.30) would be meaningless, and we have to resort to Eq. (6.27) for

a useful thermodynamical definition of $\theta_{\rm W}$. In the absence of CP-violating terms in the fundamental Yang-Mills action, like in the SM, there is no theoretical basis in the $\mathrm{SU(2)_{CMB}\times SU(2)_e}$ model for why only left-handed charged currents couple to the weak, massive gauge fields. Also, lepton universality, which comprises instable mu- and tau-leptons and their neutrinos, is a concept difficult to describe thermodynamically by an extension of our present model to $\mathrm{SU(2)_{CMB}\times SU(2)_e\times SU(2)_\mu\times SU(2)_\tau}$. However, certain considerations are made in Sec. 6. Finally, it is not clear how a neutral scalar excitation of mass 126 GeV – the Higgs boson – collectively emerges in the $\mathrm{SU(2)_{CMB}\times SU(2)_e}$ model as an excitation of the phase- and gauge-group mixed plasma of the thick boundary shell. The Standard Model is highly efficient and successful in addressing all these features. For the time being, we therefore must confine our discussion of electroweak physics to the electromagnetic coupling of electrons to thermal photons or propagating electromagnetic waves. Still, such limited understanding of the underpinning of electroweak physics in the $\mathrm{SU(2)_{CMB}\times SU(2)_e}$ model produces values of α and $\theta_{\rm W}$ which are close to their SM values, as we shall see in Secs. 6.5.3 and 6.5.2, respectively.

6.5.2 Mixing angle $\theta_{\rm W}$

During the creation of an electron-positron pair, we must assume that the fundamental gauge fields that initiate the formation of the two droplets are purely $A_{\mu,\rm e}$ since the initial two-photon state is nonthermal ($\theta_{\rm W}=0$) [31]. Once the droplet volumes define themselves and after internal thermal equilibrium is attained, there is a fixed mixing angle $\theta_{\rm W}$. An intriguing feature of the Standard Model is that the value of $\theta_{\rm W}$ can be computed at a certain four-momentum transfer from the value of $\theta_{\rm W}$ measured at another four-momentum transfer. The intriguing feature of SU(2) Yang-Mills thermodynamics is that the value of $\theta_{\rm W}$ at zero four-momentum transfer appears to be computable independently of what is assumed so far in deriving the value of α. Let us demonstrate this.
Due to mixing of $\mathrm{SU(2)_{CMB}}$ and $\mathrm{SU(2)_e}$ the deconfining-phase bulk pressure of the droplet $P_{\rm bulk}$ at temperature $T\ge T_{c,\rm e}$ ($T_{c,\rm e}$ the critical temperature for the deconfining-preconfining phase transition in $\mathrm{SU(2)_e}$) and to one-loop accuracy is given as[10]

$$\begin{aligned} P_{\rm bulk}(T) &= \left(1-\sin^2\theta_{\rm W}(T)\right)\,P_{\rm e}(T)+\sin^2\theta_{\rm W}(T)P_{\rm CMB}(T)\\ &= P_{\rm e}(T)+\sin^2\theta_{\rm W}(T)(P_{\rm CMB}(T)-P_{\rm e}(T))\\ &= P_{\rm e}(T)+\sin^2\theta_{\rm W}(T)\left(P_{\rm CMB,gs}(T)-P_{\rm e,gs}(T)\right)\\ &\quad+\sin^2\theta_{\rm W}(T)\left(P_{\rm CMB,3\,pols}(T)-P_{\rm e,3\,pols}(T)\right)\,, \end{aligned} \tag{6.31}$$

where $P_{\rm e}, P_{\rm CMB}$ denote the total pressures in deconfining $\mathrm{SU(2)_e}$ and $\mathrm{SU(2)_{CMB}}$, respectively. They are defined in detail in Eqs. (6.38), (6.39), and (6.40) below. The indices 'gs' and '3 pols' refer to the contributions to these pressures arising from the respective ground states and the two effective gauge-mode excitations with three polarisations (due to the adjoint Higgs mechanisms invoked by the thermal ground states). The contributions of the effective gauge-mode excitations with two polarisations (massless modes) cancel exactly between $\mathrm{SU(2)_e}$ and $\mathrm{SU(2)_{CMB}}$ in the term on the right-hand side of in Eq. (6.31) which is proportional to $\sin^2\theta_{\rm W}(T)$. Note that the pressure of a monopole intrinsically is nil.
From now on, T_0 and $T_{0,\rm e}$ are agreed to denote the zeros of $P_{\rm bulk}$ and $P_{\rm e}$, respectively. Therefore, Eq. (6.31) implies that

$$T_0=\frac{\lambda_0}{2\pi}\Lambda_{\rm e}\le T_{0,\rm e}=\frac{\lambda_{0,\rm e}}{2\pi}\Lambda_{\rm e}\qquad(\pi>\theta_{\rm W}\ge 0)\,. \tag{6.32}$$

The inequality (6.32) holds since the differences $P_{\rm CMB,gs}-P_{\rm e,gs}$ and $P_{\rm CMB,3\,pols}-P_{\rm e,3\,pols}$ both are positive due to Eq. (6.25) as well as [11] Eqs. (6.38), (6.39), and (6.40). This means that $P_{\rm e}(T_0)$ must be negative

[10] Components of the perfect-fluid thermal energy-momentum tensor $\theta_{\mu\nu}$ such as the pressure P or the energy density ρ are bilinear functionals of the fundamental field-strength tensor $F_{\mu\nu}$. Therefore, mixing coefficients $\sin\theta_{\rm W}$ or $\cos\theta_{\rm W}$ appear in squared form.
[11] We identify:

$$\begin{aligned} P_{\rm CMB,3\,pols}(T) &= -12\frac{\kappa^4(\Lambda_{\rm e}\lambda)^4}{(2\pi)^6}\tilde P(2a(\kappa^{-1}\lambda))\,,\\ P_{\rm CMB,gs}(T) &= -2\kappa^3\Lambda_{\rm e}^4\lambda\,,\\ P_{\rm e,3\,pols}(T) &= -12\frac{(\Lambda_{\rm e}\lambda)^4}{(2\pi)^6}\tilde P(2a(\lambda))\,,\\ P_{\rm e,gs}(T) &= -2\Lambda_{\rm e}^4\lambda\,. \end{aligned} \tag{6.33}$$

which, in turn, implies that $T_0 \le T_{0,\mathrm{e}}$. According to [43], one has

$$T_{0,\mathrm{e}} = 1.32\, T_{c,\mathrm{e}} \quad \text{or} \quad \lambda_{0,\mathrm{e}} = 1.32\, \lambda_{c,\mathrm{e}} = 18.31\,. \tag{6.34}$$

Because of Eqs. (6.32), (6.25) and (6.34), we may to a very good approximation use the asymptotic value

$$q_{\mathrm{CMB}} = \frac{4\pi}{e(\kappa^{-1}\lambda_0)} \approx \sqrt{2} \tag{6.35}$$

in Eq. (6.27). Thus, we have

$$\tan\theta_{\mathrm{W}}(\lambda_0) = \frac{e(\kappa^{-1}\lambda_0)}{e(\lambda_0)} \approx \frac{\sqrt{8}\pi}{e(\lambda_0)}\,. \tag{6.36}$$

Substituting Eq. (6.36) in Eq. (6.31), we finally arrive at

$$\begin{aligned} 0 &= P_{\mathrm{bulk}}(T_0) \\ &= \left(1-\sin^2\theta_{\mathrm{W}}(\lambda_0)\right)\, P_{\mathrm{e}}(T_0) + \sin^2\theta_{\mathrm{W}}(\lambda_0) P_{\mathrm{CMB}}(T_0) \\ &= \left(1 - \frac{e^2(\kappa^{-1}\lambda_0)}{e^2(\lambda_0)+e^2(\kappa^{-1}\lambda_0)}\right) P_{\mathrm{e}}(T_0) \\ &\quad + \frac{e^2(\kappa^{-1}\lambda_0)}{e^2(\lambda_0)+e^2(\kappa^{-1}\lambda_0)} P_{\mathrm{CMB}}(T_0) \\ &\approx \left(1 - \frac{8\pi^2}{e^2(\lambda_0)+8\pi^2}\right) P_{\mathrm{e}}(T_0) + \frac{8\pi^2}{e^2(\lambda_0)+8\pi^2} P_{\mathrm{CMB}}(T_0)\,. \end{aligned} \tag{6.37}$$

Explicitly, the pressures $P_{\mathrm{e}}(T_0)$ and $P_{\mathrm{CMB}}(T_0)$ are given as [31]

$$\begin{aligned} P_{\mathrm{e}}(T_0) &= -\Lambda_{\mathrm{e}}^4 \bar{P}(\lambda_0, a(\lambda_0)) \\ P_{\mathrm{CMB}}(T_0) &= -\kappa^4\Lambda_{\mathrm{e}}^4 \bar{P}(\kappa^{-1}\lambda_0, a(\kappa^{-1}\lambda_0))\,, \end{aligned} \tag{6.38}$$

where

$$\bar{P}(\lambda, a(\lambda)) \equiv \frac{2\lambda^4}{(2\pi)^6}\left[2\tilde{P}(0) + 6\tilde{P}(2a)\right] + 2\lambda \tag{6.39}$$

and

$$\tilde{P}(y) \equiv \int_0^\infty \mathrm{d}x\, x^2 \,\log\left[1 - \exp\left(-\sqrt{x^2+y^2}\right)\right] \;. \tag{6.40}$$

The advantage of writing $P_{\mathrm{CMB}}(T_0)$ as in Eq. (6.38) is that the precise value of $\kappa \ll 1$ is not required to be known in order to extract λ_0 and $e(\lambda_0)$ from the condition in Eq. (6.37). This is due to the rapid vanishing of the quantity $a(\lambda)$ as $\lambda \to \infty$, see Eq. (6.5). Solving Eq. (6.37) for λ_0 numerically, we have

$$\lambda_0 = 16.3 = 1.18\,\lambda_{c,\mathrm{e}}\,, \quad e(\lambda_0) = 14.88\,. \tag{6.41}$$

Indeed, due to mixing the zero λ_0 of the bulk pressure turns out to be smaller than $\lambda_{0,\mathrm{e}}$, compare Eqs. (6.34) and (6.41).
Finally, solving Eq. (6.36) for $\theta_{\mathrm{W}}(\lambda_0)$ subject to Eq. (6.41), we obtain

$$\theta_{\mathrm{W}}(\lambda_0) \equiv \theta_{\mathrm{W}}(Q=0) = \arctan\frac{\sqrt{8}\pi}{e(\lambda_0)} = 30.84^\circ\,, \tag{6.42}$$

where, with a slight abuse of notation, the argument $Q = 0$ indicates that the system is probed at vanishing four-momentum transfer (resolution referring to the maximum of the moduli of the Mandelstam variables s, t, u that contribute to the probing process). This is close to the experimentally obtained value of the Weinberg angle. In [144] the value of θ_{W} was extracted from the parity-violating asymmetry in fixed target electron-electron scattering at a resolution of $Q = 0.1612\,\mathrm{GeV}$ as

$$\theta_{\mathrm{W}}(Q = 0.1612\,\mathrm{GeV}) = 29.23^\circ \cdots 29.40^\circ\,. \tag{6.43}$$

The latest particle data group quotation of θ_{W}, measured at Q equal to the mass m_Z of the Z-boson, is [143]

$$\theta_{\mathrm{W}}(Q = m_Z = 90.2\,\mathrm{GeV}) = 28.73^\circ \cdots 28.75^\circ\,. \tag{6.44}$$

Note the tendency of a mild increase of θ_W from Eq. (6.44) to Eq. (6.43) for vastly decreasing values of resolution (logarithmic running). The thermodynamically determined value of θ_W in Eq. (6.42) is our prediction for $\theta_W(Q=0)$. The Weinberg angle at $Q=0$ appears to be determined quite accurately from bulk thermodynamics without having to make explicit assumptions on the finite-volume physics of the droplet's thick boundary shell, where $SU(2)_e$ and $SU(2)_{CMB}$ and all phases of the former theory mix. Implicitly, we assume, however, that the pressure of this shell as exerted onto the bulk is zero. Note that for an infinite-volume system, where stability constraints are irrelevant, we have $\theta_W(\lambda) = 45°$ for the mixing of the theories $SU(2)_e$ and $SU(2)_{CMB}$ in the conformal limit $\lambda \gg \lambda_0$.

6.5.3 Value of α

Considering gauge-theory mixing inside the deconfining-phase bulk of the droplet and assuming the external, effective gauge field, which probes the droplet charge, to reside in $SU(2)_e$, we may use Eq. (6.23) to obtain

$$\alpha = \frac{q^2}{4\pi} = \frac{\left(-\frac{27}{64} q_e(\lambda_0)\cos\theta_W\right)^2}{4\pi}\,. \tag{6.45}$$

Appealing to the value of θ_W in Eq. (6.42) and to the value of $e(\lambda_0)$ in Eq. (6.41) yields

$$\alpha^{-1} = 134.3\,. \tag{6.46}$$

This deviates by only 2 % from the experimental value of Eq. (6.1).
However, in contrast to the determination of the Weinberg angle θ_W, which is a quantity that depends only on the stability of bulk thermodynamics in a finite volume ($P_{\rm bulk} = 0$) and on the universality of monopole charges, the determination of the fine-structure constant α hinges in addition on phase mixing *within* $SU(2)_e$ and mixing of the gauge groups $SU(2)_e$ and $SU(2)_{CMB}$ inside the thick boundary shell. For this boundary shell, defined by a vanishing monopole charge in $SU(2)_e$ within the radial extent $\bar{r} \le r \le r_0$ ($\bar{r} = \xi r_0$ the mean radius w.r.t. the a priori distribution of monopole location), we also had to assume vanishing pressure. To understand the physics of the thick boundary shell better is the subject of future work. An according improvement of the mirror-charge construction used so far to define the droplet's charge but also the effect of droplet revolution on the probability density ρ in Eq. (6.15) could decrease the difference between the value of α in Eq. (6.46) and its experimental value in Eq. (6.1).

6.5.4 Impact of mixing on mass formula and length-scale hierarchy in powers of α

A modelling of the mixing effects within the thick boundary shell is beyond the scope of the present article. Therefore, in what follows, we content ourselves with estimating $T_{c,e}$ and the droplet radius r_0 under gauge-theory mixing, and we assume that the energy densities are the same within the droplet's thick boundary shell and the droplet's bulk. Let us determine the shift in Yang-Mills scale Λ_e when changing the model of the free electron based on pure $SU(2)_e$ to a model that invokes mixing of $SU(2)_e$ and $SU(2)_{CMB}$. For a pure $SU(2)_e$ model, the electron's rest-mass m_e, which coincides with the lowest circular breathing frequency $\omega_0 = e(\lambda_{0,e})\,H_\infty(T_0)$ of the monopole [120, 119, 43], is given as (re-writing Eq. (5) of [169])

$$\begin{aligned} m_e &= e(\lambda_{0,e})\,H_\infty(T_0) = m_m(T_0) + \frac{4\pi}{3} r_0^3 \rho(T_0) \\ &= H_\infty(T_0)\left(\frac{4\pi}{e(\lambda_{0,e})} + \frac{64\pi}{3\lambda_{0,e}^4}\chi^3\bar{\rho}(\lambda_{0,e})\right)\,, \end{aligned} \tag{6.47}$$

where the dimensionless plasma energy density $\rho(T_0)/\Lambda_e^4 \equiv \bar{\rho}(\lambda, a(\lambda))$ is defined as

$$\bar{\rho}(\lambda, a(\lambda)) \equiv \frac{2\lambda^4}{(2\pi)^6}\left[2\tilde{\rho}(0) + 6\tilde{\rho}(2a)\right] + 2\lambda\,, \tag{6.48}$$

$m_m(T_0)$ denotes the mass of a BPS monopole originating from the dissociation of a (anti)caloron of maximally nontrivial holonomy, and $\chi \equiv r_0 H_\infty(T_0) \equiv \pi r_0 T_0$. Fig. 6.6 illustrates the three phases of the ground state of $SU(2)_e$. The reason why the BPS limit is considered here is that a nontrivial-holonomy caloron sets the value of the asymptotic, adjoint Higgs field of its constituent monopole and antimonopole solely in terms of its holononmy and not dynamically by minimization of potential energy density, see [170, 171]. In Eq. (6.48), we have introduced

$$\tilde{\rho}(y) \equiv \int_0^\infty \mathrm{d}x\, x^2 \, \frac{\sqrt{x^2+y^2}}{\exp\left(\sqrt{x^2+y^2}\right)-1}\,, \tag{6.49}$$

and in Eq. (6.47) the quantity $H_\infty(T_0) = \pi T_0$ refers to the modulus of the (anti)caloron gauge-field component $A_4(r \to \infty) = a_4$, see [43]. In the case of gauge-theory mixing of $\mathrm{SU(2)_{CMB}}$ with $\mathrm{SU(2)_e}$, we generalise Eq. (6.47) to

$$\begin{aligned}\frac{m_\mathrm{e}}{H_\infty(T_0)} &= e(\lambda_0)\cos\theta_\mathrm{W} + e(\kappa^{-1}\lambda_0)\sin\theta_\mathrm{W} \\ &= \cos\theta_\mathrm{W}\frac{4\pi}{e(\lambda_0)} + \sin\theta_\mathrm{W}\frac{4\pi}{e(\kappa^{-1}\lambda_0)} + \frac{64\pi}{3\lambda_0^4}\chi^3 \\ &\times \left[\cos^2\theta_\mathrm{W}\bar{\rho}(\lambda_0, a(\lambda_0)) + \kappa^4\sin^2\theta_\mathrm{W}\bar{\rho}\left(\frac{\lambda_0}{\kappa}, a\left(\frac{\lambda_0}{\kappa}\right)\right)\right].\end{aligned} \tag{6.50}$$

Solving the second half of Eq. (6.50) for χ after appealing to Eqs. (6.41) and (6.42), we obtain

$$r_0 = 5.09\, H_\infty^{-1}(T_0)\,. \tag{6.51}$$

From Eqs. (6.51) and (6.41) we deduce

$$\frac{r_0}{|\phi|^{-1}(T_0)} = 0.155\,, \tag{6.52}$$

indicating that the droplet is contained deeply within the central region of a typical caloron or anticaloron which contributes to the emergence of the deconfining thermal ground state of $\mathrm{SU(2)_e}$. Yet, we have $r_0/\beta_0 = 1.62$ such that the radial integral in the definition of ϕ's phase reasonably well represents a sinusoidal τ-dependence, see [31], p. 127. As a consequence of Eqs. (6.41), (6.51) we have

$$r_0 = 0.622\,\Lambda_\mathrm{e}^{-1}\,. \tag{6.53}$$

With this corrected value of droplet radius r_0 due to gauge-theory mixing, compare with Eq. (6.10) for the case of pure $\mathrm{SU(2)_e}$, the ratio of screening length l_s to r_0 of Eq. (6.11) is reduced compared to the case of pure $\mathrm{SU(2)_e}$ as

$$\frac{l_s}{r_0} \sim 44.1\,. \tag{6.54}$$

Still, this is sufficiently larger than unity to justify the mirror-charge construction of Sec. 6.4.2. Recall, that such a construction requires the Coulomb nature of the static U(1) potential of the monopole away from its core region. The first part of Eq. (6.50) yields

$$\frac{m_\mathrm{e}}{H_\infty(T_0)} = 17.33\,. \tag{6.55}$$

Together with Eq. (6.51) this implies a ratio of reduced Compton length r_c to r_0 as

$$\frac{r_c}{r_0} = \frac{1}{17.33\times 5.09} = \frac{1}{88.3}\,. \tag{6.56}$$

That is, due to mixing, the core-size of the trapped monopole, which according to the first part of Eq. (6.47) is close to r_c [119], becomes even more pointlike compared to the droplet's extent than for the case of a pure $\mathrm{SU(2)_e}$ model where $r_c/r_0 = 1/52.40$. Eq. (6.55) also implies that

$$\frac{m_\mathrm{e}}{\Lambda_\mathrm{e}} = 141.82 \tag{6.57}$$

or $\Lambda_\mathrm{e} = 3.60\,\mathrm{keV}$ or $T_{c,\mathrm{e}} = 7.95\,\mathrm{keV}$.
According to Eq. (6.56), the ratio of droplet radius r_0 to Bohr radius a_0 is

$$\frac{r_0}{a_0} = \frac{r_0}{r_c}\frac{r_c}{a_0} = 88.3\frac{r_c}{a_0} = 88.3\,\alpha = 0.64\,. \tag{6.58}$$

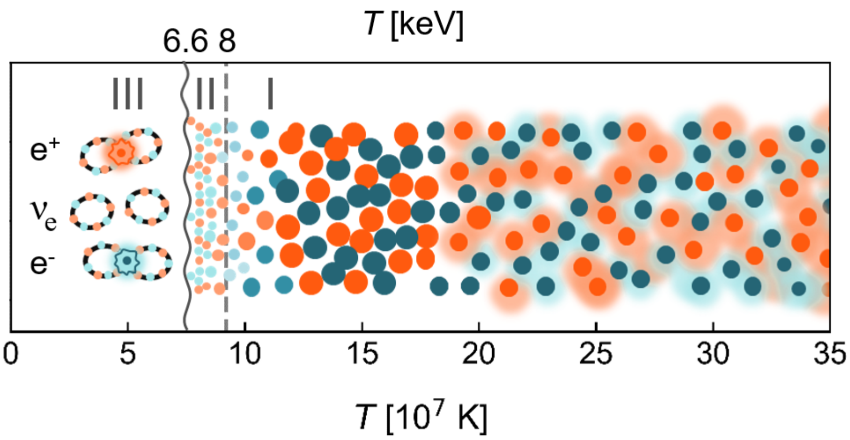

Figure 6.6: Phase diagram of $\mathrm{SU}(2)_{\mathrm{e}}$ with $T_{c,\mathrm{e}} = 0.923 \times 10^8\,\mathrm{K}$ (7.95 keV) in the infinite-volume limit. There are three distinct phases: (I) the deconfining phase, (II) the preconfining phase, and (III) the confining phase.

Such a large ratio of order unity is in line with Louis de Broglie's proposal [122] that the free electron at rest represents the oscillation of a thermal plasma of finite extent and spatially constant amplitude driven by a vibrating monopole. Namely, within the deconfining bulk of the droplet at rest, the superposition of spherical wavelets of constant frequency and wavelength but highly random phase and variable origin plausibly yield a plasma oscillation of nearly constant spatial amplitude — the basic insight of de Broglie's deduction of the electron's matter wavelength paving the way for wave mechanics [172]. Note that also outside the droplet, the spatially decaying Coulomb field a_4^3 keeps oscillating at the droplet's frequency $\omega_0 = m_{\mathrm{e}}$. This also is true of the energy density or the pressure of the plasma component due to $\mathrm{SU}(2)_{\mathrm{CMB}}$ at temperatures that locally are higher than the CMB baseline temperature within a certain, local environment of the droplet.

6.6 Discussion and Summary

In this work we have proposed the electron to be a figure-eight shaped soliton formed by a thin center-vortex loop in SU(2) Yang-Mills theory where the region of selfintersection is an extended droplet. This soliton is stable and immersed into the confining ground state of an SU(2) Yang-Mills theory of scale 3.60 keV. Moreover, the soliton is subject to the confining ground states of other Yang-Mills theories with higher scales and the Cosmic Microwave Background (CMB). In the present work, we associate the CMB with the deconfining phase of an SU(2) Yang-Mills theory of scale $\sim 10^{-4}$ eV ($\mathrm{SU}(2)_{\mathrm{CMB}}$) [31, 67].
Based on the definition of the Bohr magneton, we also link the electron's magnetic moment to revolutions of the droplet's effective charge. These revolutions are induced by the unresolved monopoles and antimonopoles moving along and constituting the center-vortex loop. The contribution of the thin vortex lines to the total mass of this soliton is negligible, see [31]. However, vortex lines may play a role in producing nonlocal interactions that magnetically correlate electrons in a 2D plane [158].

Within the bulk region of the droplet an electric monopole is trapped which internally vibrates due to kicks issued by the quantum physics of the thermal ground state [31]. This ground state locally superimposes a caloron and an anticaloron center and overlapping (anti)caloron peripheries. Under the selfconsistent assumption that the droplet's bulk can be represented by infinite-volume thermodynamics, we have derived the following statements:

(i) Bulk stability, that is, the vanishing of the thermodynamical pressure deep inside the droplet implies a mixing angle between the Yang-Mills theories $\mathrm{SU}(2)_{\mathrm{e}}$ and $\mathrm{SU}(2)_{\mathrm{CMB}}$ at one and the same temperature T_0 which practically coincides with the value of the weak mixing (or Weinberg) angle of the Standard Model of Particle Physics.

(ii) The value of the electromagnetic fine-structure constant α at vanishing energy-momentum transfer is reasonably well approximated by a mirror charge construction, suggested by the high electric conductivity of the droplet's thick boundary shell. In addition, the derivation of the value of α relies on (a) a thermodynamical $\mathrm{SU}(2)_{\mathrm{e}}$ and $\mathrm{SU}(2)_{\mathrm{CMB}}$ gauge-theory mixing plus monopole charge universality, (b) stability of the thick boundary shell by its assumed, vanishing mean pressure, and (c) the statistical average of the droplet's charge over the bulk volume w.r.t. a spatially homogeneous distribution, cut off at the mean radius (condition that the thick boundary shell is excluded as a region for positioning the isolated monopole of the $SU(2)_e$ component of the bulk plasma).

(iii) The droplet's mass formula, in generalisation of [44] now considering $SU(2)_e$ and $SU(2)_{CMB}$ gauge-theory mixing, predicts a droplet size r_0 which is comparable with the Bohr radius a_0. For the core size of the monopole r_c (the reduced Compton wave length [119, 120, 122]) we therefore obtain $r_c \sim \alpha\, r_0 \sim \alpha\, a_0 = \alpha^{-1}\, r_e$ where r_e denotes the classical electron radius. As a consequence, the monopole core indeed is an (unresolved) point particle on the scales of the droplet's extent and on the radius $|\phi|^{-1}$ of a (anti)caloron which constitutes the thermal ground state.

(iv) The Yang-Mills scale Λ_e of $SU(2)_e$ and the critical temperature $T_{c,e}$ are derived from this mass formula, applying it to the mass of the electron $m_e = 511\,\text{keV}$. One has: $\Lambda_e = 3.60\,\text{keV}$ or $T_{c,e} = 7.95\,\text{keV}$. This implies a critical temperature $T_{c',e}$ of the Hagedorn transition as $T_{c',e} = \frac{11.57}{13.87}\, 7.95\,\text{keV} = 6.63\,\text{keV}$. When the spatio-temporal design of fusion plasmas is optimised to accomplish steady-state operation, involving comparable electron temperatures (and high electron densities), these results should be taken into account in devising magnetic and inertial plasma confinement strategies.

(v) There is an environment to the stationary droplet of an extent yet to be specified which is characterised by a plasma of deconfining $SU(2)_{CMB}$ phase, slightly hotter than the CMB. This deconfining plasma vibrates at a frequency $\sim m_e$. The monopole of $SU(2)_{CMB}$ may alternate its location from the droplet's bulk region into this environment and vice versa.

Let us now briefly discuss possible links of these results to phenomena discussed in the literature. In our present approach, we would interpret the particle at rest as the droplet whose vibrating (standing) external Coulomb potential is transformed into a propagating wave upon boost [146], giving rise to observable (self-)interference effects to statistically determine the droplet's position [173]. As mentioned in the introduction, we do expect a considerable impact of the thermodynamical approach to the electron proposed here in better understanding collective plasma phenomena at electron temperatures starting at around $T \sim T_c = 6.6\,\text{keV}$ in experiments with magnetic plasma confinement which were not predicted by conventional magneto-hydrodynamics. These could include the formation of an edge transport barrier associated with a pressure pedestal, edge-localised modes, magnetic instabilities, and ion-orbit losses in the high-confinement mode [174, 175]. Note that the electron plasma density n_e in conventional tokamaks and stellerators is $n_e \sim 10^{20}\,\text{m}^{-3}$ while a macroscopically stabilised plasma droplet at $T = T_0 = 9.38\,\text{keV}$ with an energy density of $\rho(T_0) = 1.77 \times 10^4\,\text{keV}^4$ represents a number density of percolated electrons of $n_e \sim 1.79 \times 10^{28}\,\text{m}^{-3}$. Therefore, eight orders of magnitude in electron density are missing in order to achieve a macroscopically stabilised plasma state. Still, the above-mentioned effects at much lower electron densities may point to the here-proposed model of the electron.

An important question, which arises due to a modelling of the electroweak parameters θ_W and α that apparently is particular to the electron as a thermal and stable quantum particle, concerns these parameters' experimentally enshrined universality across the electroweak interactions of all leptons. As for the unstable, charged leptons μ and τ the reason why their charge is identical to that of the electron would be as follows. As soon as a τ or a μ lepton is created at rest, the according droplets in $SU(2)_{CMB}\times SU(2)_e\times SU(2)_\mu$, see Fig. 6.7 a), and in $SU(2)_{CMB}\times SU(2)_e\times SU(2)_\mu\times SU(2)_\tau$, respectively, disperse the energies invested in surplus to their quantum mass, defined by a generalisation of Eq. (6.50), into their surroundings and can only trap an $SU(2)_\mu$ or an $SU(2)_\tau$ monopole, respectively, see Fig. 6.7 b) for the muon droplet. The other monopoles are free to leave or re-enter this droplet. In case of $SU(2)_{CMB}$ this ab initio dispersion of energy does not define new phase boundaries since the CMB represents the deconfining phase (likely very close to the deconfining-preconfining transition [31]). In case of $SU(2)_\mu$ or $SU(2)_e$ new droplets are formed that embed the initial droplet, see Fig. 6.7 c) for the case of $SU(2)_e$. This process of (cascading) droplet formation invokes formerly single, round-point center-vortex loops from confining-phase ground states to define the respective droplets as their stabilised regions of self-intersection: single center-vortex loops thus turn into figure-eight shaped center-vortex loops. In the Standard Model of Particle Physics, this subprocess refers to the absorption of an antineutrino, compare Fig. 6.7 b) and Fig. 6.7 f). After quantum equilibration, the initial droplets' bulks exhibit defined mixing angles for four or three deconfining SU(2) Yang-Mills theories by two or three charge-universality conditions (in general: in the droplet representing the Nth lepton family there are N charge-universality conditions fixing the N independent components of a unit vector in an $(N+1)$-dimensional Euclidean space or N mixing angles), respectively, and a defined temperature by the condition of vanishing bulk pressure. Since the according leptons are unstable, no (temporally) coherently propagating waves in the Cartan algeba's of $\mathrm{SU(2)}_\tau$ and $\mathrm{SU(2)}_\mu$ exist that could externally probe these charges and the magnetic moments that relate to the center-vortex loops extending from μ- and τ-droplets. Therefore, even though the electron droplet contains μ- and τ-droplets and their respective, trapped monopoles, only the trapped monopole and the magnetic moment provided by the center-vortex loop in $\mathrm{SU(2)}_\mathrm{e}$ are seen externally. For the charge of μ and τ leptons, we thus are back at the derivation of the charge of an electron (or fine-structure constant α), see Sec. 6.5.3. Their decays can be figured as processes, where embedded droplets of much smaller radii $r_{0,\mu} \sim \frac{m_{0,\mathrm{e}}}{m_{0,\mu}} r_{0,\mathrm{e}}$ and $r_{0,\tau} \sim \frac{m_{0,\mathrm{e}}}{m_{0,\tau}} r_{0,\mathrm{e}}$ ($m_{0,i}$, $r_{0,i}$ the rest mass, droplet radius of charged lepton i with $i = \mathrm{e}, \mu, \tau$), subject to gauge theory mixing in $\mathrm{SU(2)}_\mathrm{CMB}\times\mathrm{SU(2)}_\mathrm{e}\times \mathrm{SU(2)}_\mu$ and $\mathrm{SU(2)}_\mathrm{CMB}\times\mathrm{SU(2)}_\mathrm{e}\times\mathrm{SU(2)}_\mu\times\mathrm{SU(2)}_\tau$, respectively, by eventual contact with the thick boundary shell of an embedding droplet (for the τ lepton droplet these embedding droplets are the droplets of $\mathrm{SU(2)}_\mu$ and $\mathrm{SU(2)}_\mathrm{e}$, for the μ lepton droplet this is the droplet of $\mathrm{SU(2)}_\mathrm{e}$) dissolve to feed their high energy densities and massive, trapped monopoles, locally into those of the nonthermally distorted respective boundary shells. This local investment of energy into the boundary shell can be thought of as a transient excitation of a $W^\pm$-boson in the Standard Model of Particle Physics. As a result, an energetic neutrino is emitted: a figure-eight shaped center-vortex loop looses its droplet together with the trapped monopole when interacting with the thick boundary shell to transform into a single center-vortex, see Fig. 6.7 d) for μ-decay and Fig. 6.7 f) the according subprocess in the Standard Model of Particle Physics.

To relate hadrons to pure Yang-Mills thermodynamics is much harder than for leptons. Hadrons are complex quantum systems of confined (anti)quarks that are effectively and efficiently described by Quantum Chromodynamics [176, 76]. To address the emergence of (anti)quarks as electrically fractionally charged particles within pure Yang-Mills theories of one and the same electric-magnetic parity is impossible. Rather, a derivation of quark properties probably would require an interplay and mixing of electric-magnetic dual SU(3) Yang-Mills models to allow a version of the fractional Quantum Hall effect [177, 178, 179] to take place.

In closing, we would like to state clearly that there cannot be any doubt that the Standard Model of Particle Physics represents a milestone development in accurately and efficiently describing the interactions of leptons and hadrons. Essentially, this theory rests on well organised weak-coupling expansions that implement the gauge principle in a perturbatively consistent way [180, 181] and that are applicable to any so far probed energy-momentum transfer. A thermodynamical approach to the *interactions* of leptons and hadrons in terms of pure Yang-Mills theory is inferior to the Standard Model. What the Standard Model is incapable of delivering though is a ground-state structure doing justice to cosmological observations [182, 183], to provide a useful framework for thermal and nonthermal phase transitions [184], a postdiction of the absolute values of (some of) its dimensionless parameters, and a deeper grasp of the nature of particle-matter-wave duality concerning charged leptons. As the present work intended to demonstrate, a computation of two of the Standard Model's dimensionless parameter values appears to be feasible. The here-proposed venue is still far from addressing other in-built features of the Standard Model such as parity violation of the weak interactions, a derivation of the electron's magnetic moment including the anomalous quantum behaviour, a quantitative grasp of the entries of the CKM matrix, or the fractional electric charges of quarks. We hope to gain more insight into these problems in the future.

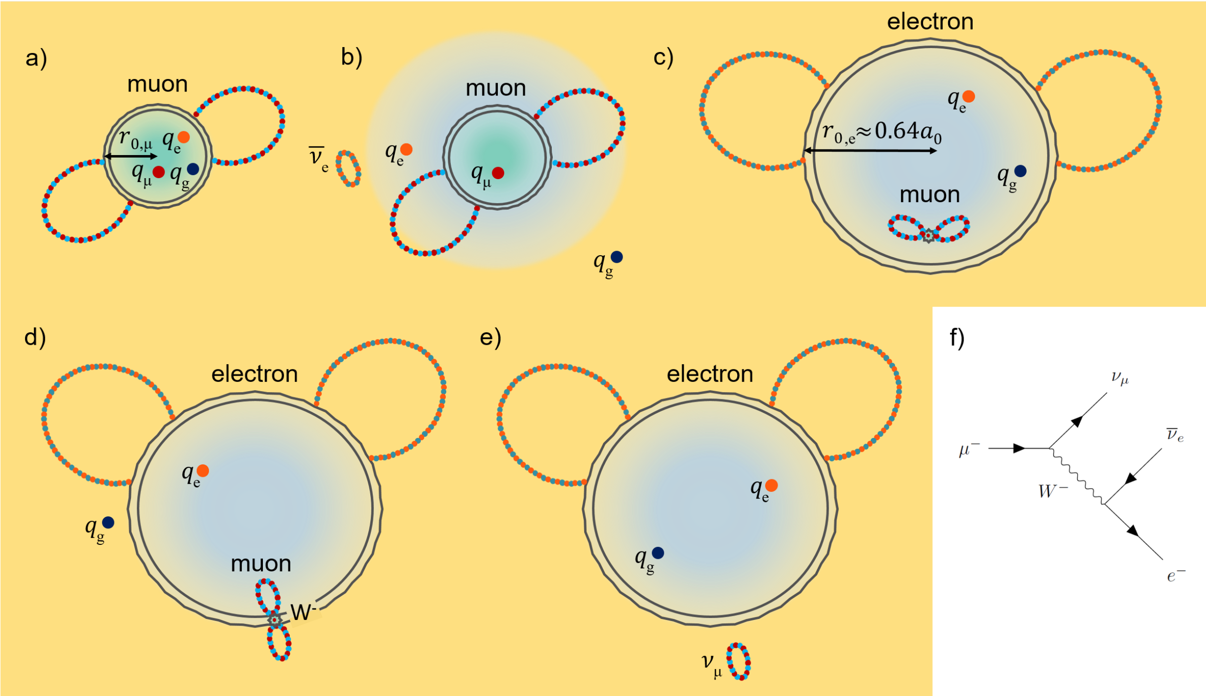

Figure 6.7: Creation and decay of a muon: **a)** A not yet quantum equilibrated muon droplet, defined as the selfintersection region of a center-vortex loop, is created within the confining phase of $SU(2)_\mu$. This droplet contains three types of monopoles: q_μ, q_e, q_g. **b)** Energy in surplus to the muon quantum mass is dissipated into the surroundings. The monopoles q_e, q_g are not trapped by the thick boundary shell of the muon droplet (turquoise) and are free to leave or re-enter. A single center-vortex loop of $SU(2)_e$ is fused with q_e to form a figure-eight shaped object subject to a new electron droplet. The monopole q_g (dark blue) in $SU(2)_{CMB}$ outside the electron droplet, at the CMB's present temperature, would be reduced to a massless and zero-charge point particle [67]. **c)** The size of the electron droplet (blue) is comparable with the Bohr radius a_0 and contains the muon droplet. **d)** The muon droplet is dissolved by the thick boundary shell of the electron droplet, rendering q_μ an irrelevant, massless, and zero-charge point particle which casts a figure-eight shaped center-vortex loop into a single one: the muon neutrino ν_μ. The localised energy injected to the boundary shell thus is a transient process which can be interpreted as a W^- boson in the Standard Model of Particle Physics. **e)** The final states of muon decay are the electron and ν_μ. **f)** Feynman-diagram of muon decay in the Standard Model of Particle Physics.

Data availability

The Python notebook which has been used for the calculations in this paper is available on GitLab[12].

Acknowledgements

RH acknowledges helpful discussion with Manfried Faber and Thierry Grandou, and he wishes to thank his wife Karin Thier for her patience and enduring support. JM thanks Karl-Heinz Kampert and Alexander Sandrock for insightful discussions and useful comments. JM's work is supported by the Vector Foundation under grant number P2021-0102 and partially by SFB 1491.

Contributions of the author JM

Contributions include manuscript writing, calculation and analysis, figure preparation, methodology, validation, funding acquisition, and review & editing.

[12]`https://git.uni-wuppertal.de/meinert/electroweak-parameters-from-yang-mills-thermodynamics`

this page is intentionally left blank

7 The Dark Sector in YMTD

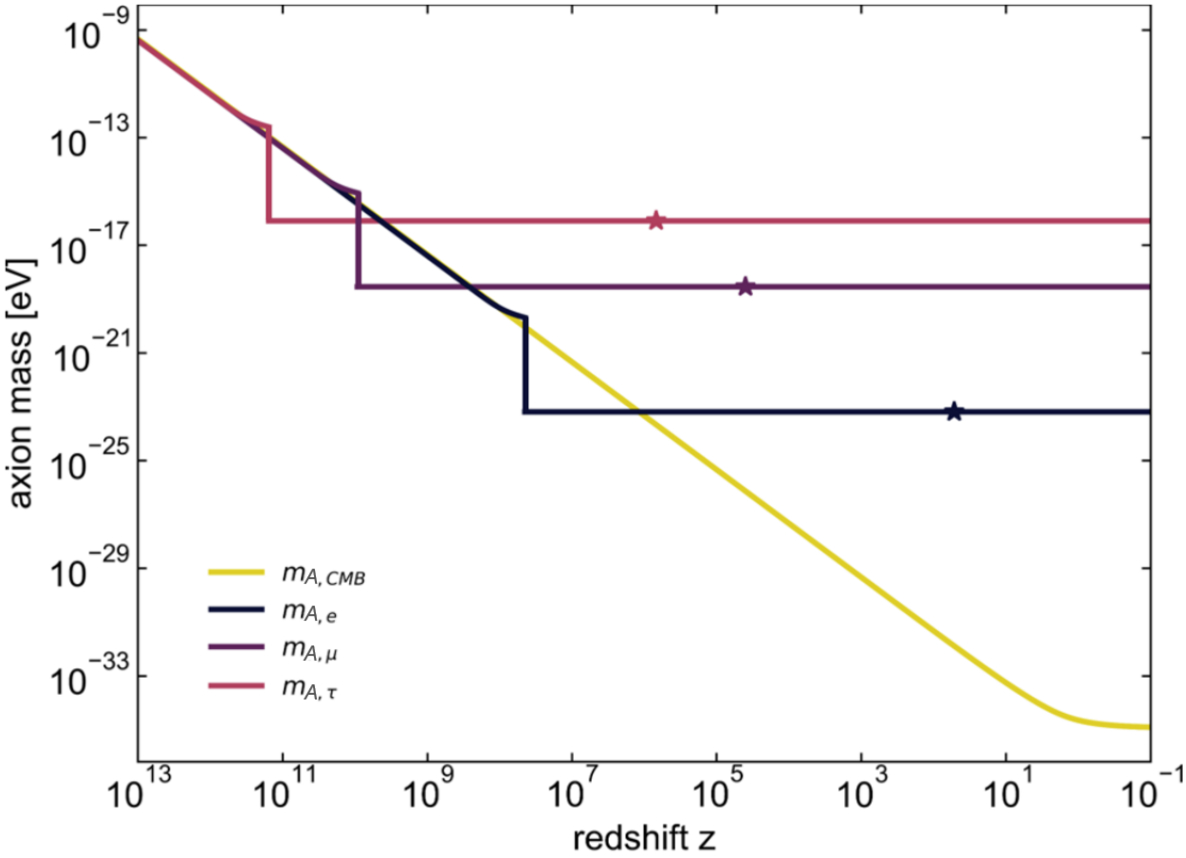

Figure 7.1: Axions have a temperature dependent mass $m_A \propto T^2/M_P$ in deconfinement phases of SU(2) Yang-Mills thermodynamics; in the confining phase, the axion mass is constant. An axion associated with the Yang-Mills scale potentially implying the third lepton family possesses a mass $m_{A,\tau}(z=0) \approx 8 \times 10^{-17}$ eV (ultramarine). Accordingly, for the second lepton family, one would have $m_{A,\mu}(z=0) \approx 3 \times 10^{-19}$ eV (orange). An axion that associates with the first lepton family carries a mass $m_{A,e}(z=0) \approx 7 \times 10^{-24}$ eV (green), and an axion, which couples to a Yang-Mills theory potentially describing the CMB would possess a mass $m_{A,\mathrm{CMB}}(z=0) \approx 10^{-35}$ eV (yellow).

This chapter is based on the article "Axion mass and the ground state of deconfining SU(2) Yang-Mills thermodynamics" [6] by Ralf Hofmann, Dmitry Antonov and JM and the conference proceedings [9].

Contents

7.1 Introduction **82**

7.2 Axion Mass Squared via The Veneziano-Witten Formula at Finite Temperature **84**

7.3 The Veneziano-Witten Integral for Deconfining SU(2) YMTD **84**

7.3.1 The topological susceptibility χ on a Harrington-Shepard (anti)caloron 84

7.3.2 Do thermal quasiparticle fluctuations contribute to χ? 87

7.4 Cosmological Implications: Bose Condensation of Axions **87**

7.5 Summary and Outlook **89**

Ralf Hofmann[1], **Janning Meinert**[2,1] **and Dmitry Antonov**[3]

[1]Institut für Theoretische Physik, Universität Heidelberg Philosophenweg 12, D-69120 Heidelberg
[2]Bergische Universität Wuppertal, Department of Physics, Gaußstraße 20, D-42103 Wuppertal
[3]Formerly at Universidade de Lisboa, Departamento de Fisica, Av. Rovisco Pais, P-1049-001 Lisbon

Abstract

For the deconfinement phase of an SU(2) Yang-Mills theory, we compute the axion mass m_A by appealing to the Veneziano-Witten formula. The topological susceptibility χ arises (i) from a precisely computable thermal ground-state contribution due to a center of a relevant (anti)caloron and (ii) from contributions due to free thermal quasi-particles in the effective theory. Both, (i) and (ii) are derived by using standard Euclidean thermal field theory techniques. While contribution (i) is positive and $\propto T^4$, contribution (ii) is negative, as demanded by reflection positivity, but negligible compared to contribution (i). As a consequence, practically from the critical temperature T_c onwards a real-valued axion mass $m_A(T) = \sqrt{\frac{2}{3}\pi}\frac{T^2}{M_P}$ emerges when the Peccei-Quinn scale is assumed to be the Planck mass M_P, independently of the Yang-Mills scale that the axion associates with. We discuss why our results deviate from those found in the dilute instanton gas and interacting instanton liquid approximations and from results obtained in lattice simulations. Assuming the universe's dark sector to be based on such ultralight axion species, which are nonrelativistic for $T \ll M_P$, we investigate the cosmological conditions for their global Bose condensation as the very early universe cooled to temperatures of the order of 10^9 eV.

7.1 Introduction

The temperature (T) dependence of the topological susceptibility χ in the deconfinement phase of an SU(2) or SU(3) Yang-Mills theory was estimated by various methods: dilute instanton gas [185], instanton liquid [186], lattice simulations [187, 188, 189, 190, 191, 192, 193], and model of the stochastic vacuum [194]. Knowing the T-dependence of χ precisely is important for understanding cosmological models whose (fuzzy) dark-matter sector is based on the quantum dynamics of ultralight axions [195, 196, 197, 198, 199, 200, 201].

Based on $\chi(T)$, the Veneziano-Witten formula can be employed to calculate the axion mass $m_A(T)$. Originally, this formula was proposed as an estimate for the mass of the pseudoscalar η'-meson in QCD. For cosmologically stable axions, however, the required smallness of axion masses and decay constants compared to particle physics scales could originate from the extreme hierarchy between the Planck mass M_P (the Peccei-Quinn scale), at which regime gravitational attraction [202] may condense massless fermion flavours [203, 48] and generate a massless, pseudoscalar, flavour-singlet field ϕ, and the Yang-Mills scales of pure SU(2) or SU(3) theories which associate with visible matter and radiation described by the Standard Model of Particle Physics in an evolving universe [5, 112, 31]. These hierarchically-smaller-than-M_P Yang-Mills scales also may have, by some as of yet unknown mechanism, been determined by physics of the Planckian regime. As in [48], we thus consider a dynamical breaking of the global symmetry $U(1)_A$ [204, 205] at the Planck scale. Gauge field configurations that are assumed to saturate the topological susceptibility χ, see Eq. (7.1), are usually taken to be *instantons* in the literature, subject to a finite-temperature electric Debye screening to modify the $T = 0$ instanton density. This only allows for instanton radii $\rho < (\pi T)^{-1}$ to contribute to the model partition function [206]. The results for χ, when computed in a dilute gas of instantons (DIGA) [185] or in a liquid of instantons (IILA) [186], have in turn inspired fit models in lattice simulations of χ [187]. Note that these instanton based approaches do not resemble the situation of a thermal ground state [31] which (i) is composed of spatially densely packed Harrington-Shepard (HS) *calorons* or *anticalorons* [207], exhibiting an intrinsic T-dependence of the topological charge density Q per isolated field configuration, and which (ii) is dominated by caloron radii $\rho \propto T^{1/2}$ [31]. Point (ii) implies that properly capturing the topological charge of a relevant gauge-field configuration requires enormous spatial volumes at high T which are not available in lattice simulations [208, 31]. Indeed, Fig. 7.2 depicts the ratio of the lattice size $L = 2/T_c$, employed in an SU(3) simulation [188], and the size of the relevant caloron radius $\rho = \frac{\lambda_c^{3/2}}{2\pi T_c}\left(\frac{T}{T_c}\right)^{1/2}$ [31] as a function of T/T_c for both SU(2) and SU(3). Therefore, throughout the deconfinement phase ($T \geq T_c$) the lattice size L

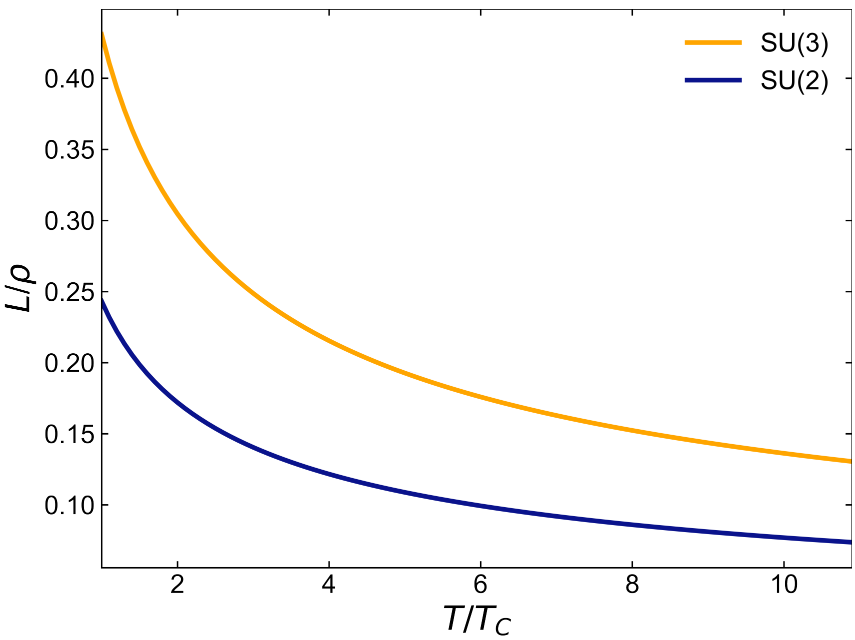

Figure 7.2: The ratio of lattice size $L = 2/T_c$, as employed in [188], and the caloron radius $\rho = \frac{\lambda_c^{3/2}}{2\pi T_c}\left(\frac{T}{T_c}\right)^{1/2}$ for SU(2) (ultramarine) and for SU(3) (orange). This caloron radius is relevant in the emergence of the thermal ground state [31]. For SU(2) and SU(3) the dimensionless critical temperatures ($\lambda \equiv 2\pi T/\Lambda$) are given as $\lambda_c = 13.87$ and $\lambda_c = 9.475$, respectively.

never accommodates the center of a relevant caloron: the spatial lattice simply falls through the topological charge distribution. That is, the integral $\int d^4x\, Q(x)$ in Eq. (7.1) below[1] over the lattice volume is not saturated. The rapid power-law decay of $\chi \sim a\, T^{-b}$ suggested for the gauge group SU(3) by DIGA [185] or by IILA [186], (for the SU(3) case b ranges as $4.9 \leq b \leq 9$, depending on the number of fermion flavours in the simulation, and there is disagreement in the normalisation a by a factor of ten between DIGA and fits to lattice results [188]) could therefore well be an artefact of the assumed diluteness of the topological charge carriers, a neglect of their intrinsic T dependence (instantons are not periodic in the Euclidean time coordinate x_4), and the above mentioned, perturbatively motivated, T dependent constraint on instanton scale on the modelling side. As mentioned above, lattice simulations [187, 188] suffer from severe finite-spatial-volume constraints, see also [193] for an insightful discussion.

The purpose of the present paper is to compute the T dependence of χ for deconfining SU(2) Yang-Mills thermodynamics and to discuss some implications for a modelling of the cosmological dark sector, based on a T dependence of the axion mass derived from the right-hand side of the Veneziano-Witten formula (VWF). Our work is organised as follows: In Sec. 7.2 we briefly review the VWF for the axion mass and comment on its interpretation in the realm of cosmology. The computation of the topological susceptibility χ, by far dominated by the spatial center of a HS caloron or anticaloron, relevant for the emergence of the thermal ground state of deconfining SU(2) Yang-Mills thermodynamics, is carried out in Sec. 7.3. Here we will show that, in contrast to lattice and DIGA/IILA modelling and as a result of the dense spatial packing of (anti)caloron centers in the deconfining thermal ground state as well as the rapid, power-law rise of the caloron scale parameter with T, the topological susceptibility χ evolves as $\chi = a\, T^4$ for $T \gg T_c$. This can be expected from dimensional analysis and, motivated by perturbative asymptotic freedom at $T = 0$ [75, 76], the irrelevance of the Yang-Mills scale Λ at large T [193]. Confirming this expectation, we compute the factor of proportionality to be $a = 2\pi^2/3$ for an SU(2) Yang-Mills theory in terms of an effective contact term in the topological charge correlation. We also show that the (negative) contribution of lower spatial resolutions to the right-hand side of VWF, which can be computed in the effective theory [31] in terms of a non-contact term, are negligible. In Sec. 7.4 we indicate cosmological implications for very high redshifts in a model of the dark sector where the present dark matter and dark energy are related to selfgravitating depercolated and global condensates of ultralight axions, respectively. More

[1]Since the correlator of Q is computed on one field configuration only — a Harrington-Shepard caloron — it naturally factorises into a local and a nonlocal part. Note that the contribution and weight of the anticaloron is identical, and therefore the average over both caloron and anticaloron reduces to the caloron contribution.

specifically, cosmological dark matter requires such condensates to be spatially confined to subgalactic scales [195, 200, 41] (fuzzy dark matter) while dark energy requires a superhorizon sized axion condensate [41]. Finally, we summarise our results and present an outlook on future research in Sec. 7.5. Throughout the paper we work in supernatural units: $\hbar = k_B = c = 1$ where $\hbar$ denotes Planck's (reduced) quantum of action, k_B is Boltzmann's constant, and c refers to the speed of light in vacuum.

7.2 Axion Mass Squared via The Veneziano-Witten Formula at Finite Temperature

The VWF for the mass of the $\mathrm{U}(1)_A$ Goldstone field A in QCD, defined on $\mathbf{R}^4$ and subject to gauge group $\mathrm{SU}(N_c)$ as well as N_f massless fundamentally charged fermion flavours, reads [209, 210]

$$\lim_{N_c\to\infty} \frac{m_A^2 f^2}{2N_f} = \lim_{N_c\to\infty} \int \mathrm{d}^4x \langle Q(x)Q(0)\rangle_T \equiv \chi\,, \tag{7.1}$$

where the topological charge density $Q(x)$ is given as

$$Q(x) \equiv \frac{1}{64\pi^2}\,\epsilon_{\mu\nu\rho\sigma}F^a_{\mu\nu}F^a_{\rho\sigma} \equiv \frac{1}{32\pi^2}\,F^a_{\mu\nu}\tilde{F}^a_{\mu\nu}\,. \tag{7.2}$$

Here, $\langle\cdots\rangle_T$ denotes the canonical ensemble average in *pure* $\mathrm{SU}(N_c)$ Yang-Mills thermodynamics, and greek indices takes on values 4,1,2,3. In the present work, we assume with [185, 186, 187, 206, 188, 189, 190, 191, 192, 193] the validity of Eq. (7.1) in the deconfinement phase of Yang-Mills thermodynamics at finite temperature ($T > 0$).
In computing the T dependence of the axion mass m_A, the large N_c limit is relevant to those $\mathrm{SU}(2)_i$ or $\mathrm{SU}(3)_j$ subgroups of $\mathrm{SU}(N_c)$ only (associated with a Yang-Mills scale Λ_i or Λ_j) which are in their deconfinement phases. We will show in Sec. 7.3.2 that for such Yang-Mills theories practically only the *thermal ground state* [31] contributes to the right-hand side of Eq. (7.1). In applying SU(2) Yang-Mills thermodynamics to cosmology, the simulated evolution of the Cosmic Microwave Background (CMB) [211], initialised at a redshift of $z \sim 10^9$ and terminating today ($z = 0$), requires a single such SU(2) theory only [31, 5]: $\mathrm{SU(2)_{CMB}}$ with $\Lambda_{\mathrm{CMB}} \sim 10^{-4}\,\mathrm{eV}$ [67]. According to [48] we may therefore fix in Eq. (7.1) $\lim_{N_c\to\infty} f^2/(2N_f) \sim M_P^2$ for $N_f \gg 1$ where M_P denotes the Planck mass $M_P = 1.22 \times 10^{19}\,\mathrm{GeV}$.

7.3 The Veneziano-Witten Integral for Deconfining SU(2) YMTD

7.3.1 The topological susceptibility χ on a Harrington-Shepard (anti)caloron

In this section, we compute the short-distance contribution to the axion mass squared, relying on Eq. (7.1), which represents a contact term in the effective theory [31]. In the deconfinement phase, the topological susceptibility χ of Eq. (7.1) originates from an HS (anti)caloron center [207] in the thermal ground state (a thermal quantum vacuum [31]. Thereby, HS (anti)caloron centers are densely packed spatially, subject to overlapping peripheries. There is no winding in these peripheries. Thus, the ground-state portion of $\langle Q(x)Q(0)\rangle_T$ is computed on a single caloron center.
At finite temperature, the spacetime average of $Q(x)$ is over the Euclidean cylinder $S_1 \times \mathbf{R}^3$, $x_4 \equiv \tau, x_i = r\hat{x}_i$ $(i = 1, 2, 3)$ where $\hat{x}$ is a unit vector in $\mathbf{R}^3$ and $r =\mid \mathbf{x} \mid\leq\mid \phi \mid^{-1}$, see Fig. 7.3.
Since the right-hand side of Eq. (7.1) is quadratic in Q and since we *average* over the contribution of an HS caloron and an HS anticaloron [31] the thermal ground-state part of $\langle Q(x)Q(0)\rangle_T$ is represented by an HS caloron which, due to spatial isotropy, spatially is centered at $r = 0$ (peak position of the HS caloron's action density).
When expressing the field strength $F^a_{\mu\nu}$, expanded into a basis t^a $(a = 1, 2, 3)$ of the Lie algebra su(2) such that $\mathrm{tr}\, t^a t^b = \frac{1}{2}\,\delta^{ab}$, in terms of $O(4)$ scalar and tensor valued functionals $P(x)$ and $P_{\mu\nu}(x)$ of the caloron prepotential $\Pi(x)$ we follow the convention of [212]. Namely, in singular gauge one has for the gauge field of an HS caloron with topological charge $k = 1$

$$A^a_\mu = -\bar{\eta}^a_{\mu\kappa}\,\frac{\partial_\kappa \Pi}{\Pi}\,, \tag{7.3}$$

where $\bar{\eta}^a_{\mu\kappa}$ denotes the (anti-selfdual) 't Hooft symbol, and Π is the prepotential given as [207]

$$\Pi(\tau, r) = 1 + \frac{\rho^2}{\beta r}\frac{\sinh\frac{2\pi r}{\beta}}{\cosh\frac{2\pi r}{\beta} - \cos\frac{2\pi\tau}{\beta}}\,. \tag{7.4}$$

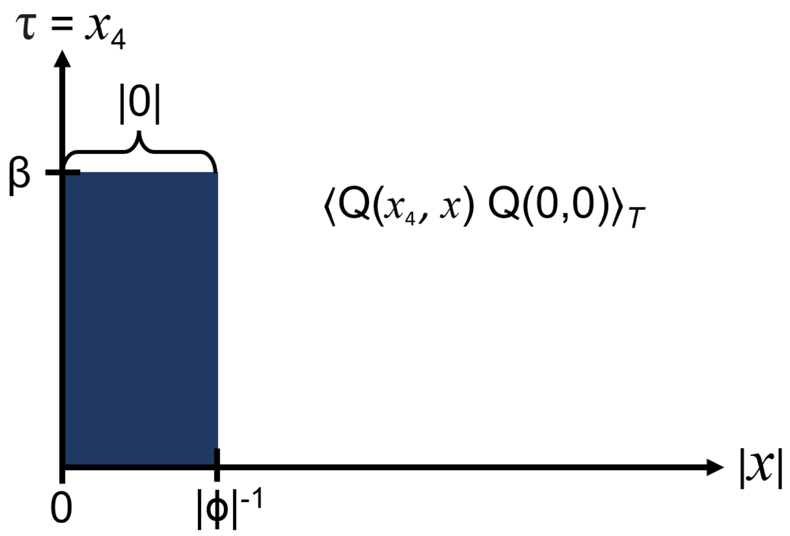

Figure 7.3: Spatially coarse-graining a fundamental-theory caloron center (integrating the correlator $\langle Q(x_4,\mathbf{x})Q(0,\mathbf{0})\rangle_T$ from $r=|\,\mathbf{x}\,|=0$ to $r=|\,\mathbf{x}\,|=|\,\phi\,|^{-1}$ and over angles) generates an effective, spatial contact term if resolution is limited as $r=|\,\mathbf{x}\,|\geq|\,\phi\,|^{-1}$. This reduces the shaded region to the line segment $0\leq x_4\leq\beta$ in the effective theory. The integral over $0\leq x_4\leq\beta$ and $\vec{x}\in\mathbf{R}^3$ of the portion of $\langle Q(x_4,\mathbf{x})Q(0,\mathbf{0}\,|)\rangle_T$, which is due to effective (quasiparticle) fluctuations, is strongly suppressed compared to the integral over $0\leq x_4\leq\beta$ of this spatial contact term, see Sec. 7.3.2.

Here, β denotes the inverse of temperature T, $\beta\equiv\frac{1}{T}$, and ρ is the associated instanton scale parameter [171, 213, 214]. Note that the second term on the right-hand side of Eq. (7.4) originates from summing the instanton prepotential in singular gauge over equidistantly shifted values of its time coordinate τ. This renders $\Pi(\tau,r)$ periodic in τ which can be seen by the dependence on $\cos\frac{2\pi\tau}{\beta}$. For the field strength, this implies staticity for sufficiently large values of r. The field strength $F^a_{\mu\nu}\equiv\partial_\mu A^a_\nu-\partial_\nu A^a_\mu+\epsilon^{abc}A^b_\mu A^c_\nu$ is expressed as

$$F^a_{\mu\nu}=\bar{\eta}^a_{\mu\nu}P-\bar{\eta}^a_{\nu\kappa}P_{\mu\kappa}+\bar{\eta}^a_{\mu\kappa}P_{\nu\kappa} \tag{7.5}$$

if we define

$$P\equiv\frac{(\partial_\kappa\Pi)(\partial_\kappa\Pi)}{\Pi^2}\,,\quad P_{\mu\nu}\equiv\frac{\Pi\partial_\mu\partial_\nu\Pi-2(\partial_\mu\Pi)(\partial_\nu\Pi)}{\Pi^2}\,. \tag{7.6}$$

Here, ϵ^{abc} denotes the 3D totally antisymmetric tensor with $\epsilon^{123}=1$. Note that

$$P_{\mu\nu}=P_{\nu\mu}\,,\qquad P_{\mu\mu}=-2P\,. \tag{7.7}$$

Therefore, one has for a selfdual caloron field[2]

$$Q\equiv\frac{1}{32\pi^2}F^a_{\mu\nu}F^a_{\mu\nu}=\frac{1}{8\pi^2}\left(P^2_{\mu\nu}-P^2\right)\,. \tag{7.8}$$

Considering that $\Pi=\Pi(\tau,r)$, we have

$$\begin{aligned}F^a_{\mu\nu}F^a_{\mu\nu} &= 4\Bigg(3\left(\frac{\partial_r\Pi}{\Pi}\right)^4+\left(\frac{\partial_r^2\Pi}{\Pi}\right)^2+2\left(\frac{\partial_r\Pi}{r\Pi}\right)^2+3\left(\frac{\partial_\tau\Pi}{\Pi}\right)^4\\ &+ \left(\frac{\partial_r\Pi}{\Pi}\right)^2\left(-4\frac{\partial_r^2\Pi}{\Pi}+6\left(\frac{\partial_\tau\Pi}{\Pi}\right)^2\right)-4\left(\frac{\partial_\tau\Pi}{\Pi}\right)^2\frac{\partial_\tau^2\Pi}{\Pi}+\left(\frac{\partial_\tau^2\Pi}{\Pi}\right)^2\\ &- 8\frac{\partial_r\Pi}{\Pi}\frac{\partial_\tau\Pi}{\Pi}\frac{\partial_r\partial_\tau\Pi}{\Pi}+2\left(\frac{\partial_r\partial_\tau\Pi}{\Pi}\right)^2\Bigg)\,.\end{aligned} \tag{7.9}$$

[2]For useful relations on the contractions of bilinears in $\bar{\eta}^a_{\mu\nu}$ see [212].

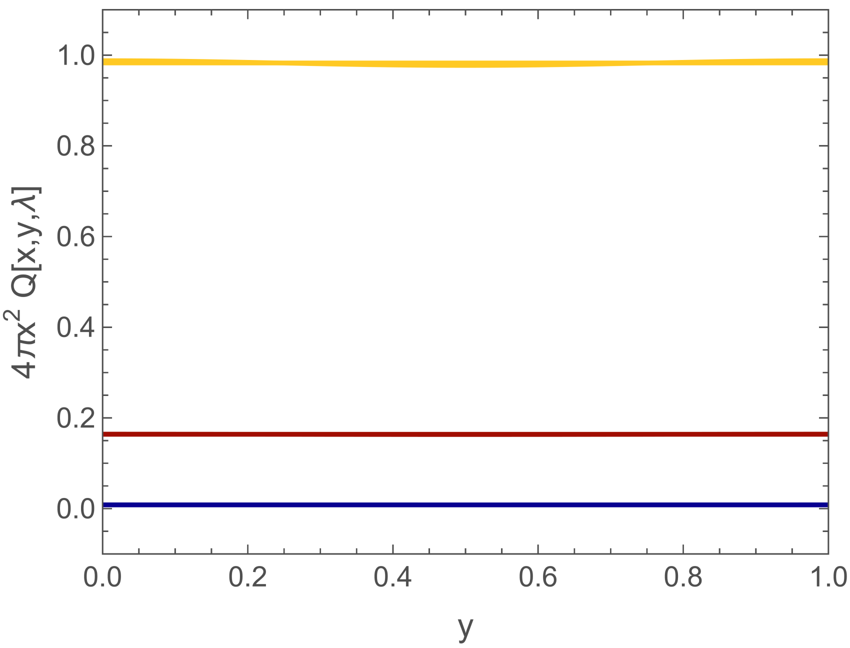

Figure 7.4: The weak y and λ dependences of function $4\pi x^2\bar{Q}(x,y,\lambda)$: $\lambda = \lambda_c, 3\,\lambda_c, 10\,\lambda_c$ and $x = 0$ (lowest set), $x = 0.5$ (uppermost set), and $x = 1$ (intermediate set).

Introducing rescaled variables, $y \equiv \frac{\tau}{\beta}$, $x \equiv \frac{r}{\beta}$, the dimensionless temperature $\lambda = \frac{2\pi T}{\Lambda}$, Λ denoting the SU(2) Yang-Mills scale, and setting $\rho =\mid \phi \mid^{-1}= \sqrt{\frac{2\pi T}{\Lambda^3}}$ to be the dominating value of the scale parameter in the thermal ground state [31], Eq. (7.4) is cast into

$$\Pi(\tau,r,T) = \bar{\Pi}(y,x,\lambda) = 1 + \frac{\lambda^3}{4\pi x}\frac{\sinh 2\pi x}{\cosh 2\pi x - \cos 2\pi y}\,. \tag{7.10}$$

Here, we have introduced the general dimensionless function $\bar{f}(y,x,\lambda) = T^{-n}f(\tau,r,T)$ where n is the mass dimension of function f. Substituting Eq. (7.10) into Eq. (7.9) and using Eq. (7.8) yields

$$\lim_{r\to 0} Q(\tau,r,T) = T^4 \lim_{x\to 0}\bar{Q}(y,x,\lambda) = 2\pi^2 T^4\lambda^6\,\frac{\left(8+\lambda^3+4\cos 2\pi y\right)^2}{3\left(2+\lambda^3-2\cos 2\pi y\right)^4}\,. \tag{7.11}$$

According to Eq. (7.11) the y and the λ dependences of $\bar{Q}(y,x=0,\lambda)$ are very weak for $\lambda \geq \lambda_c = 13.87$ [31]. At finite x this behaviour of $\bar{Q}(y,x,\lambda)$ w.r.t. variations in y and λ persists, which is demonstrated in Fig. 7.4 for $x = 0, 0.5, 1.0$ and $\lambda = \lambda_c, 3\,\lambda_c, 10\,\lambda_c$.
For $\lambda \geq \lambda_c = 13.87$ the topological charge $k \equiv 4\pi\int_0^1 \mathrm{d}y\int_0^\infty \mathrm{d}x\, x^2\bar{Q}(y,x,\lambda) = 1$ thus can, to a very good accuracy, be computed as

$$k = 4\pi\int_0^\infty \mathrm{d}x\, x^2\bar{Q}(\frac{1}{2},x,\lambda)\,. \tag{7.12}$$

If we truncate the integration over x in Eq. (7.12) at the scale $x_{\rm max} = \frac{\rho}{\beta} = \frac{|\phi|^{-1}}{\beta} = \frac{\lambda^{3/2}}{2\pi}$,

$$k = 4\pi\int_0^{\frac{\lambda^{3/2}}{2\pi}} \mathrm{d}x\, x^2\bar{Q}(\frac{1}{2},x,\lambda)\,, \tag{7.13}$$

then we obtain numerically $k = 0.9768, 0.9927, 0.9938$ for $\lambda = \lambda_c, 2\,\lambda_c, 2.5\,\lambda_c$, respectively. This shows that, practically for all λ, the topological charge of an HS (anti)caloron resides within its center. The (dimensionless) radius $x_{\rm max}$ of this center, however, grows $\propto \lambda^{3/2}$ with dimensionless temperature λ. This explains why lattice simulations, essentially operating at a fixed spatial volume at varying T, fail to capture large portions of the topological charge of a relevant (anti)caloron in $\chi(T)$, compare with Fig. 7.2. The short-distance correlation of the thermal ground state of an SU(2) Yang-Mills theory are mediated by the centers of an HS caloron or anticaloron [31]. As confirmed above, the (anti)caloron action, representing a nontrivial topological charge of this gauge-field configuration, is localised within the (anti)caloron

center. As a consequence, the ground-state contribution to the ensemble average on the right-hand side of Eq. (7.1) represents the contribution of an (anti)caloron center - a contact term within the effective, deconfining Minkowskian quantum thermodynamics [31], see also Fig. 7.3. In contrast to calorons, which are action minimisers of the 4D defining, classical, and Euclidean Yang-Mills theory and are infinitely resolved, the effective theory describes the quantum dynamics of gauge fields in (3+1)D Minkowski space at spatial distances larger than $|\phi|^{-1}$. By matching the effective theory with the fundamental one at this resolution limit, it was argued in [153] that the caloron action coincides with Planck's quantum of action $\hbar$. Light-cone localised, propagating solutions to the source-free Minkowskian Yang-Mills equations — photons —, which could be initiated by sufficiently resolving, time-periodic probes of (anti)caloron centers, were constructed recently by A. Rabinowitch [128]. Given these localised solutions, a probe's circular frequency ω thus could provoke propagating quanta of energy $\hbar\omega$.
We are now in a position to compute the thermal ground state contribution of the right-hand side of Eq. (7.1) as

$$\begin{aligned}\chi_{\text{cal. cen.}} &= \int_{\text{cal. cen.}} \mathrm{d}\tau \mathrm{d}\Omega \mathrm{d}r\, r^2\, Q(\tau,r,T)Q(0,0,T)\\ &= 4\pi T^4\,\bar{Q}(0,0,\lambda)\int_0^1 \mathrm{d}y\int_0^{\frac{\lambda^{3/2}}{2\pi}} \mathrm{d}x\, x^2\bar{Q}(y,x,\lambda)\\ &\simeq 4\pi T^4\,\bar{Q}(0,0,\lambda)\int_0^{\frac{\lambda^{3/2}}{2\pi}} \mathrm{d}x\, x^2\bar{Q}(\frac{1}{2},x,\lambda)\\ &\simeq \frac{2}{3}\frac{(12+\lambda^3)^2\pi^2}{\lambda^6}\,T^4\\ &\stackrel{\lambda\gg\lambda_c}{\longrightarrow} \frac{2}{3}\pi^2\,T^4\,,\end{aligned} \tag{7.14}$$

where $d\Omega$ denotes the angular part of the measure in the spatial integration. Therefore,

$$m_A = \sqrt{\frac{2}{3}}\pi\frac{T^2}{M_P}\,,\quad (T\gg T_c)\,. \tag{7.15}$$

Note that, due to the integral of Eq. (7.13) being close to unity and due to the function on the right-hand side in Eq. (7.11) being near to $2\pi^2T^4/3$ already at $\lambda=\lambda_c=13.87$, the T dependence of m_A as in Eq. (7.15) is an excellent approximation, already for $T\sim T_c$.

7.3.2 Do thermal quasiparticle fluctuations contribute to χ?

Eq. (7.14) associates with a contact term of the correlator $\langle Q(x_4,\mathbf{x})Q(0,\mathbf{0})\rangle_T$ in the effective theory of the deconfining phase of SU(2) Yang-Mills thermodynamics [31]. In [215] it is suggested that precisely such a contact term saturates the right-hand side of Eq. (7.1) at $T=0$, see also an associated argument for the Schwinger model in [216]. In the Appendix we show that in the effective theory for the deconfining phase of SU(2) Yang-Mills thermodynamics [31] a negative contribution to χ arises from massless and massive, effectively free thermal quasi-particles. Judged by the smallness of two- and three-loop corrections to the free quasi-particle approximation of thermodynamical quantities, this should be precise to the sub-percent level [31]. As computed in the Appendix, free quasi-particles generate in $\chi(T)$ a positive coefficient in front of $-T^4$ which is much smaller than unity. Therefore, we can consider the result of Eq. (7.14) a reliable estimate of the entire topological susceptibility χ: the expression for the axion mass m_A in Eq. (7.15), which emerges from the axial anomaly invoked by SU(2) (anti)calorons, should be accurate to the sub-percent level. In [194] $\chi(T)$ was computed in the model of the stochastic vacuum. For the nonperturbative part of the correlator $\langle Q(x_4,\mathbf{x})Q(0,\mathbf{0})\rangle_T$ a factorised negative contribution was shown to be overcompensated by a positive nonfactorised contribution. Both are expressed in terms of nonperturbative vacuum parameters measured at zero temperature, which were extracted from lattice simulations. As a result, a T^4 dependence with a positive coefficient also was found in [194].

7.4 Cosmological Implications: Bose Condensation of Axions

As a function of increasing cosmological redshift z axion masses for four different species are shown in Fig. 7.5. In the confining phase of the associated SU(2) Yang-Mills theory, the axion mass is constant in z. For the three species concerned at the present temperature of the CMB, $T_0 = 2.725\,\mathrm{K}$, and up to $z \sim 10^8$, the lowest axion mass can be extracted phenomenologically from rotation curves of low-surface-brightness galaxies [41]. The other two masses follow from Yang-Mills scaling relations (subject to a common Peccei-Quinn scale, here M_P) in the fuzzy dark matter model. Such scaling relies on a link to lepton families introduced in [41] and explicated for the first lepton family in [5]. As soon as a SU(2) Yang-Mills theory transitions to its deconfinement phase, the associated axion mass starts to depend on z via Eq. (7.15) and is subject to the T-z relation in the deconfinement phase [74]. At high redshifts ($z > 10^{12}$) all axion species exhibit the same dependence of their mass on redshift z. Note that the validity of our axion–mass computation in an expanding Friedmann-Lemaître-Robertson-Walker universe hinges on temperature T being larger than the Hubble expansion rate H. In a radiation dominated universe, we estimate $H/T = O(10)\,T/M_P$. Therefore, we demand $T/M_P \ll O(10^{-1})$ which allows us to address most of the universe's expansion history.

Let us now investigate the implications of Eq. (7.15) for the critical temperature $T_{c,B}$ of Bose condensation involving non-relativistic axion particles of mass m_A and number density[3] n_A. One has [127]

$$T_{c,B} = \frac{2\pi}{m_A}\left(\frac{n_A}{\zeta\left(\frac{3}{2}\right)}\right)^{\frac{2}{3}}, \tag{7.16}$$

where $\zeta(x)$ denotes the Riemann zeta function ($\zeta\left(\frac{3}{2}\right) = 2.6124$). If we assume that, due to the long-range quantum correlations facilitated by a super-horizon (reduced) Compton wave length[4] $m_{A,i}^{-1}$, the energy density $\rho_{\Lambda_i} = m_{A,i} n_{A,i}$ of a global axion condensate exhibits negligible redshift (or T) dependence then the dependence of the axion mass on temperature of Eq. (7.15) predicts

$$T_{c,B,i} = \left(\frac{486}{\pi^4}\right)^{1/26}\left(\frac{\rho_{\Lambda_i}}{\zeta\left(\frac{3}{2}\right)}\right)^{2/13} M_P^{5/13}\,. \tag{7.17}$$

Setting $\rho_{\Lambda_{\mathrm{CMB}}} = (10^{-3}\,\mathrm{eV})^4$ and $M_P = 1.22\times 10^{28}\,\mathrm{eV}$ yields $T_{c,B,\mathrm{CMB}} = 8.3\times 10^8\,\mathrm{eV}$ which associates with a redshift $z > 10^{12}$. This is beyond the initial redshift $z \sim 10^9$ assumed in CMB simulations [211]. Higher vacuum energy densities, $\rho_{\Lambda_i} > \rho_{\Lambda_{\mathrm{CMB}}}$, yield higher values of $T_{c,B,i}$ even though their spread is small due to the small power of 2/13 in Eq. (7.17).

Due to the large hierarchy between $T_{c,B,i}$ and M_P and by virtue of Eq. (7.15) thermal axions constitute radiation for all temperatures T within the regime $M_P \gg T > T_{c,B,i}$. However, in a radiation dominated universe, they only represent a small fraction of *radiation* energy density. This is because radiation domination arises due the Stefan-Boltzmann limit of Yang-Mills thermodynamics. For $T \sim M_P$, where we expect Einstein gravity to profoundly develop quantum behaviour, thermal axions would become nonrelativistic again.

[3] In cosmology, axion particles can be shown to be nonrelativistic [195]: roughly speaking, their speed $v_{A,i}$ is bounded from above by $v_{A,i}(z) = \frac{M(z)m_{A,i}(z)}{M_P^2}$ where $M(z)$ denotes the entire mass of the instantaneously gravitating system at redshift z after virialisation [195]. To axions that presently form a super-horizon sized, self-gravitating Bose condensate to represent dark energy we associate the gauge group $\mathrm{SU(2)_{CMB}}$ [217, 48, 41]. In ΛCDM this system presently gravitates subject to a mass $M_{\Lambda\mathrm{CDM}}(z=0)$ made from the axion condensate, dark matter, and baryons. For a spatial ball of present Hubble radius $r_{H_0} = H_0^{-1}$ — the causally connected, selfgravitating region to which a typical axion particle virialises — we have $M_{\Lambda\mathrm{CDM}}(z=0) \sim \frac{4\pi}{3}H_0^{-3}H_0^2 M_P^2\frac{3}{8\pi} = \frac{1}{2}M_P^2/H_0$. Using $H_0 = 1.34\times 10^{-32}\,h\,\mathrm{eV}$ and $h = 0.74$ [218, 35, 32] yields $M_{\Lambda\mathrm{CDM}}(z=0) \sim 7.5\times 10^{87}\,\mathrm{eV}$. Setting $m_{A,\mathrm{CMB},0} = 10^{-35}\,\mathrm{eV}$ [67], one thus arrives at $v_{A,\mathrm{CMB}}(z=0) \sim 5.04\times 10^{-4} \ll 1$. In a spatially flat, matter dominated universe $M(z)$ evolves as $M(z=0)\,(z+1)^{-3/2}$. With $m_{A,i}(z) = (1/4)^{2/3}\;m_{A,i,0}\,(z+1)^2$ [94] this produces $v_{A,i} = v_{A,i,0}\,(1/4)^{2/3}\;(z+1)^{1/2}$. In a radiation dominated universe $v_{A,i}$ does not evolve in z. Ignoring a small regime in redshift of dark-energy domination and taking the redshift of radiation-matter equality as $z \sim 3000$, the axion-particle speed $v_{A,\mathrm{CMB}}$ thus increases from its present value by a factor of $\sim (1/4)^{2/3}\,(3000+1)^{1/2} = 21.7$. Therefore, axions that associate with $\mathrm{SU(2)_{CMB}}$ are non-relativistic throughout the entire expansion history. Axion particles of species that are associated with fuzzy dark matter receive their redshift independent masses due to the Veneziano-Witten formula applied to confining phases of SU(2) Yang-Mills theories for redshifts $z < 10^8$ [41] where topological charge is carried by round-point center-vortex loops [31]. Presently, they are similarily slow as the axions of $\mathrm{SU(2)_{CMB}}$ [195, 41]. With increasing z and for $z < 10^8$ the velocities of these axion particles remains constant until the percolation of their selfgravitating lumps sets in at $z_{p,i}$. For $z > z_{p,i}$ axion velocities either decay with $(z+1)^{-3/2}$ (matter domination) or with $(z+1)^{-2}$ (radiation domination) as z increases and so are guaranteed to be non-relativistic. In the deconfining phases of the associated SU(2) Yang-Mills theories, that is, in the very early, radiation dominated universe, axion velocities do not evolve.

[4] One can readily see that the horizon size r_H remains smaller than the Compton wavelength $m_{A_i}^{-1}$ in a radiation dominated universe. Namely, $r_H m_{A_i} = O(1)/O(10)$. This shows that no gravitational back reaction occurs while maintaining the condensed state of axion particles. Thus, the condition to determine the critical temperature for condensation is solely Eq. (7.16).

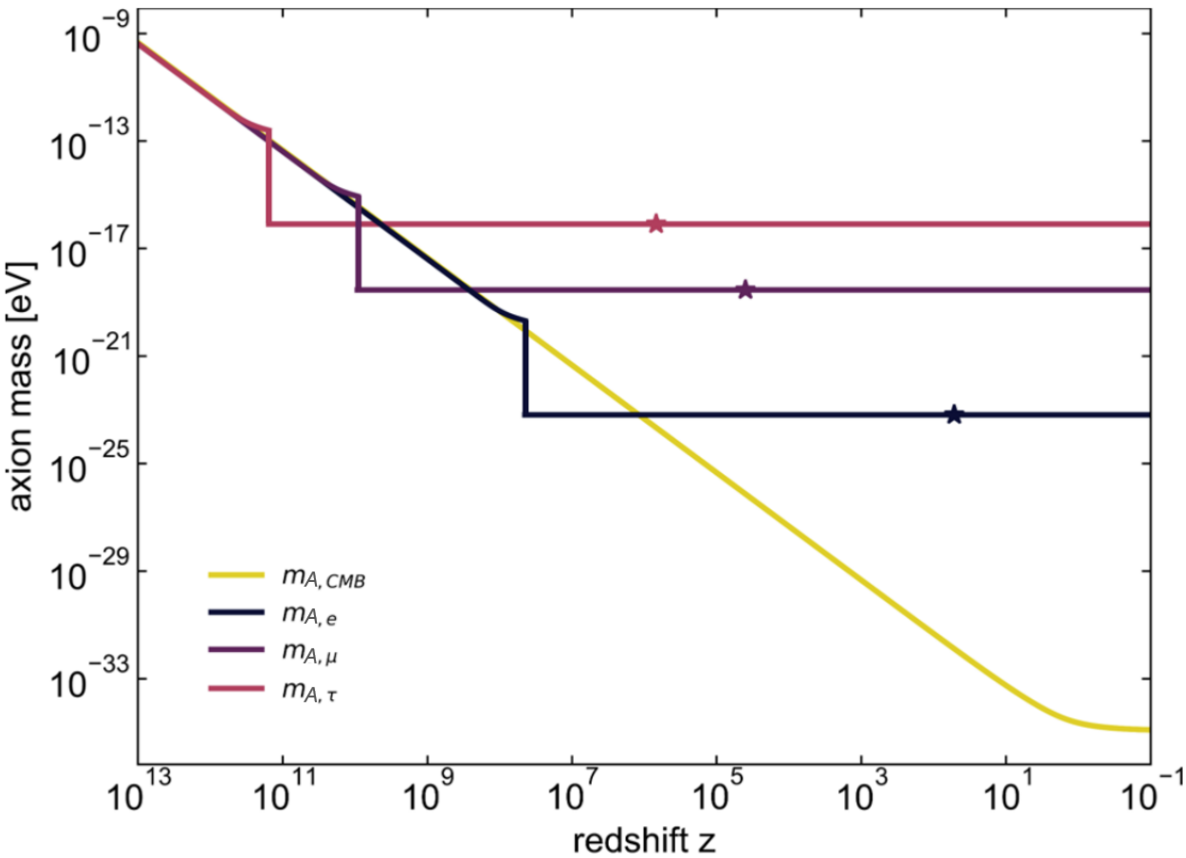

Figure 7.5: Axions have a temperature dependent mass $m_A \propto T^2/M_P$ in deconfinement phases of SU(2) Yang-Mills thermodynamics, see Eq. (7.15); in the confining phase, the axion mass is constant, see [41]. According to [41] and Eq. (7.15), the temperature dependence of m_A is shown for four axion species [41]: an axion associated with the Yang-Mills scale potentially implying the third lepton family possesses a mass $m_{A,\tau}(z=0) \approx 8 \times 10^{-17}$ eV (ultramarine). Accordingly, for the second lepton family, one would have $m_{A,\mu}(z=0) \approx 3 \times 10^{-19}$ eV (orange). An axion that associates with the first lepton family carries a mass $m_{A,e}(z=0) \approx 7 \times 10^{-24}$ eV (green), and an axion, which couples to a Yang-Mills theory potentially describing the CMB would possess a mass $m_{A,\text{CMB}}(z=0) \approx 10^{-35}$ eV (yellow). At the respective deconfinement phase transitions the axion mass, which is supported by a reduced topological susceptibility in the confining phase (round-point center-vortex loops being the topological charge carriers [31]) as compared to the deconfinement phase, see derivation of Eq. (7.14), jumps up to a higher value. To convert the T dependence of the axion mass in Eq. (7.15) into a z dependence, the temperature-redshift relation $T(z) = \mathcal{S}(z) \cdot (z+1) \cdot T_0$ was used [74]. Here, $\mathcal{S}(z)$ derives from a numerical evaluation of the SU(2) deconfinement entropy density. It is fitted as $\mathcal{S}(z) = \exp(-1 - 1.7\,z) + 1/4^{1/3}$.

7.5 Summary and Outlook

In this paper, we have revisited the computation of axion mass according to the Veneziano-Witten formula applied to the deconfining phase of an SU(2) Yang-Mills theory. Our result for the T dependence of the topological susceptibility χ deviates from what is found in the literature: a T^4 dependence, which is expected from dimensional analysis [193] and indeed shown to emerge in our computation involving the center of a Harrington-Shepard caloron to represent the thermal ground state locally [31], contrasts with power laws of large negative exponents [185, 186, 187, 188, 189, 190, 191, 192]. In Sec. 7.1 we have pointed out various possible reasons for why such a discrepancy arises. We also have shown that the contributions to χ stemming from massless and massive effective excitations of the thermal ground state of a given SU(2) Yang-Mills theory yield an extremely suppressed negative correction (reflection positivity) to the positive caloron contribution. Finally, we have investigated the consequences of this result for cosmological model building. Such models consider the dark sector as axial-anomaly induced by virtue of SU(2) Yang-Mills theories subject to a common Peccei-Quinn scale M_P [48]. Such gauge theories possibly relate to the three lepton families of the Standard Model of Particle Physics [41, 5]. A fourth SU(2) theory of scale $\Lambda_{\text{CMB}} \sim 10^{-4}\,\text{eV}$ (and Peccei-Quinn scale M_P) — $\text{SU(2)}_{\text{CMB}}$ — may generate a present axion mass of $\sim 10^{-35}\,\text{eV}$, therefore a super-horizon Compton wavelength, and thus could relate to dark energy. It is worth asking at what temperatures these theories Bose condense their axion particles in a cooling universe. We find that the associated critical temperatures depend on the respective energy densities of the condensate through a power law of fractional power 2/13. This suggests, in heating the very early universe through these transitions, that for *all* axion species the epoch of dissolving dark energy into radiation is occurring at nearly the same temperature. The results obtained here could be useful for cosmological model building in a framework where the dark sector of the universe is due to the selfgravitating quantum dynamics of ultralight axions [195, 219, 199, 198, 200, 201].

Data availability
The Python scripts and notebooks which have been used for the figures in this paper are available on GitLab[5].

Acknowledgements
The work of RH and JM was supported by the Vector Foundation under grant number P2021-0102. The authors acknowledge useful conversations with Thilo Blumenberg. JM would like to thank Karl-Heinz Kampert for useful conversations. The hospitality of Aspen Center for Physics (ACP), where part of this work was carried out by RH in September 2023, and inspiring conversations with the participants of the workshops on "Cluster Cosmology" and "Conformal Field Theory" are gratefully acknowledged. ACP is a wonderful and unique institution which allows for inspired, focused work on fundamental problems. The results of this paper were reported recently at the 22nd International Conference of Numerical Analysis and Applied Mathematics in Heraklion (ICNAAM 2024), Crete. RH and JM would like to thank the participants of the symposium on "Quantum field theory and Cosmology" within ICNAAM 2024 for interesting discussions.

Contributions of the author JM
Contributions include review & editing, figure preparation, and funding acquisition.

[5] `https://git.uni-wuppertal.de/meinert/axion-mass/`

Appendix

Here, we evaluate the contribution to the topological susceptibility χ on the right-hand side of Eq. (7.1) arising from quasi-particle fluctuations in the effective theory of deconfining SU(N_c) Yang-Mills thermodynamics [31]. Throughout this Appendix, we denote by x or y spacetime vectors in $\mathbf{R}^4$.

A: Factorised $\chi(T)$ in the model of the stochastic Yang-Mills vacuum at $T > T_c$

Here, in contrast to Secs. 7.2 and 7.3, we work with the perturbative definition, where the coupling is not absorbed into the gauge field. Let us then consider the expression $\varepsilon_{\mu\nu\lambda\rho}F_{\mu\nu}F_{\lambda\rho}$, where one of the indices can be equal to 4, and $F_{\mu\nu}$ is the antisymmetric field-strength tensor, defined either in terms of the fundamental gauge field A_μ or effective gauge fields a_μ. In the present section, both kinds of gauge fields are identified and subjected to the coupling g. In Appendix B, we refer to effective gauge fields and set $g = e$. Thus, $F_{\mu\nu} = F^a_{\mu\nu}t^a$, where $F^a_{\mu\nu} = \partial_\mu A^a_\nu - \partial_\nu A^a_\mu + gf^{abc}A^b_\mu A^c_\nu$, t^a's are SU(N_c)-generators in the fundamental representation, normalised as $\mathrm{tr}\, t^a t^b = \delta^{ab}/2$, $a = 1, \ldots, N_c^2 - 1$, and f^{abc} are the structure constants of the Lie algebra su(N_c). One readily obtains that $\varepsilon_{\mu\nu\lambda\rho}F_{\mu\nu}F_{\lambda\rho} = 4\,\varepsilon_{4ijk}F_{4i}F_{jk}$. Moreover, one has

$$\varepsilon_{4ijk}\varepsilon_{4lmn}F_{4i}(x)F_{jk}(x)F_{4l}(0)F_{mn}(0) = 2F_{4i}(x)F_{jk}(x)\left[F_{4i}(0)F_{jk}(0) + 2F_{4k}(0)F_{ij}(0)\right] . \tag{7.18}$$

For latter usage we define $x = (\mathbf{x}, x_4) = (x_1, x_2, x_3, x_4)$, $\mathbf{x}^2 = x_1^2 + x_2^2 + x_3^2$, and $|x|^2 = x_1^2 + x_2^2 + x_3^2 + x_4^2$. The local density of topological charge is defined as

$$Q(x) = \frac{g^2}{32\pi^2}\varepsilon_{\mu\nu\lambda\rho}\,\mathrm{tr}(F_{\mu\nu}(x)F_{\lambda\rho}(x))\,. \tag{7.19}$$

From Eqs. (7.18) and (7.19) it is straightforward to obtain

$$\langle Q(x)Q(0)\rangle = \frac{g^4}{128\pi^4}\left[\langle F^a_{4i}(x)F^a_{jk}(x)F^b_{4i}(0)F^b_{jk}(0)\rangle + 2\langle F^a_{4i}(x)F^a_{jk}(x)F^b_{4k}(0)F^b_{ij}(0)\rangle\right] . \tag{7.20}$$

Let us now consider the factorised part of Eq. (7.20) which consists of six pairwise products of the two-point correlation functions of the field strengths. As indicated by the lattice data in [220] the deconfinement phase transition at $T = T_c$ is associated with the disappearance of the chromo-electric condensate $\langle (gE^a_i)^2\rangle_T$, and hence also of $\langle F^a_{4i}(x)F^b_{4j}(y)\rangle_T$. Accordingly, Eq. (7.20) yields $\langle F^a_{4i}(x)F^b_{4j}(0)\rangle_T = 0$ in the stochastic Yang-Mills vacuum at $T > T_c$ [220]. Thus, one has

$$\begin{aligned}\langle Q(x)Q(0)\rangle_{T,\mathrm{factorized}} = \frac{1}{128\pi^4}\Big[&\langle g^2F^a_{4i}(0)F^a_{jk}(0)\rangle_T^2 + \langle g^2F^a_{4i}(x)F^b_{jk}(0)\rangle_T^2 \\ &+ 2\langle g^2F^a_{4i}(0)F^a_{jk}(0)\rangle_T\langle g^2F^b_{4k}(0)F^b_{ij}(0)\rangle_T \\ &+ 2\langle g^2F^a_{4i}(x)F^b_{ij}(0)\rangle_T\langle g^2F^a_{4k}(x)F^b_{jk}(0)\rangle_T\Big] .\end{aligned} \tag{7.21}$$

We thus see that $\langle Q(x)Q(0)\rangle_{T,\mathrm{factorized}}$ is fully expressed in terms of the correlation function $\langle g^2E^a_i(x)B^b_k(0)\rangle_T$ where $E^a_i = F^a_{i4}$ denotes the chromo-electric field and $B^b_k = 1/2\varepsilon_{kij}F^b_{ij}$ is the chromo-magnetic field. This correlation function can be parameterized through a scalar function $f(x)$ as

$$\langle g^2E^a_i(x)B^b_k(0)\rangle_T = \delta^{ab}\varepsilon_{ikn}x_nf(x)\,. \tag{7.22}$$

If one multiplies this equation by t^at^b and takes the trace, one obtains

$$\mathrm{tr}\,\langle g^2E^a_i(x)t^aB^b_k(0)t^b\rangle_T = \frac{N_c^2-1}{2}\,\varepsilon_{ikn}x_nf(x).$$

This parameterization can now be compared with the one adopted in Eq. (2.9) of [220] which reads

$$\mathrm{tr}\,\langle g^2E^a_i(x)t^aB^b_k(0)t^b\rangle_T = -\frac{1}{2}\varepsilon_{ikn}x_n\frac{\partial D_1^{\mathrm{BE}}}{\partial x_4}\,,$$

where the lattice values for the function $D_1^{\mathrm{BE}}(x)$ can also be found in [220].

Therefore, $f(x)$ is unambiguously related to the function $D_1^{\rm BE}(x)$ as

$$f(x) = -\frac{1}{N_c^2-1}\frac{\partial D_1^{\rm BE}}{\partial x_4} \tag{7.23}$$

Using the aforementioned definitions of the chromo-electric and the chromo-magnetic fields, one has

$$\langle g^2 F_{4i}^a(x) F_{jk}^b(0)\rangle_T = \delta^{ab}\left(\delta_{ij}\delta_{kn} - \delta_{ik}\delta_{jn}\right) x_n f(x)\,. \tag{7.24}$$

Equations (7.21) and (7.24) finally yield:

$$\begin{aligned}\langle Q(x)Q(0)\rangle_{T,\text{factorized}} &= \frac{1}{128\pi^4}\Big[\langle g^2 F_{4i}^a(x)F_{jk}^b(0)\rangle_T^2 + 2\langle g^2 F_{4i}^a(x) F_{ij}^b(0)\rangle_T \langle g^2 F_{4k}^a(x) F_{jk}^b(0)\rangle_T\Big] \\ &= -\frac{N_c^2-1}{32\pi^4}\mathbf{x}^2 f^2\,.\end{aligned} \tag{7.25}$$

Note the negative sign of this contribution to $\langle Q(x)Q(0)\rangle_T$, in accordance with the reflection-positivity property and the pseudoscalar nature of the topological charge [221, 215].

B: Contributions to topological susceptibility due to massless and massive quasi-particles

Let us now calculate contributions produced to the correlation function (7.25) by free massless and massive quasi-particles in the effective theory of SU(N_c) Yang-Mills thermodynamics ($N_c = 2, 3$) for the deconfinement phase [31]. These contributions are denoted by $\langle Q(x)Q(0)\rangle_{T,\text{factorized, free}}$ in what follows. We first assume all the N_c^2-1 effective gauge fields to be massless, and subsequently show how the corresponding contribution of massless quasi-particles dominates over that of the massive ones. For the case of free massless quasi-particles, we need to consider the Abelian part of the field-strength tensor, $f_{\mu\nu}^a = \partial_\mu a_\nu^a - \partial_\nu a_\mu^a$. Setting $g = e$ yields:

$$\langle e^2 E_i^a(x) B_k^b(y)\rangle_{T=0,\text{free}} = \frac{1}{2}\varepsilon_{klm}\langle e^2 f_{i4}^a(x) f_{lm}^b(y)\rangle_{T=0} = \varepsilon_{klm}\partial_4^x\partial_m^y\langle e^2 a_i^a(x) a_l^b(y)\rangle_{T=0}\,,$$

where $\langle e^2 a_i^a(x) a_l^b(y)\rangle_{T=0} = \frac{e^2}{4\pi^2}\frac{\delta^{ab}\delta_{il}}{(x-y)^2}$ (Feynman gauge), and we continue to work in Euclidean spacetime. Hence,

$$\langle e^2 E_i^a(x) B_k^b(0)\rangle_{T=0,\text{free}} = e^2\delta^{ab}\varepsilon_{ikn}\partial_4\partial_n\,\frac{1}{4\pi^2 x^2}\,. \tag{7.26}$$

At finite temperature $T \equiv 1/\beta$, the propagator of massless gauge modes, $\frac{1}{4\pi^2x^2}$, can be represented as an integral over the Schwinger proper time s as

$$\int_0^\infty \frac{{\rm d}s}{(4\pi s)^2}\sum_{n=-\infty}^{+\infty}\exp\left[-\frac{\mathbf{x}^2 + (x_4+\beta n)^2}{4s}\right]\,. \tag{7.27}$$

Poisson resummation casts the sum over winding modes into the sum over Matsubara frequencies as

$$\sum_{n=-\infty}^{+\infty}\exp\left[-\frac{(x_4+\beta n)^2}{4s}\right] = 2T\sqrt{\pi s}\sum_{k=-\infty}^{+\infty}\exp(-\omega_k^2 s + i\omega_k x_4)\,, \tag{7.28}$$

where $\omega_k = 2\pi T k$ is the k-th Matsubara frequency. Therefore, the x_4-differentiation in Eq. (7.26) returns the prefactor of $i\omega_k$ which vanishes for $k = 0$. Hence, we approximate the sum over Matsubara frequencies by only keeping terms with $k = \pm 1$. The finite-temperature generalisation of $\partial_4\partial_n\frac{1}{4\pi^2x^2}$ is thus approximated as

$$\frac{T^2 x_n}{4\sqrt{\pi}}\int_0^\infty \frac{{\rm d}s}{s^{5/2}}\,{\rm e}^{-(2\pi T)^2 s - \frac{\mathbf{x}^2}{4s}}\sin(2\pi T x_4)\,.$$

The s-integration in this expression, along with Eq. (7.22), yields

$$f_{\rm free}(x) \simeq \frac{2\pi e^2 T^3}{\mathbf{x}^2}\left(1 + \frac{1}{2\pi T|\mathbf{x}|}\right){\rm e}^{-2\pi T|\mathbf{x}|}\sin(2\pi T x_4)\,.$$

Thus, by employing Eq. (7.25), we obtain:

$$\langle Q(x)Q(0)\rangle_{T,\text{factorized, free}} \simeq -\frac{N_c^2-1}{8\pi^2}\frac{(e^2T^3)^2}{\mathbf{x}^2}\left(1+\frac{1}{2\pi T|\mathbf{x}|}\right)^2 \mathrm{e}^{-4\pi T|\mathbf{x}|}\sin^2(2\pi T x_4)\,. \tag{7.29}$$

By using Eq. (7.29), we calculate now $\chi_{T,\text{factorized, free}}$, given as

$$\begin{aligned}&\int \mathrm{d}^3x \int_0^\beta \mathrm{d}x_4 \langle Q(x)Q(0)\rangle_{T,\text{factorized, free}}\\ =&\quad -\frac{N_c^2-1}{8\pi^2}(e^2T^3)^2\frac{4\pi}{2T}\int_{|\phi|^{-1}}^\infty \mathrm{d}|\mathbf{x}|\left(1+\frac{1}{2\pi T|\mathbf{x}|}\right)^2 \mathrm{e}^{-4\pi T|\mathbf{x}|}\,,\end{aligned} \tag{7.30}$$

where the prefactor of $\frac{1}{2T}$ stems from $\int_0^\beta \mathrm{d}x_4 \sin^2(2\pi T x_4)$, $|\phi|^{-1} = \frac{\lambda^{3/2}}{2\pi T}$, $\lambda \geq \lambda_c = 13.87$ [31] and $e \sim \sqrt{8}\pi$ for $T \gg T_c$. Therefore, we have

$$|\ \chi_{T,\text{factorized, free}}\ |\simeq \frac{N_c^2-1}{16\pi^2}(eT)^4\,\mathrm{e}^{-2\lambda^{3/2}} \leq 4\times 10^{-39}T^4\,,\quad (\lambda\geq\lambda_c, N_c=2)\,. \tag{7.31}$$

The above calculation of the contribution $\chi_{T,\text{factorized, free}}$ of massless gauge fields to $\chi(T)$ can readily be generalized to the case of massive vector bosons of common mass m. Here, $1/(4\pi^2x^2)$ in Eq. (7.26) just needs to be replaced by $m\,K_1(m|x|)/(4\pi^2|x|)$, where K_1 is the Macdonald function. This amounts to adding the term $-m^2s$ into the exponentials in Eqs. (7.27) and (7.28) and introducing a factor of 3/2 for the additional polarisation state. We obtain (cf. Eq. (7.30))

$$\begin{aligned}\chi_{T,\text{factorized, free, massive}} &\simeq -\frac{3}{2}\frac{N_c^2-1}{32\pi^4}(eT)^4\frac{4\pi}{2T}\left[(2\pi T)^2+m^2\right]\int_{|\phi|^{-1}}^\infty \mathrm{d}|\mathbf{x}|\,\mathrm{e}^{-2\sqrt{(2\pi T)^2+m^2}\,|\mathbf{x}|}\\ &= -3\frac{N_c^2-1}{64\pi^3}\,e^4T^3\sqrt{(2\pi T)^2+m^2}\,\mathrm{e}^{-2\frac{\sqrt{(2\pi T)^2+m^2}}{2\pi T}\lambda^{3/2}}\,.\end{aligned} \tag{7.32}$$

This expression indicates an even stronger exponential suppression than that of Eq. (7.31). In the effective theory for the deconfinement phase of SU(2) Yang-Mills thermodynamics, the adjoint Higgs mechanism leaves one gauge mode massless but generates a common mass $m = 4\pi eT\lambda^{-3/2}$ [31] for the other two gauge modes. Here $e = \sqrt{8}\pi$ for $T \gg T_c$. For SU(3) two different masses emerge which, however, exhibit the same $T^{-1/2}$ power-law fall-off at high temperatures. This shows that, modulo a smaller number of polarisation states (six vs. eight for SU(2), 16 vs. 22 for SU(3)), the hypothetic contribution to $\chi_{T,\text{factorized, free}}$ of massless gauge fields dominates among the contributions of all effective excitations. Since the modulus of $\chi_{T,\text{factorized, free}}$ is ridiculously small, see Eq. (7.31), we justify the omission of (negative) contributions to χ that arise from quasi-particle modes in the effective theory.

Finally, let us discuss an important property to be respected by the full correlation function $\langle Q(x)Q(0)\rangle_T$: it should be negative for all $x \neq 0$ while yielding a positive $\chi(T)$ [221, 215] to define a positive axion mass squared according to Eq. (7.1). For the contribution $\langle Q(x)Q(0)\rangle_{T,\text{factorized, free}}$ in Eq. (7.29) this is the case, albeit subject to an exponentially strong suppression of the modulus as compared to the positive caloron contact contribution, compare with Eq. (7.11).

this page is intentionally left blank

8 Summary and Acknowledgments

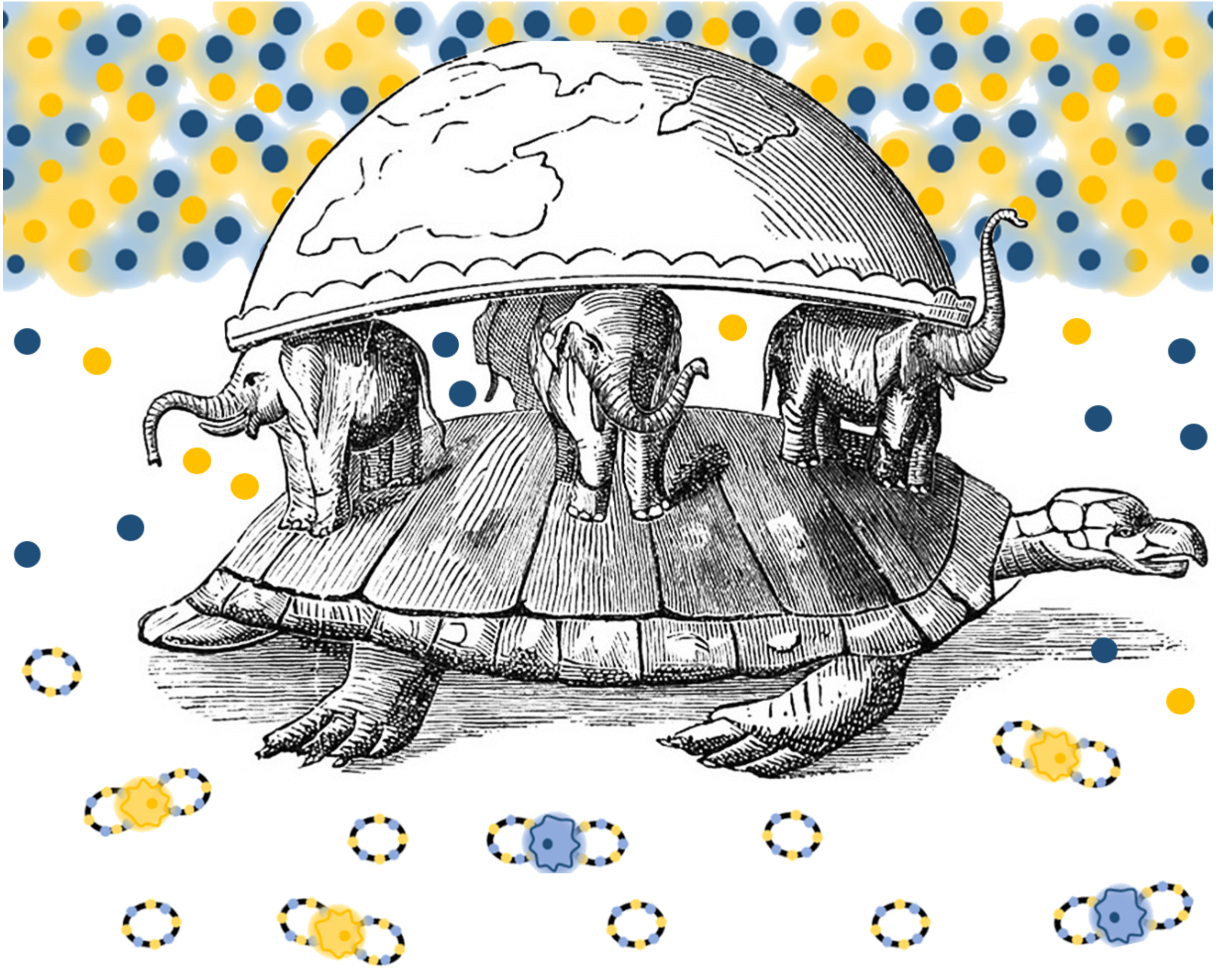

Figure 8.1: Turtles all the way down? 19th century illustration of a world turtle from Wikimedia, modified.

Contents

8.1 Summary 96
8.2 Acknowledgments 98

8.1 Summary

This thesis explores a range of research questions in astroparticle physics and cosmology. It examines anisotropies influenced by the Milky Way's magnetic field and the propagation of cosmic rays on cosmological scales through the cosmic microwave background (CMB) with a modified temperature-redshift (T-z) relation. In addition, we explore fundamental physics that may suggest a modified T-z relation within the framework of a deconfining SU(2) Yang-Mills plasma. The thesis also examines a lepton model based on mixed SU(2) Yang-Mills thermodynamics, linking the lepton mass spectrum to the mass spectrum of ultralight axions, which are proposed as candidates for the Universe's dark matter.

The starting point from cosmology is the current tensions in the cosmological standard model currently ΛCDM are the discrepancies of the locally observed Hubble parameter H_0 [32], which is inversely proportional to the size of the universe with global, model-dependent observations of cosmic microwave radiation (CMB) [36]; as well as the local density distribution of dark matter (cf. ibid. and [222]). The advantage of a non-abelian Yang-Mills theory of the photon is the mitigation of both discrepancies with a consistent implementation in the cosmological model [33, 34] without fine-tuning. The essential characteristic of the modified cosmological model is the changed temperature-redshift relation: the cosmic microwave radiation cools down more slowly than under ΛCDM. Testing the modified temperature-redshift relation with cosmic ray propagation, which directly interact with the CMB photons, is one of the main objectives of this thesis.

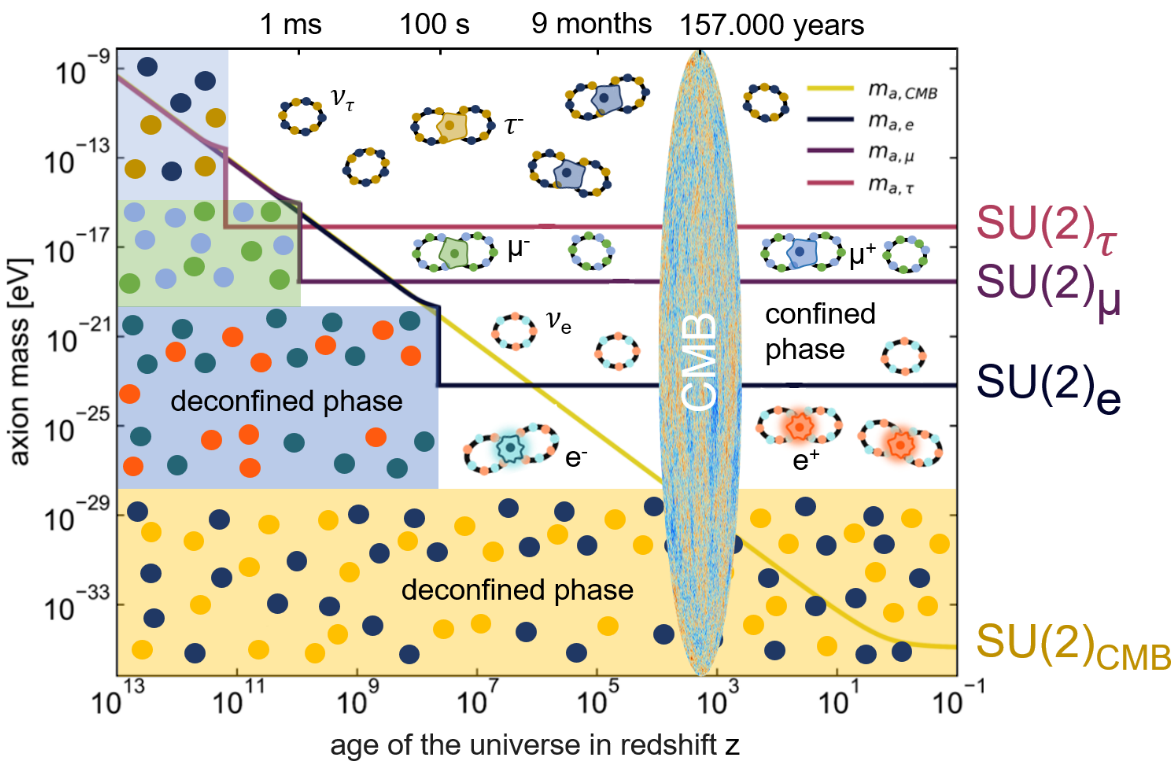

Figure 8.2: An overview of the axion masses in the framework of Yang-Mills thermodynamics, overlaid with the phase structures of the leptons and the deconfined phase of the photon. In this theoretical framework, leptons are immersed in the confined phase of the respective lepton theory after a Hagedorn phase transition. We aim to test a diluted CMB photon density which would occur in the deconfined phase of $SU(2)_{CMB}$ with the propagation of cosmic rays.

The prevailing view in the literature has been that this temperature-redshift relation could be determined from the Lyman-alpha forest and the thermal Sunyaev-Zel'dovich effect. We find that assuming a trivial frequency-redshift relation inevitably leads to a trivial temperature-redshift relation [3]. Therefore, these two methods are not sensitive to the actual temperature of the CMB, but at most to the temperature of the hydrogen and other absorbers (CO, NH_4) in the observed systems. The only method to measure the temperature of the CMB in the past seems to be via the interaction of CMB photons with propagating cosmic rays. Using cosmic ray propagation to probe the CMB photon density, we find that this particular ΛCDM modification remains viable and even supports UHECR propagation below $10^{18.5}$ eV. In particular, mild tendencies can be seen for the dominant source class of UHECRs: It seems that SU(2)$_{\rm CMB}$ favours UHECR sources, such as starburst galaxies with a relatively steady production rate, over active galactic nuclei as the primary source class of UHECRs. There are many other applications of our modified description of blackbody radiation in cosmology. The dark sector is particularly affected if one describes the thermal ground state not only of photons with an SU(2) gauge group, but each lepton family in thermodynamic equilibrium (electron, muon, tauon). An overview of the axion masses in the framework of Yang-Mills thermodynamics, overlaid with three thermal phases of the leptons and the deconfined phase of the photon, can be seen in Fig.8.2. The lightest axion species $m_{a,\gamma} \sim 10^{-35}\,$eV is associated with the Yang-Mills scale of the photon $\Lambda_{\rm CMB} \sim 10^{-4}$ eV and can be interpreted as dark energy, and three axion species interpreted as fuzzy and cold dark matter $m_{a,\ell} \sim 10^{-24} - 10^{-18}$ eV are related to the Yang-Mills scales of the leptons with $m_a \sim \Lambda^2/M_P$ in the confining phase of their respective Yang-Mills theory. The axion mass of each species is temperature dependent and proportional to $m_a \propto T^2/M_P$ in the deconfining phase. The Peccei-Quinn scale is thereby assumed to be the Planck mass M_P.

However, in order to falsify this modified cosmological model, we need laboratory experiments. If the thermal ground can be described with an SU(2) Yang-Mills theory, we expect screening effects for low frequencies and low temperatures (as well as Meissner massive photons in the so-called preconfined phase). First microwave cavity measurements were taken by the Istituto Nazionale di Ricerca Metrologica (INRiM), which show statistically significant excess noise power at 5.3 GHz and 10 K as well as mild tensions at higher frequencies up to 11.5 GHz. While this excess can be attributed to temperature gradients within the cavity, further cavity experiments at lower frequencies and temperatures are necessary to systematically probe potential deviations from Planck's radiation law. Lastly, by combining the deconfined phase of the photon and electron an electroweak mixing angle can be obtained, which can be interpreted as the Weinberg angle [5]. This thesis discusses an array of arguments which hint at a complex thermal constitution of photons and leptons, as well as a dark sector made up out of four Planck scale axion species. Further research is needed to assess the validity of this scenario and the hypothesis that photons and leptons emerge from pure SU(2) Yang-Mills theories.

8.2 Acknowledgments

I would like to express my deepest gratitude to my PhD supervisor, Professor Dr. Karl-Heinz Kampert, for giving me the opportunity to work in his group. As a leading expert in both astroparticle and particle physics, Prof. Kampert has always been a great teacher to me and provided valuable insights for my research. His ability to lead by example and to gather a team of inspiring and dedicated colleagues has created an outstanding environment for collaboration and learning, fostering a spirit of innovation and excellence. Professor Kampert's high scientific standards, passion and dedication for physics have shaped not only my research but also my overall approach to scientific inquiry. He is a true role model for young and aspiring physicists, and I am deeply appreciative of the opportunities he has provided me.

In addition, I would also like to extend my gratitude to PD Dr. Ralf Hofmann for graciously accepting the role of second corrector for this thesis. Throughout my PhD, Dr. Hofmann has been an exceptional mentor, offering invaluable guidance. His dedication to both scientific rigor, creative thinking and depth of knowledge have always inspired me to deepen my own understanding. I sincerely appreciate the enriching discussions and collaboration we have shared in recent years. His influence on my academic and personal growth has been profound, and I am truly grateful for his continued support.

Furthermore, I would like to express my deepest gratitude to my parents, Sabine and Dr. Thorsten Meinert, and my girlfriend, Inés Hidalgo Prados, for their unwavering support throughout this journey. I am also grateful to my friends for the many inspiring and thought-provoking discussions that have enriched both my work and personal growth. This thesis would not have been possible without continuous support and encouragement from my colleagues. In particular, I would like to thank Dr. Leonel Morejón, Therese Paulsen, Veronika Vašíčková, Dr. Alexander Sandrock, Dr. Baobiao Yue, Nick Schmeißer, Fabian Becker, Dr. Julian Rautenberg and Dr. Christian Pauly from BUW and from our neighboring university, RUB, I would like to especially thank Sophie Aerdker, Dr. Lukas Merten, Dr. Björn Eichmann and Professor Dr. Julia Tjus. The experimental search for a blackbody anomaly would not have been possible without Dr. Roberto Gavioso, Dr. Giorgio Brida, Dario Imbraguglio, Dr. Simone Corbellini, Dr. Christof Gaiser and PD Dr. Ralf Hofmann. It has been a great privilege to work with all of those outstanding researchers and to contribute to our joint research projects. I would also like to thank Dr. Sven Fabian, Dr. Alexander Sandrock and Dr. Baobiao Yue for corrections and discussions about the first draft of this thesis.

This research was generously supported by the Vector Foundation under grant number P2021-0102 and the DFG under the grant SFB 1491. The support of the Vector Foundation was invaluable for the success of projects c) - f) of this thesis, as seen in Fig. 1.2. In recognition of the outstanding support, I would like to specifically thank Dr. Kristine Bentz for the unwavering support of the Vector foundation. In particular, it enabled us to search experimentally for the blackbody anomaly at low temperatures. Likewise, projects a) and b) would not have been possible without generous support from the DFG.

List of Figures

1.1 Illustration from Camille Flammarion's L'atmosphère 1
1.2 Overview of the projects of this thesis 3
1.3 Cosmic ray flux spectrum - measurement with multiple experiments 4
1.4 Phase diagram of $SU(2)_{CMB}$ 6
1.5 The CMB radio excess observed by terrestrial radio antennas and balloon-borne experiments 7

2.1 Auger dipole in comparison with flux modulation induced dipole 9
2.2 Propagation distances of protons in PlanckJF12b - spectral index E^{-1} and $E^{-2.7}$ 12
2.3 EPOS-LHC composition and propagation distances in PlanckJF12b 13
2.4 The propagation length dependent anisotropy 13
2.5 A delta function like time variation of the UHECR flux alongside its induced right ascension 14
2.6 Comparison of the evolution of the dipole amplitude with energy 15
2.7 The energy dependent evolution of the dipole amplitude for different nuclei 16
2.8 Auger dipole comparison with a pure proton and a pure nitrogen injection 18

3.1 Fit to the cosmic ray flux spectum with diluted CMB photon density 19
3.2 The conventional $T(z)$ relation alongside its redshift dependent modification factor $\mathcal{S}(z)$. 23
3.3 Propagation length of protons for U(1) and the SU(2) CMB photon densities 24
3.4 Propagation length of iron for U(1) and the SU(2) CMB photon densities 25
3.5 Spectral fit to the 2017 Auger spectral flux data 26
3.6 Spectral fit using a gradient descent algorithm to the 2017 Auger spectral flux data 27
3.7 Seven modified CMB photon densities in comparison to the standard U(1) T-z relation . 28
3.8 The cosmogenic neutrino flux obtained from the gradient descent fit 29
3.9 Spectral fit to the 2017 Auger spectral flux data from the best fit parameters in Heinze et al. 30
3.10 Spectral fit to the 2017 Auger spectral flux data from the best fit parameters for $SU(2)_{CMB}$ 31

4.1 Temperature redshift evolution in ΛCDM and $SU(2)_{CMB}$ 33
4.2 The conventional $T(z)$ relation alongside its redshift dependent modification factor $\mathcal{S}(z)$. 40
4.3 The discrepancy of T-z in ΛCDM and $SU(2)_{CMB}$ 41

5.1 The CMB radio excess observed by terrestrial radio antennas and balloon-borne experiments 45
5.2 Illustration of the experimental setup of cavity at INRiM 47
5.3 The gain for the antenna $G_{21,\mathrm{A}}$ and the resistor $G_{21,\mathrm{R}}$ in dB from 5 - 11.5 GHz 50
5.4 The measured power difference between monopole antenna and resistor in dBm 50
5.5 Model fitting to the noise power difference D for $\nu = 5.3\,\mathrm{GHz}$ in **A** and $\nu = 8.8\,\mathrm{GHz}$ . . . 52
5.6 Frequency dependence of the mixing angle θ between U(1) and SU(2) radiation in the cavity 52
5.7 Cavity temperature gradient and corresponding antenna–resistor power difference 53
5.8 The scattering parameters used for calculating the gain amplification 55
5.9 Photos of the cavity at INRiM 56

6.1 Electroweak parameters from mixed SU(2) Yang-Mills thermodynamics 57
6.2 Phase diagram of the ground state of $SU(2)_{CMB}$ 62
6.3 The effective gauge coupling of the deconfining phase in SU(2) Yang-Mills thermodynamics 64
6.4 The electron as a dually interpreted magnetic monopole in SU(2) Yang-Mills theory . . . 66
6.5 The effective droplet charge due to a mirror charge construction 68
6.6 Phase diagram of the ground state of $SU(2)_{\mathrm{e}}$ 76
6.7 Illustration of the muon decay in Yang-Mills thermodynamics 79

7.1 The temperature dependent axion mass in deconfinement phases of SU(2) YMTD 81
7.2 The ratio of conventually used lattice sizes $L = 2/T_c$, and the caloron radius 83
7.3 Spatially coarse-graining a fundamental-theory caloron center 85
7.4 The weak y and λ dependences of function $4\pi x^2 \bar{Q}(x, y, \lambda)$ 86
7.5 The temperature dependent axion mass in deconfinement phases of SU(2) YMTD 89

8.1 19th century illustration of a world turtle, modified 95
8.2 Overview of the lepton and the dark sector in the framework of Yang-Mills thermodynamics 96

this page is intentionally left blank

Bibliography

[1] J. Meinert, L. Morejón, V. Vašíčková, L. Merten, S. Aerdker, J. Tjus, and K.-H. Kampert. Anisotropy and ultra-high-energy cosmic ray flux composition, in preparation, 2025.

[2] J. Meinert, L. Morejón, A. Sandrock, B. Eichmann, J. Kreidelmeyer, and K.-H. Kampert. Modified temperature–redshift relation and ultra-high-energy cosmic ray propagation. *Astrophys. J.*, 967(2):154, 2024.

[3] R. Hofmann and J. Meinert. Frequency–Redshift Relation of the Cosmic Microwave Background. *Astronomy*, 2(4):286–299, 2023.

[4] J. Meinert, R. Gavioso, G. Brida, S. Corbellini, C. Gaiser, D. Imbraguglio, and R. Hofmann. Rayleigh-jeans blackbody anomaly at low temperatures, in preparation, 2025.

[5] J. Meinert and R. Hofmann. Electroweak Parameters from Mixed SU(2) Yang–Mills Thermodynamics. *Symmetry*, 16(12):1587, 2024.

[6] R. Hofmann, J. Meinert, and D. Antonov. Axion Mass and the Ground State of Deconfining SU(2) Yang–Mills Thermodynamics. *Astronomy*, 3(4):319–333, 2024.

[7] J. Meinert, L. Morejón, A. Sandrock, B. Eichmann, J. Kreidelmeyer, and K.-H. Kampert. The impact of a modified CMB photon density on UHECR propagation. *PoS*, ICRC2023:322, 2023.

[8] J. Meinert and R. Hofmann. Electroweak mixing angle from SU(2) Yang-Mills Thermodynamics. *AIP Conference Proceedings*, ICNAAM 2024, 2024.

[9] R. Hofmann, D. Antonov, and J. Meinert. Deconfining SU(2) Yang-Mills Thermodynamics and the Temperature Dependence of the Axion Mass. *AIP Conference Proceedings*, ICNAAM 2024, 2024.

[10] V. F. Hess. Über Beobachtungen der durchdringenden Strahlung bei sieben Freiballonfahrten. *Phys. Z.*, 13:1084–1091, 1912.

[11] J. Clay. Penetrating radiation. *Proc. R. Acad.*, 30:1115–1127, 1927.

[12] P. Auger, P. Ehrenfest, R. Maze, J. Daudin, and Robley A. Fréon. Extensive cosmic-ray showers. *Rev. Mod. Phys.*, 11:288–291, Jul 1939.

[13] D. J. Bird et al. Detection of a cosmic ray with measured energy well beyond the expected spectral cutoff due to cosmic microwave radiation. *Astrophys. J.*, 441:144–150, 1995.

[14] K. Greisen. End to the cosmic ray spectrum? *Phys. Rev. Lett.*, 16:748–750, 1966.

[15] G. T. Zatsepin and V. A. Kuzmin. Upper limit of the spectrum of cosmic rays. *JETP Lett.*, 4:78–80, 1966.

[16] B. Yue et al. Constraints on BSM particles from the absence of upward-going air showers in the Pierre Auger Observatory. *PoS*, ICRC2023:1095, 2023.

[17] B. Yue. Constraints on uhe tau neutrino, tau, and tau-like particles generated from bsm scenarios with the pierre auger observatory. Poster presented at the Neutrino Conference, June 2024.

[18] K. Kotera and A. V. Olinto. The Astrophysics of Ultrahigh Energy Cosmic Rays. *Ann. Rev. Astron. Astrophys.*, 49:119–153, 2011.

[19] R. Alves Batista. The Quest for the Origins of Ultra-High-Energy Cosmic Rays. In *28th European Cosmic Ray Symposium*, 12 2024.

[20] J. Meinert. Condensates of ultralight axions and a link of leptonic scales to dark matter. Master's thesis, Universität Heidelberg, ITP, 2021.

[21] V. Verzi. Measurement of the energy spectrum of ultra-high energy cosmic rays using the Pierre Auger Observatory. *PoS*, ICRC2019:450, 2020.

[22] J. Matthews and Telescope Array Collaboration. Highlights from the Telescope Array Experiment. In *35th International Cosmic Ray Conference (ICRC2017)*, volume 301 of *International Cosmic Ray Conference*, page 1096, July 2017.

[23] M. R. Finger. *Reconstruction of energy spectra for different mass groups of high-energy cosmic rays.* PhD thesis, Karlsruher Institut für Technologie (KIT), 2011.

[24] V. Grebenyuk, D. Karmanov, I. Kovalev, I. Kudryashov, A. Kurganov, A. Panov, D. Podorozhny, et al. Energy spectra of abundant cosmic-ray nuclei in the nucleon experiment. *Adv. Space Res.*, 64(12):2546–2558, 2019. Advances in Cosmic-Ray Astrophysics and Related Areas.

[25] M. Amenomori et al. The All-particle spectrum of primary cosmic rays in the wide energy range from 10^{14} eV to 10^{17} eV observed with the Tibet-III air-shower array. *Astrophys. J.*, 678:1165–1179, 2008.

[26] R. Alfaro, C. Alvarez, J. D. Álvarez, R. Arceo, J. C. Arteaga-Velázquez, D. Avila Rojas, et al. All-particle cosmic ray energy spectrum measured by the hawc experiment from 10 to 500 tev. *Phys. Rev. D*, 96:122001, Dec 2017.

[27] M. G. Aartsen et al. Cosmic ray spectrum and composition from PeV to EeV using 3 years of data from IceTop and IceCube. *Phys. Rev. D*, 100(8):082002, 2019.

[28] N. M. Budnev et al. The primary cosmic-ray energy spectrum measured with the Tunka-133 array. *Astropart. Phys.*, 117:102406, 2020.

[29] M. Bertaina et al. KASCADE-Grande energy spectrum of cosmic rays interpreted with post-LHC hadronic interaction models. *PoS*, ICRC2015:359, 2016.

[30] C. Evoli. The cosmic-ray energy spectrum, December 2020. Reference for the GitHub repository: https://github.com/carmeloevoli/The_CR_Spectrum.

[31] R. Hofmann. *The Thermodynamics of Quantum Yang-Mills Theory: Theory and Applications.* World Sci. Publ., 2016.

[32] A. G. Riess et al. A Comprehensive Measurement of the Local Value of the Hubble Constant with 1 km s^{-1} Mpc^{-1} Uncertainty from the Hubble Space Telescope and the SH0ES Team. *Astrophys. J. Lett.*, 934(1):L7, 2022.

[33] S. Hahn, R. Hofmann, and D. Kramer. $SU(2)_{CMB}$ and the cosmological model: angular power spectra. *Mon. Not. Roy. Astron. Soc.*, 482(4):4290, 2019.

[34] R. Hofmann, J. Meinert, and S. S. Balaji. Cosmological Parameters from Planck Data in SU(2)CMB, Their Local ΛCDM Values, and the Modified Photon Boltzmann Equation. *Ann. Phys. (Berlin)*, 535(7):2200517, 2023.

[35] A. G. Riess, G. S. Anand, W. Yuan, S. Casertano, A. Dolphin, L. M. Macri, L. Breuval, et al. JWST Observations Reject Unrecognized Crowding of Cepheid Photometry as an Explanation for the Hubble Tension at 8σ Confidence. *Astrophys. J. Lett.*, 962(1):L17, 2024.

[36] N. Aghanim et al. Planck 2018 results. VI. Cosmological parameters. *Astron. Astrophys.*, 641:A6, 2020. [Erratum: Astron.Astrophys. 652, C4 (2021)].

[37] N. Schöneberg, J. Lesgourgues, and D. C. Hooper. The BAO+BBN take on the Hubble tension. *J. Cosmol. Astropart. Phys.*, 10:029, 2019.

[38] J. M. Shull, B. D. Smith, and C. W. Danforth. The Baryon Census in a Multiphase Intergalactic Medium: 30% of the Baryons May Still Be Missing. *Astrophys. J.*, 759:23, 2012.

[39] S. D. Johnson, J. S. Mulchaey, H.-W. Chen, et al. The physical origins of the identified and still missing components of the warm–hot intergalactic medium: Insights from deep surveys in the field of blazar 1es1553+113. *Astrophys. J. Lett.*, 884(2):L31, oct 2019.

[40] S. Hahn and R. Hofmann. $SU(2)_{CMB}$ at high redshifts and the value of H_0. *Mon. Not. Roy. Astron. Soc.*, 469(1):1233–1245, 2017.

[41] J. Meinert and R. Hofmann. Axial Anomaly in Galaxies and the Dark Universe. *Universe*, 7(6):198, 2021.

[42] M. Seiffert, D. J. Fixsen, A. Kogut, S. M. Levin, M. Limon, P. M. Lubin, P. Mirel, J. Singal, T. Villela, E. Wollack, and C. A. Wuensche. Interpretation of the ARCADE 2 absolute sky brightness measurement. *Astrophys. J.*, 734(1):6, may 2011.

[43] R. Hofmann. The isolated electron: De Broglie's 'hidden' thermodynamics, SU(2) Quantum Yang-Mills theory, and a strongly perturbed BPS monopole. *Entropy*, 19:575, 2017.

[44] R. Hofmann and T. Grandou. On Emergent Particles and Stable Neutral Plasma Balls in SU(2) Yang-Mills Thermodynamics. *Universe*, 8(2):117, 2022.

[45] D. Clowe, A. Gonzalez, and M. Markevitch. Weak lensing mass reconstruction of the interacting cluster 1E0657-558: Direct evidence for the existence of dark matter. *Astrophys. J.*, 604:596–603, 2004.

[46] V. C. Rubin and Jr. F., W.Kent. Rotation of the Andromeda Nebula from a Spectroscopic Survey of Emission Regions. *Astrophys. J.*, 159:379–403, 1970.

[47] D. N. Spergel et al. First year Wilkinson Microwave Anisotropy Probe (WMAP) observations: Determination of cosmological parameters. *Astrophys. J. Suppl.*, 148:175–194, 2003.

[48] F. Giacosa, R. Hofmann, and M. Neubert. A model for the very early Universe. *J. High Energy Phys.*, 02:077, 2008.

[49] S. U. Ji and S. J. Sin. Late time phase transition and the galactic halo as a bose liquid: 2. The Effect of visible matter. *Phys. Rev. D*, 50:3655–3659, 1994.

[50] A. Abdul Halim et al. Large-scale Cosmic-ray Anisotropies with 19 yr of Data from the Pierre Auger Observatory. *Astrophys. J.*, 976(1):48, 2024.

[51] T. Bister, G. R. Farrar, and M. Unger. The Large-scale Anisotropy and Flux (de)magnification of Ultrahigh-energy Cosmic Rays in the Galactic Magnetic Field. *Astrophys. J. Lett.*, 975(1):L21, 2024.

[52] A. di Matteo et al. UHECR arrival directions in the latest data from the original Auger and TA surface detectors and nearby galaxies. *PoS*, ICRC2021:308, 2021.

[53] A. M. Taylor, J. H. Matthews, and A. R. Bell. UHECR echoes from the Council of Giants. *Mon. Not. Roy. Astron. Soc.*, 524(1):631–642, 2023.

[54] R. Adam et al. Planck intermediate results.: XLII. Large-scale Galactic magnetic fields. *Astron. Astrophys.*, 596:A103, 2016.

[55] M. Unger and G. R. Farrar. The Coherent Magnetic Field of the Milky Way. *Astrophys. J.*, 970(1):95, 2024.

[56] R. Jansson and G. R. Farrar. The Galactic Magnetic Field. *Astrophys. J. Lett.*, 761:L11, 2012.

[57] A. Bakalová, J. Vícha, and P. Trávníček. Modification of the dipole in arrival directions of ultra-high-energy cosmic rays due to the Galactic magnetic field. *J. Cosmol. Astropart. Phys.*, 12:016, 2023.

[58] R. Alves Batista, A. Dundovic, M. Erdmann, K.-H. Kampert, D. Kuempel, et al. CRPropa 3 - a Public Astrophysical Simulation Framework for Propagating Extraterrestrial Ultra-High Energy Particles. *J. Cosmol. Astropart. Phys.*, 05:038, 2016.

[59] R. Alves Batista and others. CRPropa 3.2 — an advanced framework for high-energy particle propagation in extragalactic and galactic spaces. *J. Cosmol. Astropart. Phys.*, 09:035, 2022.

[60] A. Aab et al. Combined fit of spectrum and composition data as measured by the Pierre Auger Observatory. *J. Cosmol. Astropart. Phys.*, 04:038, 2017. [Erratum: J. Cosmol. Astropart. Phys. 03, E02 (2018)].

[61] D. Bergman et al. Testing the Compatibility of the Depth of the Shower Maximum Measurements performed at Telescope Array and the Pierre Auger Observatory - Auger-TA Mass Composition Working Group Report. *EPJ Web Conf.*, 283:02008, 2023.

[62] E. L. Wright. Theoretical overview of cosmic microwave background anisotropy. In *Carnegie Observatories Centennial Symposium. 2. Measuring and Modeling the Universe*, pages 291–308, 5 2003.

[63] D. J. Fixsen et al. ARCADE 2 Measurement of the Extra-Galactic Sky Temperature at 3-90 GHz. *Astrophys. J.*, 734:5, 2011.

[64] J. Dowell and G. B. Taylor. The Radio Background Below 100 MHz. *Astrophys. J. Lett.*, 858(1):L9, 2018.

[65] S. A. Tompkins, S. P. Driver, A. S. G. Robotham, R. A. Windhorst, et al. The cosmic radio background from 150 MHz to 8.4 GHz and its division into AGN and star-forming galaxy flux. *Mon. Not. Roy. Astron. Soc*, 521(1):332–353, 01 2023.

[66] A. Caputo, M. Regis, M. Taoso, and S. J. Witte. Detecting the Stimulated Decay of Axions at RadioFrequencies. *J. Cosmol. Astropart. Phys.*, 03:027, 2019.

[67] R. Hofmann. Low-frequency line temperatures of the CMB. *Ann. Phys. (Berlin)*, 18:634, 2009.

[68] B. J. Harrington and Harvey K. Shepard. Periodic Euclidean Solutions and the Finite Temperature Yang-Mills Gas. *Phys. Rev. D*, 17:2122, 1978.

[69] J. C. Mather, D. J. Fixsen, R. A. Shafer, C. Mosier, and D. T. Wilkinson. Calibrator design for the COBE far infrared absolute spectrophotometer (FIRAS). *Astrophys. J.*, 512:511–520, 1999.

[70] T. Tröster, Ariel. G. Sánchez, C. Asgari, M.and Blake, M. Crocce, C. Heymans, et al. Cosmology from large-scale structure. *Astron. Astrophys.*, 633:L10, Jan 2020.

[71] H. Miyatake et al. Cosmological inference from the emulator based halo model II: Joint analysis of galaxy-galaxy weak lensing and galaxy clustering from HSC-Y1 and SDSS, 11 2021.

[72] D. A. Riechers, A. Weiss, F. Walter, C. L. Carilli, P. Cox, R. Decarli, and R. Neri. Microwave background temperature at a redshift of 6.34 from H_2O absorption. *Nature*, 602(7895):58–62, February 2022.

[73] F. J. Tipler and D. W. Piasecki. Using UHE Cosmic Rays to Probe the CBR and Test Standard Model Particle Physics, 9 2018.

[74] S. Hahn and R. Hofmann. Exact determination of asymptotic CMB temperature-redshift relation. *Mod. Phys. Lett. A*, 2016(05):1850029, 2018.

[75] D. J. Gross and F. Wilczek. Ultraviolet Behavior of Nonabelian Gauge Theories. *Phys. Rev. Lett.*, 30:1343–1346, 1973.

[76] H. D. Politzer. Reliable Perturbative Results for Strong Interactions? *Phys. Rev. Lett.*, 30:1346–1349, 1973.

[77] V. S. Berezinskii, S. V. Bulanov, V. A. Dogiel, and V. S. Ptuskin. *Astrophysics of cosmic rays.* North-Holland, Amsterdam, 1990.

[78] J Heinze, A. Fedynitch, D. Boncioli, and W. Winter. A new view on Auger data and cosmogenic neutrinos in light of different nuclear disintegration and air-shower models. *Astrophys. J.*, 873(1):88, 2019.

[79] P. Perrotta. *Programming Machine Learning: From Coding to Deep Learning, 1st edition.* Pragmatic Bookshelf, 05 2020.

[80] M.o Ave, N. Busca, Angela V. Olinto, Alan A. Watson, and T. Yamamoto. Cosmogenic neutrinos from ultra-high energy nuclei. *Astropart. Phys.*, 23:19–29, 2005.

[81] M. G. Aartsen et al. Neutrino astronomy with the next generation IceCube Neutrino Observatory, 11 2019. arXiv: 1911.02561 [astro-ph.HE].

[82] J. Álvarez-Muñiz et al. The Giant Radio Array for Neutrino Detection (GRAND): Science and Design. *Sci. China Phys. Mech. Astron.*, 63(1):219501, 2020.

[83] M. G. Aartsen et al. Differential limit on the extremely-high-energy cosmic neutrino flux in the presence of astrophysical background from nine years of IceCube data. *Phys. Rev. D*, 98(6):062003, 2018.

[84] A. Aab et al. Probing the origin of ultra-high-energy cosmic rays with neutrinos in the EeV energy range using the Pierre Auger Observatory. *J. Cosmol. Astropart. Phys.*, 10:022, 2019.

[85] T. Bister. Sensitivity of the combined fit of energy spectrum, shower depth distributions, and arrival directions at the Pierre Auger Observatory. *EPJ Web Conf.*, 283:03008, 2023.

[86] P. Abreu et al. Arrival Directions of Cosmic Rays above 32 EeV from Phase One of the Pierre Auger Observatory. *Astrophys. J.*, 935(2):170, 2022.

[87] J. Bellido. Depth of maximum of air-shower profiles at the Pierre Auger Observatory: Measurements above $10^{17.2}$ eV and Composition Implications. *PoS*, ICRC2017:506, 2018.

[88] T. Pierog, I. Karpenko, J. M. Katzy, E. Yatsenko, and K. Werner. EPOS LHC: Test of collective hadronization with data measured at the CERN Large Hadron Collider. *Phys. Rev. C*, 92(3):034906, 2015.

[89] F. Riehn, R. Engel, A. Fedynitch, T. K. Gaisser, and T. Stanev. A new version of the event generator Sibyll. *PoS*, ICRC2015:558, 2016.

[90] S. Ostapchenko. Monte Carlo treatment of hadronic interactions in enhanced Pomeron scheme: I. QGSJET-II model. *Phys. Rev. D*, 83:014018, 2011.

[91] J. C. Mather, E. S. Cheng, D. A. Cottingham, Jr. Eplee, R. E., D. J. Fixsen, T. Hewagama, R. B. Isaacman, et al. Measurement of the Cosmic Microwave Background Spectrum by the COBE FIRAS Instrument. *Astrophys. J.*, 420:439, January 1994.

[92] N. Aghanim et al. Planck 2018 results. VI. Cosmological parameters. *Astron. Astrophys.*, 641:A6, 2020.

[93] S. Weinberg. *Gravitation and Cosmology: Principles and Applications of the General Theory of Relativity.* J. Wiley and Sons, New York, 1972.

[94] R. Hofmann. SU(2) Yang-Mills Theory: Waves, Particles, and Quantum Thermodynamics. *Entropy*, 18:310, 2016.

[95] M. Szopa and R. Hofmann. A Model for CMB anisotropies on large angular scales. *J. Cosmol. Astropart. Phys.*, 03:001, 2008.

[96] R. Hofmann. The fate of statistical isotropy. *Nature Phys.*, 9(11):686–689, 2013.

[97] R. Hofmann. Relic photon temperature versus redshift and the cosmic neutrino background. *Ann. Phys. (Berlin)*, 527:254, 2015.

[98] A. Songaila, L. L. Cowie, S. Vogt, M. Keane, A. M. Wolfei, E. M. Hu, A. L. Oren, D. R. Tytleri, and K. M. Lanzetta. Measurement of the microwave background temperature at a redshift of 1.776. *Nature*, 371(6492):43–45, September 1994.

[99] J. Ge, J. Bechtold, and J. H. Black. A New Measurement of the Cosmic Microwave Background Radiation Temperature at z = 1.97. *Astrophys. J.*, 474(1):67–73, January 1997.

[100] R. Srianand, P. Petitjean, and C. Ledoux. The cosmic microwave background radiation temperature at a redshift of 2.34. *Nature*, 408(6815):931–935, December 2000.

[101] P. Molaro, S. A. Levshakov, M. Dessauges-Zavadsky, and S. D'Odorico. The cosmic microwave background radiation temperature at $z_{abs} = 3.025$ toward QSO 0347-3819. *Astron. Astrophys.*, 381:L64–L67, January 2002.

[102] P. Noterdaeme, P. Petitjean, R. Srianand, C. Ledoux, and S. López. The evolution of the cosmic microwave background temperature. Measurements of T_{CMB} at high redshift from carbon monoxide excitation. *Astron. Astrophys.*, 526:L7, February 2011.

[103] P. Noterdaeme, J. K. Krogager, S. Balashev, J. Ge, N. Gupta, T. Krühler, C. Ledoux, M. T. Murphy, I. Pâris, et al. Discovery of a Perseus-like cloud in the early Universe. H I-to-H_2 transition, carbon monoxide and small dust grains at $z_{abs} \approx 2.53$ towards the quasar J0000+0048. *Astron. Astrophys.*, 597:A82, January 2017.

[104] A. Maeder. Scale-invariant Cosmology and CMB Temperatures as a Function of Redshifts. *Astrophys. J.*, 847(1):65, September 2017.

[105] S. Muller, A. Beelen, J. H. Black, S. J. Curran, C. Horellou, S. Aalto, F. Combes, M. Guélin, and C. Henkel. A precise and accurate determination of the cosmic microwave background temperature at z = 0.89. *Astron. Astrophys.*, 551:A109, March 2013.

[106] Y. B. Zeldovich and R. A. Sunyaev. The Interaction of Matter and Radiation in a Hot-Model Universe. *Astrophys. Space Sci.*, 4(3):301–316, July 1969.

[107] R. A. Sunyaev and Y. B. Zeldovich. The Observations of Relic Radiation as a Test of the Nature of X-Ray Radiation from the Clusters of Galaxies. *Comm. Astrophys. Space Phys.*, 4:173, November 1972.

[108] J. N. Bahcall and Richard A. Wolf. Fine-Structure Transitions. *Astrophys. J.*, 152:701, June 1968.

[109] K. C. Roth, D. M. Meyer, and I. Hawkins. Interstellar Cyanogen and the Temperature of the Cosmic Microwave Background Radiation. *Astrophys. J.*, 413:L67, August 1993.

[110] G. Hurier, N. Aghanim, M. Douspis, and E. Pointecouteau. Measurement of the T_{CMB} evolution from the Sunyaev-Zel'dovich effect. *Astron. Astrophys.*, 561:A143, January 2014.

[111] F. Giacosa and R. Hofmann. A Planck-scale axion and SU(2) Yang-Mills dynamics: Present acceleration and the fate of the photon. *Eur. Phys. J. C*, 50:635–646, 2007.

[112] T. Trombetti and C. Burigana. Semi-analytical description of clumping factor and cosmic microwave background free–free distortions from reionization. *Mon. Not. R. Astron. Soc.*, 437(3):2507–2520, 11 2013.

[113] S. P. Oh. Observational signatures of the first luminous objects. *Astrophys. J.*, 527:16, 1999.

[114] N. Fornengo, R. Lineros, M. Regis, and M. Taoso. Possibility of a dark matter interpretation for the excess in isotropic radio emission reported by arcade. *Phys. Rev. Lett.*, 107:271302, Dec 2011.

[115] M. Baiesi, Carlo Burigana, Livia Conti, Gianmaria Falasco, Christian Maes, Lamberto Rondoni, and Tiziana Trombetti. Possible nonequilibrium imprint in the cosmic background at low frequencies. *Phys. Rev. Res.*, 2:013210, Feb 2020.

[116] P. L. Biermann, B. B. Nath, L. I. Caramete, B. C. Harms, T. Stanev, and J. B. Tjus. Cosmic backgrounds due to the formation of the first generation of supermassive black holes. *Mon. Not. R. Astron. Soc.*, 441(2):1147–1156, 05 2014.

[117] J. Bowman, A. Rogers, R. Monsalve, T. J. Mozdzen, and N. Mahesh. An absorption profile centred at 78 megahertz in the sky-averaged spectrum. *Nature*, 555:67, 2018.

[118] R. Barkana. Possible interaction between baryons and dark-matter particles revealed by the first stars. *Nature*, 555:71, 2018.

[119] G. Fodor and I. Rácz. What does a strongly excited 't Hooft–Polyakov magnetic monopole do? *Phys. Rev. Lett.*, 92(15), apr 2004.

[120] P. Forgács and M. S. Volkov. Resonant excitations of the 't Hooft–Polyakov monopole. *Phys. Rev. Lett.*, 92(15), apr 2004.

[121] L. De Broglie. Recherches sur la théorie des quanta. *Ann. Phys.*, 10(3):22–128, 1925.

[122] L. De Broglie. *The Thermodynamics of the Isolated Particle*. Gauthier-Villars, Paris, 1964. Translated by D. H. Delphenich.

[123] E. Schrödinger. Quantisierung als eigenwertproblem. *Ann. Phys. (Berlin)*, 384(4):361–376, 1926.

[124] M. Born. Zur Quantenmechanik der Stoßvorgänge. *Zeitschrift für Physik*, 37(12):863, 1926.

[125] C. Falquez. Investigation of Thermal Ground-State Effects in SU(2) Yang-Mills Thermodynamics. Master's thesis, KIT, Karlsruhe, 2011.

[126] S. N. Bose. Planck's law and light quantum hypothesis. *Z. Phys.*, 26:178–181, 1924.

[127] A. Einstein. Quantentheorie des einatomigen idealen gases – zweite abhandlung. *Sitzungsber. Preuss. Akad. Wiss. Berlin*, page 3, January 1925.

[128] A. S. Rabinowitch. On a new class of progressive waves in Yang–Mills fields with SU(2) symmetry. *Nucl. Phys. B*, 1001:116505, 2024.

[129] J. C. Mather et al. A Preliminary measurement of the Cosmic Microwave Background spectrum by the Cosmic Background Explorer (COBE) satellite. *Astrophys. J. Lett.*, 354:L37–L40, 1990.

[130] D. J. Fixsen. The temperature of the cosmic microwave background. *Astrophys. J.*, 707(2):916–920, November 2009.

[131] J. Ludescher and R. Hofmann. Thermal photon dispersion law and modified black-body spectra. *Ann. Phys. (Berlin)*, 18:271–280, 2009.

[132] C. Falquez, R. Hofmann, and T. Baumbach. Modification of black-body radiance at low temperatures and frequencies. *Ann. Phys. (Berlin)*, 522:904–911, 2010.

[133] D. M. Ripa, D. Imbraguglio, C. Gaiser, P. P. M. Steur, D. Giraudi, M. Fogliati, M. Bertinetti, G. Lopardo, R. Dematteis, and R. M. Gavioso. Refractive index gas thermometry between 13.8 k and 161.4 k. *Metrologia*, 58(2):025008, mar 2021.

[134] B. Gao et al. Realization of an ultra-high precision temperature control in a cryogen-free cryostat. *Review of Scientific Instruments*, 89(10):104901, 10 2018.

[135] G. 't Hooft. Renormalizable Lagrangians for Massive Yang-Mills Fields. *Nucl. Phys. B*, 35:167–188, 1971.

[136] G. 't Hooft. Renormalization of Massless Yang-Mills Fields. *Nucl. Phys. B*, 33:173–199, 1971.

[137] G. 't Hooft and M. J. G. Veltman. Regularization and Renormalization of Gauge Fields. *Nucl. Phys. B*, 44:189–213, 1972.

[138] A. Sommerfeld. Zur quantentheorie der spektrallinien. *Ann. Phys. (Berlin)*, 356(17):1–94, 1916.

[139] L. Morel, Z. Yao, P. Cladé, and S. Guellati-Khélifa. Determination of the fine-structure constant with an accuracy of 81 parts per trillion. *Nature*, 588:61–65, 2020.

[140] S. L. Glashow. The renormalizability of vector meson interactions. *Nucl. Phys.*, 10:107–117, 1959.

[141] A. Salam and J. C. Ward. Electromagnetic and weak interactions. *Phys. Lett.*, 13:168–171, 1964.

[142] A. Salam and J. C. Ward. Weak and electromagnetic interactions. *Nuovo Cim.*, 11:568–577, 1959.

[143] R. L. Workman et al. Review of Particle Physics. *PTEP*, 2022:083C01, 2022.

[144] P. L. Anthony et al. Precision measurement of the weak mixing angle in Moller scattering. *Phys. Rev. Lett.*, 95:081601, 2005.

[145] A. Pich. The standard model of electroweak interactions, 1994. arXiv: 9412274 [hep-ph].

[146] L. de Broglie. The reinterpretation of wave mechanics. *Foundations of Physics*, 1:5–15, 1970.

[147] G. Dattoli. The fine structure constant and numerical alchemy, 2010. arXiv: 1009.1711 [gen-ph].

[148] U.D. Jentschura and I. Nándori. Attempts at a determination of the fine-structure constant from first principles: a brief historical overview. *The European Physical Journal H*, 39(5):591–613, December 2014.

[149] M. A. Faessler. Weinberg angle and integer electric charges of quarks, August 2013. arXiv: 1308.5900 [hep-ph].

[150] C. Englert, D. J. Miller, and D. D. Smaranda. The Weinberg angle and 5d RGE effects in a SO(11) GUT theory. *Phys. Lett. B*, 807:135548, 2020.

[151] R. P. Feynman. The theory of positrons. *Phys. Rev.*, 76:749–759, Sep 1949.

[152] C. Bargsten, R. Hollinger, M. G. Capeluto, Vural K., A. Pukhov, S. Wang, A. Rockwood, et al. Energy penetration into arrays of aligned nanowires irradiated with relativistic intensities: Scaling to terabar pressures. *Science Advances*, 3(1):e1601558, 2017.

[153] R. Hofmann and Dariush Kaviani. The quantum of action and finiteness of radiative corrections: Deconfining SU(2) Yang-Mills thermodynamics. *Quant. Matt.*, 1:41–52, 2012.

[154] D. Diakonov, N. Gromov, V. Petrov, and S. Slizovskiy. Quantum weights of dyons and of instantons with nontrivial holonomy. *Phys. Rev. D*, 70(3), aug 2004.

[155] J. Ludescher, Jochen Keller, F. Giacosa, and R. Hofmann. Spatial Wilson loop in continuum, deconfining SU(2) Yang-Mills thermodynamics. *Ann. Phys. (Berlin)*, 19:102–120, 2010.

[156] P. Gerhold, E.-M. Ilgenfritz, and M. Müller-Preussker. An KvBLL caloron gas model and confinement. *Nucl. Phys. B*, 760(1-2):1–37, jan 2007.

[157] G. 't Hooft. On the Phase Transition Towards Permanent Quark Confinement. *Nucl. Phys. B*, 138:1–25, 1978.

[158] J. Moosmann and R. Hofmann. Evolving center-vortex loops. *ISRN Math. Phys.*, 2012:236783, 2012.

[159] L. Del Debbio, M. Faber, J. Greensite, and S. Olejnik. Center dominance, center vortices, and confinement. In *NATO Advanced Research Workshop on Theoretical Physics: New Developments in Quantum Field Theory*, pages 47–64, 6 1997.

[160] M. A. Grayson. The shape of a figure-eight under the curve shortening flow. *Inventiones mathematicae*, 96(1):177–180, 1989.

[161] G. Breit. An interpretation of dirac's theory of the electron. *Proc. Natl. Acad. Sci.*, 14(1928):553–559, 1928.

[162] E. Schrödinger. Über die kräftefreie bewegung in der relativistischen quantenmechanik. *Akad. Wiss. Kommiss. W. de Gruyter*, pages 418–428, 1930.

[163] J. Schwinger. On quantum-electrodynamics and the magnetic moment of the electron. *Phys. Rev.*, 73:416–417, Feb 1948.

[164] M. Zahn. MIT OpenCourseWare, 2.7: The Method of Images with Point Charges and Spheres, 2023. `https://shorturl.at/MPOrP`.

[165] J. Ludescher and R. Hofmann. CMB dipole revisited. arXiv: 0902.3898 [hep-th], February 2009.

[166] T. S. Roussy, L. Caldwell, T. Wright, W. B. Cairncross, Y. Shagam, et al. An improved bound on the electron's electric dipole moment. *Science*, 381(6653):46–50, 2023.

[167] R. Hofmann. Electromagnetic waves and photons. arXiv: 1508.02270 [gen-ph], July 2015.

[168] S. Weinberg. A Model of Leptons. *Phys. Rev. Lett.*, 19:1264–1266, 1967.

[169] T. Grandou, R. Hofmann, and P. H. Tsang. Chiral Symmetry Breaking out of QCD Effective Locality. *AIP Conf. Proc.*, 2116(1):170005, 2019.

[170] K.-M. Lee and C. Lu. SU(2) calorons and magnetic monopoles. *Phys. Rev. D*, 58:025011, 1998.

[171] T. C. Kraan and Pierre van Baal. Periodic instantons with nontrivial holonomy. *Nucl. Phys. B*, 533:627–659, 1998.

[172] E. Schrödinger. Quantisierung als Eigenwertproblem. *Ann. Phys.*, 386(18):109–139, 1926.

[173] P. G. Merli, G. F. Missiroli, and G. Pozzi. On the statistical aspect of electron interference phenomena. *Am. J. Phys.*, 44(3):306–307, March 1976.

[174] F.M. Laggner, A. Diallo, M. Cavedon, and E. Kolemen. Inter-elm pedestal localized fluctuations in tokamaks: Summary of multi-machine observations. *Nucl. Mater. Energy*, 19:479–486, 2019.

[175] W. Stacey. Effect of ion orbit loss on the structure in the h-mode tokamak edge pedestal profiles of rotation velocity, radial electric field, density, and temperature. *Phys. Plasmas*, 20:2508–, 09 2013.

[176] D. J. Gross and F. Wilczek. Ultraviolet behavior of non-abelian gauge theories. *Phys. Rev. Lett.*, 30:1343–1346, Jun 1973.

[177] D. C. Tsui, H. L. Stormer, and A. C. Gossard. Two-dimensional magnetotransport in the extreme quantum limit. *Phys. Rev. Lett.*, 48:1559–1562, May 1982.

[178] R. B. Laughlin. Quantized hall conductivity in two dimensions. *Phys. Rev. B*, 23:5632–5633, May 1981.

[179] R. B. Laughlin. Anomalous quantum hall effect: An incompressible quantum fluid with fractionally charged excitations. *Phys. Rev. Lett.*, 50:1395–1398, May 1983.

[180] J. C. Taylor. Ward Identities and Charge Renormalization of the Yang-Mills Field. *Nucl. Phys. B*, 33:436–444, 1971.

[181] A. A. Slavnov. Ward Identities in Gauge Theories. *Theor. Math. Phys.*, 10:99–107, 1972.

[182] A. G. Riess, A. V. Filippenko, P. Challis, A. Clocchiatti, A. Diercks, P. M. Garnavich, et al. Observational evidence from supernovae for an accelerating universe and a cosmological constant. *Astron. J.*, 116(3):1009, Sep 1998.

[183] S. Perlmutter et al. Measurements of Ω and Λ from 42 high redshift supernovae. *Astrophys. J.*, 517:565–586, 1999.

[184] M. J. Choi, L. Bardōczi, J.-M. Kwon, T. S. Hahm, H. K. Park, J. Kim, et al. Effects of plasma turbulence on the nonlinear evolution of magnetic island in tokamak. *Nat. Commun.*, 12:375, 2021.

[185] D. J. Gross, Robert D. Pisarski, and Laurence G. Yaffe. Qcd and instantons at finite temperature. *Rev. Mod. Phys.*, 53:43–80, Jan 1981.

[186] T. Schäfer and E. V. Shuryak. Instantons in qcd. *Rev. Mod. Phys.*, 70:323–425, Apr 1998.

[187] E. Berkowitz, M. I. Buchoff, and E. Rinaldi. Lattice qcd input for axion cosmology. *Phys. Rev. D*, 92:034507, Aug 2015.

[188] S. Borsanyi, M. Dierigl, Z. Fodor, S. D. Katz, S. W. Mages, D. Nogradi, J. Redondo, A. Ringwald, and K. K. Szabo. Axion cosmology, lattice QCD and the dilute instanton gas. *Phys. Lett. B*, 752:175–181, 2016.

[189] C. Gattringer, M. Göckeler, P.E.L. Rakow, S. Schaefer, and A. Schäfer. A comprehensive picture of topological excitations in finite temperature lattice qcd. *Nucl. Phys. B*, 618(1):205–240, 2001.

[190] C. Gattringer, R. Hoffmann, and S. Schaefer. The topological susceptibility of su(3) gauge theory near tc. *Phys. Lett. B*, 535(1):358–362, 2002.

[191] P. T. Jahn, Guy D. Moore, and D. Robaina. $\chi_{\rm top}(t \gg T_{\rm c})$ in pure-glue qcd through reweighting. *Phys. Rev. D*, 98:054512, Sep 2018.

[192] F. Burger, E.-M. Ilgenfritz, M. P. Lombardo, M. Müller-Preussker, and A. Trunin. Topology (and axion's properties) from lattice qcd with a dynamical charm. *Nuclear Physics A*, 967:880–883, 2017. The 26th International Conference on Ultra-relativistic Nucleus-Nucleus Collisions: Quark Matter 2017.

[193] L. Giusti and M. Lüscher. Topological susceptibility at $t > t_{\mathrm{c}}$ from master-field simulations of the su(3) gauge theory. *Eur. Phys. J. C*, 79:207, Sep 2019.

[194] D. Antonov. Topological susceptibility of the gluon plasma in the stochastic-vacuum approach. *Universe*, 10(9), 2024.

[195] S.-J. Sin. Late time cosmological phase transition and galactic halo as Bose liquid. *Phys. Rev. D*, 50:3650–3654, 1994.

[196] A. Suárez, V.H. Robles, and T. Matos. A Review on the Scalar Field/Bose-Einstein Condensate Dark Matter Model. *Astrophys. Space Sci. Proc.*, 38:107–142, 2014.

[197] J. Magana and T. Matos. A brief Review of the Scalar Field Dark Matter model. *J. Phys. Conf. Ser.*, 378:012012, 2012.

[198] H.-Y. Schive, T. Chiueh, and T. Broadhurst. Cosmic Structure as the Quantum Interference of a Coherent Dark Wave. *Nature Phys.*, 10:496–499, 2014.

[199] L. A. Martinez-Medina, V. H. Robles, and T. Matos. Dwarf galaxies in multistate scalar field dark matter halos. *Phys. Rev. D*, 91:023519, Jan 2015.

[200] L. Hui, J. P. Ostriker, S. Tremaine, and E. Witten. Ultralight scalars as cosmological dark matter. *Phys. Rev. D*, 95(4):043541, 2017.

[201] J. C. Niemeyer. Small-scale structure of fuzzy and axion-like dark matter. *Prog. Part. Nucl. Phys.*, 113:103787, jul 2020.

[202] A. Perez and C. Rovelli. Physical effects of the immirzi parameter in loop quantum gravity. *Phys. Rev. D*, 73:044013, Feb 2006.

[203] P. Candelas and D. J. Raine. General-relativistic quantum field theory: An exactly soluble model. *Phys. Rev. D*, 12:965, Aug 1975.

[204] R.D. Peccei and H. R. Quinn. CP Conservation in the Presence of Instantons. *Phys. Rev. Lett.*, 38:1440–1443, 1977.

[205] R.D. Peccei and H. R. Quinn. Constraints Imposed by CP Conservation in the Presence of Instantons. *Phys. Rev. D*, 16:1791–1797, 1977.

[206] O. Wantz and E. P. S. Shellard. Axion cosmology revisited. *Phys. Rev. D*, 82:123508, Dec 2010.

[207] B. J. Harrington and Harvey K. Shepard. Periodic euclidean solutions and the finite-temperature yang-mills gas. *Phys. Rev. D*, 17:2122–2125, Apr 1978.

[208] R. Hofmann. Nonperturbative approach to Yang-Mills thermodynamics. *Int. J. Mod. Phys. A*, 20:4123–4216, 2005.

[209] G. Veneziano. U(1) without instantons. *Nucl. Phys. B*, 159(1):213–224, 1979.

[210] E. Witten. Current algebra theorems for the U(1) "goldstone boson". *Nucl. Phys. B*, 156(2):269–283, 1979.

[211] C.-P. Ma and E. Bertschinger. Cosmological perturbation theory in the synchronous and conformal newtonian gauges. *Astrophys. J.*, 455:7, Dec 1995.

[212] U. Herbst. The Deconfining phase of SU(2) Yang-Mills thermodynamics. Other thesis, Universität Heidelberg, 6 2005.

[213] T. C. Kraan and P. van Baal. Exact T duality between calorons and Taub - NUT spaces. *Phys. Lett. B*, 428:268–276, 1998.

[214] T. C. Kraan and P. van Baal. Monopole constituents inside SU(n) calorons. *Phys. Lett. B*, 435:389–395, 1998.

[215] E. Seiler. Some more remarks on the witten–veneziano formula for the η' mass. *Phys. Lett. B*, 525(3):355–359, 2002.

[216] S. Azakov, H. Joos, and A. Wipf. Witten–veneziano relation for the schwinger model. *Phys. Lett. B*, 479(1):245–248, 2000.

[217] J. A. Frieman, C. T. Hill, A. Stebbins, and I. Waga. Cosmology with ultralight pseudo Nambu-Goldstone bosons. *Phys. Rev. Lett.*, 75:2077–2080, 1995.

[218] A. G. Riess et al. A 2.4% Determination of the Local Value of the Hubble Constant. *Astrophys. J.*, 826(1):56, 2016.

[219] T. Matos and F. S. Guzman. Scalar fields as dark matter in spiral galaxies. *Class. Quant. Grav.*, 17:L9–L16, 2000.

[220] M. D'Elia, A. Di Giacomo, and E. Meggiolaro. Gauge invariant field strength correlators in pure Yang-Mills and full QCD at finite temperature. *Phys. Rev. D*, 67:114504, 2003.

[221] E. Vicari and H. Panagopoulos. θ dependence of su(n) gauge theories in the presence of a topological term. *Phys. Rep.*, 470(3–4):93–150, January 2009.

[222] S.-S. Li et al. KiDS-1000: Cosmology with improved cosmic shear measurements. *Astron. Astrophys.*, 679:A133, 2023.

this is the last page